NASA
CR
3743
c.1

NASA Contractor Report 3743

LOAN COPY: R
AFWL TECHNICA
KIRTLAND AFB, N
0062363
TECH LIBRARY KAFB, NM

Effects of Nacelle Configuration/Position on Performance of Subsonic Transport

L. H. Bangert, D. K. Krivec,
and R. N. Segall

CONTRACT NAS1-16644
NOVEMBER 1983

25th Anniversary
1958-1983

NASA

TECH LIBRARY KAFB, NM

0062363

NASA Contractor Report 3743

Effects of Nacelle Configuration/Position on Performance of Subsonic Transport

L. H. Bangert, D. K. Krivec,
and R. N. Segall
Lockheed-California Company
Burbank, California

Prepared for
Langley Research Center
under Contract NAS1-16644

National Aeronautics
and Space Administration

Scientific and Technical
Information Branch

1983

TABLE OF CONTENTS

Section		Page
	LIST OF FIGURES	v
	LIST OF TABLES	xv
	LIST OF SYMBOLS	xvii
	SUMMARY	xxi
1	INTRODUCTION	1-1
1.1	Background	1-1
1.2	Objectives	1-2
2	WIND TUNNEL AND MODELS	2-1
2.1	NASA-LaRC 16-Foot Transonic Wind Tunnel	2-1
2.2	Aircraft Model	2-1
2.3	Nacelle Models	2-4
3	TEST PROCEDURE	3-1
3.1	Test Conditions	3-1
3.2	Data Reduction	3-6
4	RESULTS	4-1
4.1	Installed Drag Comparisons	4-1
4.1.1	Comparison of WB, D/BAS, UTW, and C/BAS/REC Configurations	4-3
4.1.2	Effects of Boundary-Layer Diverter on C-Nacelle	4-28
4.1.3	Effects of the Pressure Pylons	4-28
4.2	Installed Lift Comparisons	4-38
4.3	Installed Pitching Moment Comparisons	4-60
5	CONCLUSIONS	5-1
6	RECOMMENDATIONS	6-1
7	REFERENCES	7-1
	APPENDIX	A-1

LIST OF FIGURES

Figure		Page
1	NASA transonic transport model aft mounted nacelle installation.	2-2
2	Aircraft model instrumentation.	2-3
3	Basic features of the C-nacelle	2-5
4	Basic features of the D-nacelle	2-5
5	Photographs of nacelle installations.	2-6
6	Forebody/inlet lip design method for the D-nacelle.	2-10
7	C-nacelle instrumentation	2-12
8	D-nacelle instrumentation	2-13
9	Summary installed drag comparison	4-2
10	Drag polars at Mach 0.80 for WB, D/BAS, C/BAS/REC, and UTW configurations	4-4
11	Drag coefficient versus Mach number at C_L = 0.45 for WB, D/BAS, C/BAS/REC and UTW configurations	4-5
12	Airplane model cross-sectional area distribution for WB, D/BAS and UTW configurations.	4-7
13	Airplane model cross-sectional area distribution for WB, D/BAS and C/BAS/REC configurations.	4-8
14	Maximum L/D versus Mach number for WB, D/BAS, C/BAS/REC and UTW configurations	4-9
15	Wing upper and lower surface pressure distribution, wing body, Mach number = 0.800, C_L = 0.4585, 1.0677 deg. angle of attack	4-10
16	Wing upper and lower surface pressure distribution, D-nacelle/basic pylon, Mach number = 0.800, C_L = 0.4397, 0.5866 deg. angle of attack	4-12
17	Wing pressure distribution, WB and D/BAS configurations, Mach = 0.80, 2Y/B = 0.328	4-15

LIST OF FIGURES (Continued)

Figure		Page
18	Wing pressure distribution, WB and D/BAS configurations, Mach = 0.80, 2Y/B = 0.440	4-16
19	D-nacelle, pressure pylon, external pressure distribution, 0.5668 deg. angle of attack, Mach number = 0.800, C_L = 0.4334	4-17
20	Wing upper and lower surface pressure distribution, UTW nacelle, Mach number = 0.800, C_L = 0.4553, 1.7290 deg. angle of attack	4-19
21	Wing pressure distribution, WB and UTW configurations, Mach = 0.80, 2Y/B = 0.328	4-22
22	Wing pressure distribution, WB and UTW configurations, Mach = 0.80, 2Y/B = 0.440	4-23
23	Wing upper and lower surface pressure distribution, C-nacelle/basic pylon/rec div, Mach number = 0.800, C_L = 0.4334, 0.0773 deg. angle of attack.	4-24
24	C-nacelle, pressure pylon/rec div, external pressure distribution, 0.0723 deg. angle of attack, Mach number = 0.800, C_L = 0.4367	4-26
25	Drag polars at Mach 0.80 for WB, C/BAS/REC, and C/BAS/HL configurations	4-29
26	Drag coefficient versus Mach number at C_L = 0.45 for WB, C/BAS/REC and C/BAS/HL configurations	4-30
27	Maximum L/D versus Mach number for WB, C/BAS/HL and C/BAS/REC configurations.	4-31
28	Wing upper and lower surface pressure distribution, C-nacelle/basic pylon/HL div, Mach number = 0.800, C_L = 0.4207, 0.0665 deg. angle of attack	4-32
29	Drag polars at Mach 0.80 for WB, D/BAS, D/PRES, and C/PRES/REC configurations	4-34
30	Drag coefficient versus Mach number at C_L = 0.45 for WB, D/BAS, D/PRES and C/PRES/REC configurations	4-35

LIST OF FIGURES (Continued)

Figure		Page
31	Airplane model cross-sectional area distribution for WB, D/BAS, D/PRES and C/PRES/REC configurations	4-36
32	Maximum L/D versus Mach number for WB, D/BAS, C/PRES/REC and D/PRES configurations	4-37
33	Wing upper and lower surface pressure distribution, D-nacelle/press pylon, Mach number = 0.800, C_L = 0.4574, 0.5692 deg. angle of attack.	4-39
34	Wing upper and lower surface pressure distribution, C-nacelle/press pylon/rec div, Mach number = 0.800, C_L = 0.4367, 0.0723 deg. angle of attack.	4-41
35	Lift coefficient versus angle of attack at M = 0.80 for WB, D/BAS, C/BAS/REC, C/BAS/HL and UTW configurations . .	4-43
36	Normalized wing section normal force coefficient versus semispan station at Mach 0.80 and α = 1.3 degrees	4-45
37	Wing upper and lower surface pressure distribution, wing body, Mach number = 0.800, C_L = 0.4951, 1.3120 deg. angle of attack	4-47
38	Wing upper and lower surface pressure distribution, D-nacelle/basic pylon, Mach number = 0.800, C_L = 0.5503, 1.3105 deg. angle of attack	4-49
39	Wing pressure distribution, WB and D/BAS configurations, Mach = 0.80, 2Y/B = 0.328	4-51
40	Wing pressure distribution, WB and D/BAS configurations, Mach = 0.80, 2Y/B = 0.440	4-52
41	Wing upper and lower surface pressure distribution, UTW nacelle, Mach number = 0.800, C_L = 0.3773, 1.2300 deg. angle of attack	4-53
42	Wing pressure distribution, WB and UTW configurations, Mach = 0.80, 2Y/B = 0.328	4-55
43	Wing pressure distribution, WB and UTW configurations, Mach = 0.80, 2Y/B = 0.440	4-56

LIST OF FIGURES (Continued)

Figure		Page
44	Wing upper and lower surface pressure distribution, C-nacelle/basic pylon/rec div, Mach number = 0.800, C_L = 0.6077, 1.3063 deg. angle of attack.	4-57
45	Lift coefficient versus angle of attack at Mach 0.80 for WB, D/BAS, D/PRES and C/PRES/REC configurations	4-59
46	Lift coefficient versus pitching moment coefficient at M = 0.80 for WB, D/BAS, C/BAS/HL, C/BAS/REC and UTW configurations.	4-61
47	Angle of attack versus pitching moment coefficient at M = 0.80 for WB, D/BAS, C/BAS/HL, C/BAS/REC and UTW configurations.	4-62
48	Normalized wing section pitching moment coefficient versus semispan station at Mach 0.80 and α = 1.3 degress. . .	4-64
49	Lift coefficient versus pitching moment coefficient at M = 0.80 for WB, D/BAS, D/PRES and C/PRES/REC configurations.	4-65
50	Angle of attack versus pitching moment coefficient at M = 0.80 for WB, D/BAS, D/PRES, and C/PRES/REC configurations.	4-66
A1	Drag polars at Mach 0.70 for WB, D/BAS, C/BAS/REC, and UTW configurations	A-2
A2	Drag polars at Mach 0.70 for WB, C/BAS/REC, and C/BAS/HL configurations	A-3
A3	Drag polars at Mach 0.70 for WB, D/BAS, D/PRES, and C/PRES/REC configurations	A-4
A4	Drag polars at Mach 0.75 for WB, D/BAS, C/BAS/REC, and UTW configurations	A-5
A5	Drag polars at Mach 0.75 for WB, C/BAS/REC, and C/BAS/HL configurations	A-6
A6	Drag polars at Mach 0.75 for WB, D/BAS, D/PRES, and C/PRES/REC configurations	A-7

LIST OF FIGURES (Continued)

Figure		Page
A7	Drag polars at Mach 0.78 for WB, D/BAS, C/BAS/REC, and UTW configurations	A-8
A8	Drag polars at Mach 0.78 for WB, C/BAS/REC, and C/BAS/HL configurations	A-9
A9	Drag polars at Mach 0.78 for WB, D/BAS, D/PRES, and C/PRES/REC configurations	A-10
A10	Drag polars at Mach 0.79 for WB, D/BAS, C/BAS/REC, and UTW configurations	A-11
A11	Drag polars at Mach 0.79 for WB, C/BAS/REC, and C/BAS/HL configurations	A-12
A12	Drag polars at Mach 0.79 for WB, D/BAS, D/PRES, and C/PRES/REC configurations	A-13
A13	Drag polars at Mach 0.81 for WB, D/BAS, C/BAS/REC, and UTW configurations	A-14
A14	Drag polars at Mach 0.81 for WB, C/BAS/REC, and C/BAS/HL configurations	A-15
A15	Drag polars at Mach 0.81 for WB, D/BAS, D/PRES, and C/PRES/REC configurations	A-16
A16	Drag polars at Mach 0.83 for WB, D/BAS, and C/BAS/REC configurations	A-17
A17	Drag polars at Mach 0.83 for WB, C/BAS/REC, and C/BAS/HL configurations	A-18
A18	Drag polars at Mach 0.83 for WB, D/BAS, D/PRES, and C/PRES/REC configurations	A-19
A19	Drag polars at Mach 0.85 for WB, D/BAS, and C/BAS/REC configurations	A-20
A20	Drag polars at Mach 0.85 for WB, C/BAS/REC, and C/BAS/HL configurations	A-21
A21	Drag polars at Mach 0.85 for WB, D/BAS, D/PRES, and C/PRES/REC configurations	A-22

LIST OF FIGURES (Continued)

Figure		Page
A22	Wing upper and lower surface pressure distribution, wing body, Mach number = 0.700, C_L = 0.4419, 1.2820 deg. angle of attack	A-23
A23	Wing upper and lower surface pressure distribution, D-nacelle/basic pylon, Mach number = 0.700, C_L = 0.4621, 1.0637 deg. angle of attack	A-25
A24	Wing upper and lower surface pressure distribution, C-nacelle/basic pylon/rec div, Mach number = 0.700, C_L = 0.4491, 0.5517 deg. angle of attack	A-27
A25	Wing upper and lower surface pressure distribution, UTW nacelle, Mach number = 0.700, C_L = 0.4734, 2.1730 deg. angle of attack	A-29
A26	Wing upper and lower surface pressure distribution, wing body, Mach number = 0.850, C_L = 0.4385, 1.1070 deg. angle of attack	A-31
A27	Wing upper and lower surface pressure distribution, D-nacelle/basic pylon, Mach number = 0.850, C_L = 0.4641, 0.8533 deg. angle of attack	A-33
A28	Wing upper and lower surface pressure distribution, C-nacelle/basic pylon/rec div, Mach number = 0.850, C_L = 0.4715, 0.5949 deg. angle of attack	A-35
A29	D-nacelle, pressure pylon, external pressure distribution 0.8229 deg. angle of attack, Mach number = 0.700, C_L = 0.4416	A-37
A30	C-nacelle, pressure pylon/rec div, external pressure distribution, 0.5561 deg. angle of attack, Mach number = 0.700, C_L = 0.4503	A-39
A31	D-nacelle, pressure pylon, external pressure distribution, 0.8474 deg. angle of attack, Mach number = 0.850, C_L = 0.4481	A-41
A32	C-nacelle, pressure pylon/rec div, external pressure distribution, 0.6041 deg. angle of attack, Mach number = 0.850, C_L = 0.4671	A-43

LIST OF FIGURES (Continued)

Figure		Page
A33	Oil flow photograph for D/BAS configuration at M = 0.8, α = 0.67 deg.	A-45
A34	Oil flow photograph for D/BAS configuration at M = 0.8, α = 2.48 deg.	A-48
A35	Oil flow photograph for D/BAS configuration at M = 0.85, α = 0.49 deg.	A-50
A36	Oil flow photograph for C/BAS/REC configuration at M = 0.80, α = 0.20 deg.	A-51
A37	Oil flow photograph for C/BAS/REC configuration at M = 0.85, α = 0.40 deg.	A-53
A38	Lift coefficient versus angle of attack at M = 0.70 for WB, D/BAS, C/BAS/REC, C/BAS/HL and UTW configurations	A-55
A39	Lift coefficient versus angle of attack at Mach 0.70 for WB, D/BAS, D/PRES and C/PRES/REC configurations	A-56
A40	Lift coefficient versus angle of attack at M = 0.75 for WB, D/BAS, C/BAS/REC, C/BAS/HL and UTW configurations	A-57
A41	Lift coefficient versus angle of attack at Mach 0.75 for WB, D/BAS, D/PRES and C/PRES/REC configurations	A-58
A42	Lift coefficient versus angle of attack at M = 0.78 for WB, D/BAS, C/BAS/REC, C/BAS/HL and UTW configurations	A-59
A43	Lift coefficient versus angle of attack at Mach 0.78 for WB, D/BAS, D/PRES and C/PRES/REC configurations	A-60
A44	Lift coefficient versus angle of attack at M = 0.79 for WB, D/BAS, C/BAS/REC, C/BAS/HL and UTW configurations	A-61
A45	Lift coefficient versus angle of attack at Mach 0.79 for WB, D/BAS, D/PRES and C/PRES/REC configurations	A-62
A46	Lift coefficient versus angle of attack of M = 0.81 for WB, D/BAS, C/BAS/REC, C/BAS/HL and UTW configurations	A-63

LIST OF FIGURES (Continued)

Figure		Page
A47	Lift coefficient versus angle of attack at Mach 0.81 for WB, D/BAS, D/PRES and C/PRES/REC configurations	A-64
A48	Lift coefficient versus angle of attack at M = 0.83 for WB, D/BAS, C/BAS/REC and C/BAS/HL configurations	A-65
A49	Lift coefficient versus angle of attack at Mach 0.83 for WB, D/BAS, D/PRES and C/PRES/REC configurations	A-66
A50	Lift coefficient versus angle of attack at M = 0.85 for WB, D/BAS, C/BAS/REC and C/BAS/HL configurations	A-67
A51	Lift coefficient versus angle of attack at Mach 0.85 for WB, D/BAS, D/PRES and C/PRES/REC configurations	A-68
A52	Lift coefficient versus pitching moment coefficient at M = 0.70 for WB, D/BAS, C/BAS/HL, C/BAS/REC and UTW configurations	A-69
A53	Lift coefficient versus pitching moment coefficient at M = 0.70 for WB, D/BAS, D/PRES and C/PRES/REC configurations	A-70
A54	Lift coefficient versus pitching moment coefficient at M = 0.75 for WB, D/BAS, C/BAS/HL, C/BAS/REC and UTW configurations	A-71
A55	Lift coefficient versus pitching moment coefficient at M = 0.75 for WB, D/BAS, D/PRES and C/PRES/REC configurations	A-72
A56	Lift coefficient versus pitching moment coefficient at M = 0.78 for WB, D/BAS, C/BAS/HL, C/BAS/REC and UTW configuration	A-73
A57	Lift coefficient versus pitching moment coefficient at M = 0.78 for WB, D/BAS, D/PRES and C/PRES/REC configuration	A-74
A58	Lift coefficient versus pitching moment coefficient at M = 0.79 for WB, D/BAS, C/BAS/HL, C/BAS/REC and UTW configurations	A-75

LIST OF FIGURES (Continued)

Figure		Page
A59	Lift coefficient versus pitching moment coefficient at M = 0.79 for WB, D/BAS, D/PRES and C/PRES/REC configurations	A-76
A60	Lift coefficient versus pitching moment coefficient at M = 0.81 for WB, D/BAS, C/BAS/HL, C/BAS/REC and UTW configurations	A-77
A61	Lift coefficient versus pitching moment coefficient at M = 0.81 for WB, D/BAS, D/PRES and C/PRES/REC configurations	A-78
A62	Lift coefficient versus pitching moment coefficient at M = 0.83 for WB, D/BAS, C/BAS/HL and C/BAS/REC configurations	A-79
A63	Lift coefficient versus pitching moment coefficient at M = 0.83 for WB, D/BAS, D/PRES and C/PRES/REC configurations	A-80
A64	Lift coefficient versus pitching moment coefficient at M = 0.85 for WB, D/BAS, C/BAS/HL and C/BAS/REC configurations	A-81
A65	Lift coefficient versus pitching moment coefficient at M = 0.85 for WB, D/BAS, D/PRES and C/PRES/REC configurations	A-82

LIST OF TABLES

Table		Page
I.	Comparison of Nacelle Characteristics	2-8
II.	Wind Tunnel Test Run Log, Test Number 367	3-2
III.	Transition Grit Summary	3-5
IV.	Internal Drag Summary	3-8

LIST OF SYMBOLS

Symbol	
A	Cross-sectional area
A_{WING}	Wing reference area, 529.59 in.^{2}
B	Wing span
BDC	Bottom dead center
BL	Aircraft buttline, inches
c	Airfoil chord
$\bar{c}$	Mean aerodynamic chord (MAC)
C_D	Drag coefficient
ΔC_D	Nacelle-on minus nacelle-off drag coefficient increment; also, a drag coefficient increment
C_L	Lift coefficient
C_m	Wing section pitching moment coefficient
C_M	Pitching moment coefficient
C_n	Wing section normal force coefficient
C_p	Pressure coefficient, $(p-p_o)/q_o$
Counts	Drag coefficient x 10^4
C/BAS/HL	Wing-body plus C-nacelle, basic pylon, and highlight diverter
C/BAS/REC	Wing-body plus C-nacelle, basic pylon, and recessed diverter
C/PRES/REC	Wing-body plus C-nacelle, pressure pylon, and recessed diverter
$D_{EXIT,INT}$	Internal diameter at nacelle exit plane
D_{INT}	Internal drag force of flow-through nacelle
D/BAS	Wing-body plus D-nacelle and basic pylon
D/PRES	Wing-body plus D-nacelle and pressure pylon

LIST OF SYMBOLS (Continued)

Symbol	
FUS STA	Fuselage station, inches
h	Height of the rectangle having the same area as half of a circle, $2hR = \pi R^2/2$
L/D	Lift-to-drag ratio
$(L/D)_{MAX}$	Maximum lift-to-drag ratio
m	Mass flow rate
M	Mach number
MAC	Mean aerodynamic chord ($\bar{c}$)
M_{DD}	Drag-divergence Mach number
MFR	Mass flow ratio, A_o/A_{HL}
NAC STA	Nacelle station, inches
p	Static pressure
p_T	Total pressure
Δp	$p-p_o$
q	Dynamic pressure
R	Radius
Re	Reynolds number
SAR	Specific air range
SFC	Specific fuel consumption
T_T	Total temperature
t/c	Wing section maximum thickness to chord ratio
USB	Upper surface blowing
UTW	Wing-body plus conventional underwing-forward pylon-mounted nacelle

LIST OF SYMBOLS (Continued)

Symbol	
V	Velocity
W	Weight flow rate
W_{AC}	Weight of aircraft
$\dot{W}_F$	Fuel weight flow rate
WB	Wing-body
WL	Aircraft waterline, inches
x	Longitudinal distance from airfoil leading edge
2Y/B	Wing semispan location
α	Angle of attack, degrees
δ	Total pressure divided by sea level pressure, $P_T/14.696$ psia
θ	Nominal roll angle of row of nacelle pressure orifices
$\sqrt{\theta}$	Square root of total temperature divided by sea level standard day temperature, $\sqrt{T_T/518.69^{\circ}R}$

Subscripts:

ex	Exit
HL	Highlight
o	Freestream
TH	Throat

SUMMARY

An experimental study was conducted to explore possible reductions in installed propulsion system drag due to underwing-aft nacelle locations. Both circular (C) and D inlet cross section nacelles were tested. The primary objectives were: to determine the relative installed drag of the C and D-nacelle installations; and, to compare the drag of each aft nacelle installation with that of a conventional underwing-forward, pylon-mounted (UTW) nacelle installation. The tests were performed in the NASA-Langley Research Center 16-Foot Transonic Wind Tunnel at Mach numbers from 0.70 to 0.85, airplane angles of attack from -2.5 to 4.1 degrees, and Reynolds numbers per foot from 3.4 to 4.0 million. The nacelles were installed on the NASA USB full-span transonic transport model with horizontal tail on. The D-nacelle installation had the smallest drag of those tested. The UTW nacelle installation had the largest drag, at 6.8 percent larger than the D at Mach number 0.80 and $C_L = 0.45$. Each tested configuration still had some interference drag, however. This interference could probably be reduced in each case by eliminating local regions of supersonic flow. The C and D-nacelle installations and the wing-body (WB) each had a drag-divergence Mach number (M_{DD}) of about 0.81. M_{DD} was about 0.78 for the UTW installation, however. The effect of the aft nacelles on airplane lift was to increase C_L at a fixed angle of attack relative to the WB. There was higher lift on the inboard wing sections because of higher pressures on the wing lower surface. The effects of the UTW installation on lift were opposite to those of the aft nacelles.

1. INTRODUCTION

1.1 Background

The location and shape of the propulsion system can have a major influence on the performance of subsonic cruise aircraft. Because of the need to minimize fuel consumption at cruise conditions, it is important to minimize the installed drag of the propulsion system. Previous studies (ref. 1) have suggested that it may be difficult to eliminate interference drag for conventional underwing-forward, pylon-mounted, mixed flow nacelles and supercritical wings. For such installations, modifications to the wing surface contours might be required to avoid extensive regions of supersonic flow. In this respect, unconventional propulsion installations may have some relative advantages.

In the present study, the possible advantages of an underwing-aft nacelle location were explored. Some of these were anticipated to be: (1) less disturbance of flow over the upper surface of the wing; (2) a more favorable cross-sectional area distribution, giving lower wave drag and higher drag-divergence Mach number, M_{DD}; and (3) enhanced wing lift due to more favorable underwing pressure distributions. The primary disadvantage of the underwing-aft nacelle location is the increased tendency to flutter. Increased strength and weight of the inboard wing, and/or active controls on ailerons, would probably be required for flutter suppression. The present study adopted the viewpoint that the potential for drag reduction should be established first. The relative advantages and disadvantages of the underwing-aft location would then be considered in a total aircraft design study.

The underwing-aft location also suggested possibilities for shaping the nacelles so that they were more highly blended with the wing. Thus, the possible drag benefits of a non-circular, D-nacelle shape were also explored.

1.2 Objectives

There were two primary objectives in the present study:

1. Obtain experimental data to evaluate the relative effects of circular and D-shaped nacelles in an underwing-aft position on installed propulsion system drag.

2. Compare the results for the underwing-aft nacelles with results for previously tested underwing-forward, pylon-mounted nacelles.

2. WIND TUNNEL AND MODELS

2.1 NASA-LaRC 16-Foot Transonic Wind Tunnel

The test program was conducted in the NASA-Langley 16-foot transonic wind tunnel. This NASA-LaRC facility is a continuous flow, single return, atmospheric wind tunnel with a slotted octagonal throat and test section which is 15.5 feet wide and 32 feet long. The tunnel has an air speed capability ranging from Mach number 0.2 to 1.3. The test program used only the Mach 0.7 to 0.85 speed range. Over this reduced range, the Reynolds number per foot was between 3.4×10^6 and 4.0×10^6, depending upon tunnel air speed and atmospheric temperature and pressure. The angle of attack capability of the main strut support for the model is -5 to 15 degrees. A range of -2.5 to 4.1 degrees was used for this test.

2.2 Aircraft Model

The transonic transport aircraft model used in this test was a high supercritical wing, full span, T-tail, sting mounted, NASA-owned model. The fuselage had an overall length of 62 inches, and the wing span was 63.12 inches. General dimensions are shown in figure 1. This model is also known as the Upper Surface Blowing (USB) model. It was also used during previous NASA-LaRC tests of an underwing-forward, pylon mounted, circular (UTW) nacelle installation.

The upper and lower wing surfaces of the aircraft model were instrumented with 379 static pressure taps. The port wing was instrumented from the fuselage centerline to the 44 percent semi-span station ($2Y/B = 0.44$). The starboard wing was instrumented from 55 percent to 95 percent semispan. Specific locations of the pressure taps are shown in figure 2. All scanivalves were mounted inside the model so that only electrical leads and reference pressure and backing pressure lines were required to bridge the force balance. As a result, both force and pressure data could be obtained simultaneously without introducing large tare forces.

FIGURE 1. NASA TRANSONIC TRANSPORT MODEL
AFT-MOUNTED NACELLE INSTALLATION

DIMENSIONS ARE IN INCHES

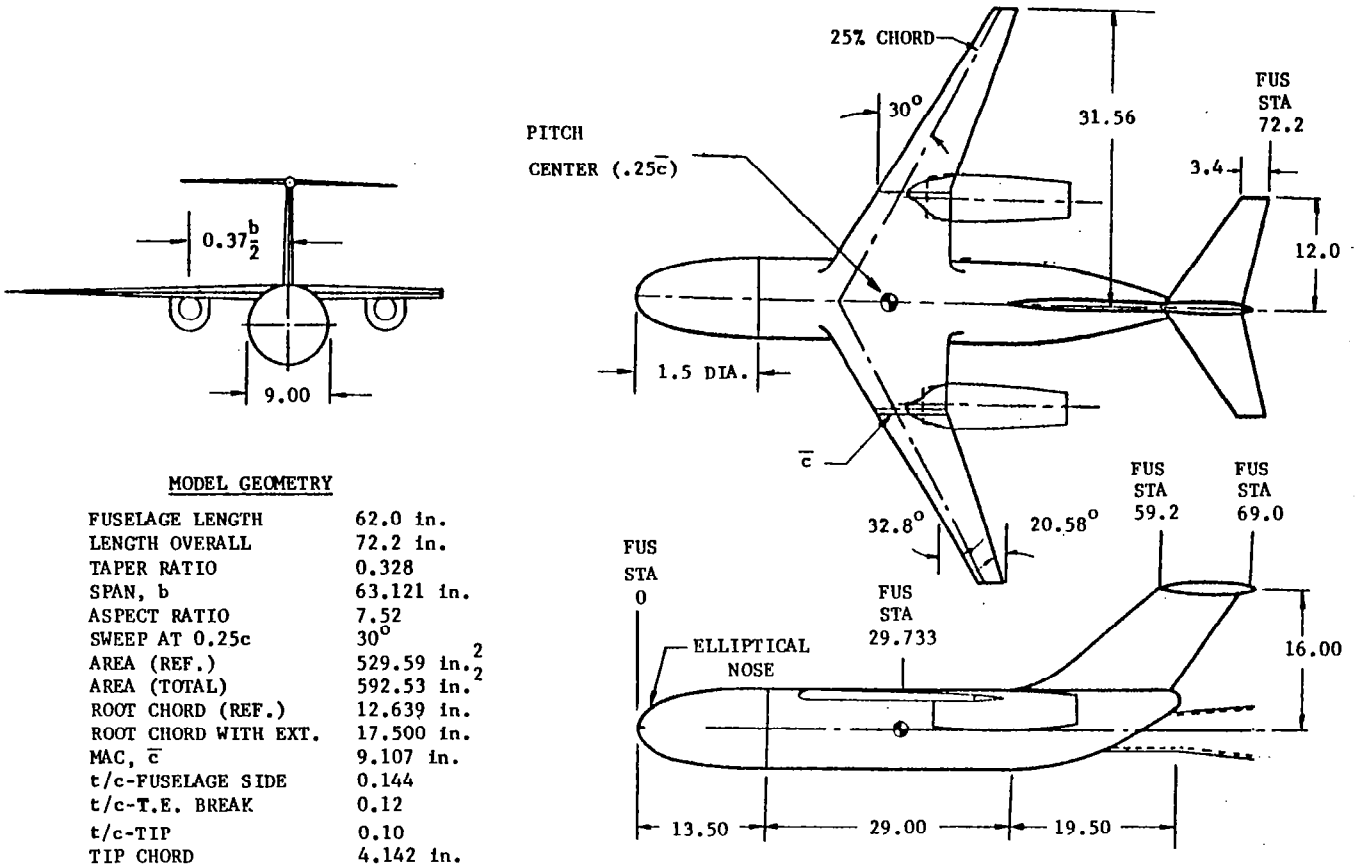

MODEL GEOMETRY

FUSELAGE LENGTH	62.0 in.
LENGTH OVERALL	72.2 in.
TAPER RATIO	0.328
SPAN, b	63.121 in.
ASPECT RATIO	7.52
SWEEP AT 0.25c	30°
AREA (REF.)	529.59 in.^{2}
AREA (TOTAL)	592.53 in.^{2}
ROOT CHORD (REF.)	12.639 in.
ROOT CHORD WITH EXT.	17.500 in.
MAC, $\bar{c}$	9.107 in.
t/c-FUSELAGE SIDE	0.144
t/c-T.E. BREAK	0.12
t/c-TIP	0.10
TIP CHORD	4.142 in.

FIGURE 2. AIRCRAFT MODEL INSTRUMENTATION

UPPER WING SURFACE

X/C

2Y/B=0.0	2Y/B=.1540, .25,.328, .370,.44,.55	2Y/B=.75, .85	2Y/B=.95
.0500	.0000	.0000	.0250
.0750	.0125	.0250	.0750
.1000	.0250	.0500	.1000
.1500	.0500	.1000	.1500
.2000	.0750	.1500	.2000
.2500	.1000	.2000	.2500
.3000	.1500	.2500	.3500
.3500	.2000	.3000	.4500
.4000	.2500	.3500	.5500
.4500	.3000	.4000	.6500
.5000	.3500	.4500	.8000
.5500	.4000	.5000	.9000
.6000	.4500	.5500	
.6500	.5000	.6000	
.7000	.5500	.6500	
.7500	.6000	.7000	
.8000	.6500	.8000	
.8500	.7000	.9500	
.9000	.7500		
.9500	.8000		
	.8500		
	.9000		
	.9500		

STATIC PRESSURE
TAP LOCATIONS, 2Y/B

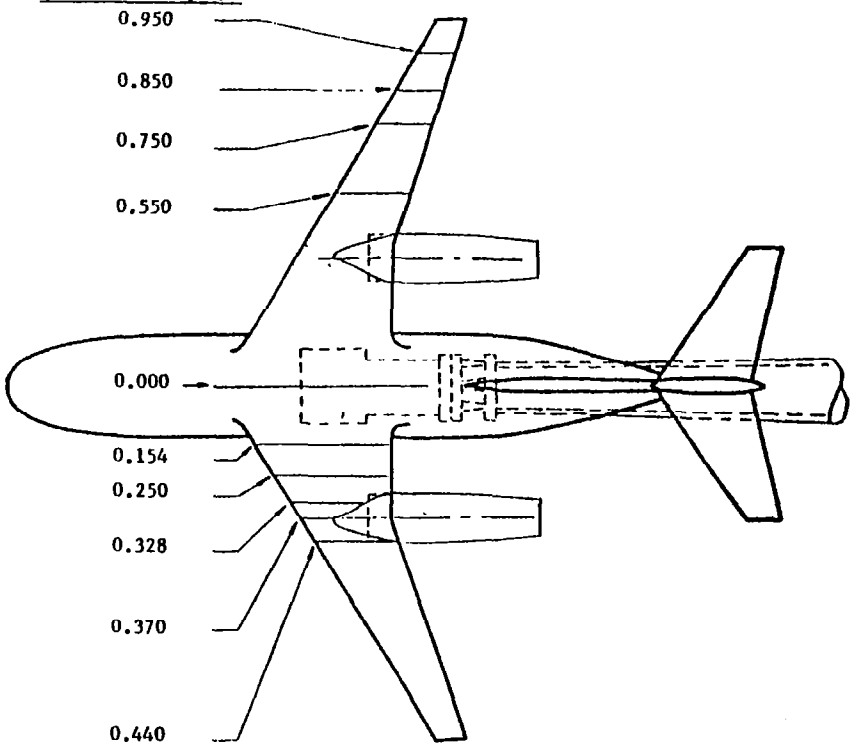

LOWER WING SURFACE

X/C

2Y/B=.1540, .25,.328, .370,.44,.55	2Y/B=.75, .85,.95
.0125	.0250
.0250	.0750
.0500	.1000
.0750	.1500
.1000	.2000
.1500	.2500
.2000	.3500
.2500	.4500
.3000	.5500
.3500	.6500
.4000	.8000
.4500	.9000
.5000	
.5500	
.6000	
.6500	
.7000	
.7500	
.8000	
.8500	
.9000	
.9500	

A six component NASA-LaRC facility force balance (Number 838) was used to measure aerodynamic forces on the model. The balance was located inside the fuselage cavity. The designed maximum normal force, axial force and pitching moment for this balance were $\pm$ 3000 lb, $\pm$ 250 lb and $\pm$ 7500 in-lb, respectively. Quoted accuracy was 0.5 percent of full scale reading for all components (equivalent to 5.5 drag counts at Mach number 0.8 for this model). During this test, the force balance was dead-weight calibrated up to 1600 lb normal force, 200 lb axial force, and 1500 in-lb pitching moment.

Pitching moment is presented relative to a point located axially at 25 percent mean aerodynamic chord (MAC) and vertically at WL 0. The MAC had a chord length of 9.107 inches and was located at 41.76 percent semi-span station. The 25 percent MAC point was at fuselage station 29.733.

2.3 Nacelle Models

Two types of underwing-aft mounted, flow-through nacelle models were designed by Lockheed and fabricated by NASA: one circular and one D-shaped. The basic features of the circular (C-nacelle) and D-nacelle designs are shown in figures 3 and 4, respectively. Each nacelle had a basic (low-profile) pylon and a pressure (high-profile) pylon. The latter permitted pressure tubing to be routed from the wing to the nacelle without any modification to the wing structure. The C-nacelle was tested with two boundary-layer diverters: a recessed diverter and a highlight diverter. The C and D-nacelles were of the same length, maximum diameter, highlight area, design Mach number, and design mass flow ratio (MFR) as the UTW nacelle to allow direct comparison with test results for the UTW nacelle. A more detailed comparison of the aft mounted and UTW nacelle characteristics is given in table I. Photographs of the nacelles installed on the aircraft model are shown in figure 5.

The contours of the C and D-nacelles were selected to minimize drag at free-stream Mach number (M_o) of 0.80, MFR = 0.70, and lift coefficient (C_L) of 0.45 (corresponding to angle of attack, α, of about one degree). The internal

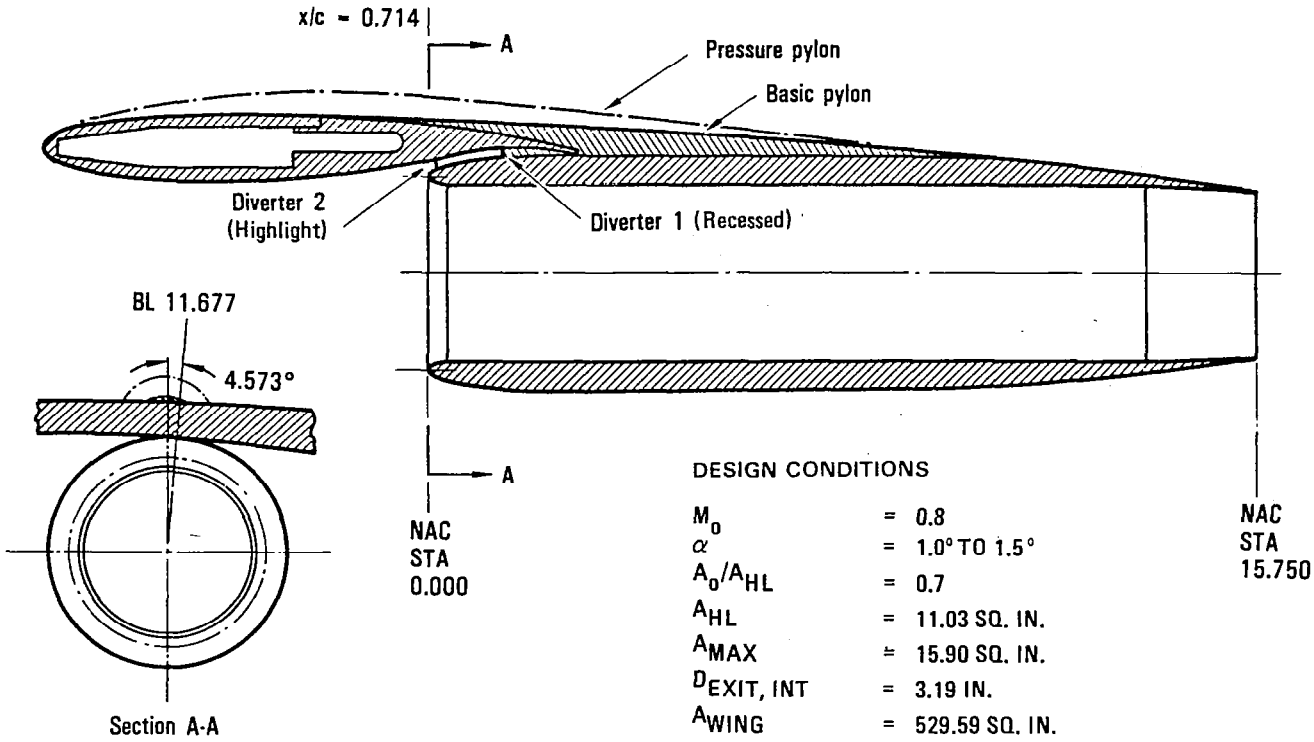

Figure 3. - Basic features of the C-nacelle.

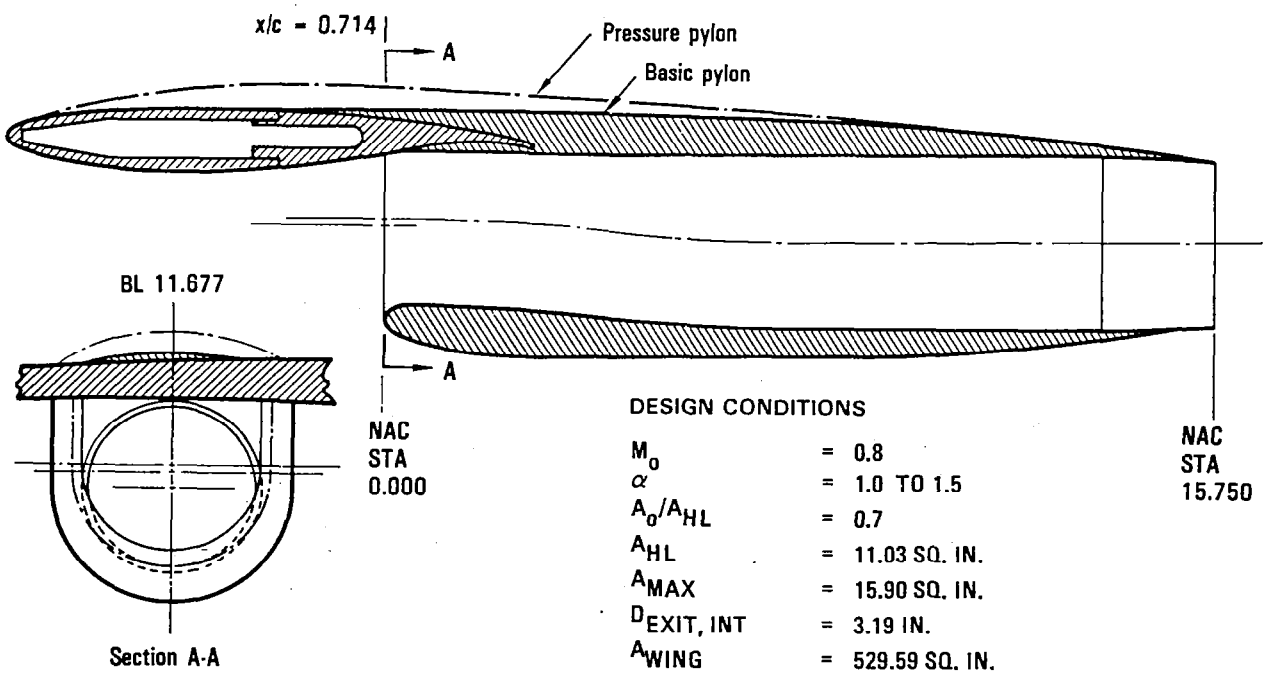

Figure 4. - Basic features of the D-nacelle.

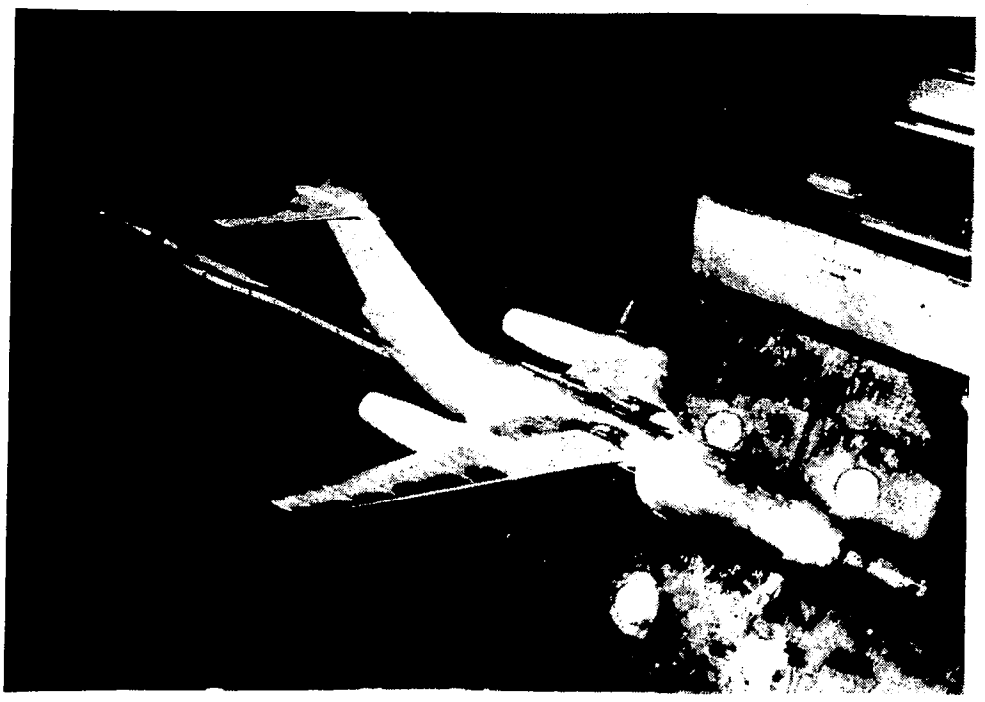

a. Aft mounted D-nacelle (similar for C-nacelle).

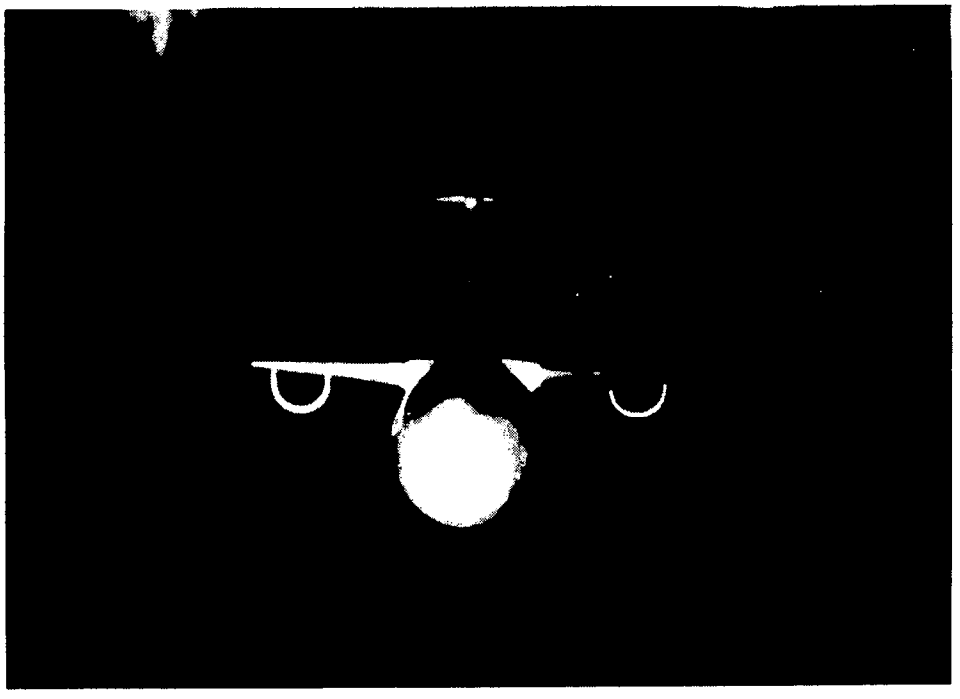

b. Aft mounted D-nacelle.

Figure 5. - Photographs of nacelle installations.

c. Aft mounted C-nacelle.

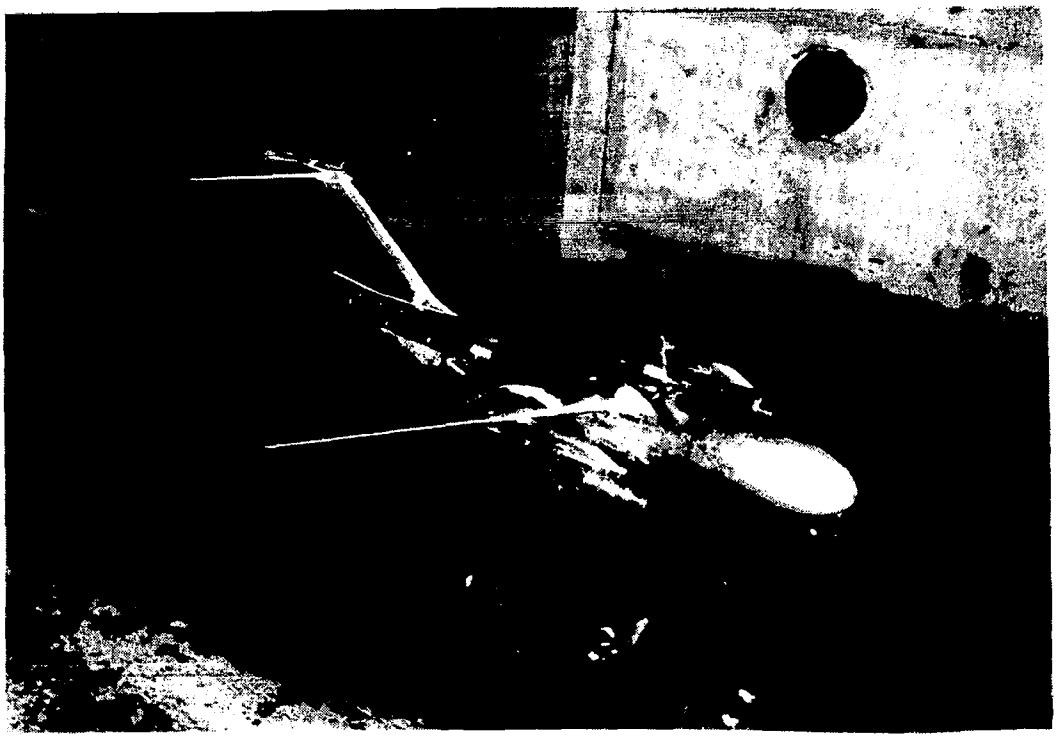

d. UTW nacelle.

Figure 5. - Photographs of nacelle installations.

TABLE I. COMPARISON OF NACELLE CHARACTERISTICS

ITEM	AFT MOUNTED NACELLE	UTW NACELLE
DESIGN MACH NUMBER	0.8	0.8
DESIGN MASS FLOW RATIO	0.7	0.7
AIRCRAFT ANGLE OF ATTACK, DEG.	1.5	1.5
NACELLE LENGTH, IN.	15.75	15.75
NACELLE MAX RADIUS, IN.	2.25	2.25
HIGHLIGHT RADIUS, IN.	1.874	1.874
THROAT RADIUS, IN.	1.703	1.795
CONTRACTION RATIO	1.21	1.09
FOREBODY CONTOUR	SHAPED ELLIPSE	NACA-1
FOREBODY LENGTH, IN.	2.713	3.375
EXT. CYLINDRICAL LENGTH, IN.	5.087	3.975
AFTBODY LENGTH, IN.	7.95	8.4
AFTBODY BOATTAIL ANGLE, DEG.	7.0	8.8
AFTBODY RADIUS OF CURVATURE, IN.	$37 \rightarrow \infty$	55
INLET LIP CONTOUR	TAILORED LEMNISCATE	ELLIPSE
INLET LIP ASPECT RATIO	2.00	1.86

nacelle contours had either converging or constant area sections to avoid internal flow separation. The external contours were selected using design methods derived from the results of references 2 and 3. Also, the first and second derivatives of the nacelle coordinates in the axial direction (x) were continuous (except for the internal contour at the end of the cylindrical section near the nacelle exit plane). This was done to minimize the occurrence of unwanted pressure disturbances that might lead to shock formation and/or boundary-layer separation. Nacelle and pylon contours were also chosen to be compatible with the wing of the aircraft; i.e., no modification to the wing hardware was required except for the holes necessary to attach the nacelles. A detailed numerical tabulation of nacelle and pylon contour coordinates is given in reference 4.

The C-nacelle was placed at the same span location as the UTW nacelle. The C-nacelle was located vertically as close to the wing as possible in order to minimize wetted area. The vertical position of the nacelle was limited by the trailing edge of the wing and the constraint of not modifying the wing.

Axial position was chosen to provide no predicted adverse pressure gradient for the flow in the gap between the nacelle and wing; and also to allow minimal entrainment of air outside of the boundary layers into this gap.

The D-nacelle was placed at the same span and axial locations as the C-nacelle. The vertical position of the D-nacelle was chosen so that the flat-top internal contour projected to the highlight plane.

The inlet for the D-nacelle was designed for the same throat, highlight, nacelle maximum, and capture areas as the C-nacelle. The upper half of each of these circular areas for the C-nacelle was replaced by an equivalent rectangular area for the D-nacelle. The flat tops of these rectangular areas were superimposed (frontal view), resulting in a non-alignment of the centers of each area. Whereas the design mass flow ratio for the C-nacelle was 0.70, the equivalent axisymmetric mass flow ratio for the bottom of the D-nacelle was 0.55 because of this non-alignment of centers. This design method, shown schematically in figure 6, results in a forebody for the bottom of the D-nacelle which has a large external projected area relative to the C-nacelle.

Internal and external contours for the D-nacelle were gradually transformed in the axial direction from a D to a circular shape. The aft end of the D-nacelle was circular for 7.95 inches forward of the exit plane, and had the same internal and external contours throughout this region as the C-nacelle.

Basic pylons for both the C and D-nacelles originated at the maximum thickness point on the wing upper surface for the chosen nacelle span location. The pylon contour at the pylon leading edge point was made tangent to the wing surface. Both basic pylons were designed so that they: (1) blended smoothly into the respective nacelles at the wing trailing edge; (2) faired smoothly on to the nacelle afterbodies; and (3) provided a smooth intersection with the wing upper surface.

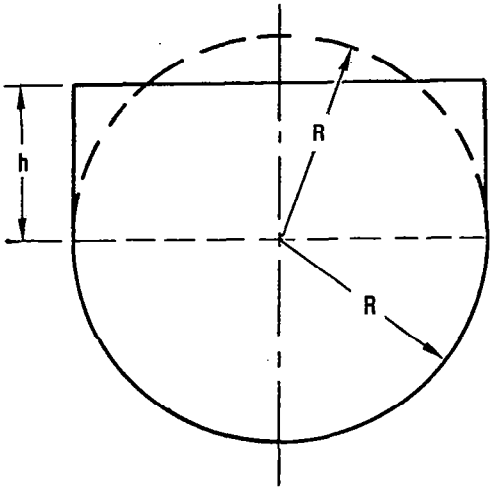

Rectangular area = $\frac{\pi R^2}{2}$; h = $\frac{\pi R}{4}$

R_{HL} = 1.874 in.

R_{TH} = 1.703

R_{MAX} = 2.250

R_0 = $\sqrt{MFR}\ R_{HL}$ = 1.5679

Superimposed with common top

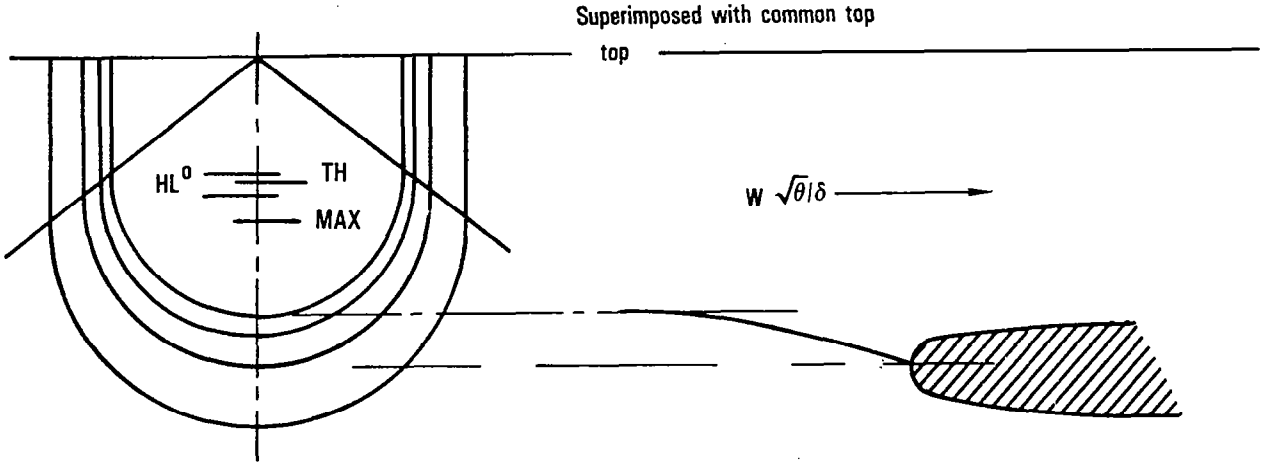

Equivalent BDC axisymmetric MFR = $\left[\frac{R_0}{R_{HL} + (h_{HL} - h_0)}\right]^2$ = 0.550

Figure 6. - Forebody/inlet lip design method for the D-nacelle.

Pressure pylons were designed to be similar to the basic pylons, except that the leading edge points were near the wing leading edge. Sufficient internal volume was provided for routing the pressure tubes over the wing trailing edge to avoid the wing structure. This resulted in a larger pylon than the basic pylon.

Two wing/nacelle boundary-layer diverters were designed for the C-nacelle. The highlight diverter leading edge was slightly aft of the nacelle highlight plane. The recessed diverter leading edge was placed at the axial station where the wing and nacelle boundary-layers were predicted to fill the gap between the wing and nacelle. Both diverters blended smoothly onto the pylon at the wing trailing edge.

The port pressure pylons and nacelles (both C and D) were instrumented with static pressure taps. The C-nacelle had 88 external and 12 internal taps. The D-nacelle had 83 external and 16 internal taps. Each pressure pylon had 29 taps. Instrumentation is shown schematically in figures 7 and 8.

FIGURE 7. C-NACELLE INSTRUMENTATION
PORT NACELLE

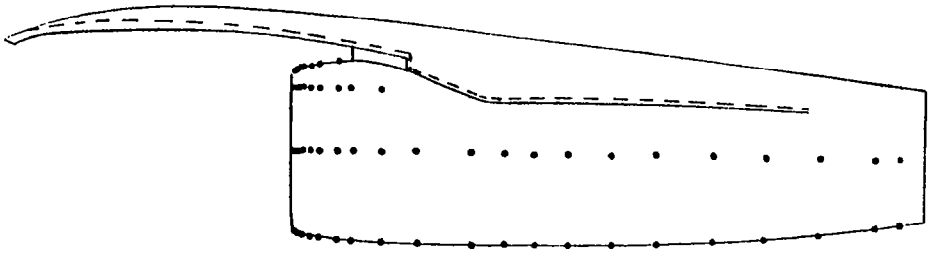

SIDE VIEW

NACELLE EXTERNAL PRESSURE
TAP LOCATIONS
(INBOARD AND OUTBOARD SIDES)

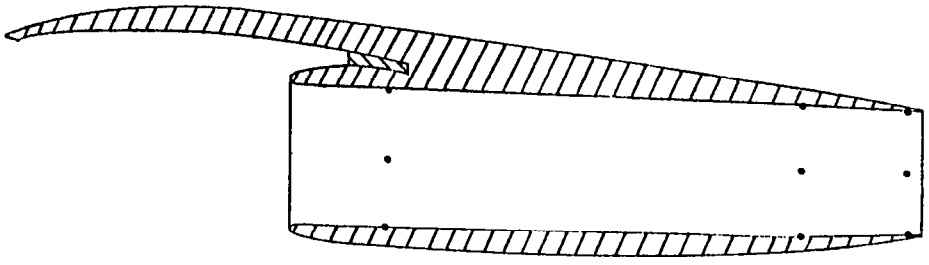

SIDE VIEW

NACELLE INTERNAL PRESSURE
TAP LOCATIONS
(INBOARD AND OUTBOARD SIDES)

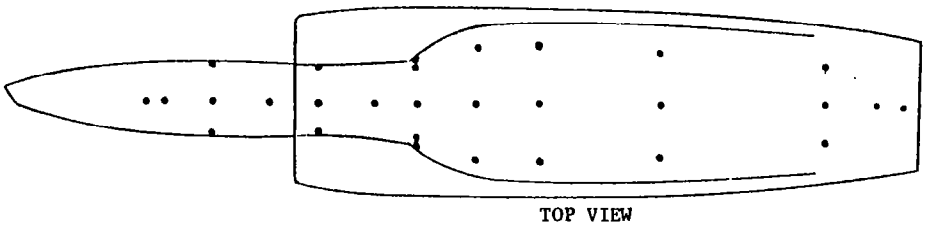

TOP VIEW

PYLON PRESSURE
TAP LOCATIONS

FIGURE 8. D-NACELLE INSTRUMENTATION

PORT NACELLE

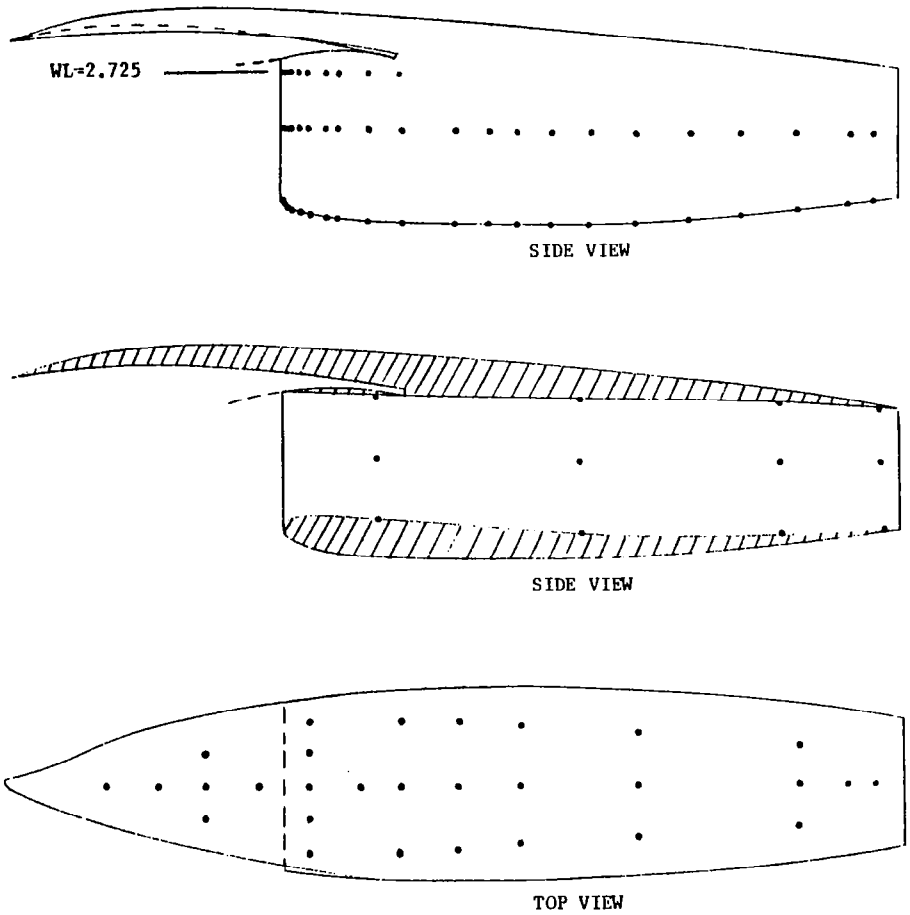

NACELLE EXTERNAL PRESSURE TAP LOCATIONS (INBOARD AND OUTBOARD SIDES)

NACELLE INTERNAL PRESSURE TAP LOCATIONS (INBOARD AND OUTBOARD SIDES)

PYLON PRESSURE TAP LOCATIONS

3. TEST PROCEDURE

3.1 Test Conditions

Six model Configurations were tested:

1.	WB:	Wing-Body
2.	D/BAS:	Wing-Body plus D-Nacelle and Basic Pylon
3.	D/PRES:	Wing-Body plus D-Nacelle and Pressure Pylon
4.	C/BAS/REC:	Wing-Body plus C-Nacelle, Basic Pylon, and Recessed Diverter
5.	C/BAS/HL:	Wing-Body plus C-Nacelle, Basic Pylon, and Highlight Diverter
6.	C/PRES/REC:	Wing-Body plus C-Nacelle, Pressure Pylon and Recessed Diverter

These configurations were tested through a Mach number range of 0.7 to 0.85 and an angle of attack range of -2.5 to 4.1 degrees. Lift and drag force data, pitching moment data, and wing pressure data were obtained. For configurations involving pressure pylons, nacelle and pylon pressure data were also obtained. Oil flow photographs were taken at selected conditions. A detailed run log is shown in table II.

Test conditions were chosen based on the model design conditions and the conditions for the previous UTW tests. Tests at Mach numbers 0.83 and 0.85 were added in order to more precisely define the drag rise characteristics. Mach number 0.81 was the highest Mach number in the UTW tests for direct comparison with the present tests. Angles of attack were chosen to fully define the drag polar, especially in the region near the design lift coefficient of 0.45.

All tests were conducted with the tail fixed in the same position that was used during the UTW tests.

TABLE II. WIND TUNNEL TEST RUN LOG, TEST NUMBER 367

RUN NUMBER	CONFIGURATION	DATE	MACH NUMBER	ANGLE OF ATTACK SCHEDULE*	Re/FT $\times 10^{-6}$	TEST TYPE**
111	WB	5/7/82	0.80	A	3.8	1
			0.85	A	3.8	1
			0.83	A	3.8	1
			0.81	A	3.7	1
112		5/7/82	0.80	A	3.7	1
			0.79	A	3.7	1
			0.78	A	3.7	1
			0.75	A	3.6	1
			0.70	A	3.5	1
113	D/BAS	5/10/82	0.80	A	3.9	1
			0.85	A	3.9	1
			0.83	A	3.8	1
			0.81	A	3.8	1
114		5/10/82	0.80	A	3.8	1
			0.79	A	3.7	1
			0.78	A	3.7	1
			0.75	A	3.6	1
			0.70	A	3.5	1
116	C/BAS/HL	5/11/82	0.80	A	3.9	1
			0.85	A	3.9	1
			0.83	A	3.8	1
			0.81	A	3.8	1
117		5/11/82	0.80	A	3.8	1
			0.79	A	3.8	1
			0.78	A	3.7	1
			0.75	A	3.7	1
			0.70	A	3.6	1
118	C/BAS/REC	5/12/82	0.80	A	3.9	1
			0.85	A	3.9	1
			0.83	A	3.8	1
			0.81	A	3.8	1

TABLE II. (Continued)

RUN NUMBER	CONFIGURATION	DATE	MACH NUMBER	ANGLE OF ATTACK SCHEDULE*	Re/FT $\times 10^{-6}$	TEST TYPE**
119	C/BAS/REC	5/12/82	0.80	B	3.8	1
↓	↓		0.79	B	3.8	1
			0.78	B	3.8	1
			0.75	B	3.7	1
			0.70	B	3.6	1
126	C/PRES/REC	5/20/82	0.80	B	3.8	2
↓	↓		0.85	B	3.7	2
			0.83	B	3.7	2
			0.81	B	3.7	2
127		5/20/82	0.80	B	3.7	2
↓	↓		0.79	B	3.7	2
			0.78	B	3.6	2
			0.75	B	3.6	2
			0.70	B	3.5	2
128	D/PRES	5/25/82	0.80	B	3.8	2
↓	↓		0.85	B	3.8	2
			0.83	B	3.7	2
			0.81	B	3.7	2
129		5/25/82	0.80	B	3.7	2
↓	↓		0.79	B	3.7	2
			0.78	B	3.6	2
			0.75	B	3.6	2
			0.70	B	3.5	2
131	WB	5/26/82	0.80	A	3.8	1
↓	↓		0.85	A	3.8	1
			0.75	A	3.6	1
			0.70	A	3.5	1

TABLE II. (Continued)

RUN NUMBER	CONFIGURATION	DATE	MACH NUMBER	ANGLE OF ATTACK SCHEDULE*	Re/FT $\times 10^{-6}$	TEST TYPE**
-	WB	-	0.80	0.9°	-	3
-	WB	-	0.80	1.9°	-	3
-	WB	-	0.80	4.0°	-	3
-	D/BAS	-	0.80	0.67°	-	3
-	D/BAS	-	0.80	2.48°	-	3
-	D/BAS	-	0.85	0.49°	-	3
-	C/BAS/REC	-	0.80	0.20°	-	3
-	C/BAS/REC	-	0.85	0.4°	-	3

* NOMINAL ANGLE OF ATTACK SCHEDULE:

A = -1.5, -0.75, 0, 0.5, 0.75, 1.0, 1.25, 1.5, 2.0, 2.5, 3.0, 3.5, 4.0, 0 DEGREES.

B = -2.5, -1.5, -0.75, 0, 0.5, 0.75, 1.0, 1.25, 1.5, 2.0, 2.5, 3.0, 3.5, 4.0, 0 DEGREES

**TEST TYPE:
1 = FORCE AND WING PRESSURES.
2 = FORCE AND WING/NACELLE/PYLON PRESSURES.
3 = OIL FLOW.

Both boundary-layer diverters for the C-nacelle were tested using the basic pylon. The diverter exhibiting the lower drag (which proved to be the recessed diverter) was chosen for tests to obtain nacelle pressure data; i.e., tests using the pressure pylon.

Boundary-layer transition grit was placed on the model at the same locations as for the earlier UTW tests. Information regarding grit size and location is given in table III.

Oil flow tests were conducted for the WB, D/BAS and C/BAS/REC model configurations. Photographs of the starboard (noninstrumented) nacelle were taken.

TABLE III. TRANSITION GRIT SUMMARY

GRIT TYPE	AVERAGE GRIT DIAMETER, INCHES	GRIT STRIP WIDTH, INCHES	LOCATION
80	0.0065	0.1	Wing lower surface, 40% x/c
90	0.0057	0.1	Wing upper surface, straight line from 13.5% x/c at wing/fuselage juncture to 40% x/c at break in wing planform (2Y/B = 0.4103)
90	0.0057	0.1	Wing upper surface, straight line from 40% x/c at break in wing planform to 35% x/c at wing tip.
100	0.0048	0.1	Fuselage, FUS STA 1.0
100	0.0048	0.1	Vertical tail, 10% x/c
100	0.0048	0.1	Upper and lower horizontal tail surfaces, 10% x/c
120	0.0040	0.1	Vertical tail bullet fairing, 1.0 inch from leading edge
120	0.0040	0.1	Nacelles, internal and external, NAC STA 0.375

3.2 Data Reduction

Axial and normal force balance measurements were resolved into lift and drag forces and corrected for fuselage cavity force and flow-through nacelle internal drag.

The cavity force correction was determined from sixteen pressure measurements located around the sting in the aft fuselage cavity.

The measured drag coefficient was corrected for the drag due to the airflow captured by the nacelle; i.e., the internal drag of the flow-through nacelle. This internal drag includes additive drag and nacelle internal pressure and friction drags. For the D-nacelle, the inlet ingested some air that had also scrubbed the wing. Consequently, the wing pressure and friction drags caused by the captured airflow were also included in the internal drag of the D-nacelle.

The internal drag was calculated in three basic steps. First, measured internal static pressures were used to determine the captured mass flow rate. For the aft mounted nacelles, calculated mass flow rates using this method agree within one percent with an alternate method which used an assumed nacelle exit static pressure and an empirical correlation to estimate the area in the vena-contracta downstream of the exit plane. The assumed exit static pressure was the freestream static pressure. Agreement between these methods substantiates the calculated mass flow rates. This alternate method could not be used for the UTW nacelle, however, because the local exit pressure was significantly altered by the wing flow field and was not known. For consistency, the internal pressure measurements were used to determine mass flow rates for both the aft mounted and the UTW nacelles. Since mass flow rate did not change significantly with angle of attack for any of the configurations, the average value for all angles of attack was used at each Mach number.

The second step was a one-dimensional flow calculation with area change and friction. This calculation gave the total pressure recovery from the

nacelle entrance to the nacelle exit, based on a friction coefficient of 0.0035. The total pressure recovery from the freestream to the nacelle entrance was assumed to be one, except for the D-nacelle. In that case, the total pressure loss due to wing scrubbing was separately determined.

The third step was the determination of the internal drag. This was calculated as the change in the impulse function ($mV + \Delta pA$) from the freestream to the nacelle exit. The value of the impulse function at the exit was determined from the nacelle mass flow rate and total pressure recovery. In order to correctly compute the internal drag, the force must be resolved into its lift and drag components. Internal drag is equal to:

$$D_{INT} = (mV + \Delta pA)_o - (mV + \Delta pA)_{ex} \cos(\alpha)$$

The effect of α on D_{INT} is small, however, (less than 0.4 drag counts at three degrees angle-of-attack). Therefore, the drag value determined at zero degrees angle-of-attack was used at all angles of attack. Correspondingly, no internal lift correction was made.

Results from the internal drag calculations are shown in table IV for the C, D, and UTW nacelles.

TABLE IV. INTERNAL DRAG SUMMARY

CONFIGURATION	MACH NUMBER	MASS FLOW RATIO	NACELLE TOTAL PRESSURE RECOVERY	INTERNAL DRAG FOR ONE NACELLE, COUNTS
D-NACELLE	0.70	0.6902	0.98721, 0.98280*	5.3, 7.4*
	0.75	0.6929	0.98581, 0.98079*	5.3, 7.2*
	0.78	0.6952	0.98497, 0.97958*	5.2, 7.1*
	0.79	0.6959	0.98470, 0.97918*	5.1, 7.1*
	0.80	0.6974	0.98438, 0.97874*	5.1, 7.1*
	0.81	0.6980	0.98412, 0.97835*	5.1, 7.0*
	0.83	0.7001	0.98356, 0.97753*	5.0, 7.0*
	0.85	0.7018	0.98305, 0.97675*	5.0, 6.9*
C-NACELLE	0.70	0.6799	0.98786	4.8
	0.75	0.6829	0.98655	4.6
	0.78	0.6849	0.98579	4.6
	0.79	0.6854	0.98556	4.5
	0.80	0.6861	0.98531	4.5
	0.81	0.6874	0.98503	4.5
	0.83	0.6887	0.98458	4.4
	0.85	0.6912	0.98406	4.4
UTW NACELLE	0.70	0.6832	0.99208	3.0
	0.75	0.6841	0.99137	2.7
	0.78	0.6870	0.99089	2.7
	0.79	0.6871	0.99077	2.7
	0.80	0.6893	0.99056	2.7
	0.81	0.6907	0.99039	2.7
	0.82	0.6908	0.99027	2.7

* INCLUDES WING SCRUBBING LOSS

4. RESULTS

4.1 Installed Drag Comparisons

A summary drag comparison of the nacelle configurations is given in figure 9. The bars show the drag increment relative to the WB at the design conditions of Mach number 0.80 and $C_L = 0.45$. The WB drag was 357 counts. The D/BAS nacelle configuration had the smallest drag of the configurations tested. The conventional UTW configuration had the largest drag, at 6.8 percent larger than the D/BAS. Relative to the D/BAS, the other nacelle configurations had larger drags, as follows: D/PRES, 1.0 percent; C/BAS/REC, 2.3 percent; C/PRES/REC, 3.5 percent; and C/BAS/HL, 3.8 percent.

The shaded region on each bar in figure 9 is an estimate of friction drag based on nacelle/pylon/diverter wetted area and a friction drag coefficient of 0.0035. Each configuration apparently still had some interference drag, over and above friction drag. Thus, there seems to be potential for further drag reduction on each configuration.

The D-nacelle swallowed some wing boundary layer. In an actual aircraft installation, the D-nacelle installation would have lower total pressure recovery and higher specific fuel consumption (SFC) than would the C-nacelle and UTW-nacelle installations. This increase in SFC can be represented as an equivalent drag increase by considering its effect on specific air range (SAR). By definition,

$$SAR = V_o/\dot{W}_F$$

where V_o is freestream velocity and $\dot{W}_F$ is fuel weight flow rate. For level, unaccelerated flight,

$$SAR = (V_O/SFC)(C_L/C_D)/W_{AC}$$

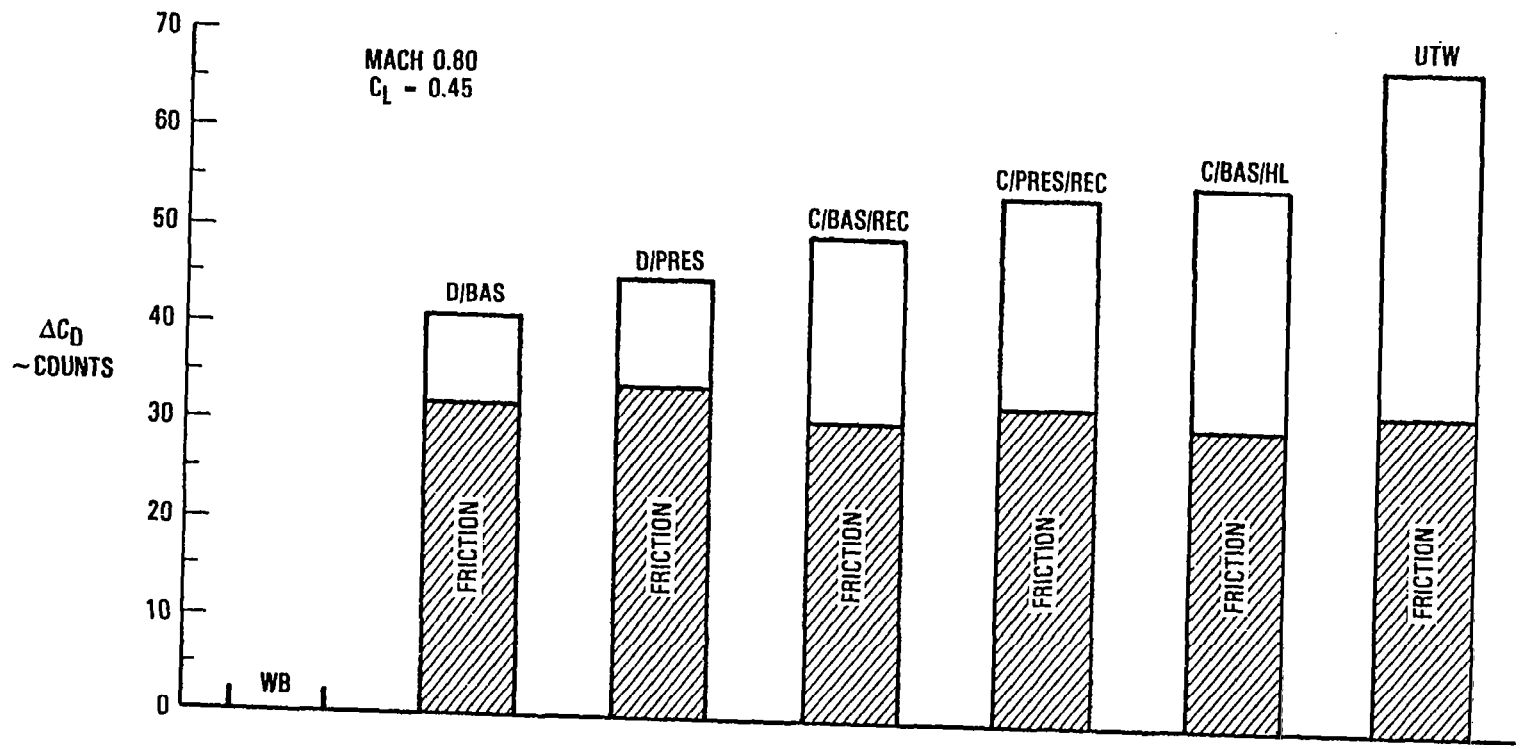

FIGURE 9. SUMMARY INSTALLED DRAG COMPARISON

where C_L and C_D are aircraft lift and drag coefficients, respectively, and W_{AC} is aircraft weight. Then,

$$\Delta(SAR)/SAR = - \Delta(SFC)/SFC - \Delta C_D/C_D$$

at fixed aircraft weight and speed. Thus, a fractional change in SFC is equivalent to a fractional change in C_D, insofar as SAR is concerned. The fractional increase in SFC was estimated to be 0.7 percent, based on the calculated total pressure recovery of the D-nacelle and on characteristics of advanced turbofan engines. The equivalent drag increase for the D-nacelle was about 0.7 percent, or about 3 drag counts.

4.1.1 Comparison of WB, D/BAS, UTW, and C/BAS/REC Configurations. - Drag polars for the WB, D/BAS, UTW, and C/BAS/REC configurations at Mach number 0.80 are compared in figure 10. The solid lines are least-squares curve fits of the polars. These curve fits were used to prepare figure 9. Curve fits were developed for all of the configurations at all of the test Mach numbers, to aid in accurate comparison of the different nacelle configurations. In figure 10, note that the D/BAS and C/BAS/REC polars converged with the WB polar at a high C_L of about 0.74, whereas the design C_L was 0.45. By contrast, the UTW polar diverged from the WB polar as C_L increased.

The UTW tests were performed at an earlier time than the aft nacelle tests. The drag levels for the WB differed slightly between the two tests. The UTW drag data shown in this report were obtained by taking the drag difference between the UTW and the WB from the original test, and adding that difference to the WB drag data from the aft nacelle test.

Drag polars for all of the nacelle configurations at test Mach numbers other than 0.80 are given in figures A1 - A21 of the Appendix.

Drag rise comparisons for the WB, D/BAS, C/BAS/REC, and UTW configurations at $C_L = 0.45$ are shown in figure 11. The least-squares curve fits of the drag polars were used to prepare this figure. M_{DD} was about 0.81 for the

FIGURE 10. DRAG POLARS AT MACH 0.80 FOR WB, D/BAS, C/BAS/REC, AND UTW CONFIGURATIONS

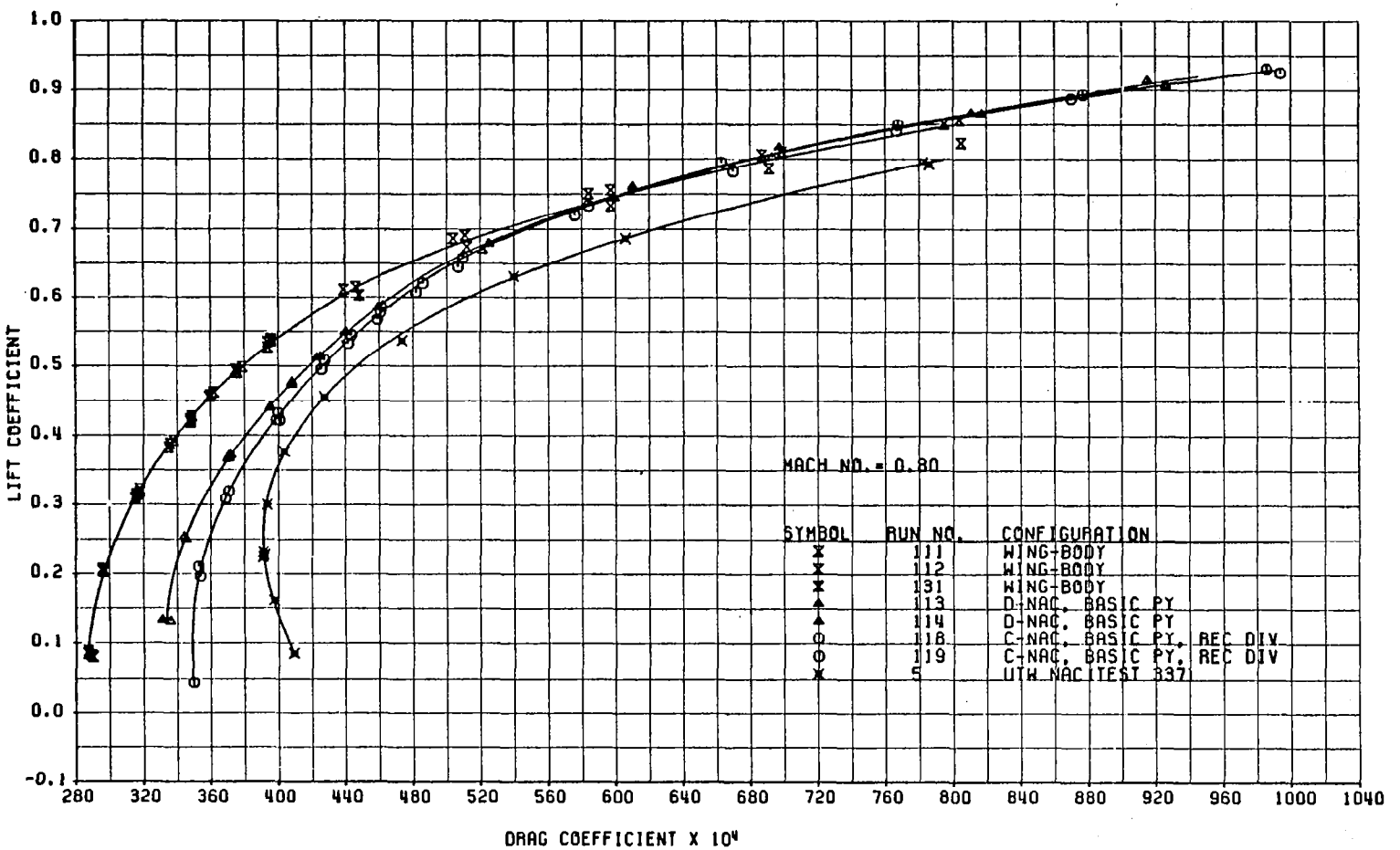

FIGURE 11. DRAG COEFFICIENT VERSUS MACH NUMBER

AT CL=0.45 FOR WB, D/BAS, C/BAS/REC

AND UTW CONFIGURATIONS

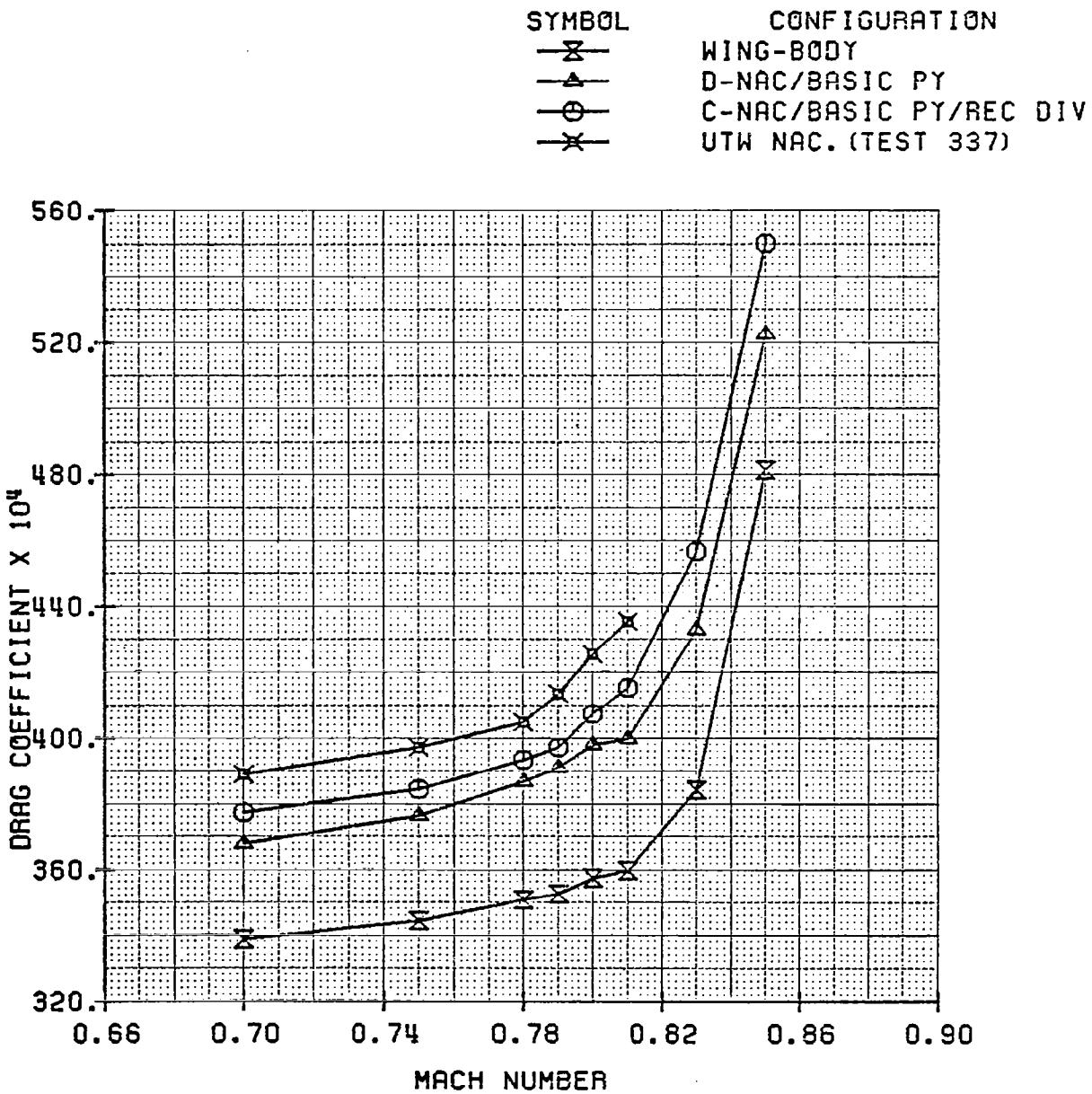

WB, the D/BAS, and the C/BAS/REC; but was about 0.78 for the UTW. Drag differences among the configurations persisted at lower Mach numbers down to 0.70. Wave drag effects are expected to be small at Mach number 0.70, however, because this is significantly below the apparent M_{DD}. Thus, there may also be form drag differences among the configurations.

The D/BAS installation had a more favorable area progression than the UTW, as shown in figure 12, because it had a smaller maximum area and fewer regions of rapid area change. This may explain the higher M_{DD} and lower wave drag of the D/BAS configuration. The area distribution for the C/BAS/REC was nearly the same as for the D/BAS, as shown in figure 13.

Figure 14 compares maximum L/D through the test Mach number range for the WB, D/BAS, C/BAS/REC, and UTW configurations. These results were obtained graphically from the least-squares curve fits of the drag polars. Figure 14 shows that the D/BAS and C/BAS/REC installations had significantly higher maximum L/D than the UTW. At Mach number 0.80, the value for the UTW was about 11 percent lower than for the D/BAS.

In order to examine some of the previously noted behavior more closely, some detailed static pressure data at the design Mach number 0.80 and C_L approximately 0.45, will be considered next. Wing upper and lower surface pressure distributions for the WB are shown in figure 15. On the upper surface, there was a strong recompression near mid-chord from semispan station 0.328 outboard. Note that for freestream Mach number 0.80, a local Mach number of 1.0 corresponds to C_p of -0.43, assuming isentropic flow.

For comparison, wing surface pressures for the D/BAS configuration are shown in figure 16. There were some detailed differences on the upper surface near the nacelle pylon, especially at 2Y/B = 0.370, where there apparently was a shock at x/c of about 0.40. For the lower wing surface of the D/BAS, the inboard C_p profiles out to 2Y/B = 0.370 were similar to those for the WB.

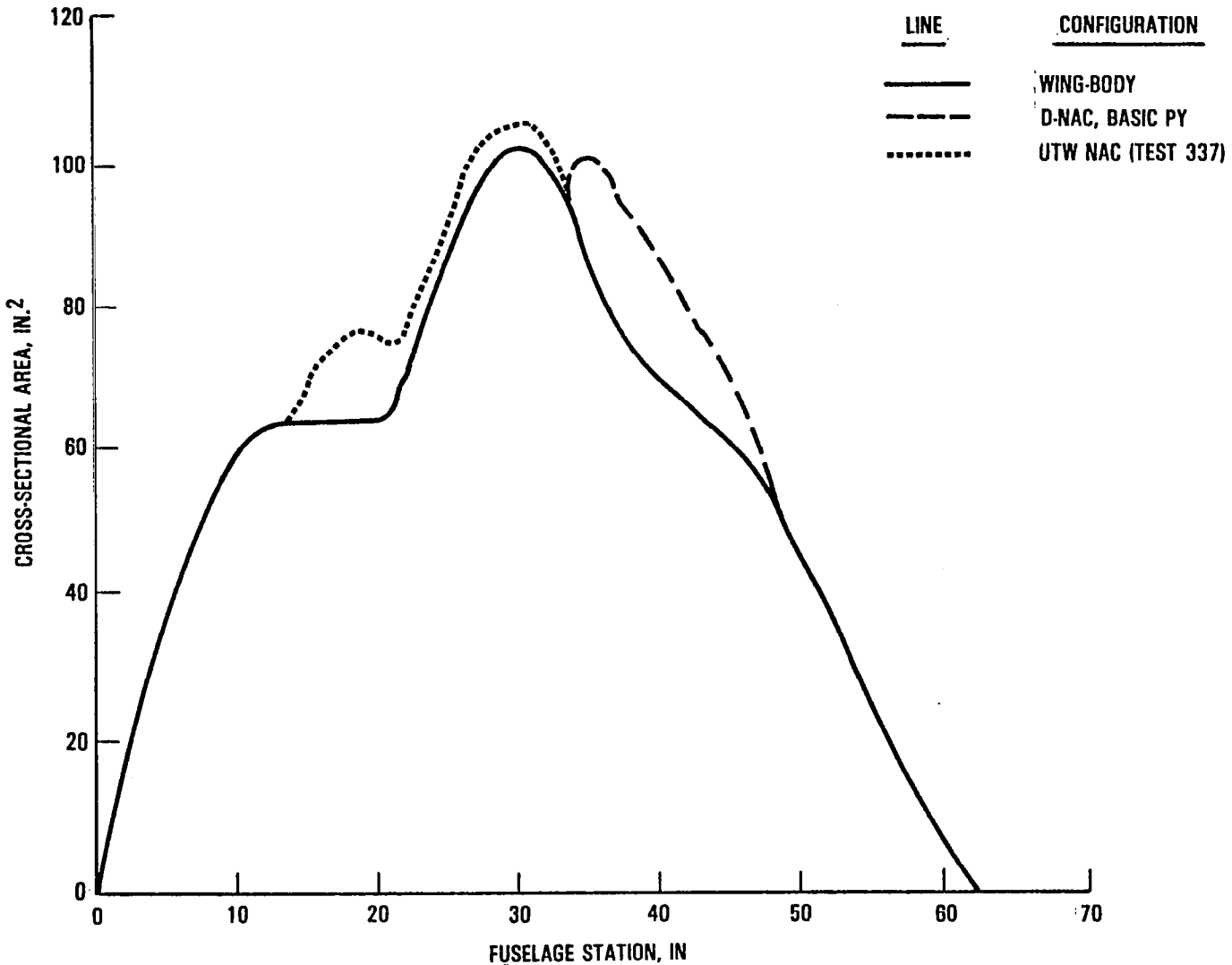

FIGURE 12. AIRPLANE MODEL CROSS SECTIONAL AREA DISTRIBUTION FOR WB, D/BAS AND UTW CONFIGURATIONS

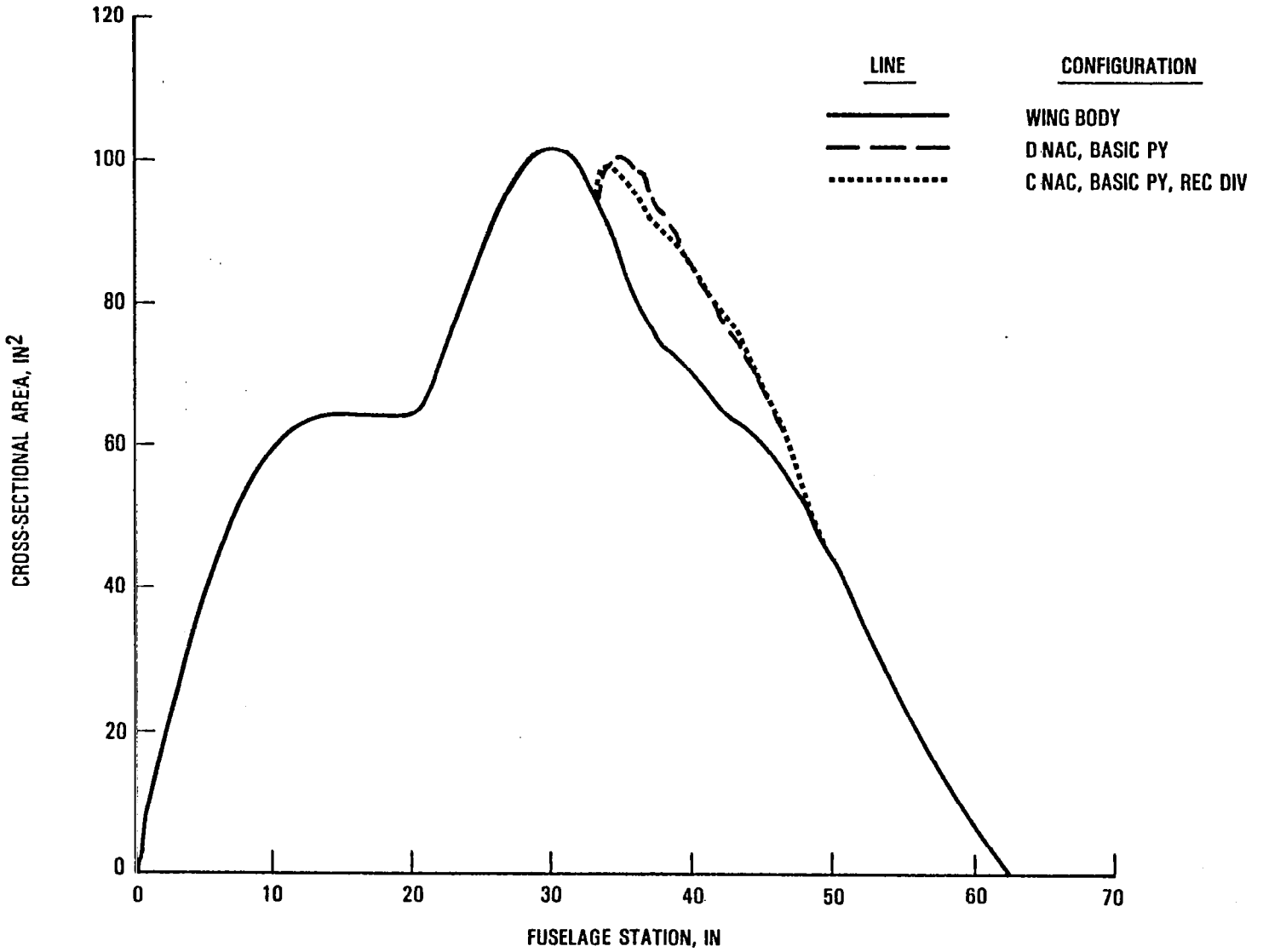

FIGURE 13. AIRPLANE MODEL CROSS-SECTIONAL AREA DISTRIBUTION FOR WB, D/BAS, AND C/BAS/REC CONFIGURATIONS

FIGURE 14. MAXIMUM L/D VERSUS MACH NUMBER

FOR WB, D/BAS, C/BAS/REC

AND UTW CONFIGURATIONS

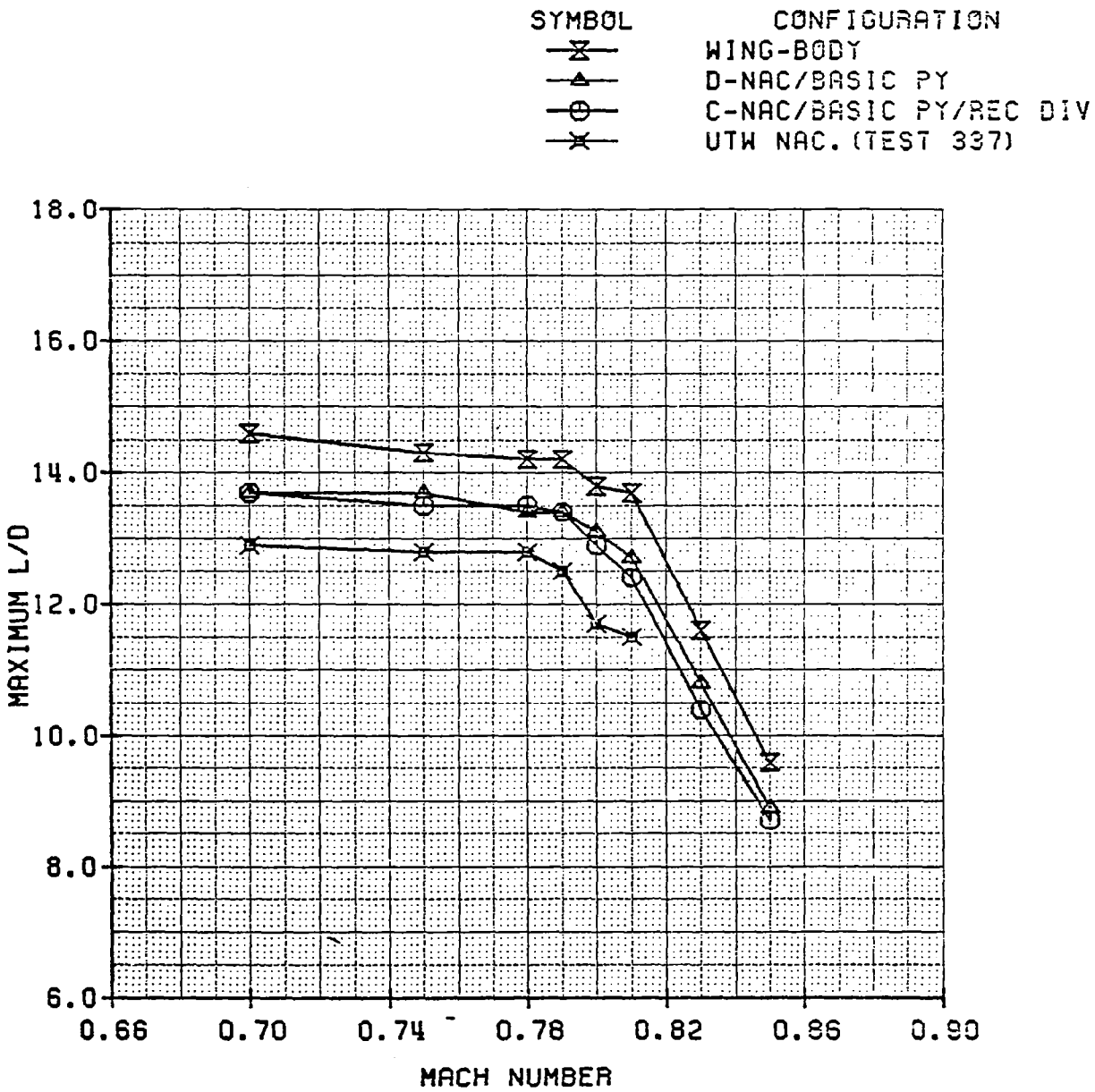

FIGURE 15a.

WING UPPER SURFACE PRESSURE DISTRIBUTION

WING BODY

MACH NUMBER = 0.800 CL = 0.4585

1.0677 DEG. ANGLE OF ATTACK

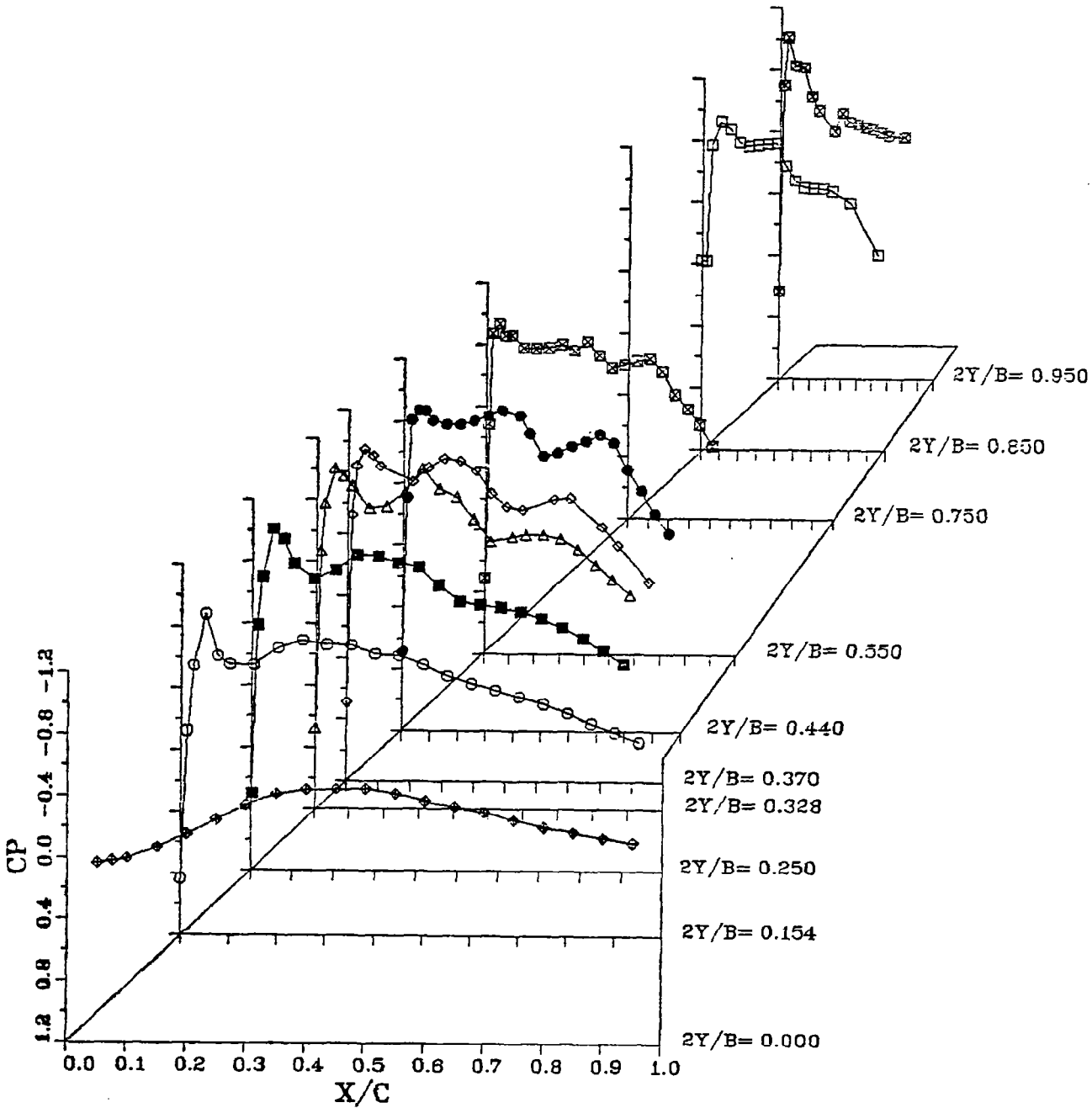

FIGURE 15b.

WING LOWER SURFACE PRESSURE DISTRIBUTION

WING BODY

MACH NUMBER = 0.800 CL = 0.4585

1.0677 DEG. ANGLE OF ATTACK

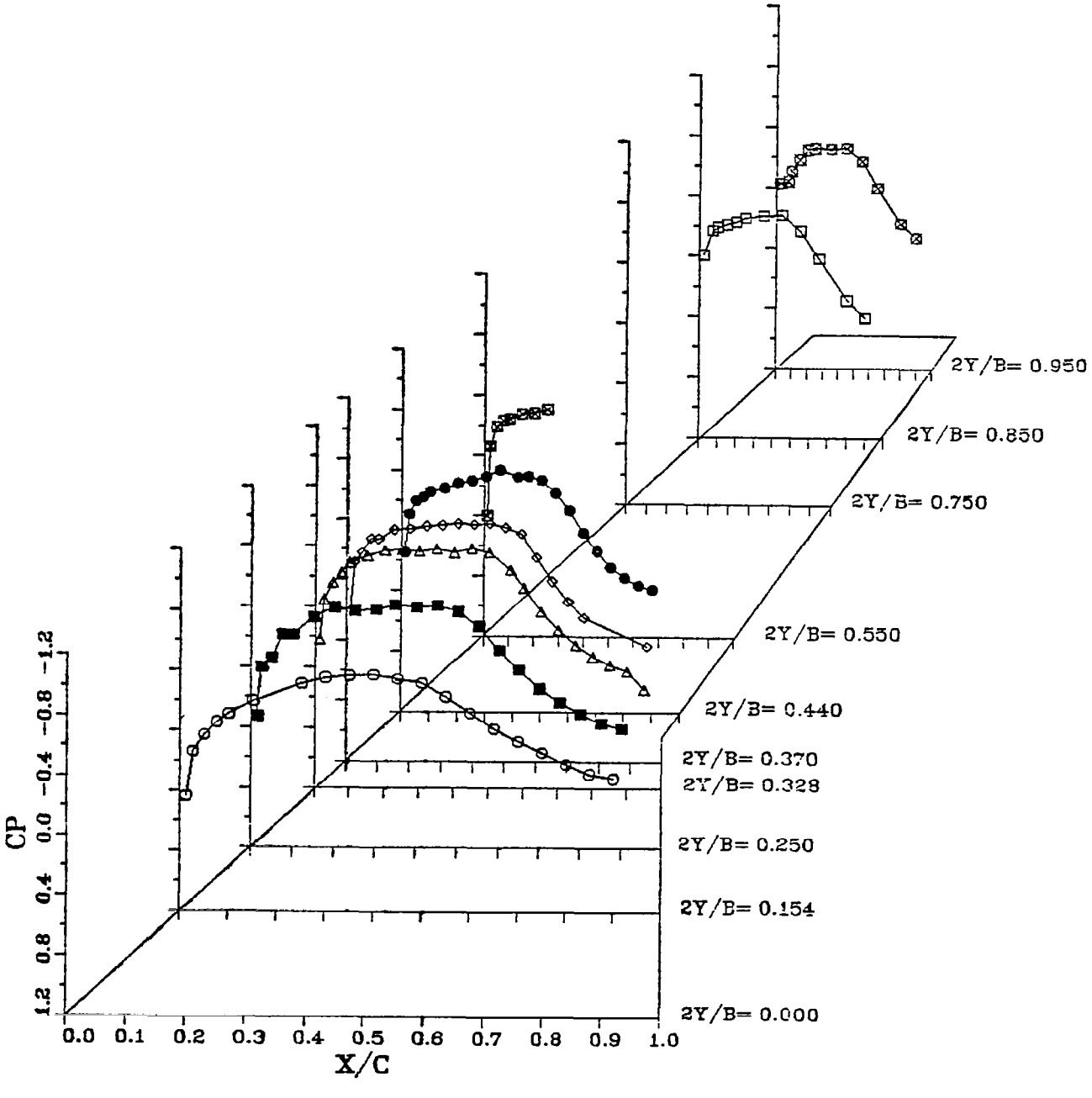

FIGURE 16a.

WING UPPER SURFACE PRESSURE DISTRIBUTION

D NACELLE / BASIC PYLON

MACH NUMBER = 0.800 CL = 0.4397

0.5866 DEG. ANGLE OF ATTACK

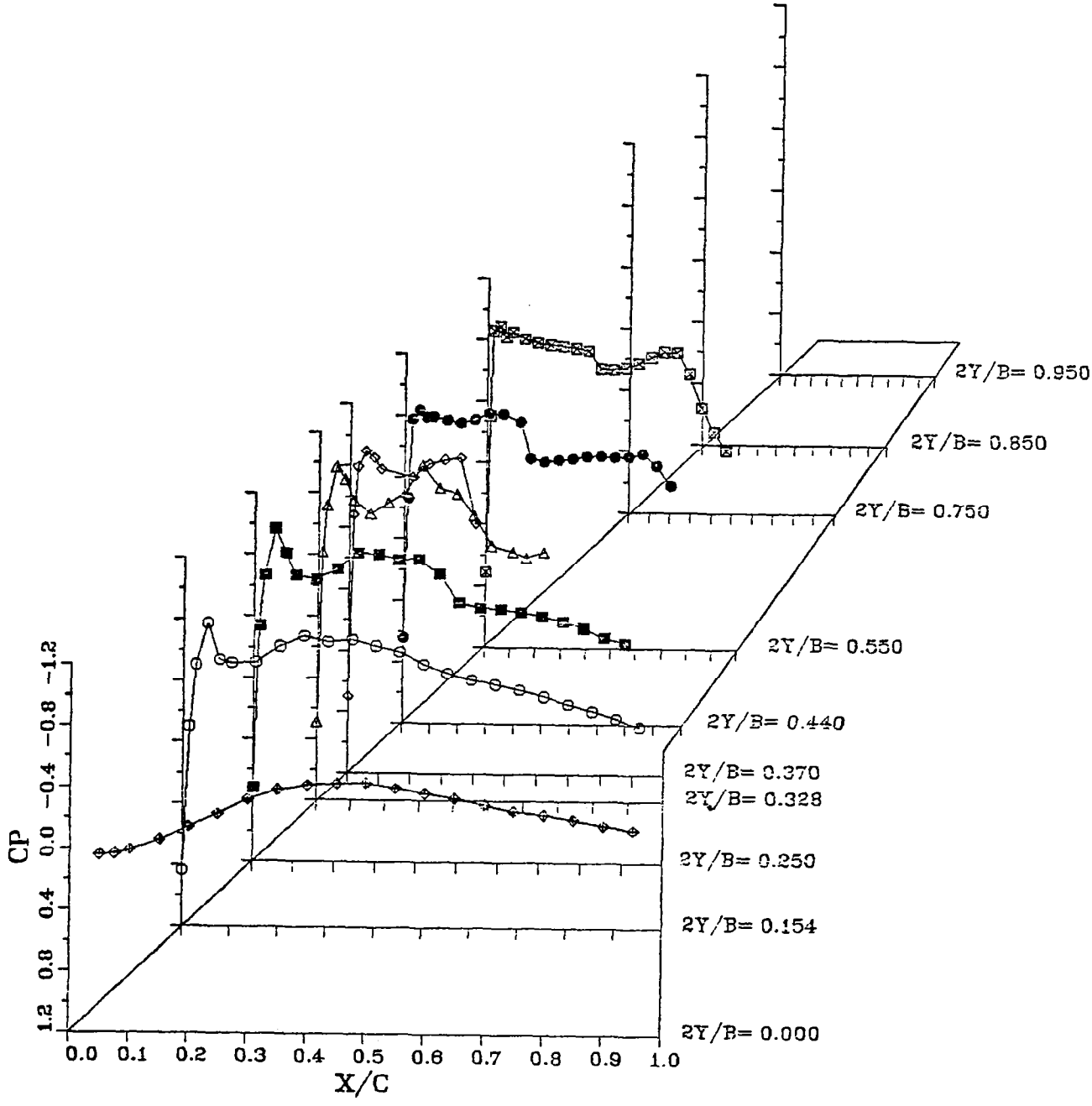

FIGURE 16b.

WING LOWER SURFACE PRESSURE DISTRIBUTION

D NACELLE / BASIC PYLON

MACH NUMBER = 0.800 CL = 0.4397

0.5866 DEG. ANGLE OF ATTACK

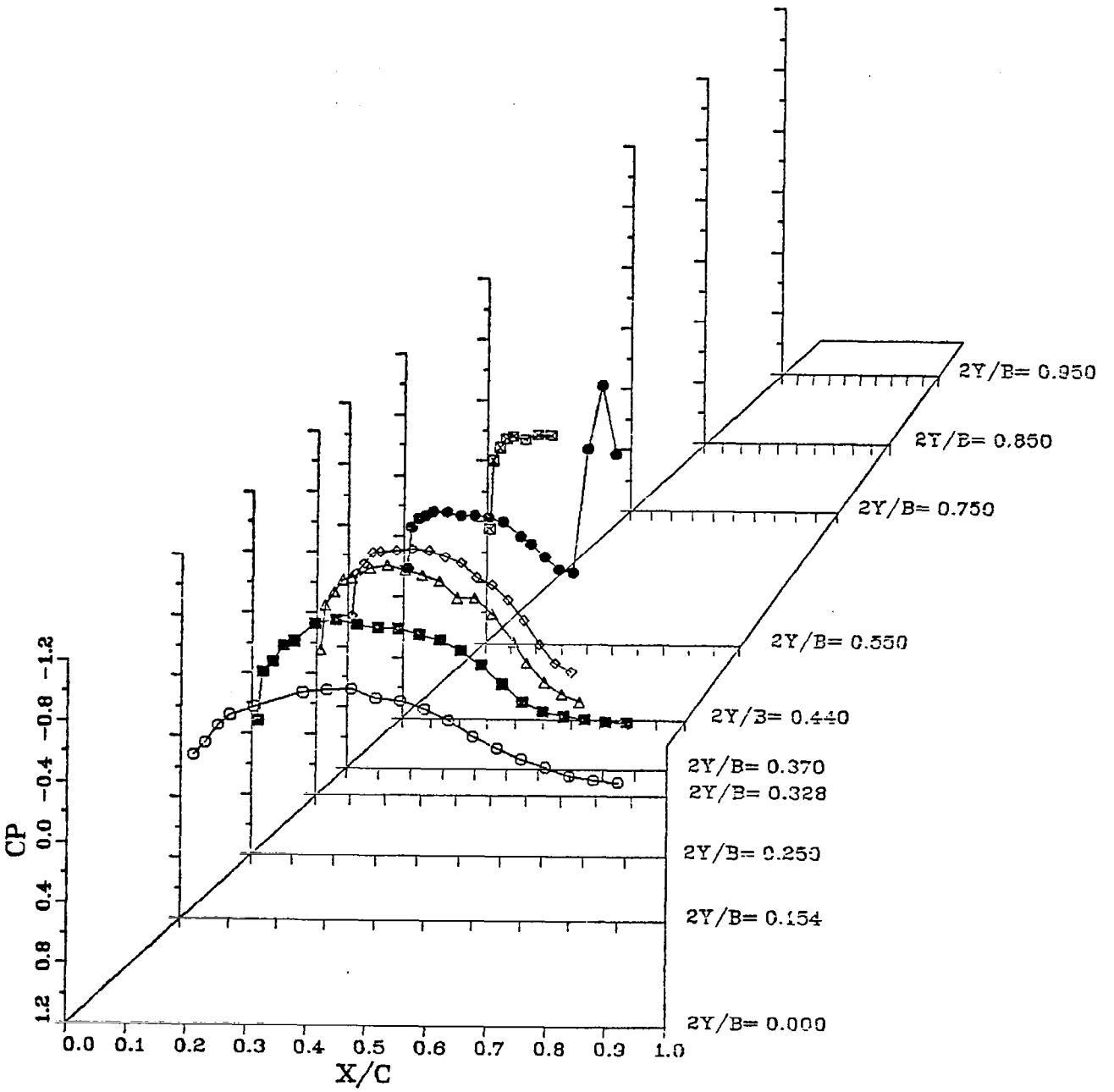

(The nacelle highlight plane was at x/c = 0.714 and the nacelle centerline was at 2Y/B = 0.370.) The flow remained subsonic and there were no strong adverse pressure gradients. Outboard of the nacelle at 2Y/B = 0.440, however, there was a sudden expansion to supersonic speed just downstream of the inlet lip; followed by what seems to have been a shock. The maximum measured Mach number was about 1.3 at x/c = 0.70. The Mach number at x/c = 0.75 was about 1.05. The pressure taps farther downstream were covered over by the nacelle. The presence of this abrupt expansion and shock indicates that the D/BAS nacelle installation design might be improved. There was apparently more outflow at this location than was expected when the nacelles were designed. The measured interference drag (figure 9) can possibly be reduced by adjusting the nacelle design to eliminate this behavior.

Figure 17 directly compares the upper and lower wing surface pressures for the WB and D/BAS at 2Y/B = 0.328. Corresponding data are shown in figure 18 at 2Y/B = 0.440. These figures further illustrate the flow behavior described relative to figures 15 and 16.

Comparison of the lower surface pressure profiles in figures 15b and 16b also reveals that the pressures were generally higher for the D/BAS in the areas forward of the nacelle.

Pressure measurements were made on the nacelles when the pressure pylons were installed. Figure 19 shows C_p distributions on the D/BAS at Mach number 0.80 and C_L = 0.43. On the inboard side, the flow remained subsonic, except possibly for a small region near the inlet lip. On the outboard side near the lip, the pressures were lower and Mach numbers higher than inboard. This is consistent with the wing pressure data of figures 16 and 18. Note that the highly-rounded lip contour at 180 degrees gave relatively weak pressure gradients in this region.

Wing pressure data for the earlier-tested UTW nacelle installation are shown in figure 20. The lower wing surface pressures indicate that the flow was qualitatively different from the flows for the aft nacelle configurations.

FIGURE 17. WING PRESSURE DISTRIBUTION

WB AND D/BAS CONFIGURATIONS

MACH=0.80 2Y/S=0.328

SYMBOL	CONFIGURATIONS	CL
—⧗—	WING-BODY, UPPER	0.4585
-⧗-	WING-BODY, LOWER	0.4585
—▲—	D-NAC/BASIC PY, UPPER	0.4397
-▲-	D-NAC/BASIC PY, LOWER	0.4397

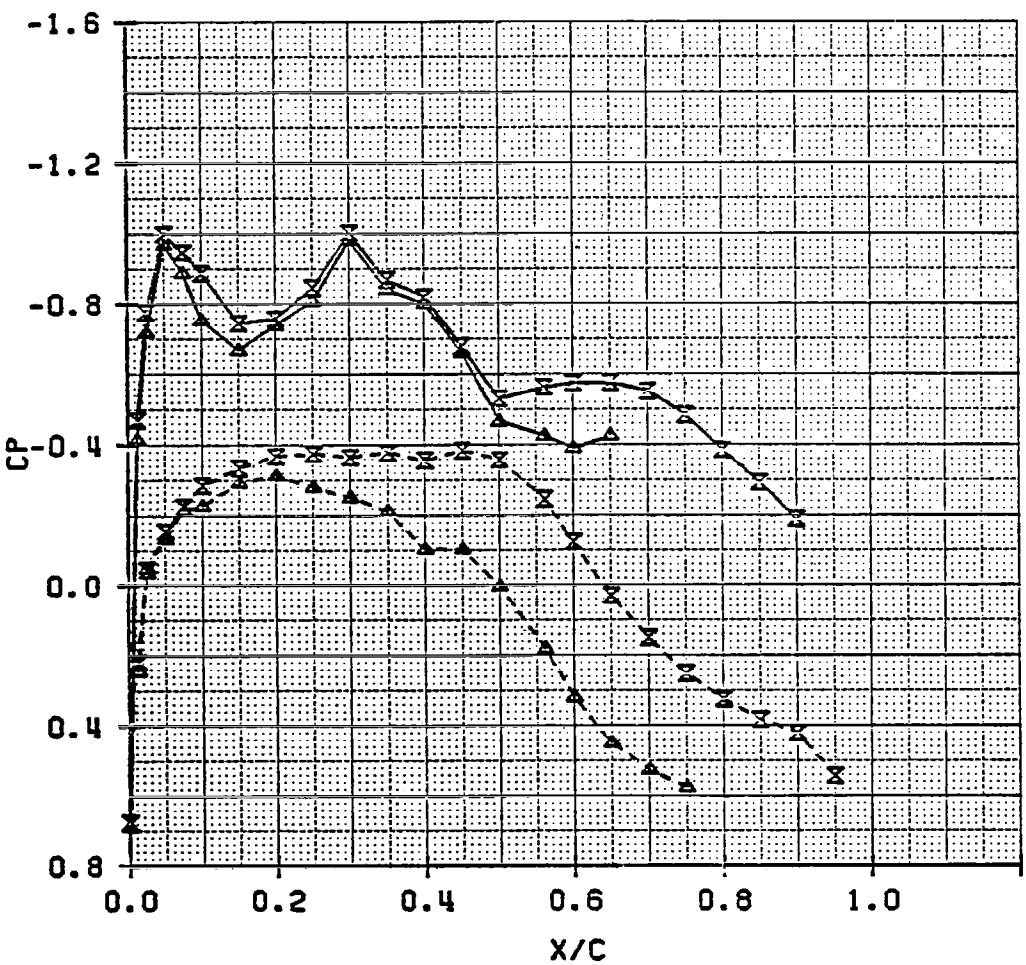

FIGURE 18. WING PRESSURE DISTRIBUTION

WB AND D/BAS CONFIGURATIONS

MACH=0.80 2Y/B=0.440

SYMBOL	CONFIGURATIONS	CL
—⧖—	WING-BODY, UPPER	0.4585
-⧖-	WING-BODY, LOWER	0.4585
—△—	D-NAC/BASIC PY, UPPER	0.4397
-△-	D-NAC/BASIC PY, LOWER	0.4397

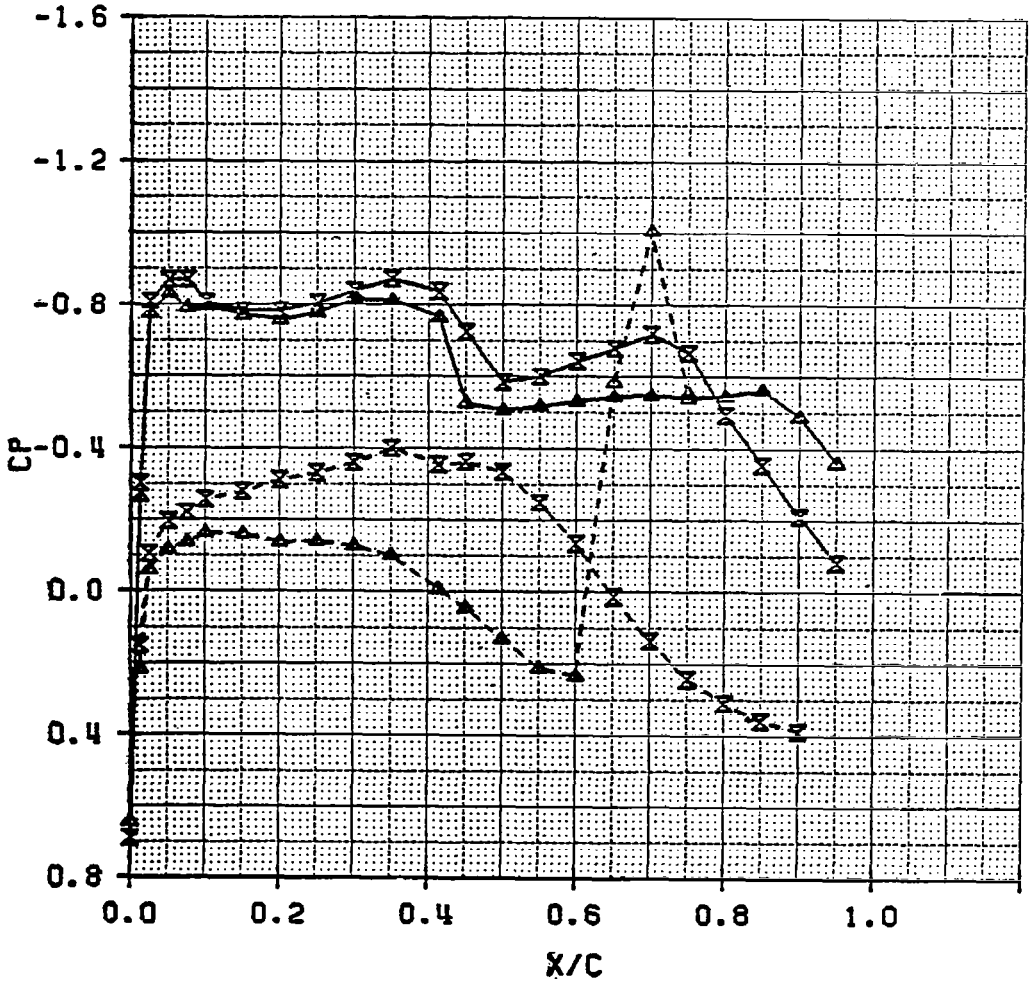

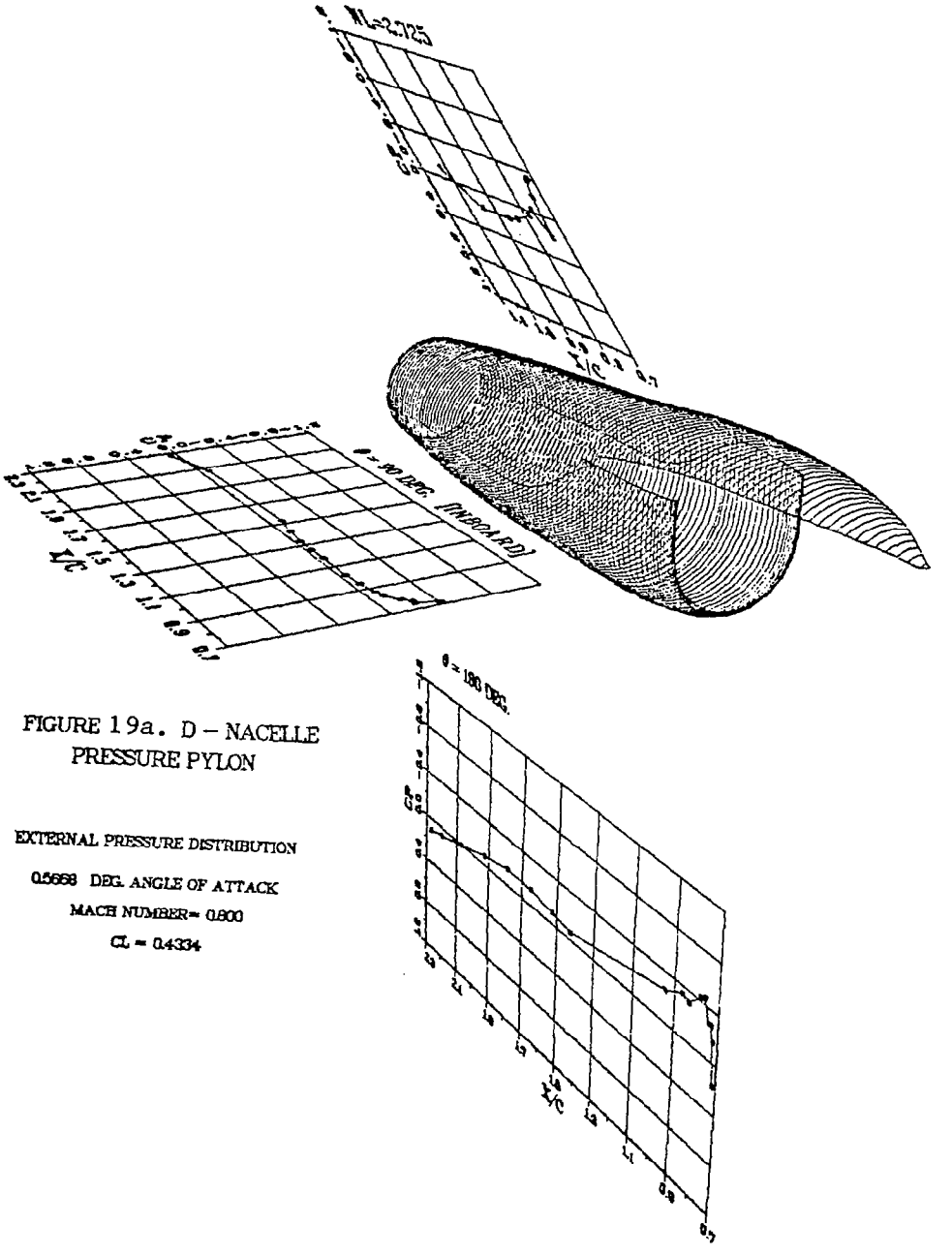

FIGURE 19a. D – NACELLE PRESSURE PYLON

EXTERNAL PRESSURE DISTRIBUTION

0.5668 DEG. ANGLE OF ATTACK

MACH NUMBER= 0.800

CL = 0.4334

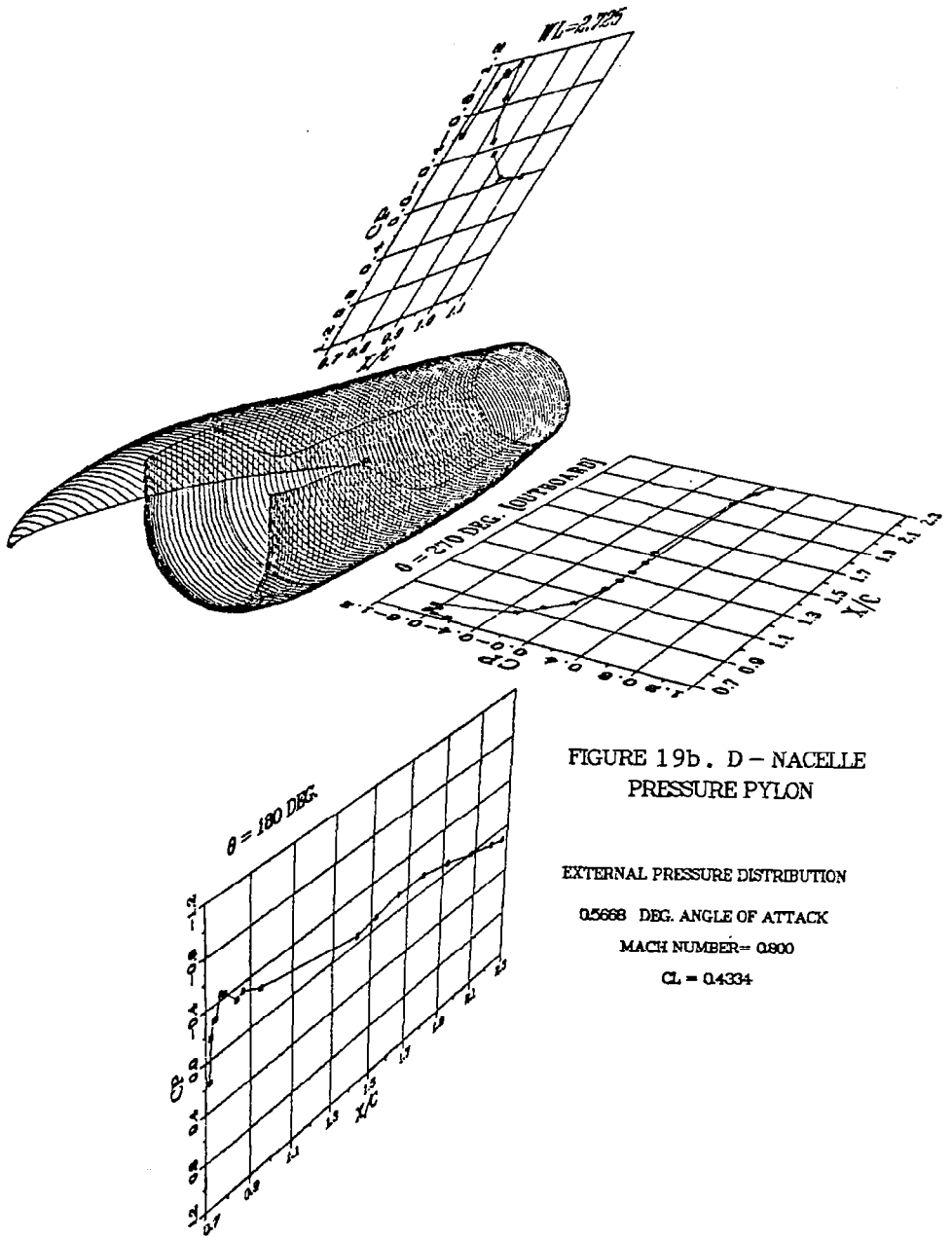

FIGURE 19b. D – NACELLE PRESSURE PYLON

EXTERNAL PRESSURE DISTRIBUTION

0.5668 DEG. ANGLE OF ATTACK

MACH NUMBER= 0.800

CL = 0.4334

FIGURE 20a.

WING UPPER SURFACE PRESSURE DISTRIBUTION

UTW NACELLE

MACH NUMBER = 0.800 CL = 0.4553

1.7290 DEG. ANGLE OF ATTACK

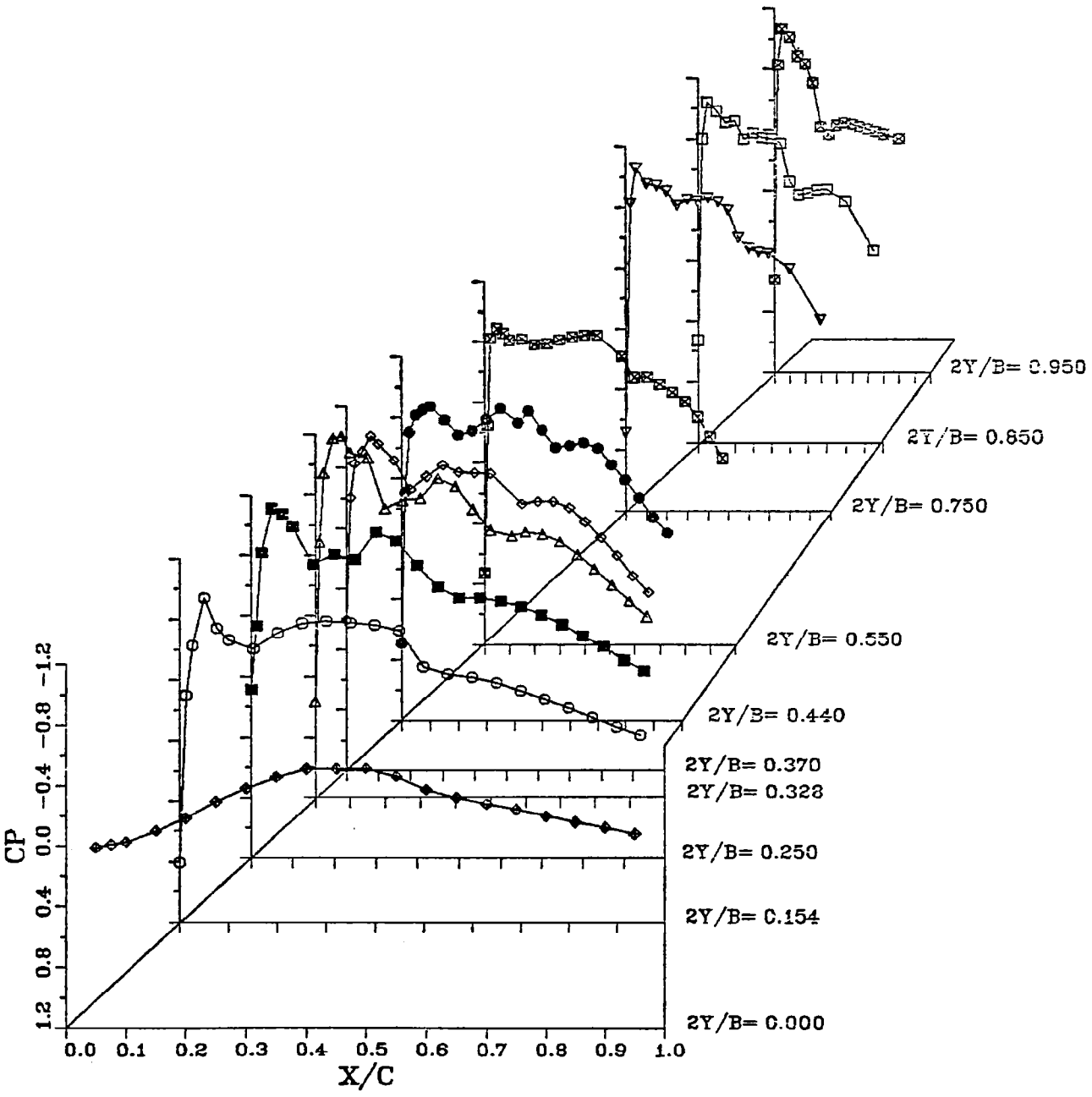

FIGURE 20b.

WING LOWER SURFACE PRESSURE DISTRIBUTION

UTW NACELLE

MACH NUMBER = 0.800 CL = 0.4553

1.7290 DEG. ANGLE OF ATTACK

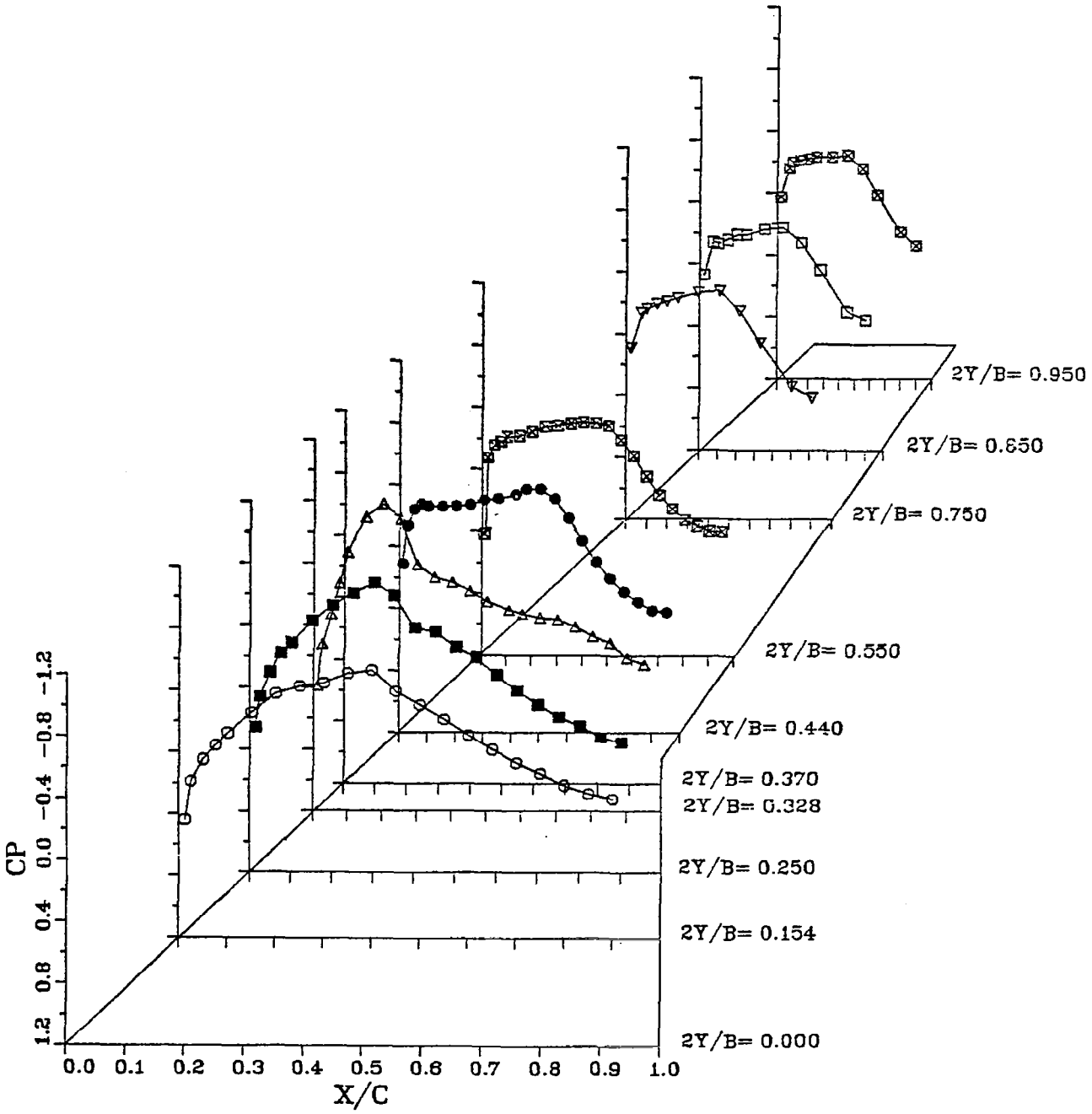

At the inboard semispan stations 0.154, 0.250, and 0.328, the flow was accelerated to supersonic speed, followed by a shock. The pressure taps at 2Y/B = 0.370 were covered by the pylon. Outboard of the nacelle, the flow was subsonic with moderate pressure gradients similar to those for the WB. This rather severe channel flow problem exhibited by the UTW installation was at least partly responsible for the large interference drag shown in figure 9. It also suggests that the UTW installation design could be improved; e.g., by moving the nacelles outboard.

In figures 21 and 22, the wing pressures for the WB and UTW are directly compared at 2Y/B of 0.328 and 0.440, respectively. These figures further illustrate the relative flow acceleration underwing and inboard for the UTW; as well as the similar flow behavior outboard.

Wing pressure profiles for the C/BAS/REC are shown in figure 23. The lower wing surface profiles inboard of the nacelle again show moderate pressure gradients and subsonic flow. At 2Y/B = 0.440, however, there was an expansion to supersonic speed at x/c = 0.70 (Mach number approximately 1.1). This was followed by an apparent shock, as the flow was subsonic at x/c = 0.75 and further downstream. This behavior was qualitatively similar to that for the D/BAS, and indicates that the design of the C/BAS/REC installation could also be improved by eliminating this expansion/shock near the outboard inlet lip of the nacelle.

Figure 24 gives C_p distributions on the C/PRES/REC nacelle at Mach number 0.80 and C_L = 0.44. These data also show subsonic flow inboard, except near the inlet lip where there were typical supersonic peaks. Outboard there was also evidence of the strong expansion and recompression shown in figure 23, as the peak supersonic Mach numbers were higher at 270 and 330 degrees than at 90 and 30 degrees, respectively. When compared with the D/PRES results of figure 19, the measured Mach numbers near the inlet lip were generally higher for the C/BAS/REC.

FIGURE 21. WING PRESSURE DISTRIBUTION

WB AND UTW CONFIGURATIONS

MACH=0.80 2Y/B=0.328

SYMBOL	CONFIGURATIONS	CL
—⧗—	WING-BODY, UPPER	0.4585
-⧗-	WING-BODY, LOWER	0.4585
—✕—	UTW NAC(TEST 337), UPPER	0.4397
-✕-	UTW NAC(TEST 337), LOWER	0.4397

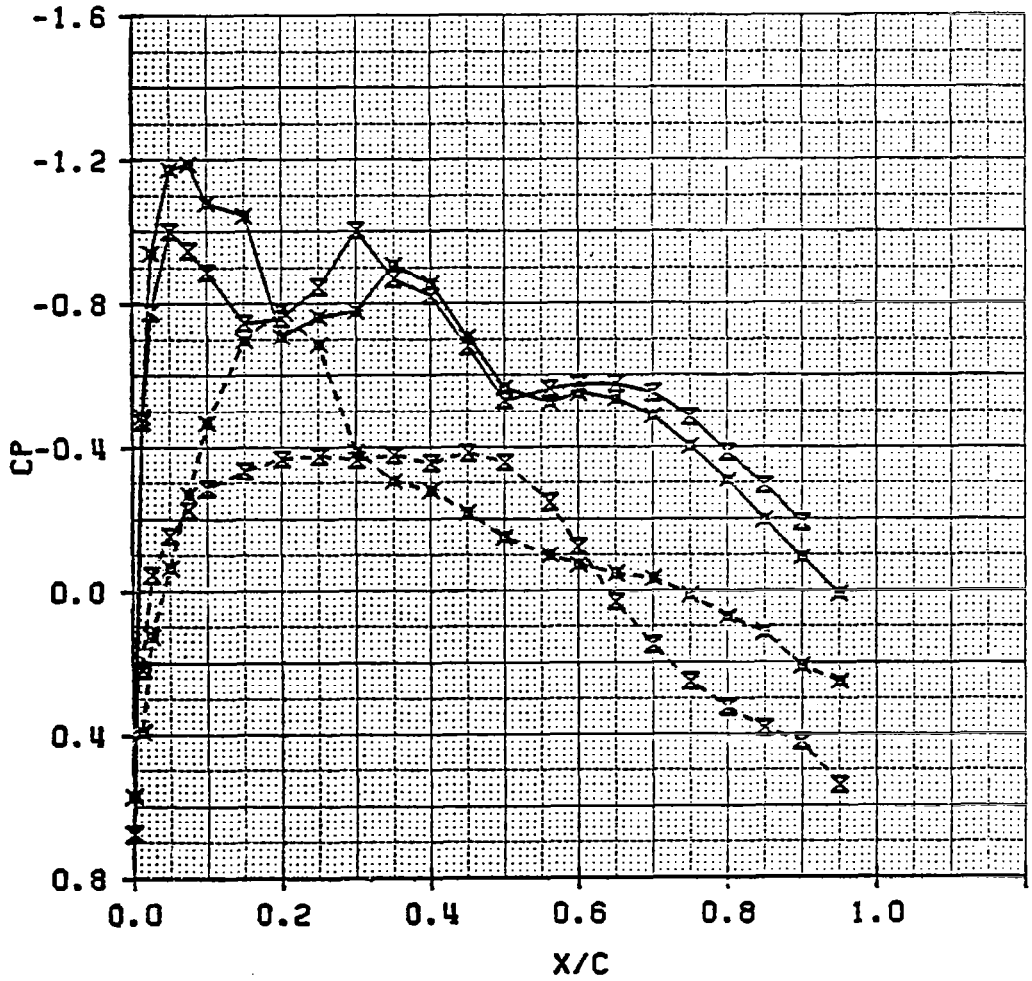

FIGURE 22. WING PRESSURE DISTRIBUTION

WB AND UTW CONFIGURATIONS

MACH=0.80 2Y/B=0.440

SYMBOL	CONFIGURATIONS	CL
—⧖—	WING-BODY, UPPER	0.4585
-⧖-	WING-BODY, LOWER	0.4585
—✕—	UTW NAC(TEST 337), UPPER	0.4397
-✕-	UTW NAC(TEST 337), LOWER	0.4397

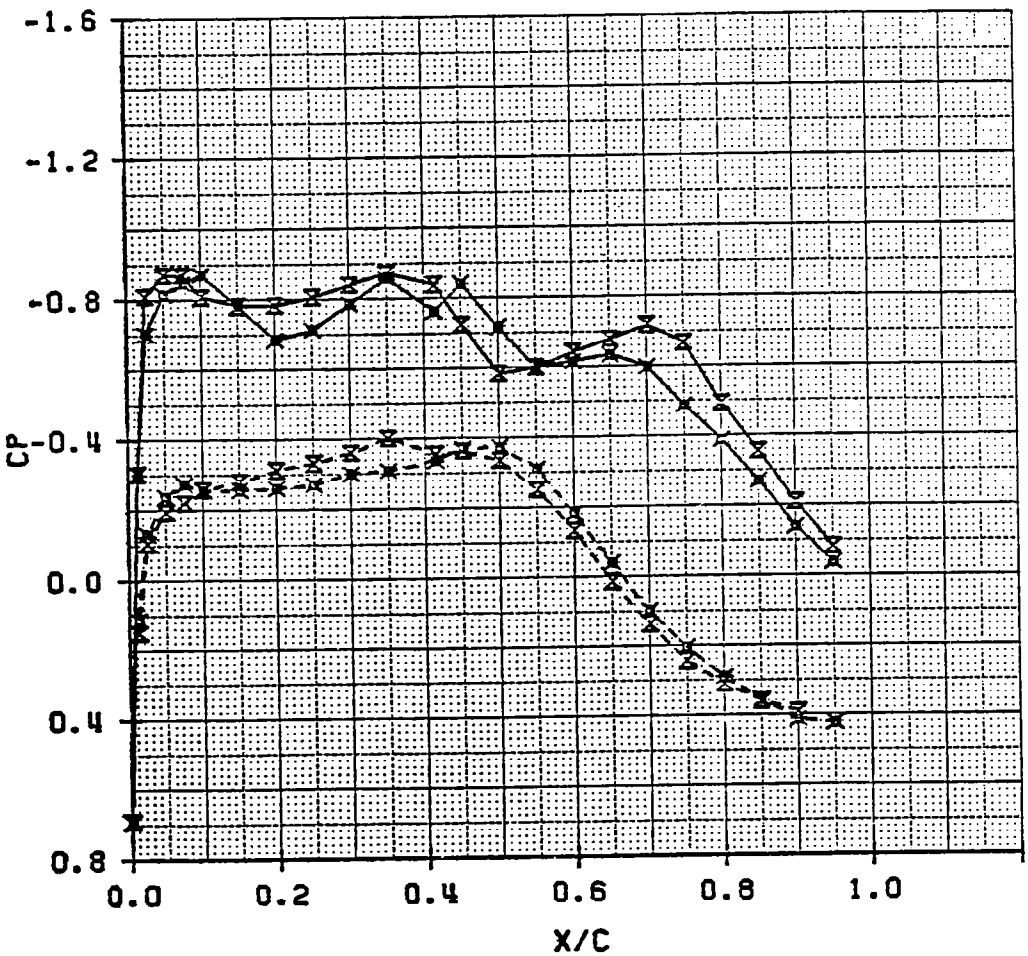

FIGURE 23a.

WING UPPER SURFACE PRESSURE DISTRIBUTION

C NACELLE / BASIC PYLON / REC DIV

MACH NUMBER = 0.800 CL = 0.4334

0.0773 DEG. ANGLE OF ATTACK

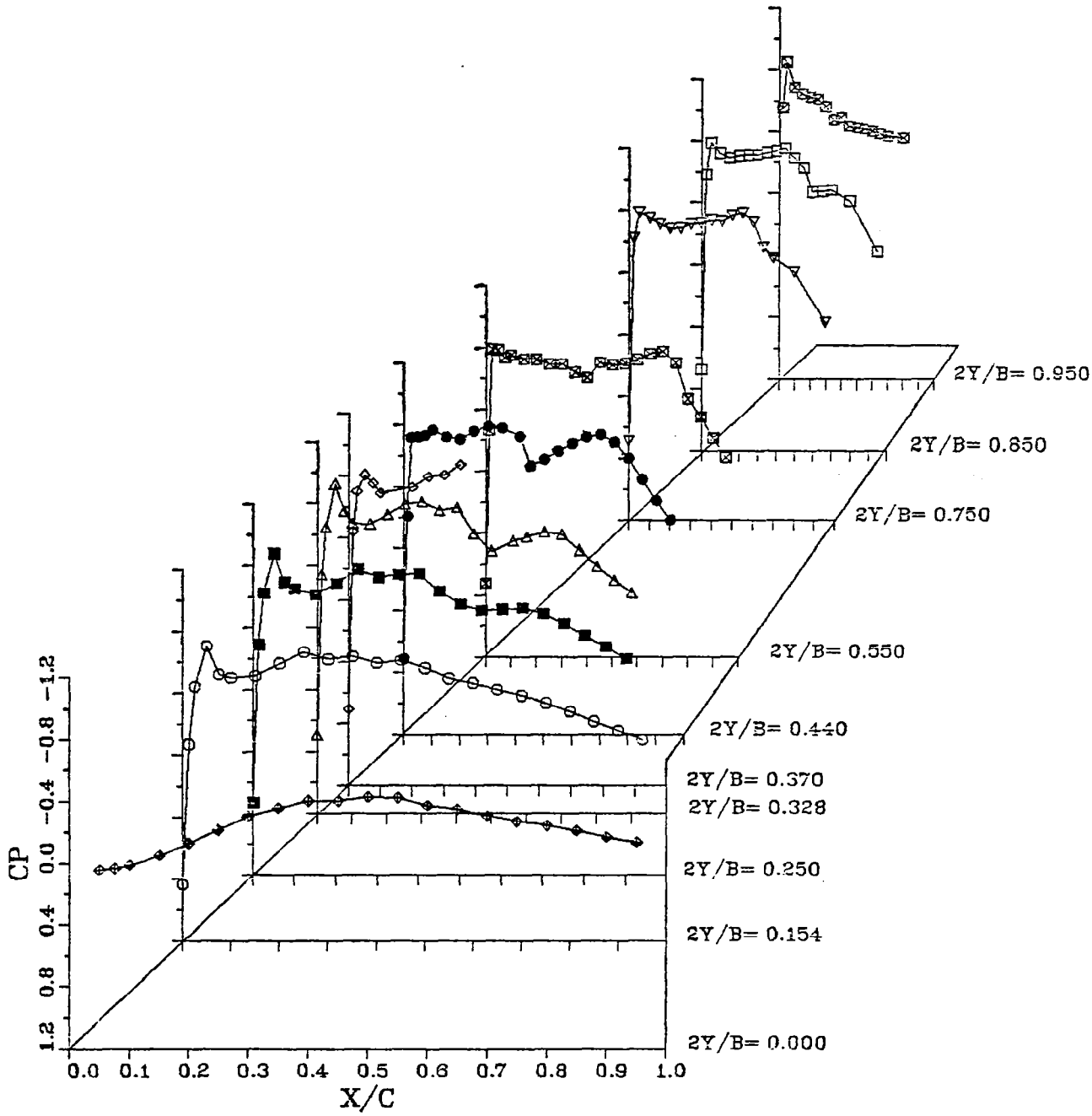

FIGURE 23b.

WING LOWER SURFACE PRESSURE DISTRIBUTION

C NACELLE / BASIC PYLON / REC DIV

MACH NUMBER = 0.800 CL = 0.4334

0.0773 DEG. ANGLE OF ATTACK

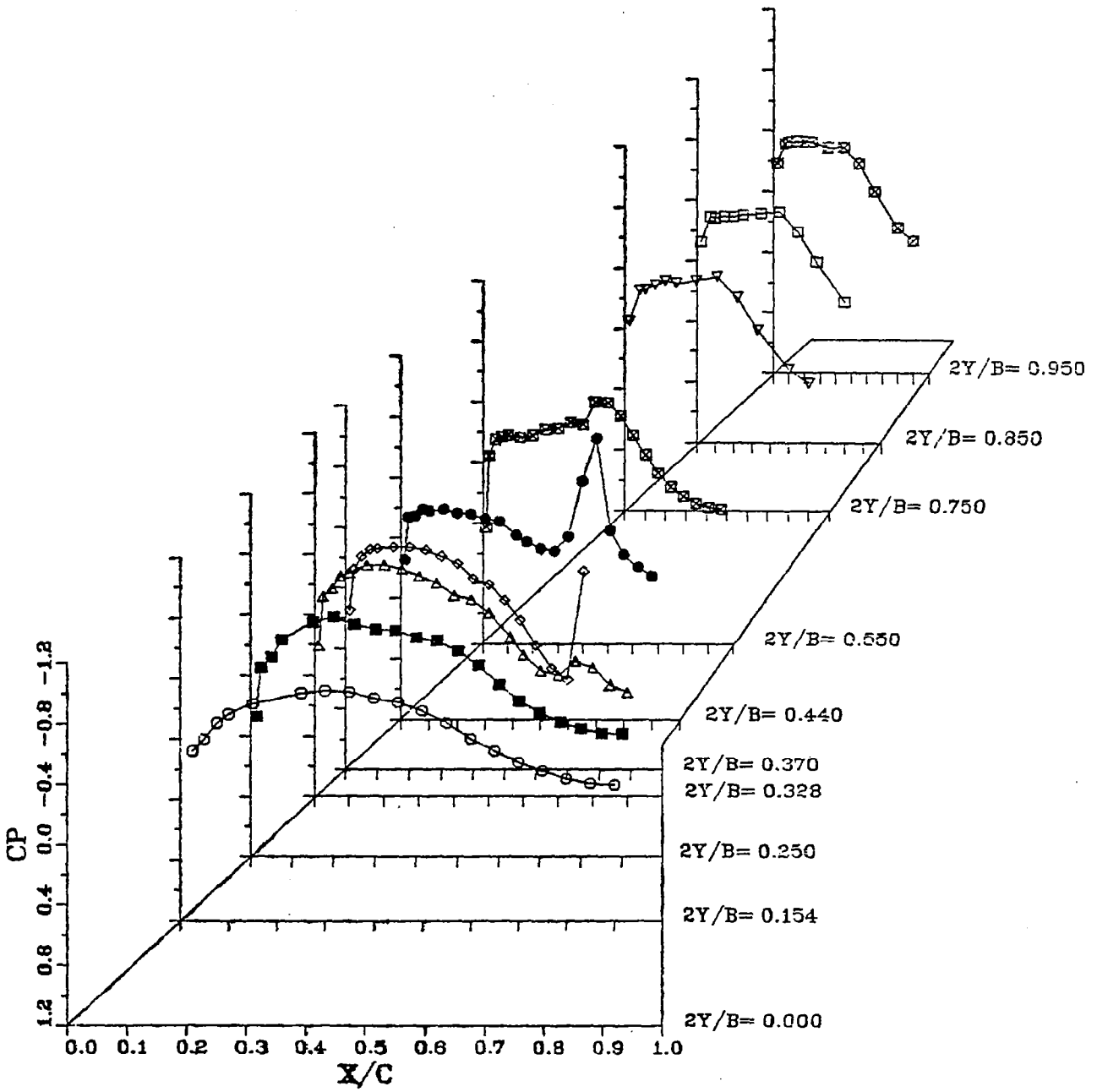

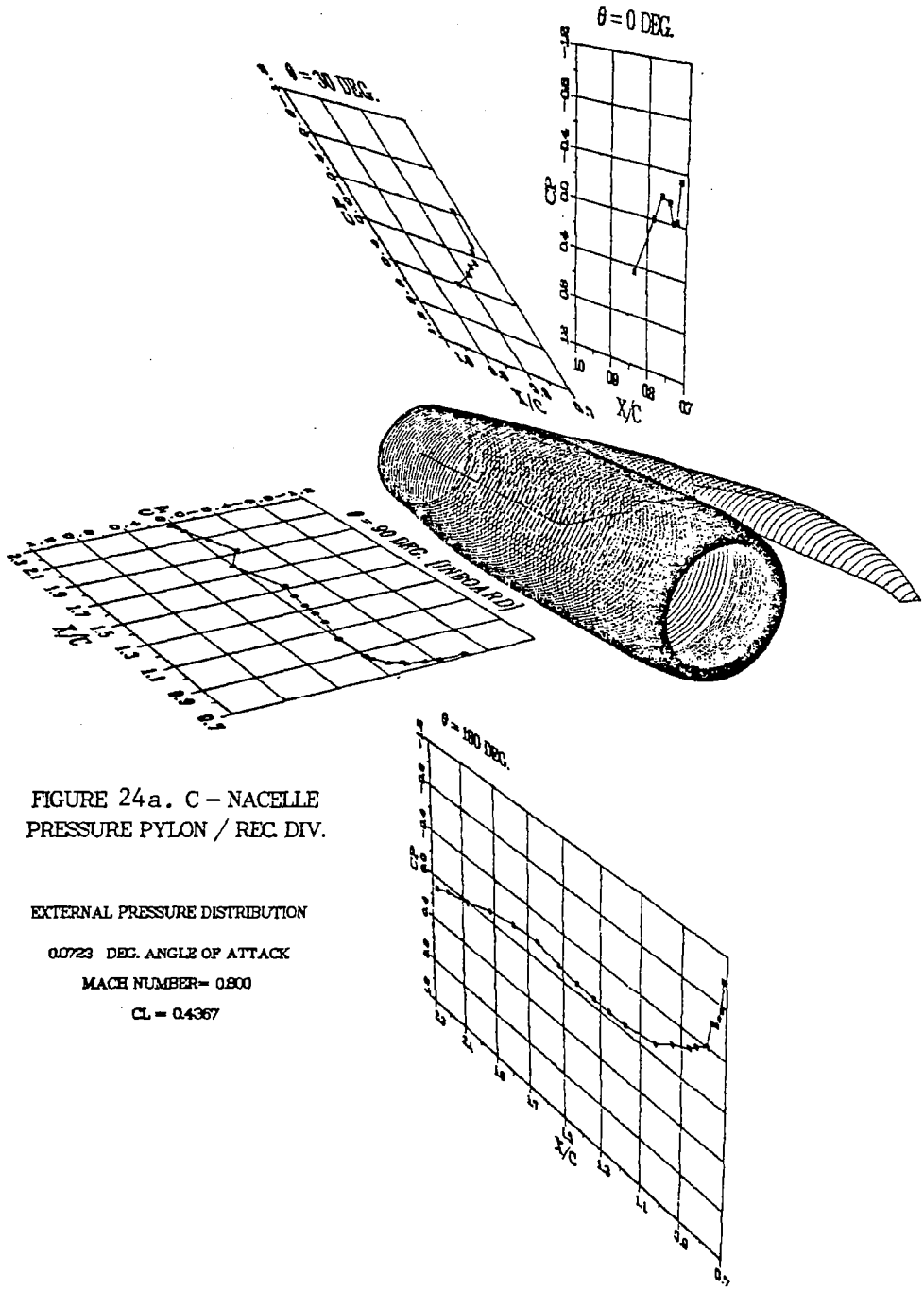

FIGURE 24a. C – NACELLE PRESSURE PYLON / REC. DIV.

EXTERNAL PRESSURE DISTRIBUTION

0.0723 DEG. ANGLE OF ATTACK

MACH NUMBER= 0.800

CL = 0.4367

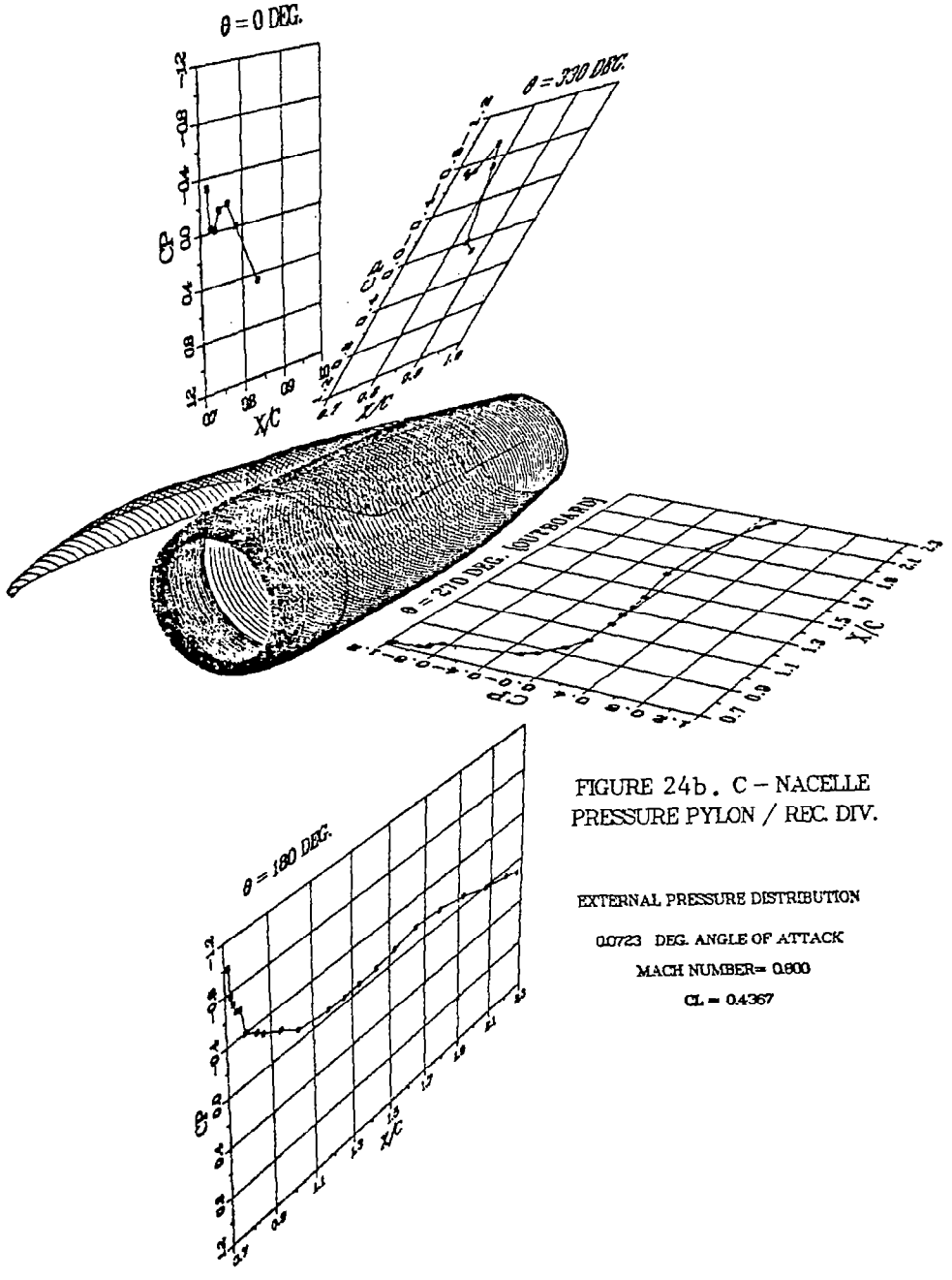

FIGURE 24b. C – NACELLE PRESSURE PYLON / REC. DIV.

EXTERNAL PRESSURE DISTRIBUTION

0.0723 DEG. ANGLE OF ATTACK

MACH NUMBER= 0.800

CL = 0.4367

4.1.2 Effects of Boundary - Layer Diverter on C-Nacelle. - Figure 25 shows the drag polars at Mach number 0.80 for the WB, C/BAS/REC, and C/BAS/HL. There were only small drag differences due to the boundary-layer diverters for the C-nacelle, and these differences disappeared at high C_L. The C/BAS/REC had lower drag in the ordinary operating C_L range.

Figure 26 again shows that the highlight diverter with the C-nacelle caused only a small drag increase over the recessed diverter. Figure 27 indicates that the boundary-layer diverter had a small effect on maximum L/D, consistent with figures 25 and 26.

Figure 28 shows the wing pressures for the C/BAS/HL configuration. These Cp distributions are very similar to those for the C/BAS/REC in figure 23, and further confirm that the highlight diverter had only a small effect.

4.1.3 Effects of the Pressure Pylons. - Drag polars at Mach number 0.80 are shown in figure 29 for the WB, D/BAS, D/PRES, and C/PRES/REC configurations.

The configurations with pressure pylons had higher drag throughout the normal operating range of C_L. Thus, there was no apparent drag advantage from these bodies on the wing upper surface. They also had less distinct values of M_{DD} and higher wave drag, as shown in figure 30. There is a suggestion that M_{DD} may be less than 0.81 for the D/PRES and C/PRES/REC configurations. The pressure pylons on the D/PRES and C/PRES/REC configurations caused small increases in maximum cross-sectional area. This is shown in figure 31, and may account for the more unfavorable wave drag characteristics revealed in figure 30.

The adverse effect of the pressure pylons at Mach numbers greater than 0.78 is again apparent in Figure 32 for maximum L/D. The abrupt decrease in $(L/D)_{MAX}$ for the D/PRES above Mach number 0.78 was probably due to its higher wave drag and possibly lower M_{DD}.

FIGURE 25. DRAG POLARS AT MACH 0.80 FOR WB, C/BAS/REC, AND C/BAS/HL CONFIGURATIONS

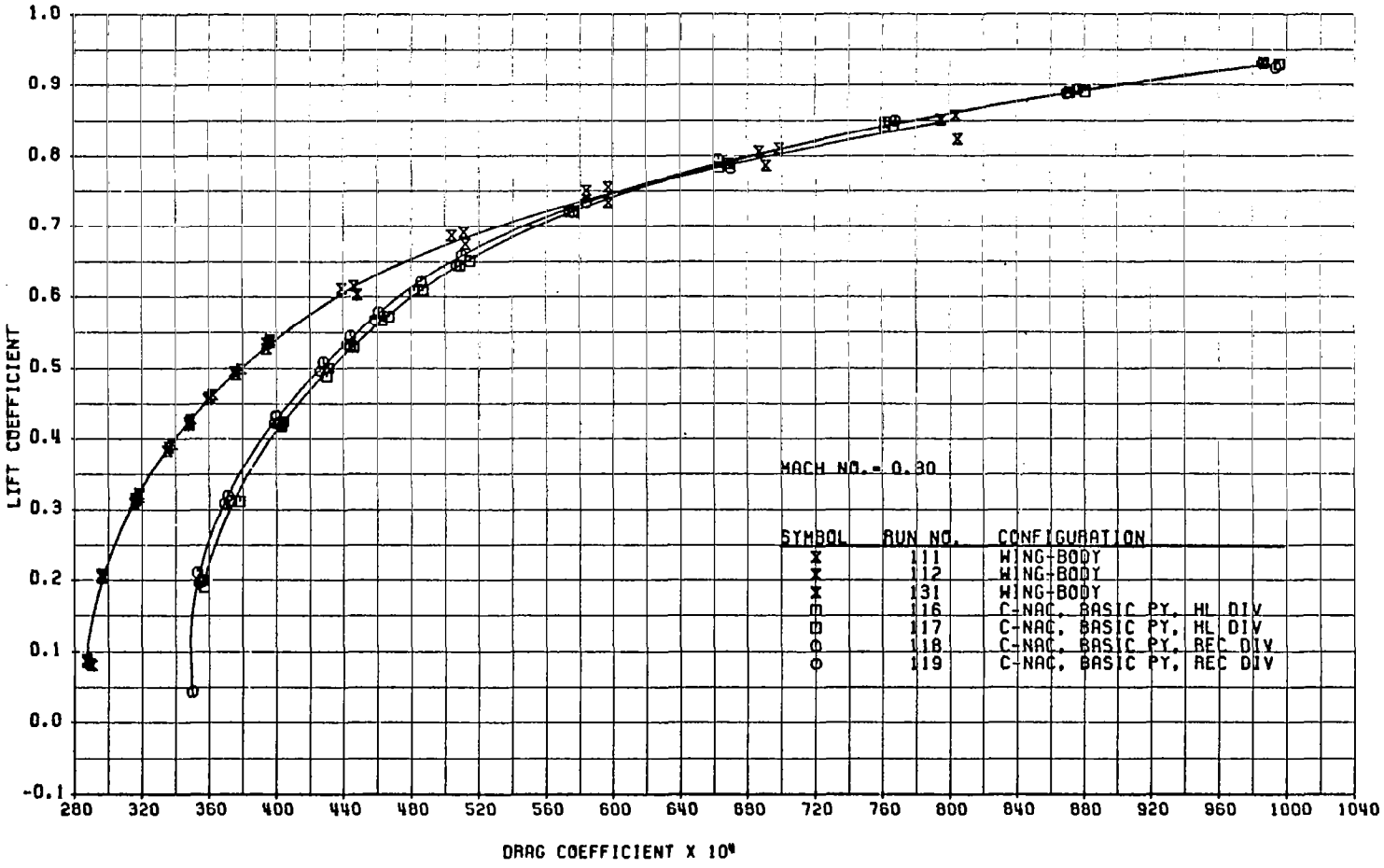

FIGURE 26. DRAG COEFFICIENT VERSUS MACH NUMBER AT CL=0.45 FOR WB, C/BAS/REC AND C/BAS/HL CONFIGURATIONS

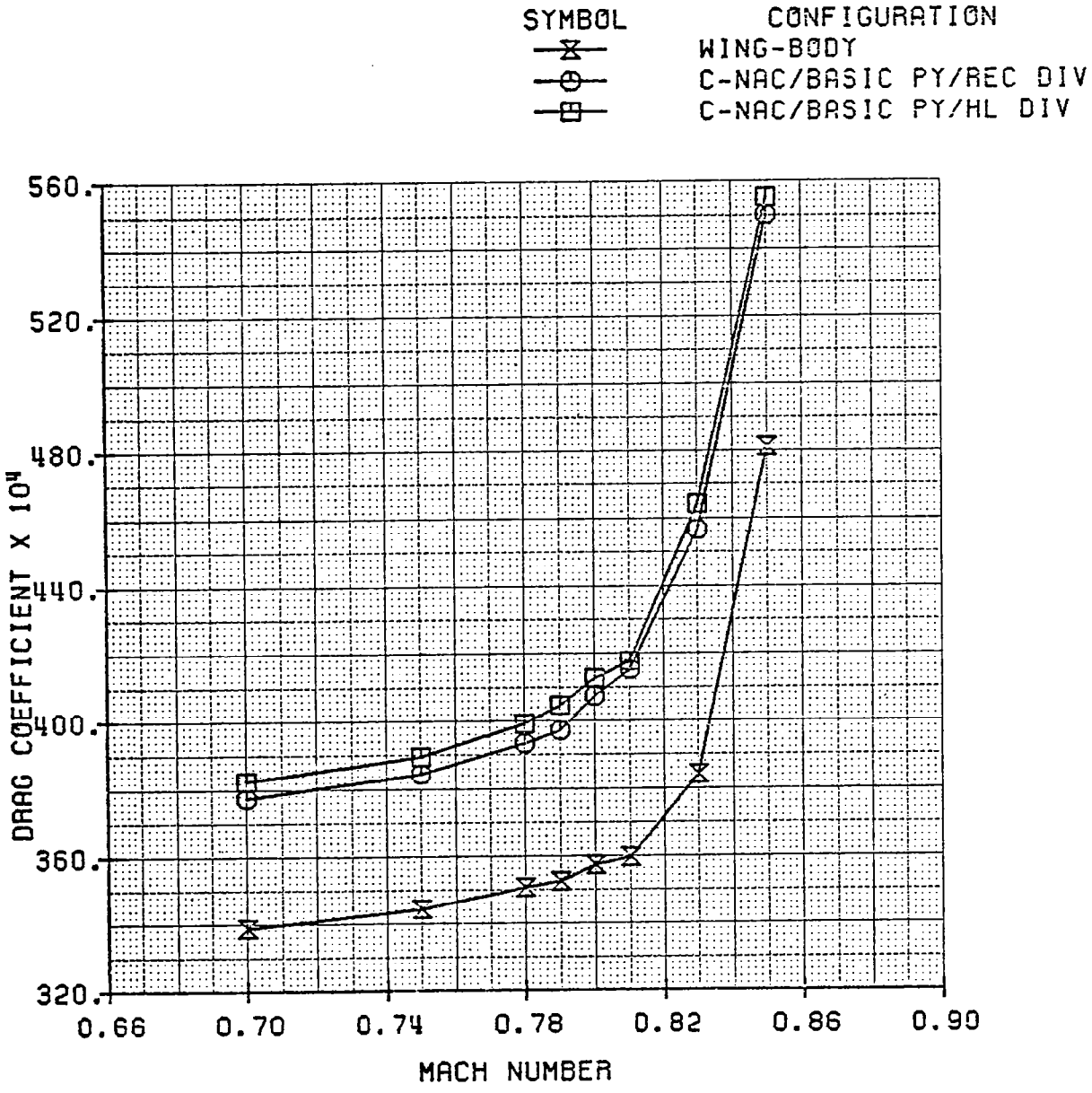

FIGURE 27. MAXIMUM L/D VERSUS MACH NUMBER

FOR WB, C/BAS/HL AND

C/BAS/REC CONFIGURATIONS

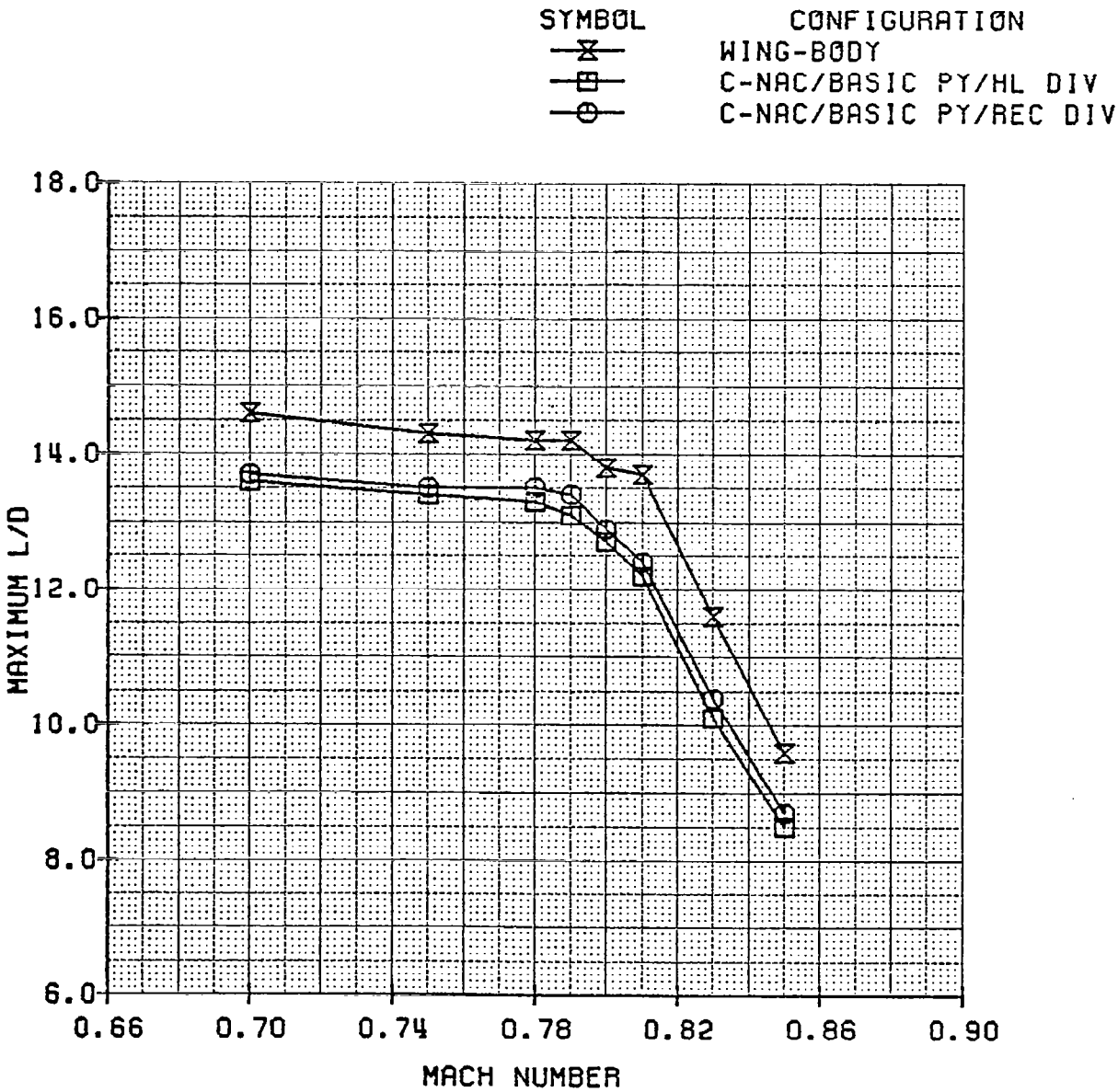

FIGURE 28a.

WING UPPER SURFACE PRESSURE DISTRIBUTION

C NACELLE / BASIC PYLON / HL DIV

MACH NUMBER = 0.800 CL = 0.4207

0.0665 DEG. ANGLE OF ATTACK

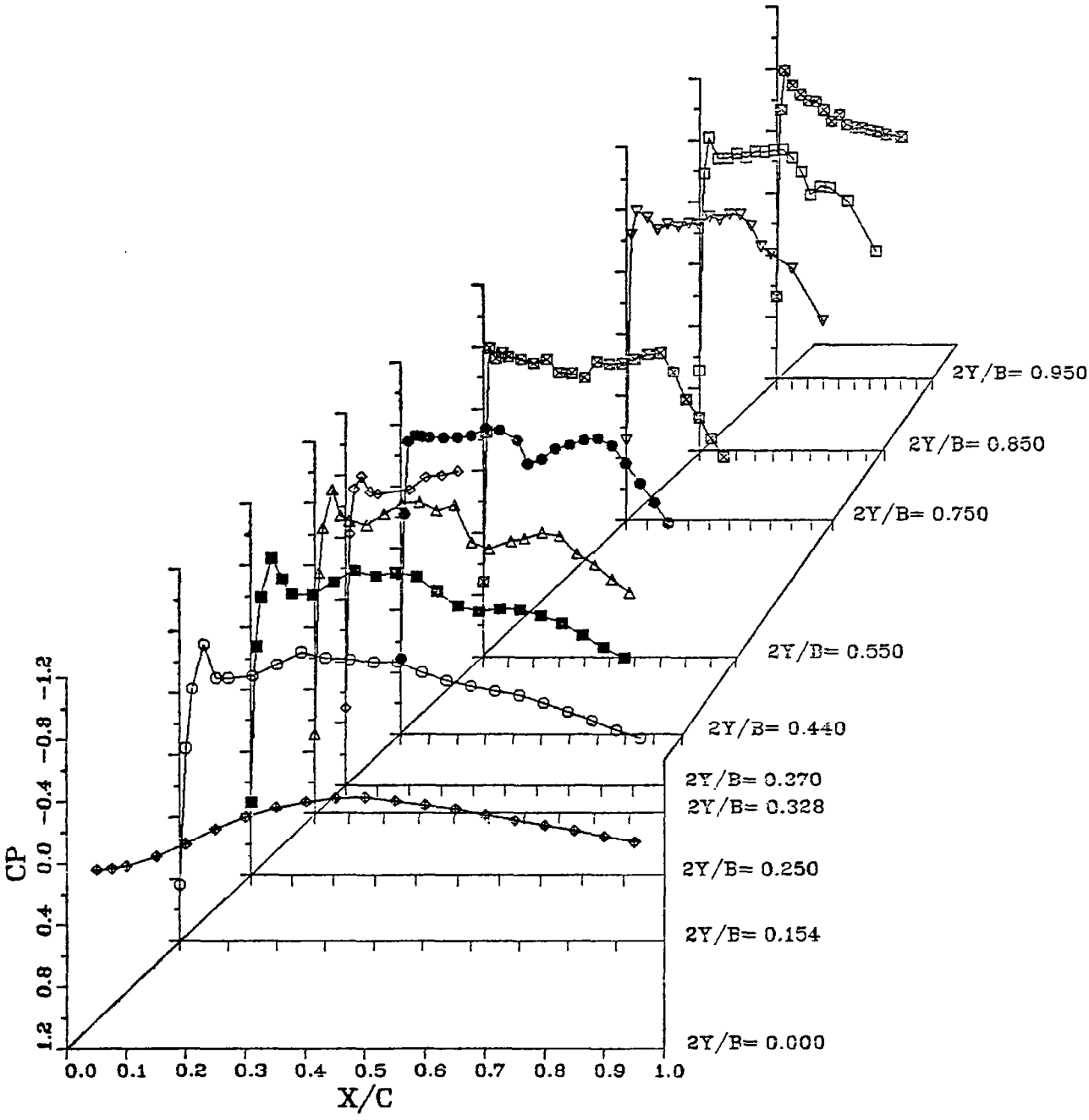

FIGURE 28b.

WING LOWER SURFACE PRESSURE DISTRIBUTION

C NACELLE / BASIC PYLON / HL DIV

MACH NUMBER = 0.800 CL = 0.4207

0.0665 DEG. ANGLE OF ATTACK

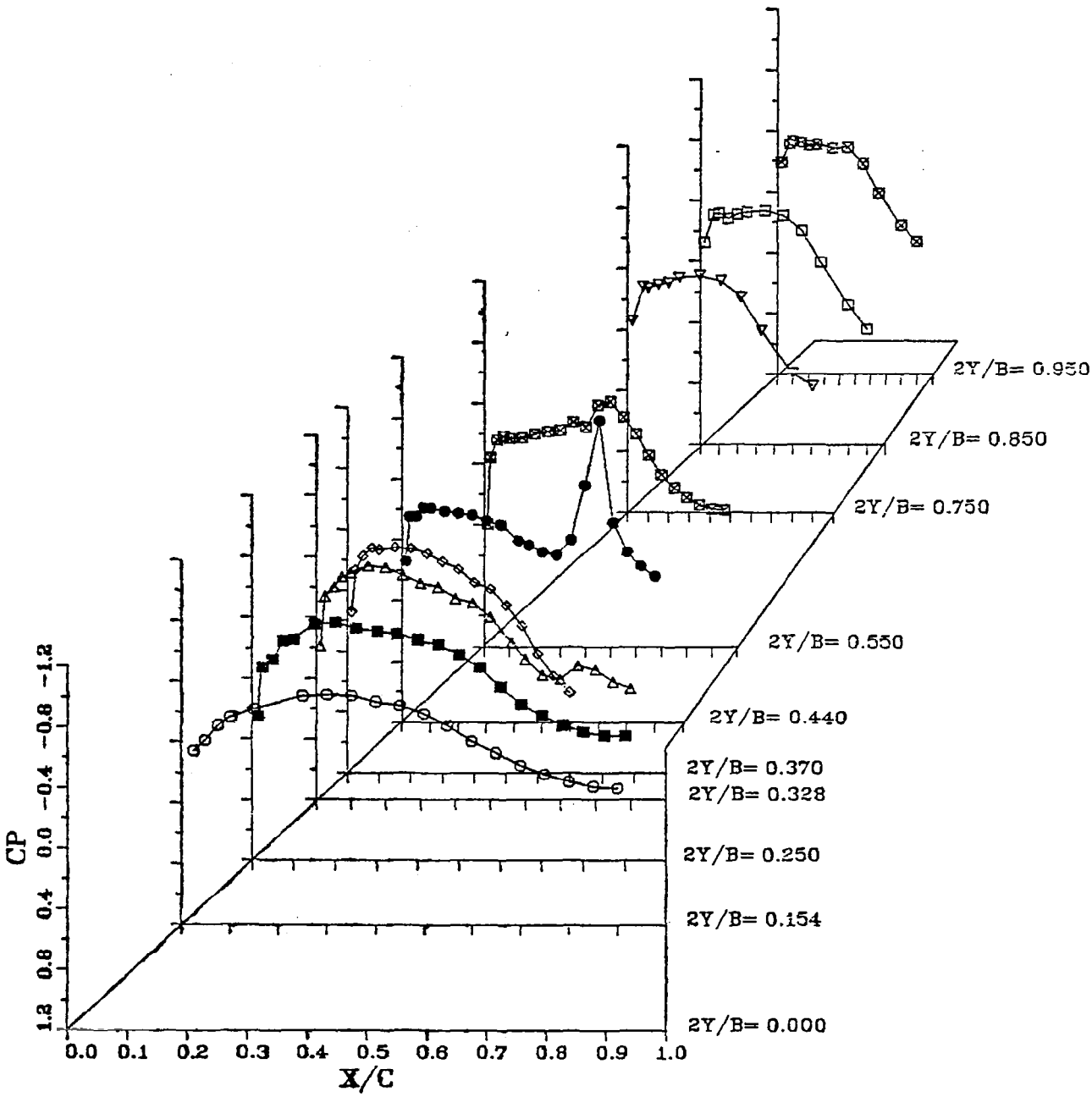

FIGURE 29. DRAG POLARS AT MACH 0.80 FOR WB, D/BAS, D/PRES, AND C/PRES/REC CONFIGURATIONS

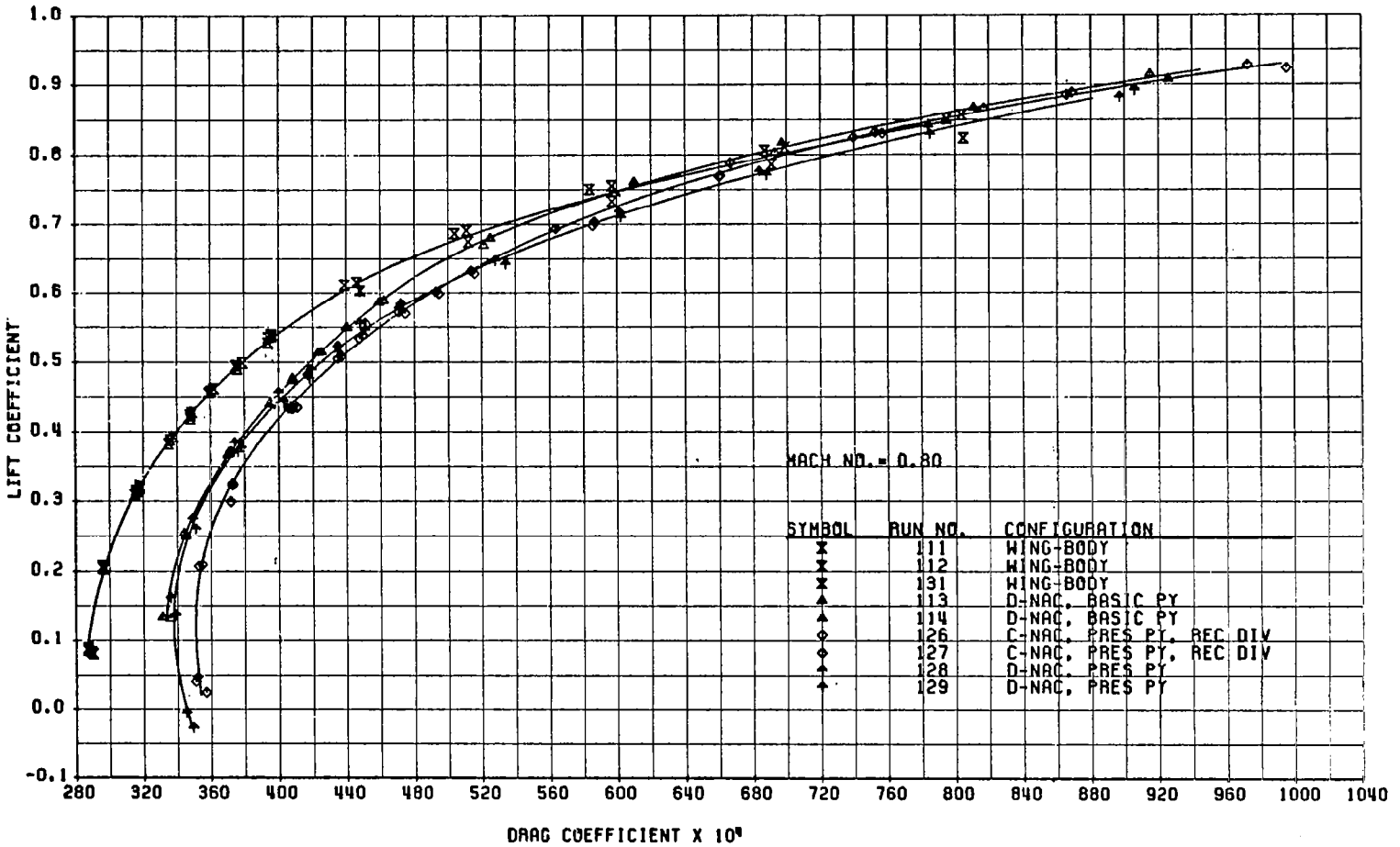

FIGURE 30. DRAG COEFFICIENT VERSUS MACH NUMBER AT CL=0.45 FOR WB, D/BAS, D/PRES AND C/PRES/REC CONFIGURATIONS

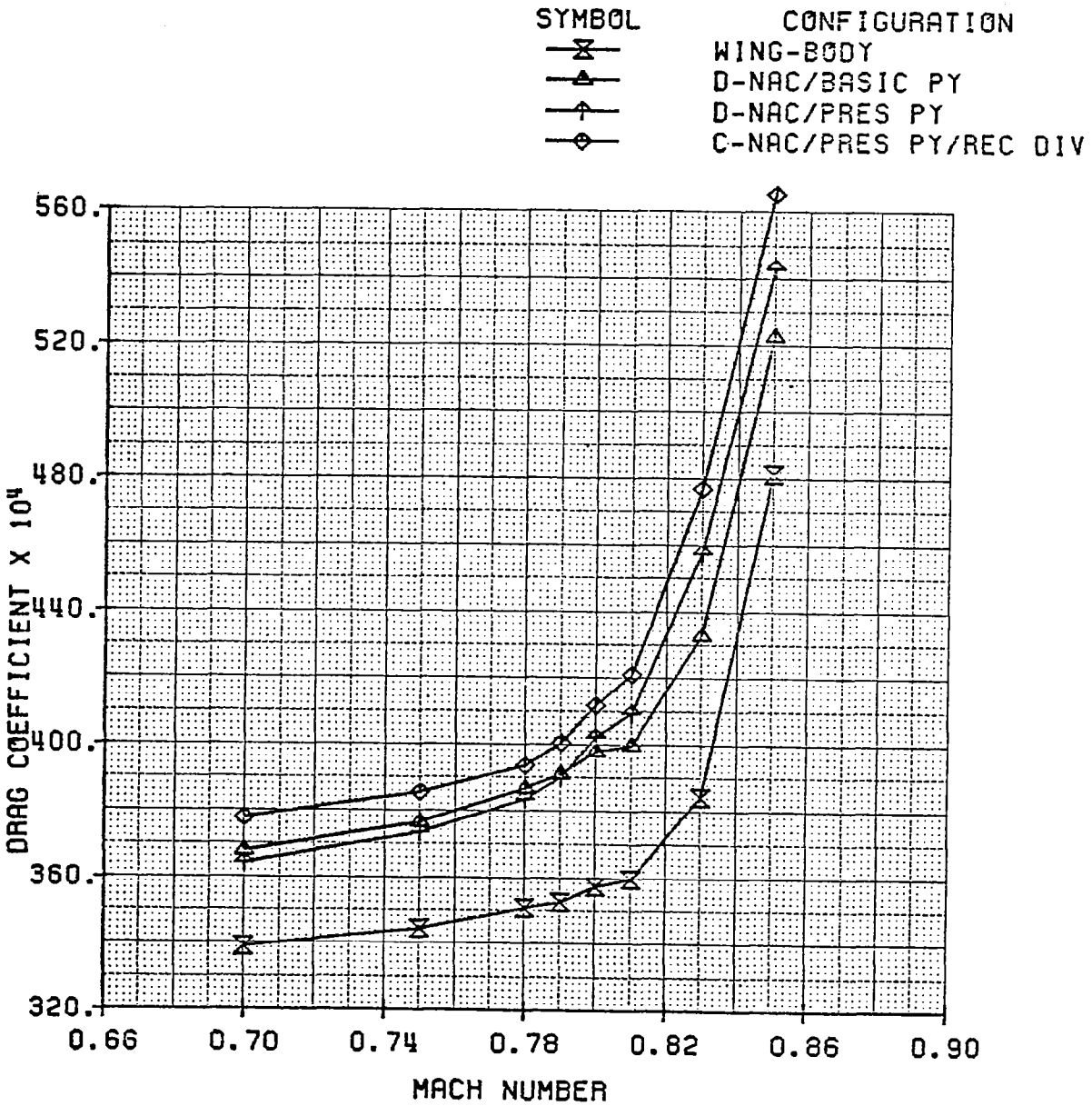

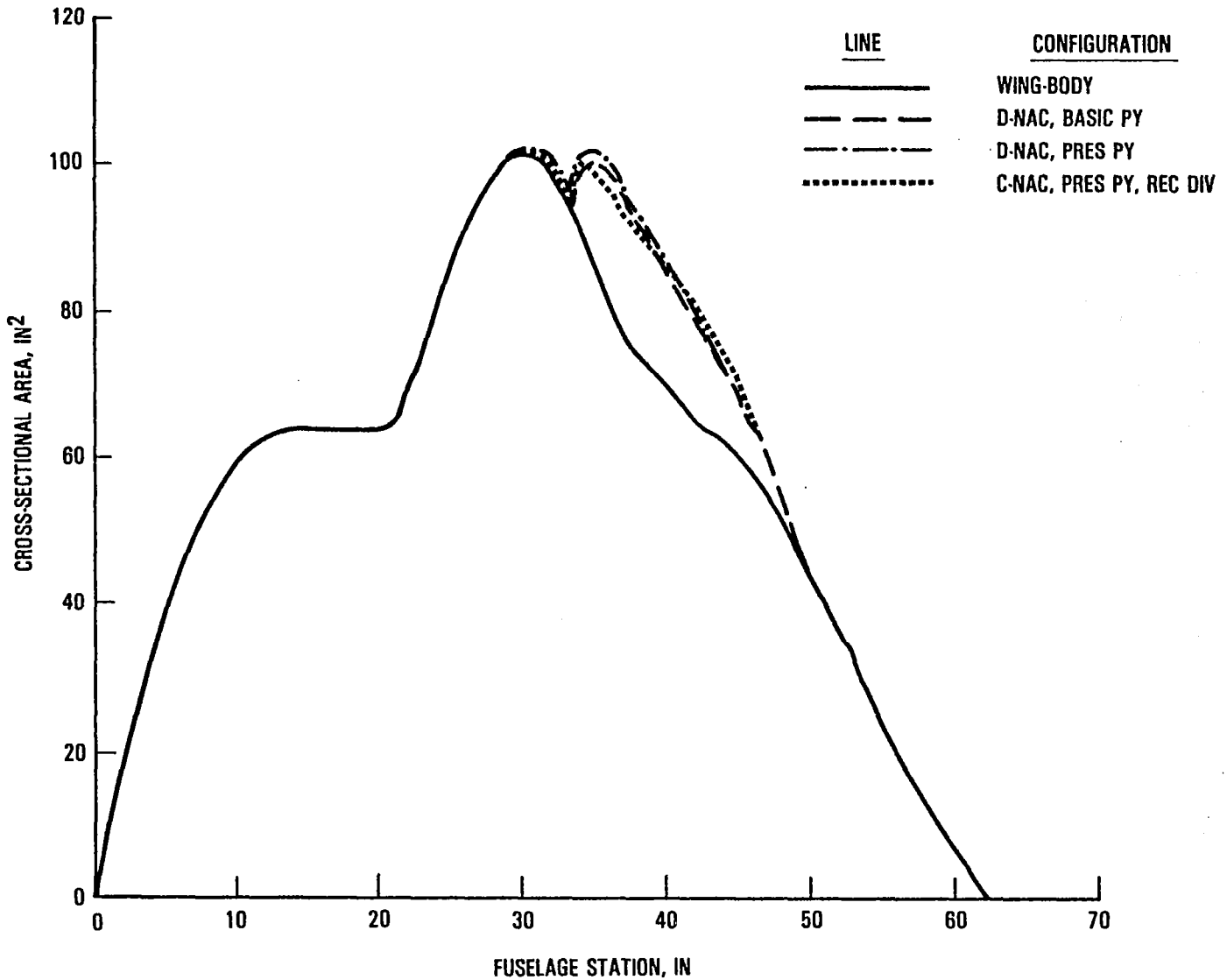

FIGURE 31. AIRPLANE MODEL CROSS-SECTIONAL AREA DISTRIBUTION FOR WB, D/BAS, D/PRES AND C/PRES/REC CONFIGURATIONS

FIGURE 32. MAXIMUM L/D VERSUS MACH NUMBER

FOR WB, D/BAS, C/PRES/REC

AND D/PRES CONFIGURATIONS

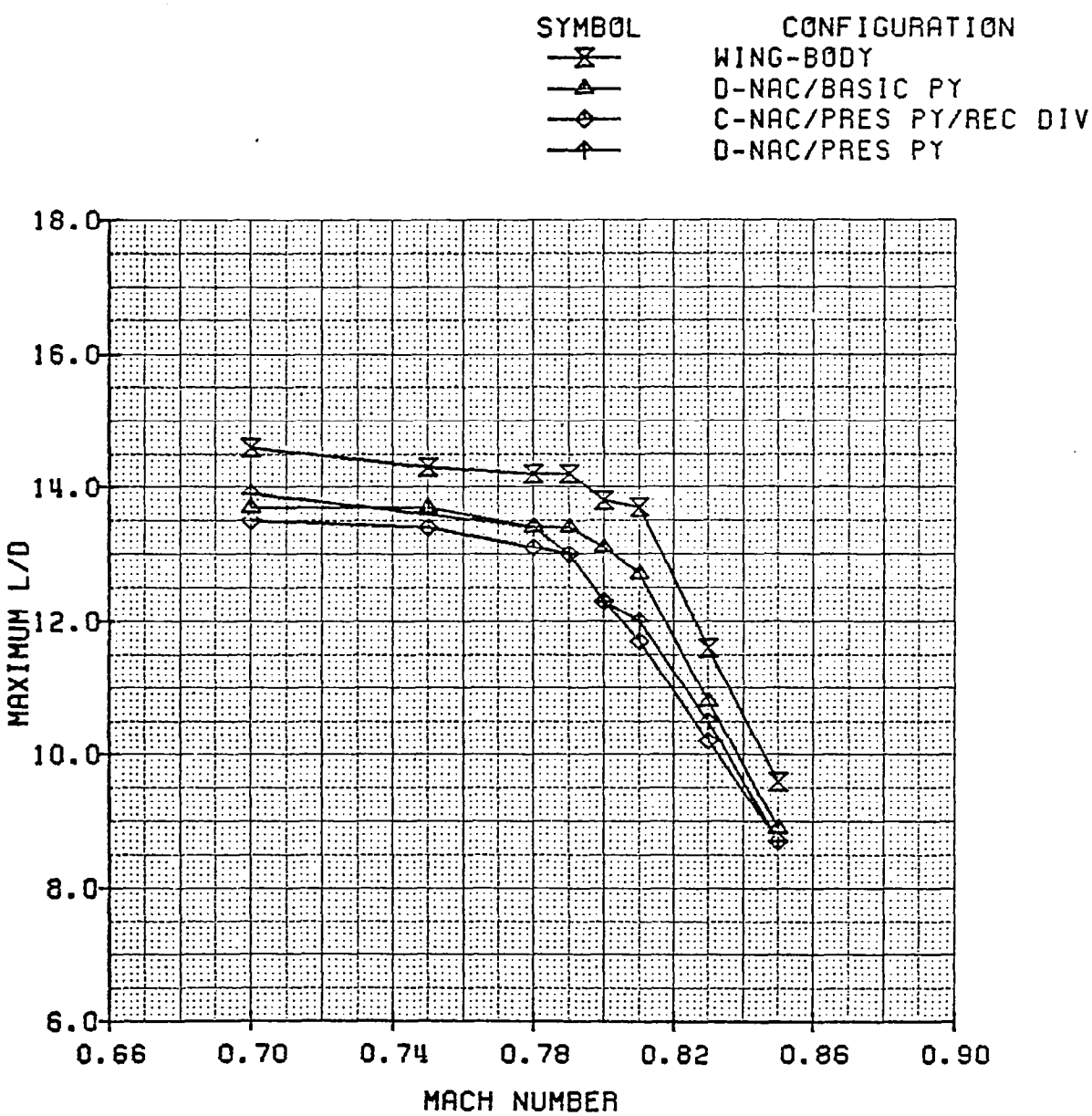

The wing C_p distributions for the D/PRES configuration are given in figure 33. On the upper surface at 2Y/B = 0.154 and x/c = 0.05, a local compression was indicated. The remaining pressures at 2Y/B = 0.154, 0.250, and 0.328 were similar to those for the D/BAS in figure 16. The pressure taps at 2Y/B = 0.370 were covered by the pressure pylon. The outboard pressure profiles at 2Y/B = 0.440 were different, but there was no clear indication of why the D/PRES configuration had higher drag. The wing lower surface pressures were nearly the same for the D/PRES and D/BAS. This was expected because the two nacelle geometries were the same under the wing.

Figure 34 for the C/PRES/REC can be compared with figure 23 to assess the effects of the pressure pylon. Again, the profiles were different on the upper surface at 2Y/B = 0.440. There was possibly a stronger shock for the C/PRES/REC at x/c greater than 0.70. Otherwise, there were no distinct differences due to the pressure pylon that appeared in the wing pressure data.

Additional wing and nacelle C_p profiles are given in the Appendix.

A number of oil flow photographs were taken. These photographs were inconclusive for interpretation of the flow behavior. Selected oil flow photographs are shown in the Appendix.

4.2 Installed Lift Comparisons

Lift curves at Mach number 0.80 for the WB, D/BAS, C/BAS/REC, C/BAS/HL, and UTW configurations are given in figure 35. The lift-curve slope was nearly the same for all five configurations. There was a significant increase in C_L at a given α for the aft nacelle installations compared with the WB. This was in sharp contrast to the UTW, which had a lower C_L at a given angle of attack. This behavior of the aft nacelles was roughly similar to that of trailing-edge flaps, in that the lift curve shifted upward relative to the WB, and the zero-lift α shifted to a more negative value.

FIGURE 33a.

WING UPPER SURFACE PRESSURE DISTRIBUTION

D NACELLE / PRESS PYLON

MACH NUMBER = 0.800 CL = 0.4574

0.5692 DEG. ANGLE OF ATTACK

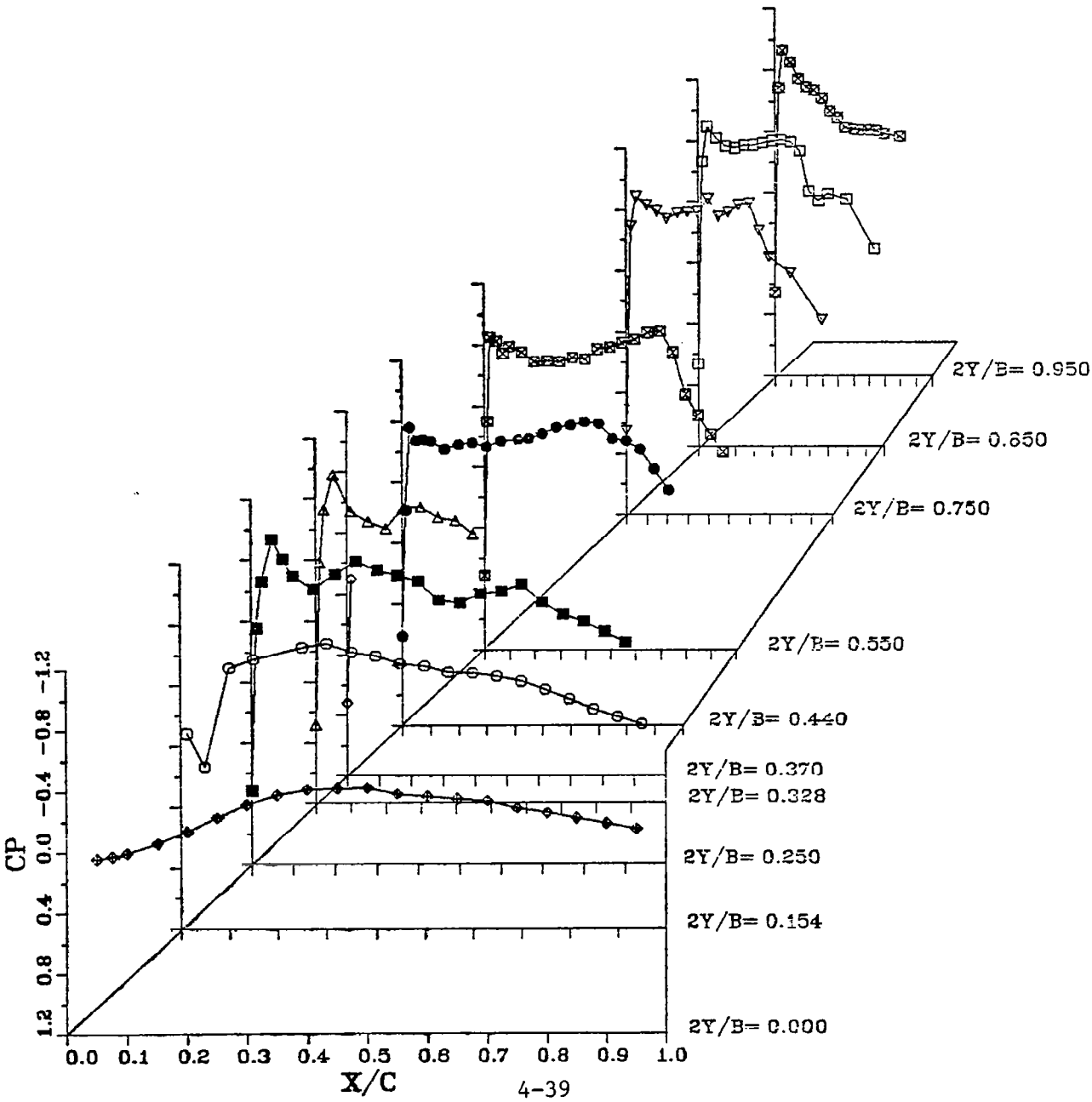

FIGURE 33b.

WING LOWER SURFACE PRESSURE DISTRIBUTION

D NACELLE / PRESS PYLON

MACH NUMBER = 0.800 CL = 0.4574

0.5692 DEG. ANGLE OF ATTACK

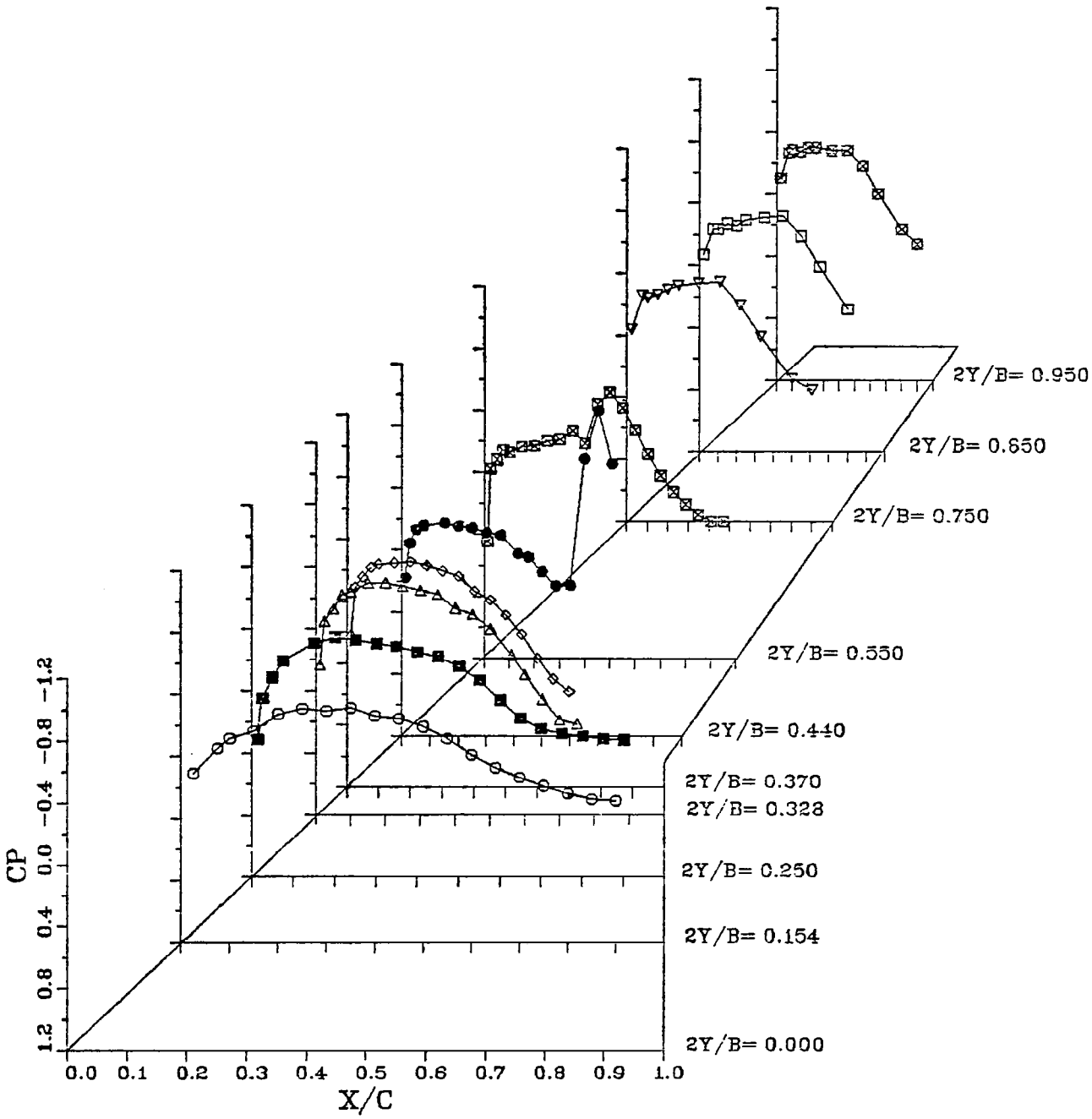

FIGURE 34a.

WING UPPER SURFACE PRESSURE DISTRIBUTION

C NACELLE / PRESS PYLON / REC DIV

MACH NUMBER = 0.800 CL = 0.4367

0.0723 DEG. ANGLE OF ATTACK

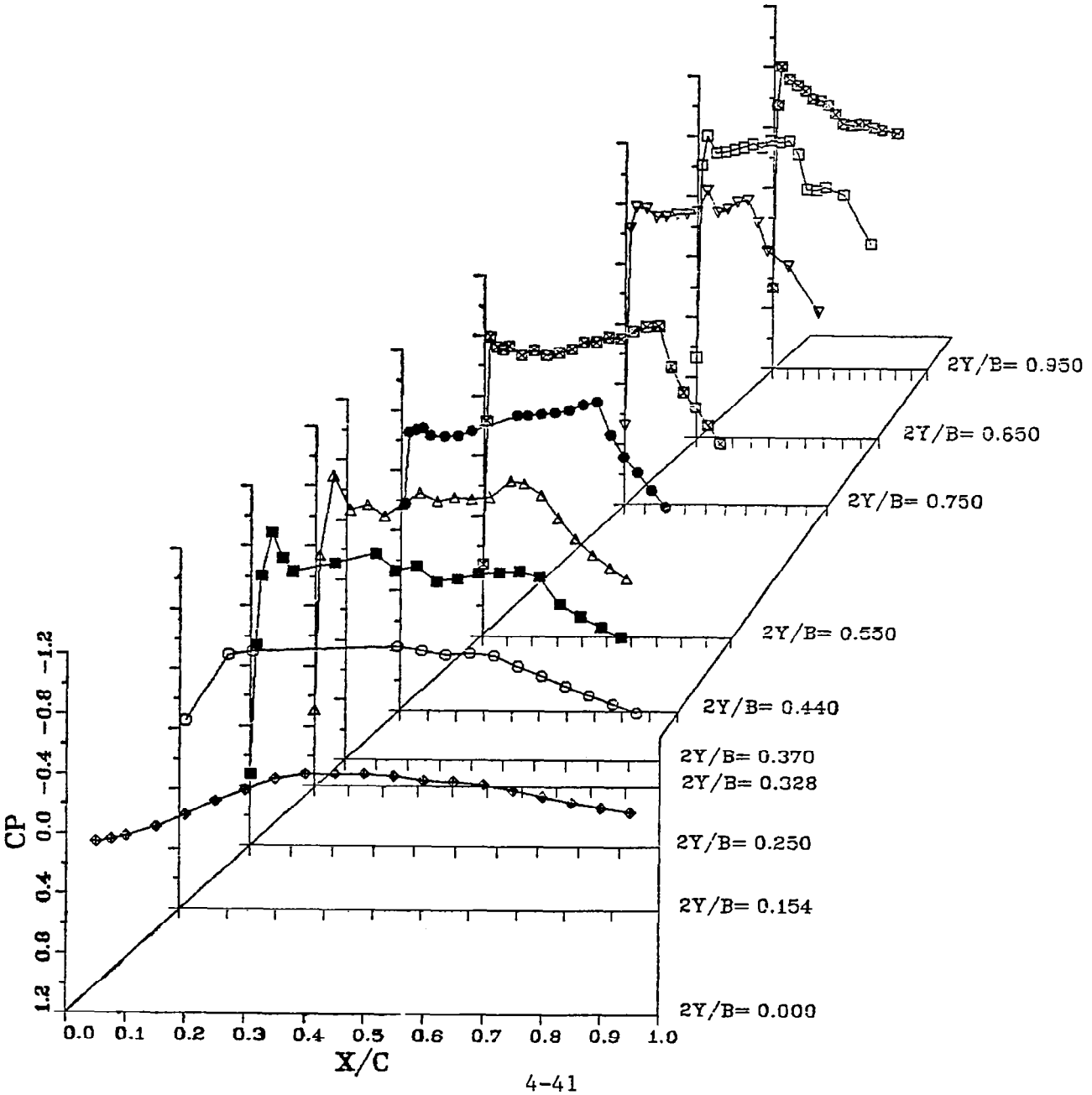

FIGURE 34b.

WING LOWER SURFACE PRESSURE DISTRIBUTION

C NACELLE / PRESS PYLON / REC DIV

MACH NUMBER = 0.800 CL = 0.4367

0.0723 DEG. ANGLE OF ATTACK

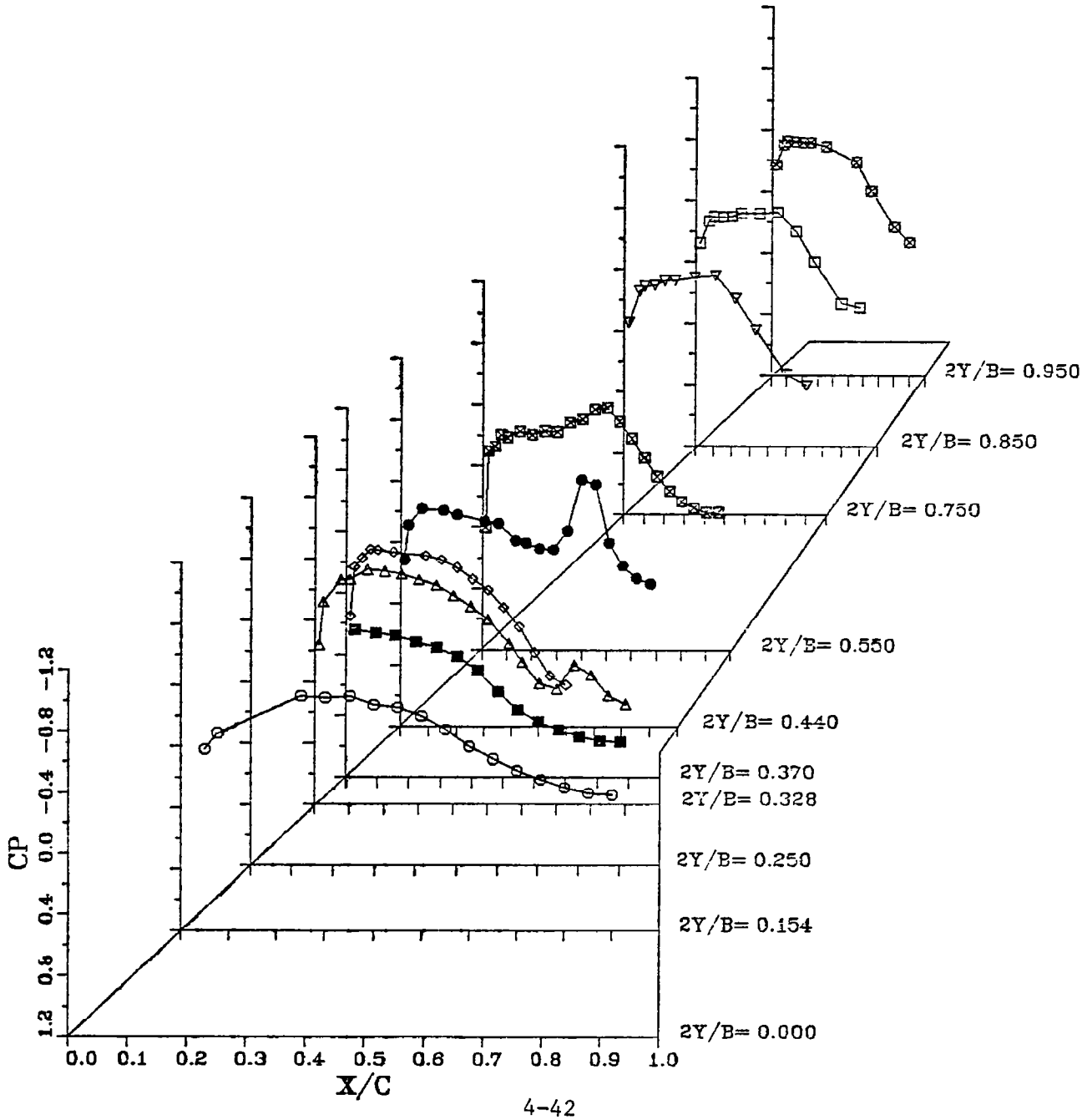

FIGURE 35. LIFT COEFFICIENT VERSUS ANGLE OF ATTACK AT M=0.80 FOR WB, D/BAS, C/BAS/REC, C/BAS/HL AND UTW CONFIGURATIONS

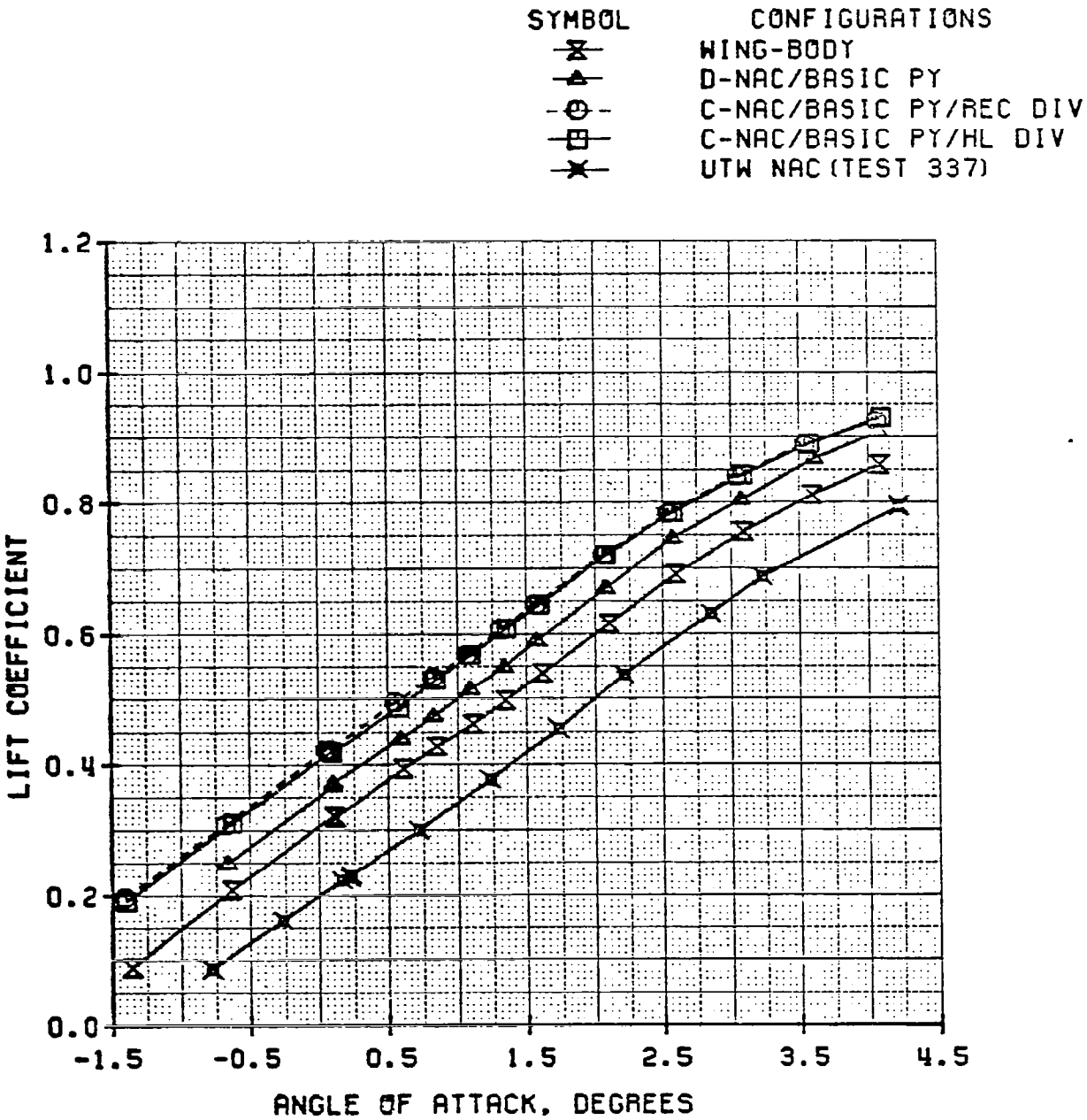

Figure 35 also shows that the highlight diverter had a very small effect on the lift curve, compared to the recessed diverter.

Normalized wing section normal force coefficient, $C_n(c/\bar{c})$, versus semispan station, 2Y/B, is shown in figure 36 at Mach number 0.80. The data for the WB, D/BAS, and C/BAS/REC are at α = 1.31 degrees; while that for the UTW are at α = 1.23 degrees. C_n was obtained by numerically integrating the measured C_p's with respect to x/c at each wing section. The results are compared at fixed α so that the only geometry differences are due to the nacelle configurations. The aft nacelle installations showed much higher lift at the inboard wing sections than did the WB. (The nacelle centerline was at 2Y/B = 0.370.) In contrast, the UTW nacelle installation had much lower lift at the inboard wing sections. These differences are responsible for at least part of the measured differences in C_L at fixed α shown in figure 35. Results for the D/BAS are only given at 2Y/B = 0.154 and 0.250. At the other wing sections, there were too many pressures missing or covered by the nacelle/pylon to permit a meaningful integration (e.g., see figures 16-18.)

The tests discussed in this report were performed with a fixed tail. This was done in order to get direct drag comparisons with the UTW data from earlier tests. The tail incidence was the same for both tests. The aft nacelles seem to cause an increase in wing lift at fixed α, and so apparently cause an increase in wing downwash at the inboard wing sections. There is then a corresponding tendency to increase the download on the tail at fixed α. (The relative change in dynamic pressure at the tail is not known, however.) Thus, the measured increase in aircraft C_L, at fixed α, due to adding the aft nacelles may possibly underestimate the potential benefit. This question can only be resolved by tests with the tail off.

Similarly, the lift penalty caused by adding the UTW nacelles at fixed α may possibly be underestimated. Again, tests with the tail off are required to resolve this issue.

FIGURE 36. NORMALIZED WING SECTION NORMAL FORCE COEFFICIENT VERSUS SEMISPAN STATION AT MACH 0.80 AND α=1.3 DEGREES

SYMBOL	CONFIGURATION
⧗	WING-BODY
△	D-NAC/BASIC PY
⏲	C-NAC/BASIC PY/REC DIV
⌘	UTW NAC(1.2 DEG.)

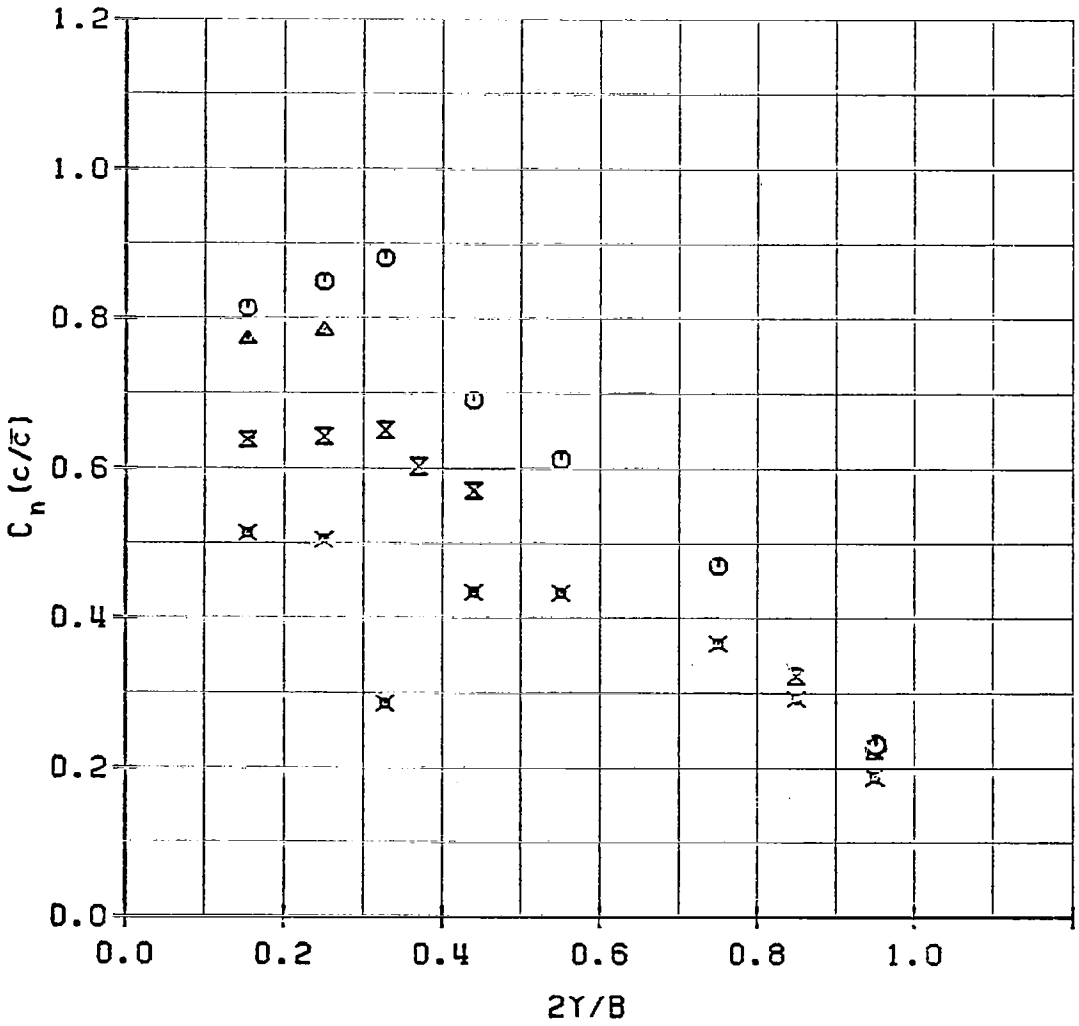

Additional information about the effects of the nacelles on C_L can be obtained by comparing C_p profiles at the same Mach number and the same angle of attack. Figure 37 shows wing surface pressures for the WB at Mach number 0.80 and α = 1.3 degrees. For comparison, figure 38 has the same information at the same conditions for the D/BAS installation. Differences in wing upper surface pressures appear to be small. There were major differences on the wing lower surface at sections 2Y/B = 0.154, 0.250, 0.328, and 0.440, however. The C_p's for the D/BAS were generally higher than for the WB.

Figures 39 and 40 show specific comparisons of the WB and D/BAS at 2Y/B = 0.328 and 0.440, respectively. These figures again illustrate the increase in pressure on the wing lower surface for the D/BAS. Figure 40 also shows the sudden expansion and recompression on the wing lower surface between x/c = 0.60 and 0.75 for the D/BAS. This was apparently caused by flow around the outboard lip of the D/BAS nacelle.

Wing pressure distributions for the UTW at α = 1.23 degrees are shown in figure 41. When these are compared with those for the WB in figure 37, the major differences are on the wing lower surface at 2Y/B = 0.154, 0.250, and 0.328. For the UTW, the flow in this region became supersonic (C_p less than -0.43), as noted previously for figure 20.

Direct comparisons of the wing C_p profiles of the WB and UTW at 2Y/B = 0.328 and 0.440 are shown in figures 42 and 43, respectively. At 2Y/B = 0.328, the UTW clearly had lower pressures over most of the wing lower surface. The flow was supersonic for x/c approximately 0.09 to 0.27. The C_p's for the UTW were also generally higher on the wing upper surface.

Figure 44 shows wing pressures for the C/BAS/REC at Mach number 0.80 and α = 1.31 degrees. The differences in measured C_p's between this configuration and the D/BAS appear to be small on both upper and lower wing surfaces.

C_L versus α for the WB, D/BAS, D/PRES, and C/PRES/REC configurations is shown in figure 45 at Mach number 0.80. The slope of the lift curves

FIGURE 37a.

WING UPPER SURFACE PRESSURE DISTRIBUTION

WING BODY

MACH NUMBER = 0.800 CL = 0.4951

1.3120 DEG. ANGLE OF ATTACK

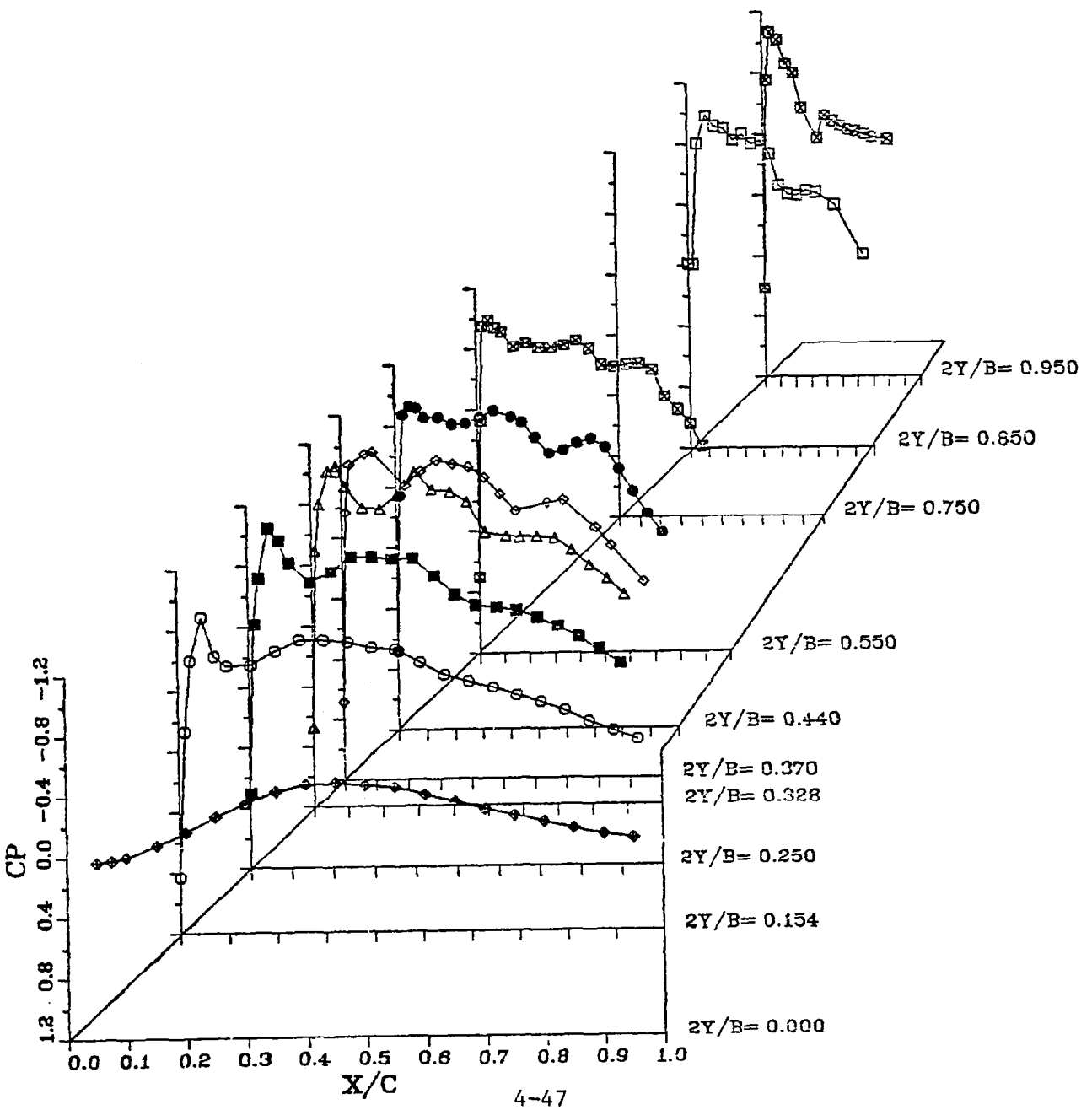

FIGURE 37b.

WING LOWER SURFACE PRESSURE DISTRIBUTION

WING BODY

MACH NUMBER = 0.800 CL = 0.4951

1.3120 DEG. ANGLE OF ATTACK

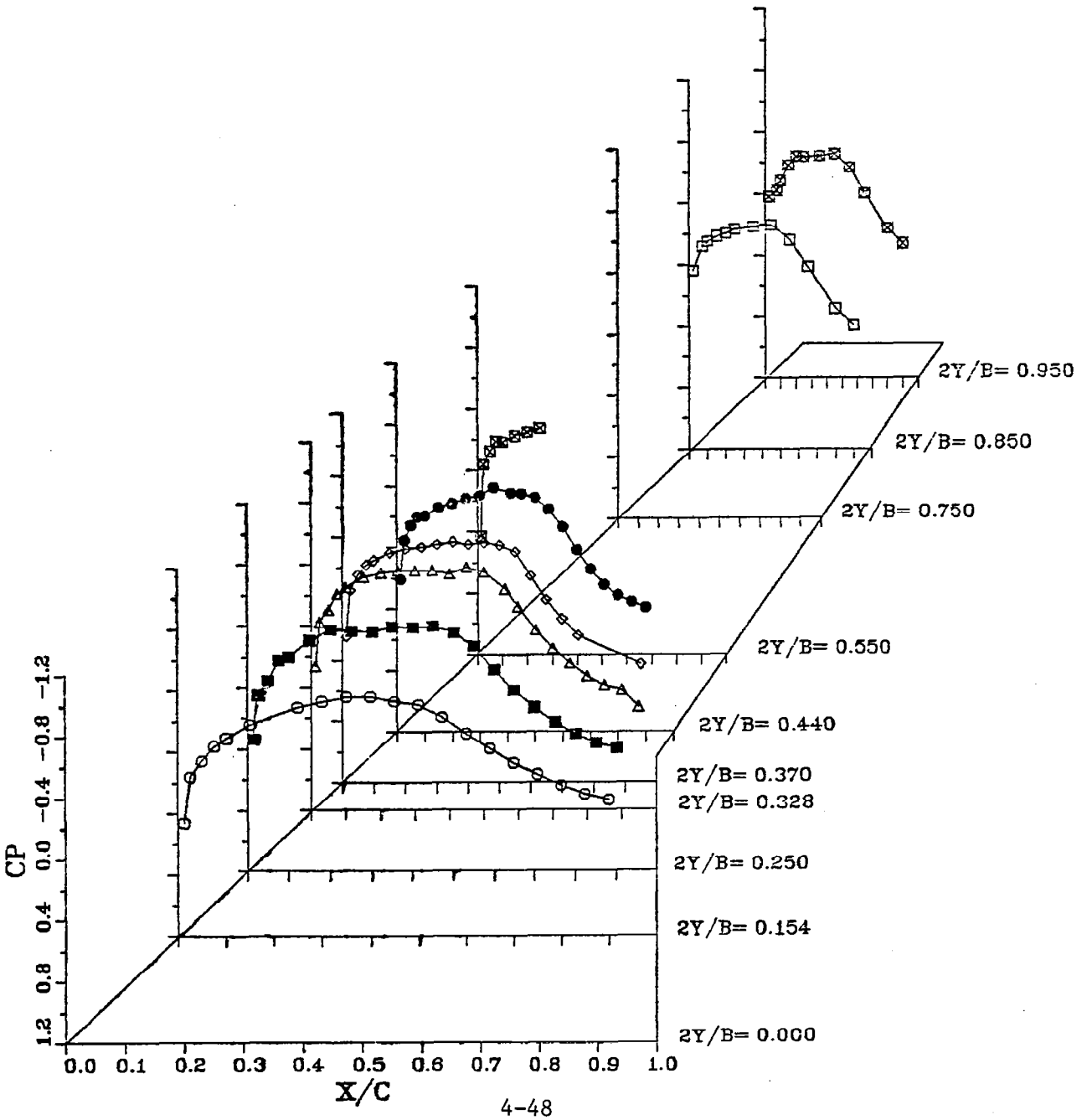

FIGURE 38a.

WING UPPER SURFACE PRESSURE DISTRIBUTION

D NACELLE / BASIC PYLON

MACH NUMBER = 0.800 CL = 0.5503

1.3105 DEG. ANGLE OF ATTACK

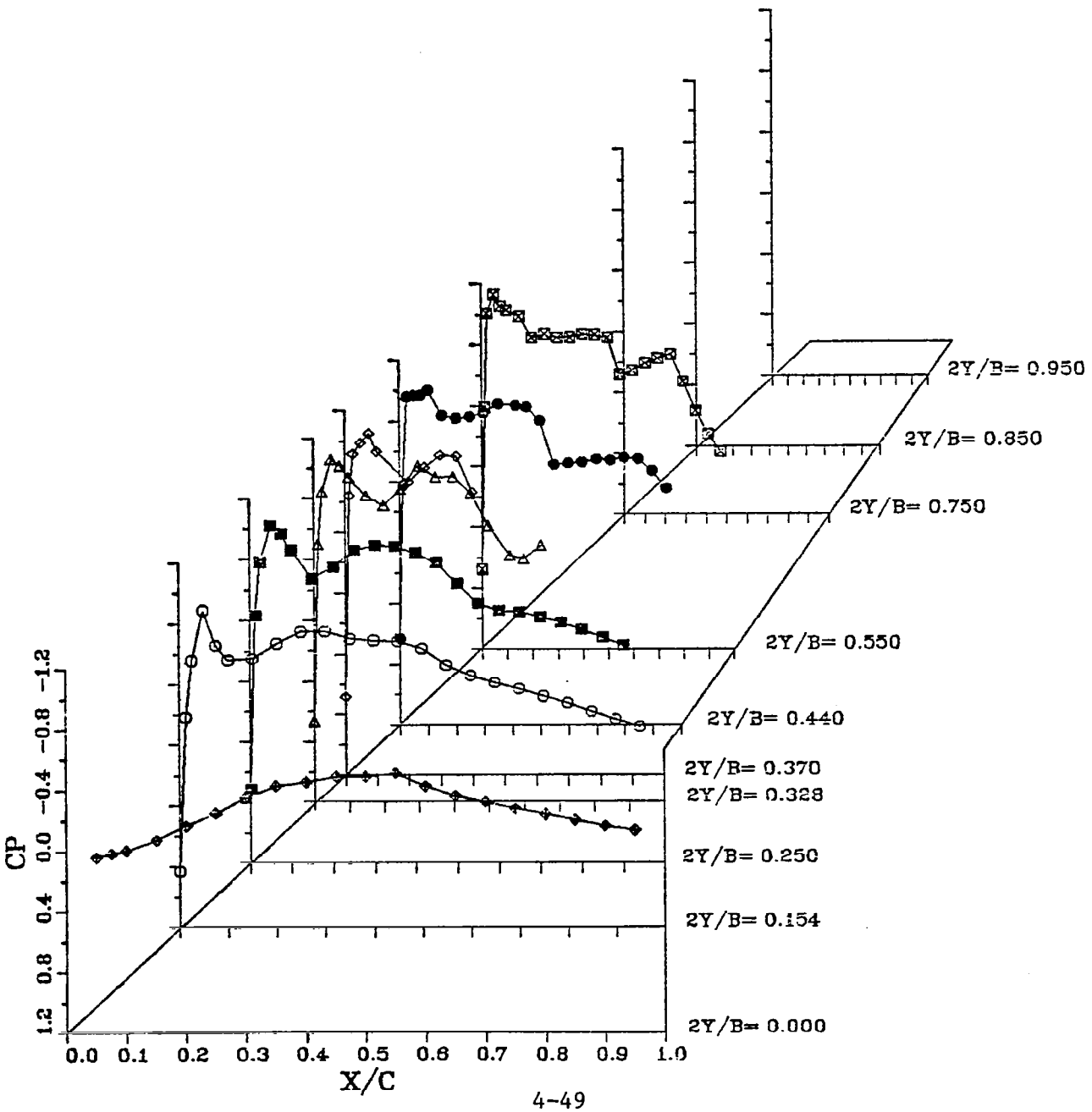

FIGURE 38b.

WING LOWER SURFACE PRESSURE DISTRIBUTION

D NACELLE / BASIC PYLON

MACH NUMBER = 0.800 CL = 0.5503

1.3105 DEG. ANGLE OF ATTACK

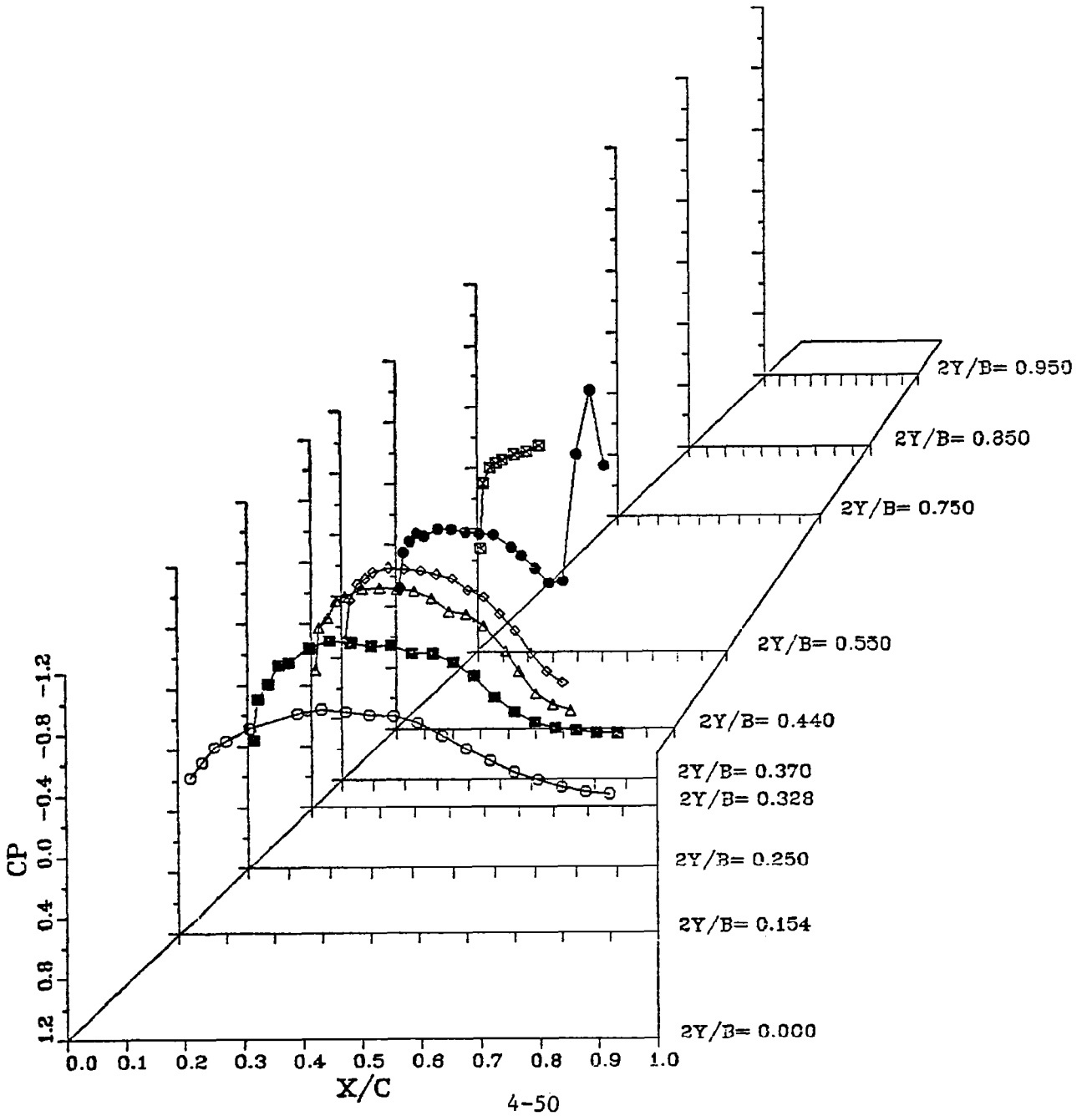

FIGURE 39. WING PRESSURE DISTRIBUTION

WB AND D/BAS CONFIGURATIONS

MACH=0.80 2Y/B=0.328

SYMBOL	CONFIGURATIONS	α,DEG
—⧖—	WING-BODY, UPPER	1.31
-⧖-	WING-BODY, LOWER	1.31
—▲—	D-NAC/BASIC PY, UPPER	1.31
-▲-	D-NAC/BASIC PY, LOWER	1.31

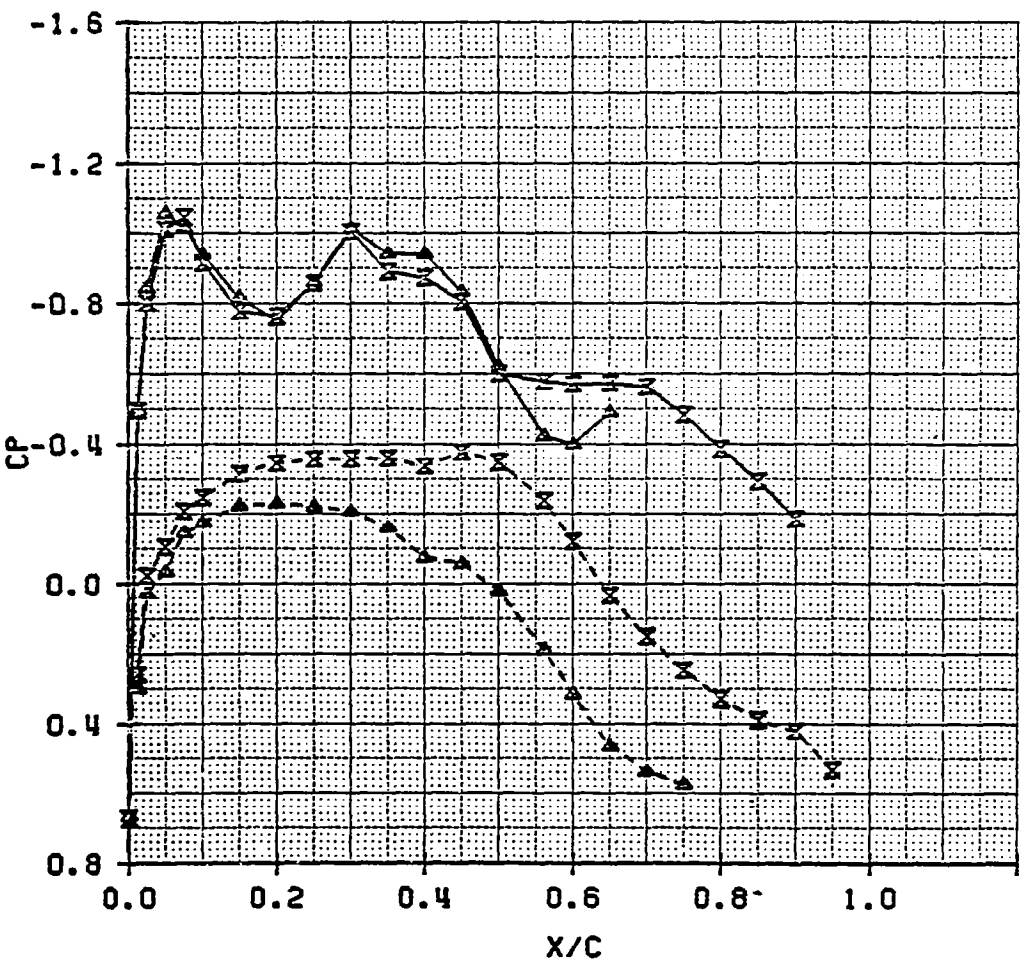

FIGURE 40. WING PRESSURE DISTRIBUTION

WB AND D/BAS CONFIGURATIONS

MACH=0.80 2Y/B=0.440

SYMBOL	CONFIGURATIONS	α,DEG
—⧗—	WING-BODY, UPPER	1.31
-⧗-	WING-BODY, LOWER	1.31
—△—	D-NAC/BASIC PY, UPPER	1.31
-△-	D-NAC/BASIC PY, LOWER	1.31

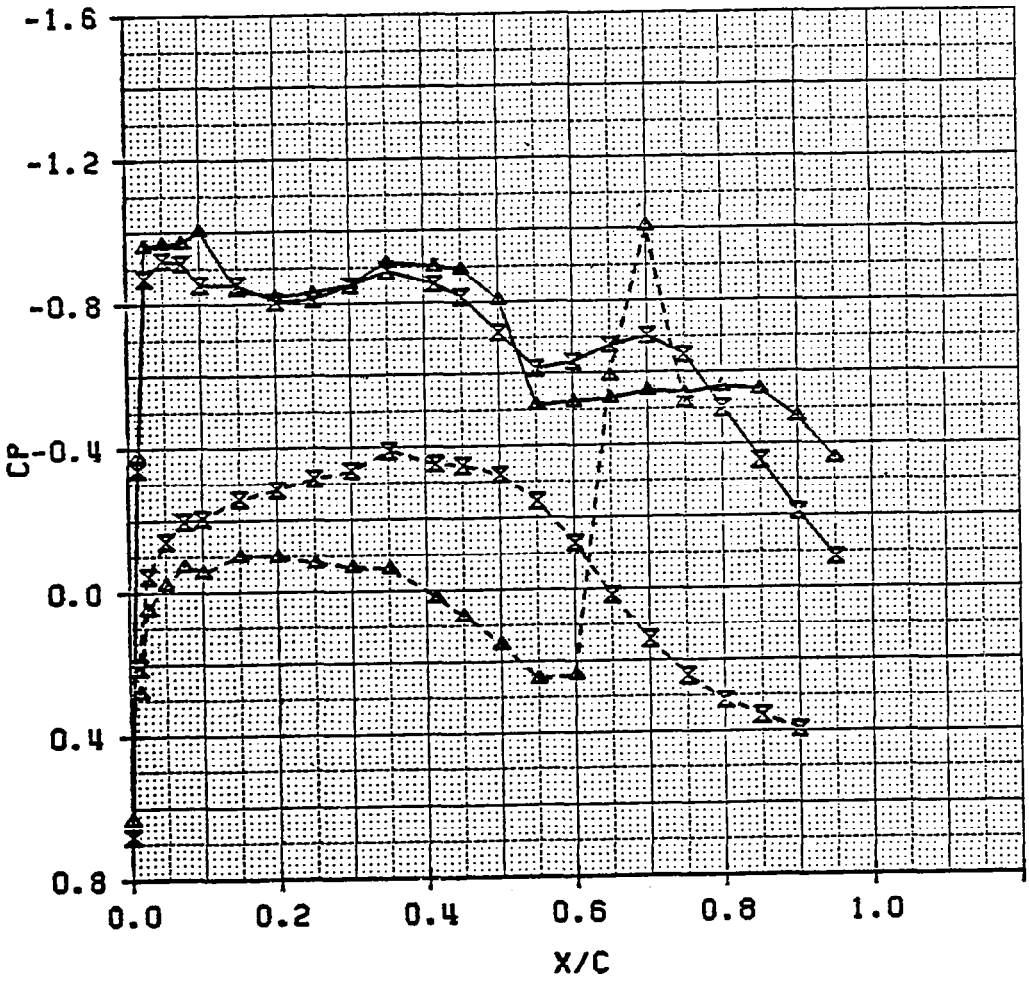

FIGURE 41a.

WING UPPER SURFACE PRESSURE DISTRIBUTION

UTW NACELLE

MACH NUMBER = 0.800 CL = 0.3773

1.2300 DEG. ANGLE OF ATTACK

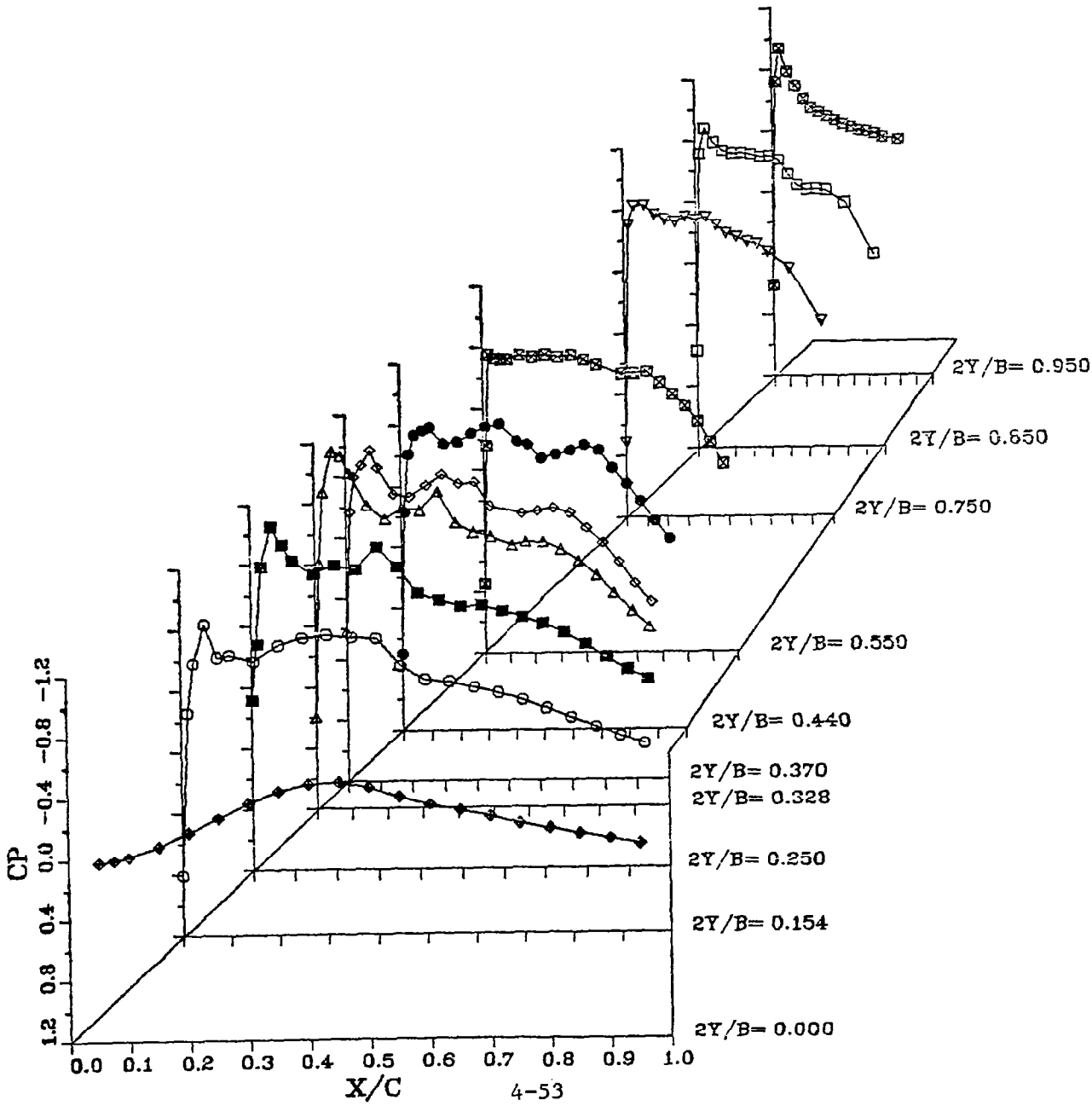

FIGURE 41b.

WING LOWER SURFACE PRESSURE DISTRIBUTION

UTW NACELLE

MACH NUMBER = 0.800 CL = 0.3773

1.2300 DEG. ANGLE OF ATTACK

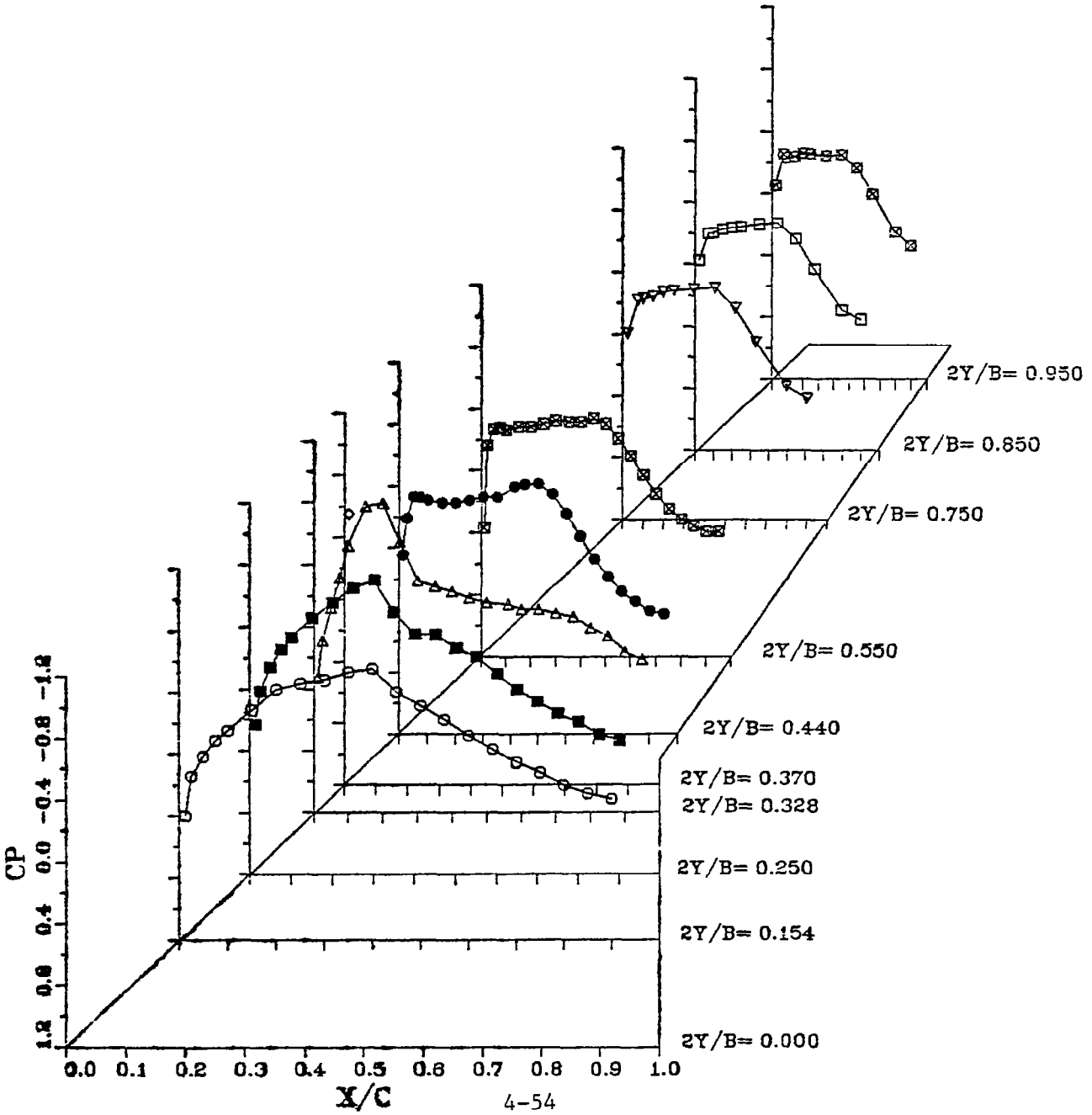

FIGURE 42. WING PRESSURE DISTRIBUTION

WB AND UTW CONFIGURATIONS

MACH=0.80 2Y/B=0.328

SYMBOL	CONFIGURATIONS	α,DEG
—⧖—	WING-BODY, UPPER	1.31
--⧖--	WING-BODY, LOWER	1.31
—✳—	UTW NAC(TEST 337), UPPER	1.23
--✳--	UTW NAC(TEST 337), LOWER	1.23

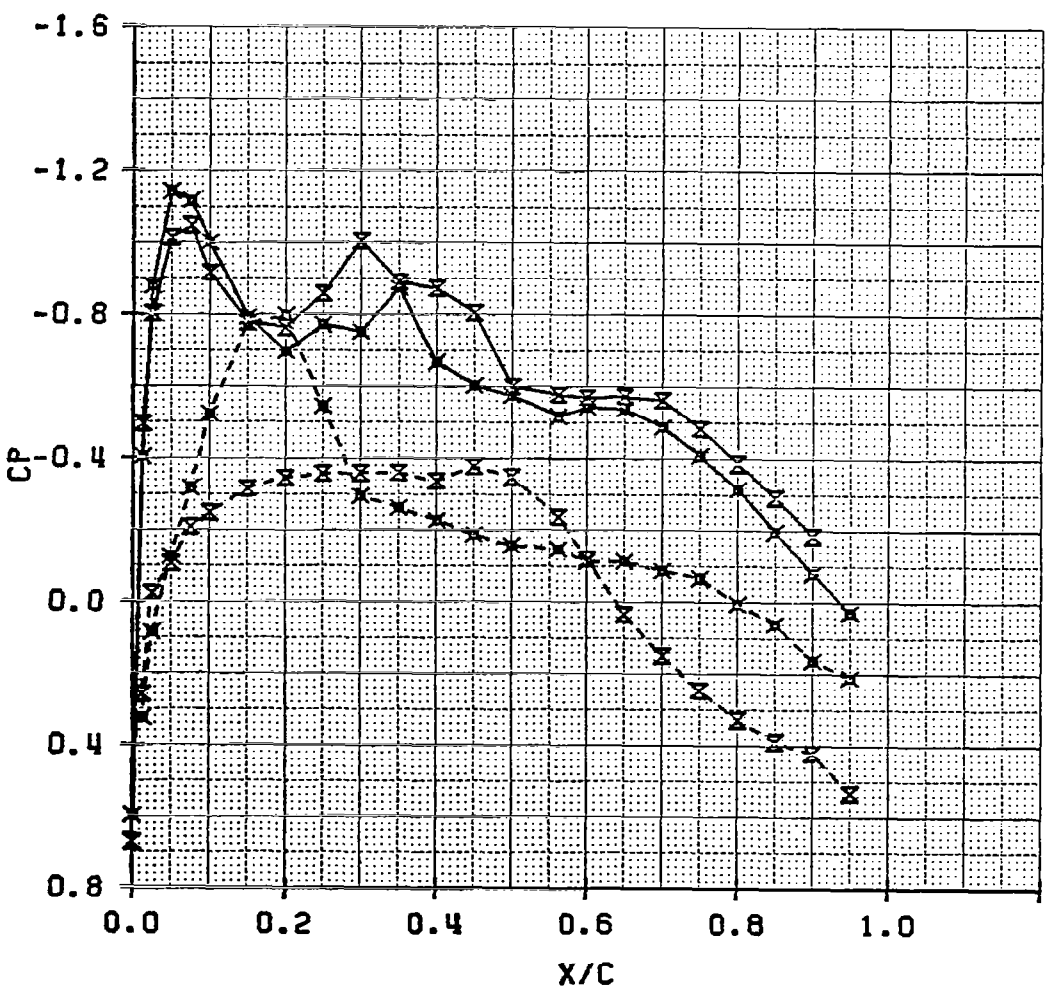

FIGURE 43. WING PRESSURE DISTRIBUTION

WB AND UTW CONFIGURATIONS

MACH=0.80 2Y/B=0.440

SYMBOL	CONFIGURATIONS	α,DEG
—⧗—	WING-BODY, UPPER	1.31
--⧗--	WING-BODY, LOWER	1.31
—✕—	UTW NAC(TEST 337), UPPER	1.23
--✕--	UTW NAC(TEST 337), LOWER	1.23

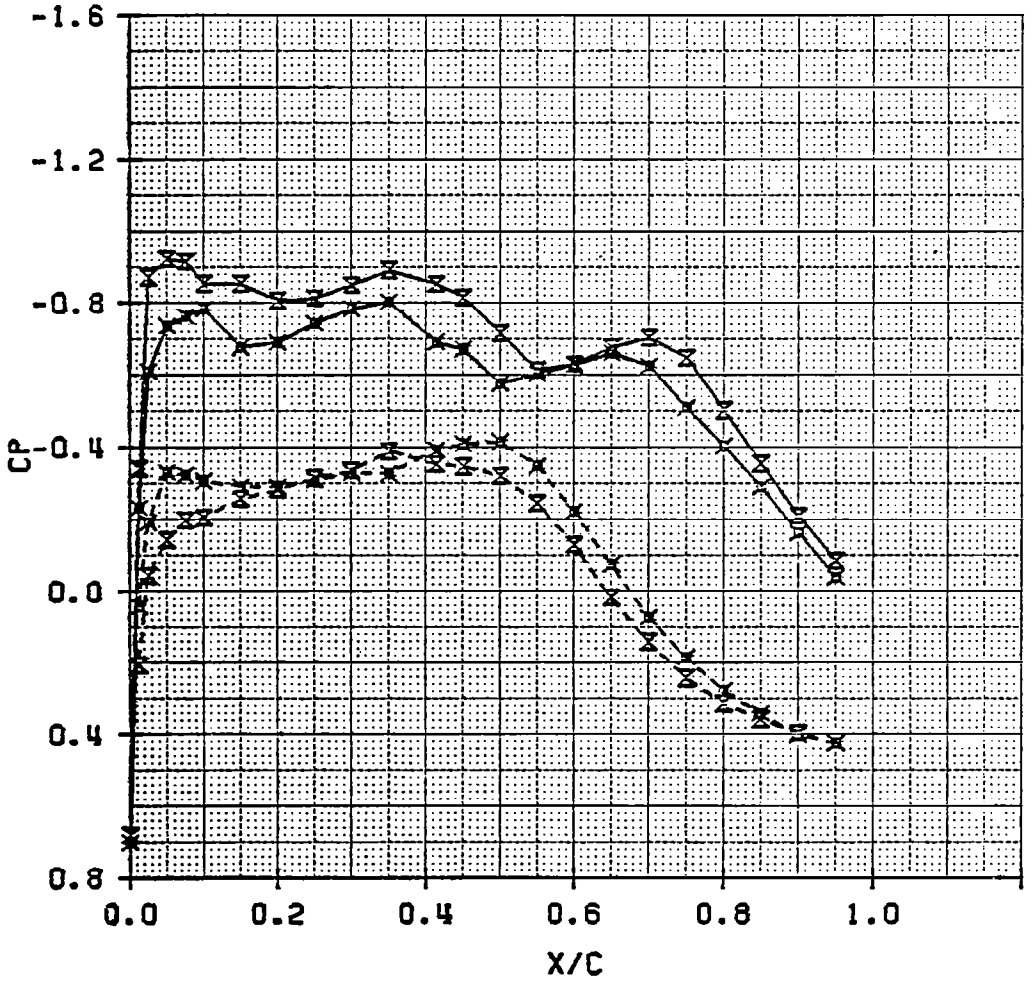

FIGURE 44a.

WING UPPER SURFACE PRESSURE DISTRIBUTION

C NACELLE / BASIC PYLON / REC DIV

MACH NUMBER = 0.800 CL = 0.6077

1.3063 DEG. ANGLE OF ATTACK

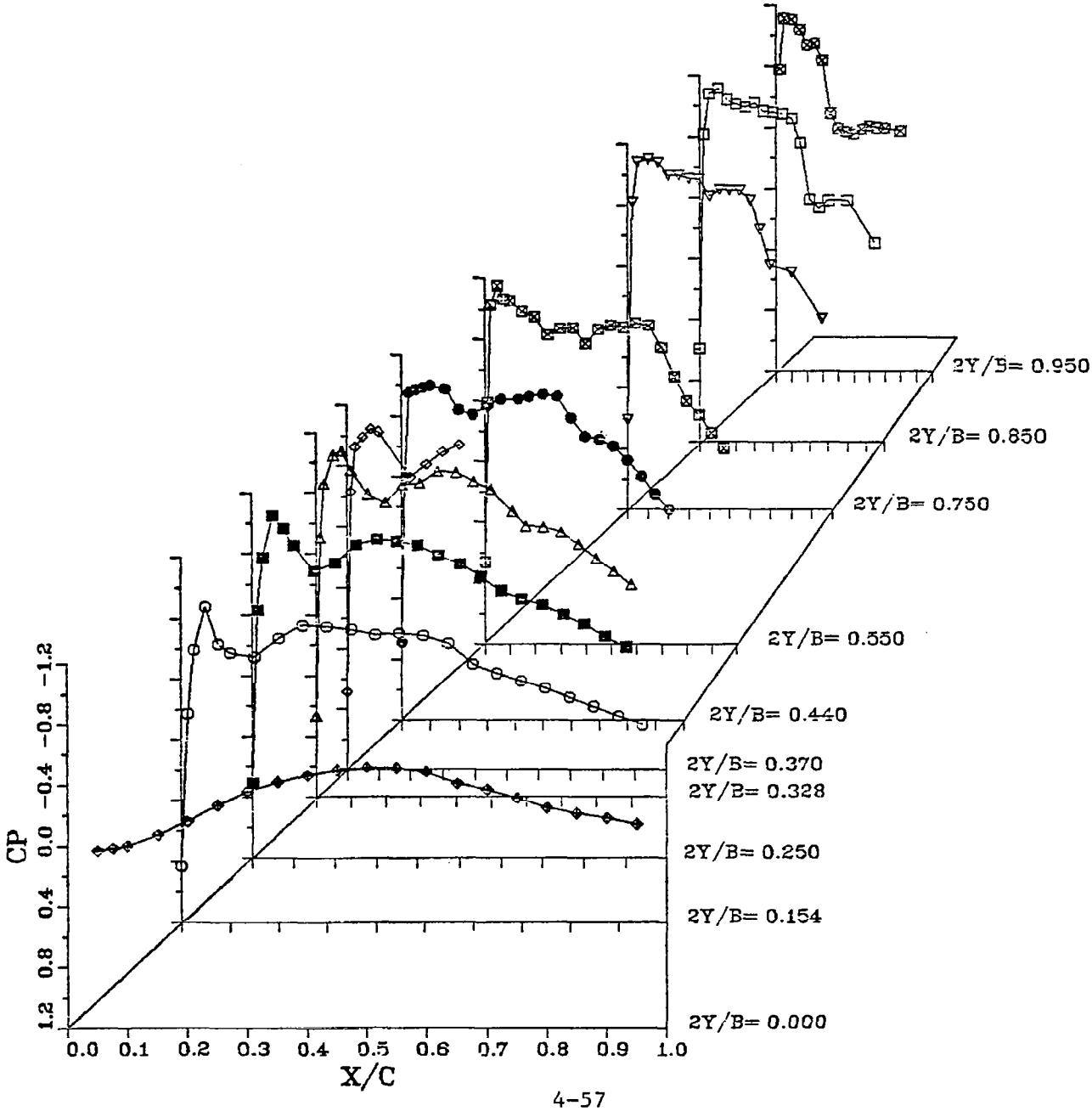

FIGURE 44b.

WING LOWER SURFACE PRESSURE DISTRIBUTION

C NACELLE / BASIC PYLON / REC DIV

MACH NUMBER = 0.800 CL = 0.6077

1.3063 DEG. ANGLE OF ATTACK

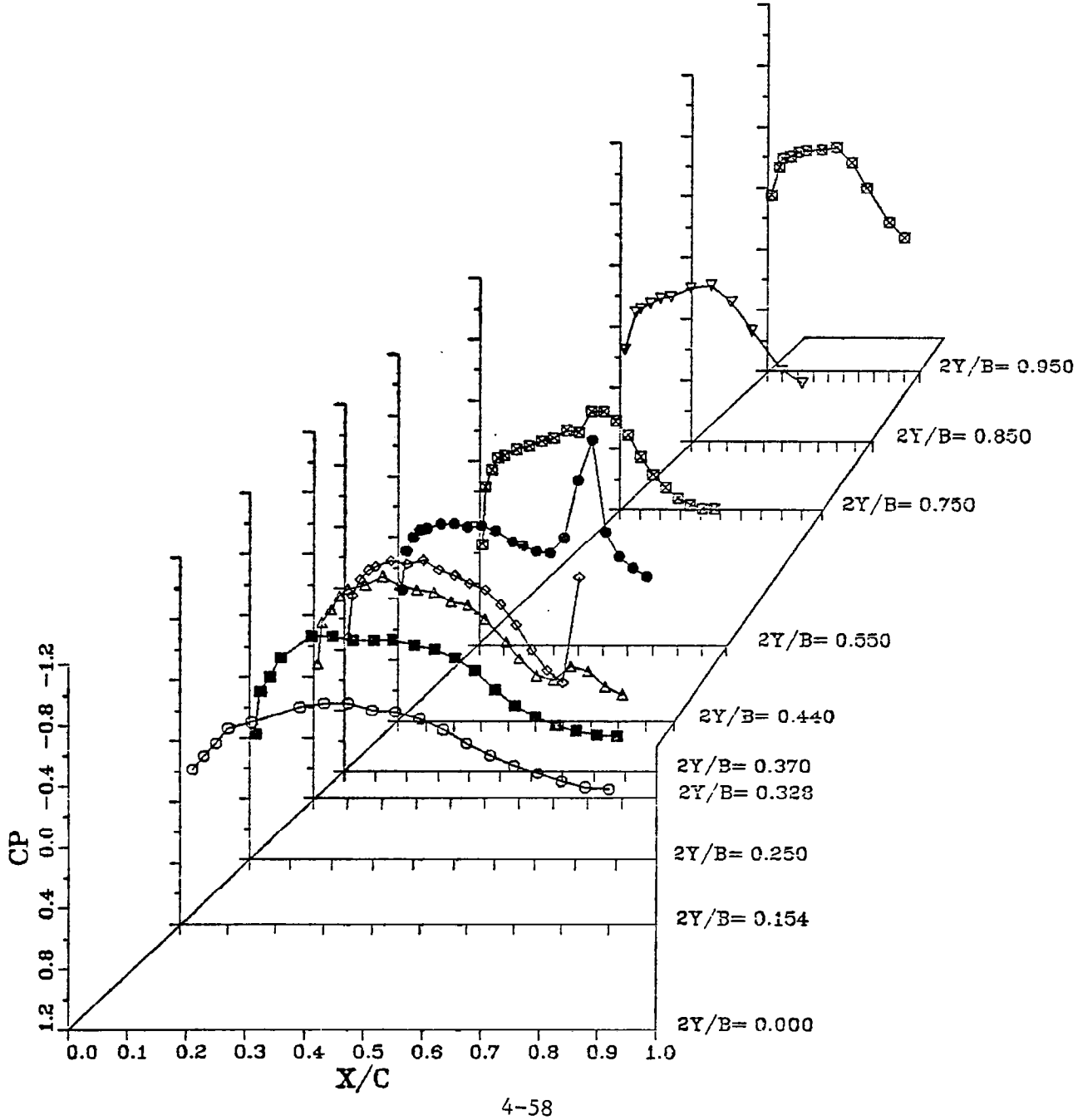

FIGURE 45. LIFT COEFFICIENT VERSUS ANGLE OF ATTACK AT MACH 0.80 FOR WB, D/BAS, D/PRES AND C/PRES/REC CONFIGURATIONS

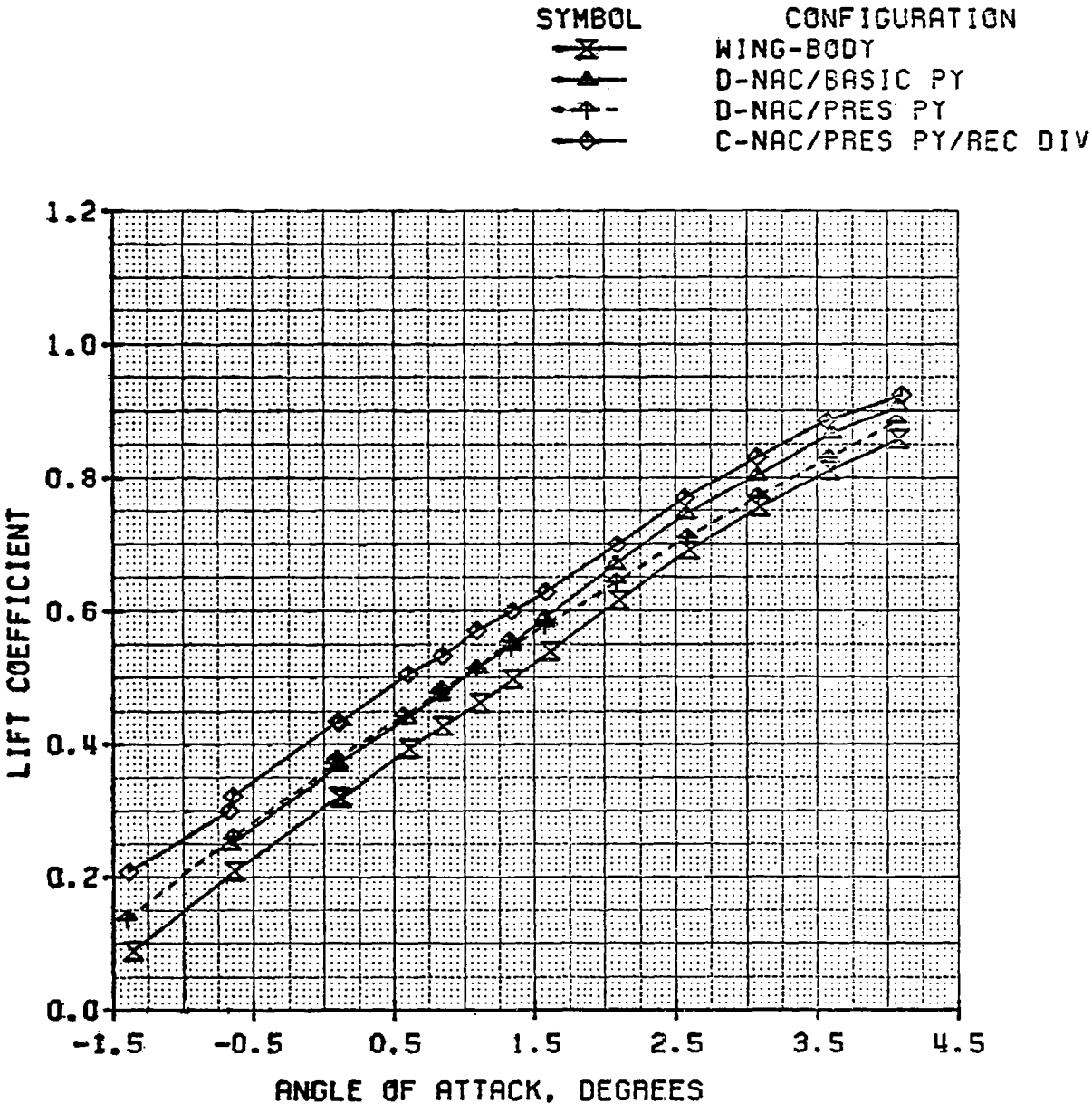

decreased at about 1.5 degrees for both the D/PRES and the C/PRES/REC installations. At lower α, the pressure pylons had only a small effect.

Lift curves for all of the configurations are given in the Appendix in figures A38 - A51 at test Mach numbers 0.70, 0.75, 0.78, 0.79, 0.81, 0.83, and 0.85.

4.3 Installed Pitching Moment Comparisons

Results for C_M versus C_L for the WB, D/BAS, C/BAS/REC, C/BAS/HL, and UTW configurations at Mach number 0.80 are given in figure 46. C_M was measured about an axis through the one-fourth mean aerodynamic chord point. (See figure 1.) Figure 46 indicates a significant increase in C_M (nose-up) at a fixed C_L for the D/BAS and C/BAS configurations relative to the WB. Conversely, C_M was significantly lower at fixed C_L for the UTW installation.

The main question here is whether adding the aft nacelles caused the pitching moment of the wing-body-nacelles to increase or decrease relative to that of the WB, independent of tail effects. If adding the aft nacelles caused an increase in pitching moment, then less download on the tail would be required for trim. There would then be less trim drag. (Alternatively, the tail moment arm about the center of gravity could be decreased.) The opposite would be true if adding the aft nacelles caused a decrease in pitching moment. This question cannot be answered unambiguously from the present data, as all data were taken with the tail on.

As discussed in section 4.2, the relative increase in C_L at fixed α for the aft nacelles may possibly have increased the downwash at the tail. There would then be a tendency for increased download on the tail, and a tendency for increased C_M, at fixed α, due to the tail.

Figure 47 shows C_M versus α at Mach number 0.80 for the WB, D/BAS, C/BAS/REC, C/BAS/HL, and UTW configurations. This figure shows the relative changes in C_M due to nacelle configuration at constant wing, fuselage, and

FIGURE 46. LIFT COEFFICIENT VERSUS PITCHING MOMENT COEFFICIENT AT M=0.80 FOR WB, D/BAS, C/BAS/HL, C/BAS/REC AND UTW CONFIG.

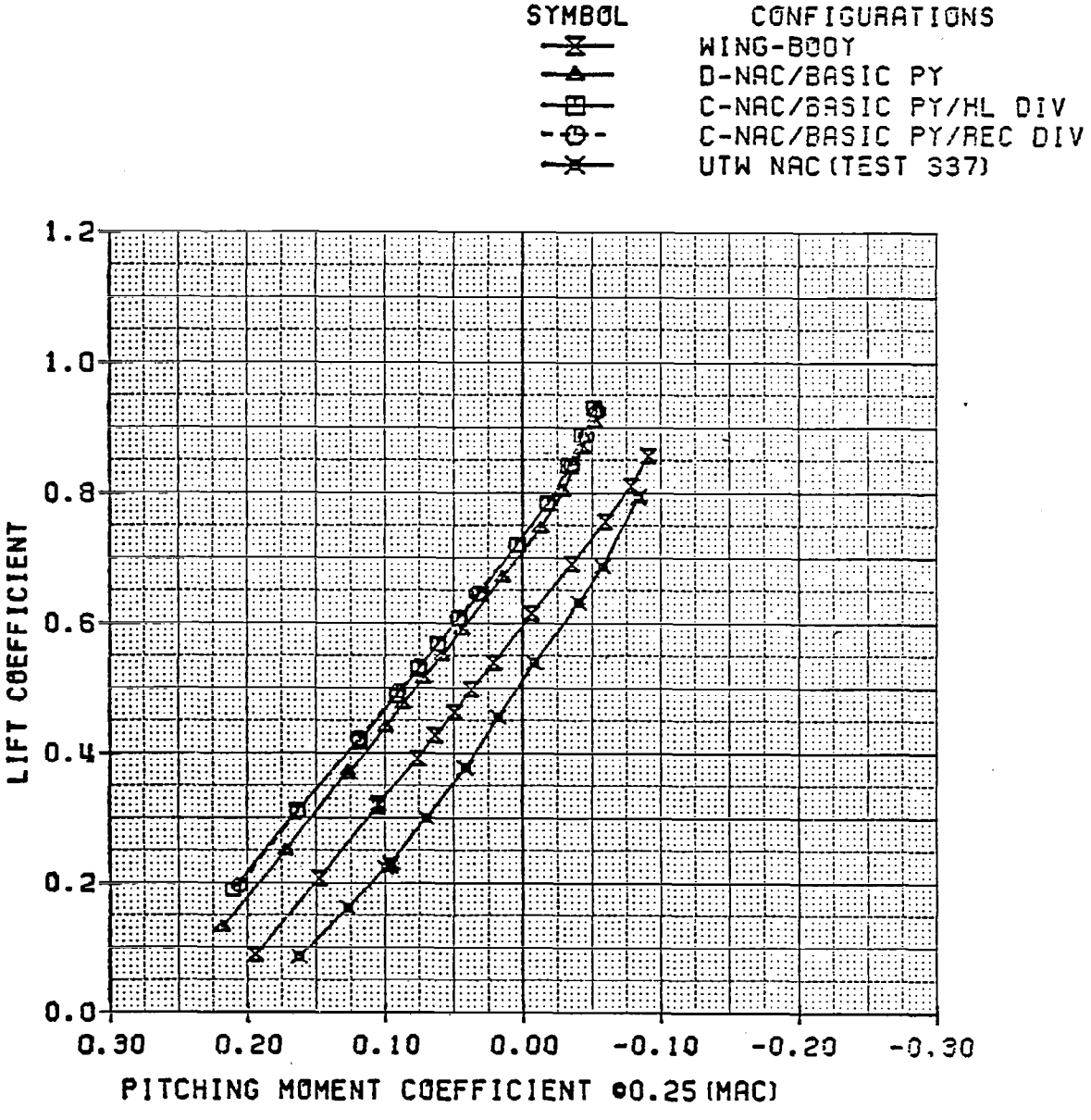

FIGURE 47. ANGLE OF ATTACK VERSUS PITCHING MOMENT COEFFICIENT AT M=0.80 FOR WB, D/BAS, C/BAS/HL, C/BAS/REC AND UTW CONFIG.

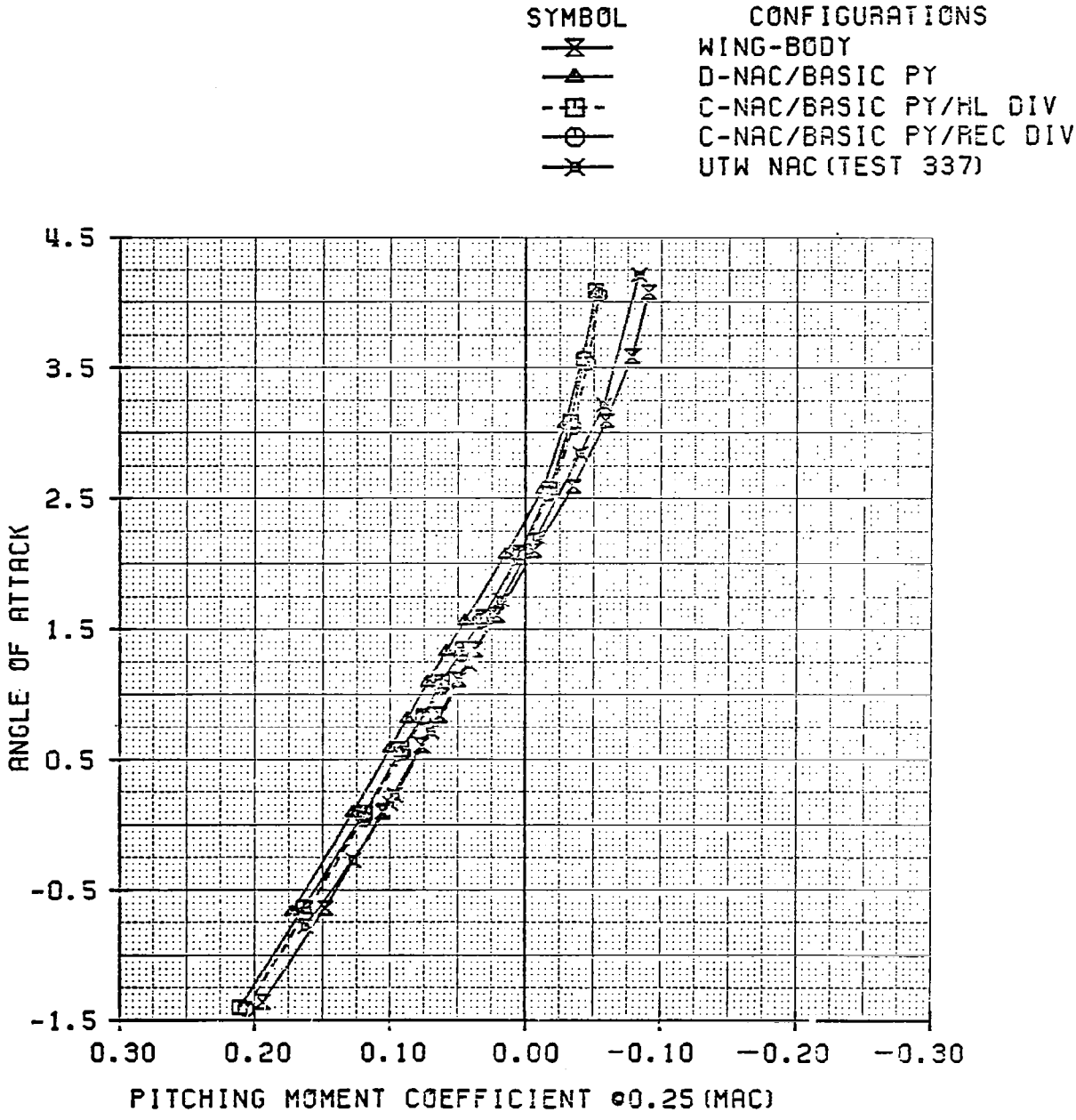

tail geometry. If changes in nacelle configuration had no effect on tail loading, then, from figure 47, the aft nacelles would have caused an increase in C_M relative to the WB. If changes in nacelle configuration affected the downloading on the tail, however, then the increase in C_M at constant α for the aft nacelles might have been partly or completely caused by an increase in tail pitching moment. Again, tests with the tail off are required to determine the effect of the aft nacelles on C_M.

Figures 35 and 47 show that at fixed α, the D/BAS had a higher C_M than the C/BAS, while the C/BAS had a higher C_L. Again, if nacelle configuration did not affect tail loading, then the D/BAS produced the larger C_M. If the higher C_L of the C/BAS resulted in a higher download on the tail, this would also imply that the D/BAS produced a larger C_M. Thus, the data suggests that the D/BAS was more effective than the C/BAS in increasing C_M, but this must be confirmed by tests with the tail off.

Figure 48 shows normalized section pitching moment, $C_m(c/\bar{c})^2$ for the wing versus 2Y/B at Mach number 0.80. The data for the WB, D/BAS, and C/BAS/REC are at $\alpha = 1.31$ degrees; while those for the UTW are at $\alpha = 1.23$ degrees. C_m was obtained in a manner similar to that used for C_n. Comparing figures 48 and 36, the relatively large differences in $C_n(c/\bar{c})$ at the inboard sections seemed to contribute little to changes in $C_m(c/\bar{c})^2$. The exception was the UTW installation at 2Y/B = 0.328.

C_M versus C_L and C_M versus α are shown in figures 49 and 50, respectively, for the W/B, D/BAS, D/PRES, and C/PRES/REC configurations. These data at Mach number 0.80 indicate that the pressure pylons had only a minor effect on C_M.

C_M versus C_L for all of the configurations is given in the Appendix in Figures A52 - A65 at test Mach numbers 0.70, 0.75, 0.78, 0.79, 0.81, 0.83, and 0.85.

FIGURE 48. NORMALIZED WING SECTION PITCHING MOMENT COEFFICIENT VERSUS SEMISPAN STATION AT MACH 0.80 AND α=1.3 DEGREES

SYMBOL	CONFIGURATION
⧗	WING-BODY
△	D-NAC/BASIC PY
⊙	C-NAC/BASIC PY/REC DEV
⧖	UTW NAC(1.2 DEG.)

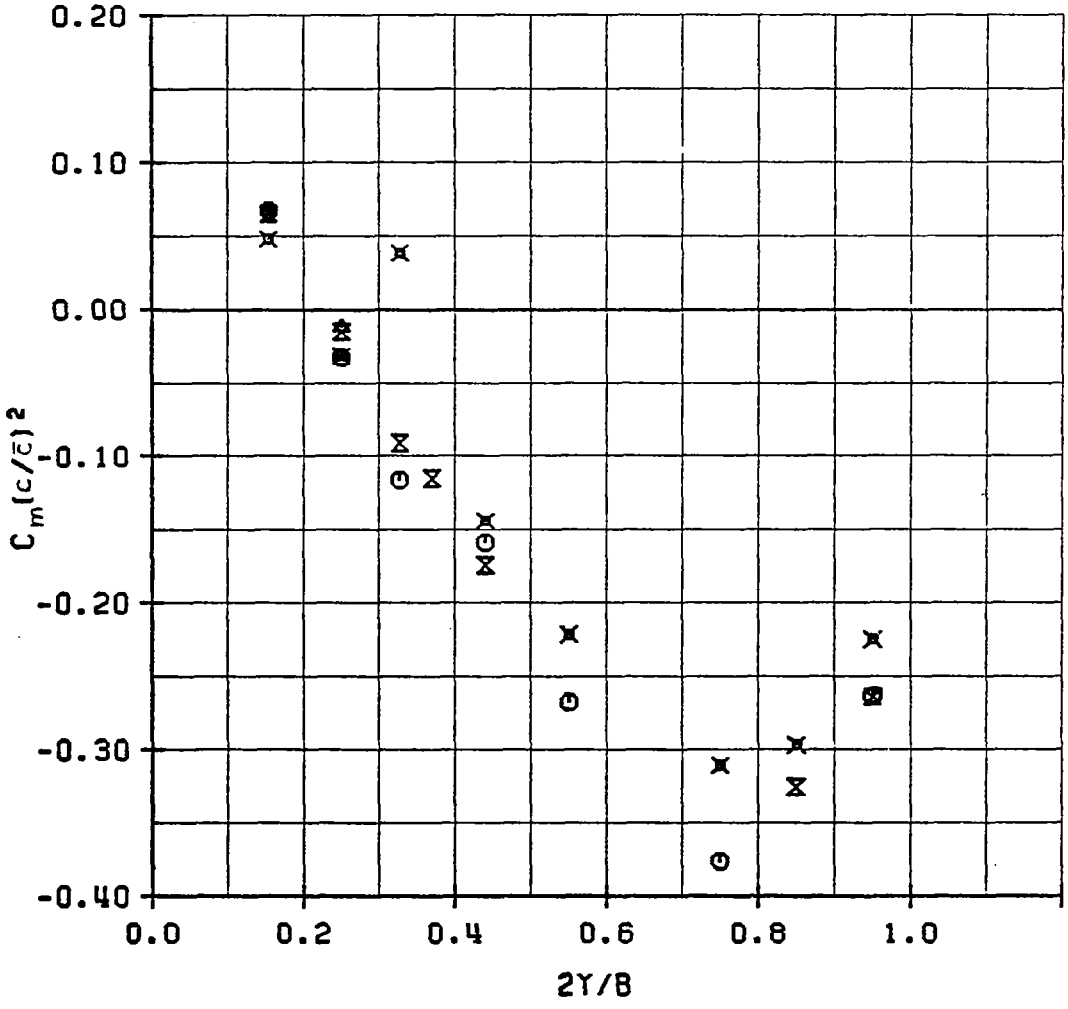

FIGURE 49. LIFT COEFFICIENT VERSUS PITCHING MOMENT COEFFICIENT AT M=0.80 FOR WB, D/BAS, D/PRES AND C/PRES/REC CONFIG.

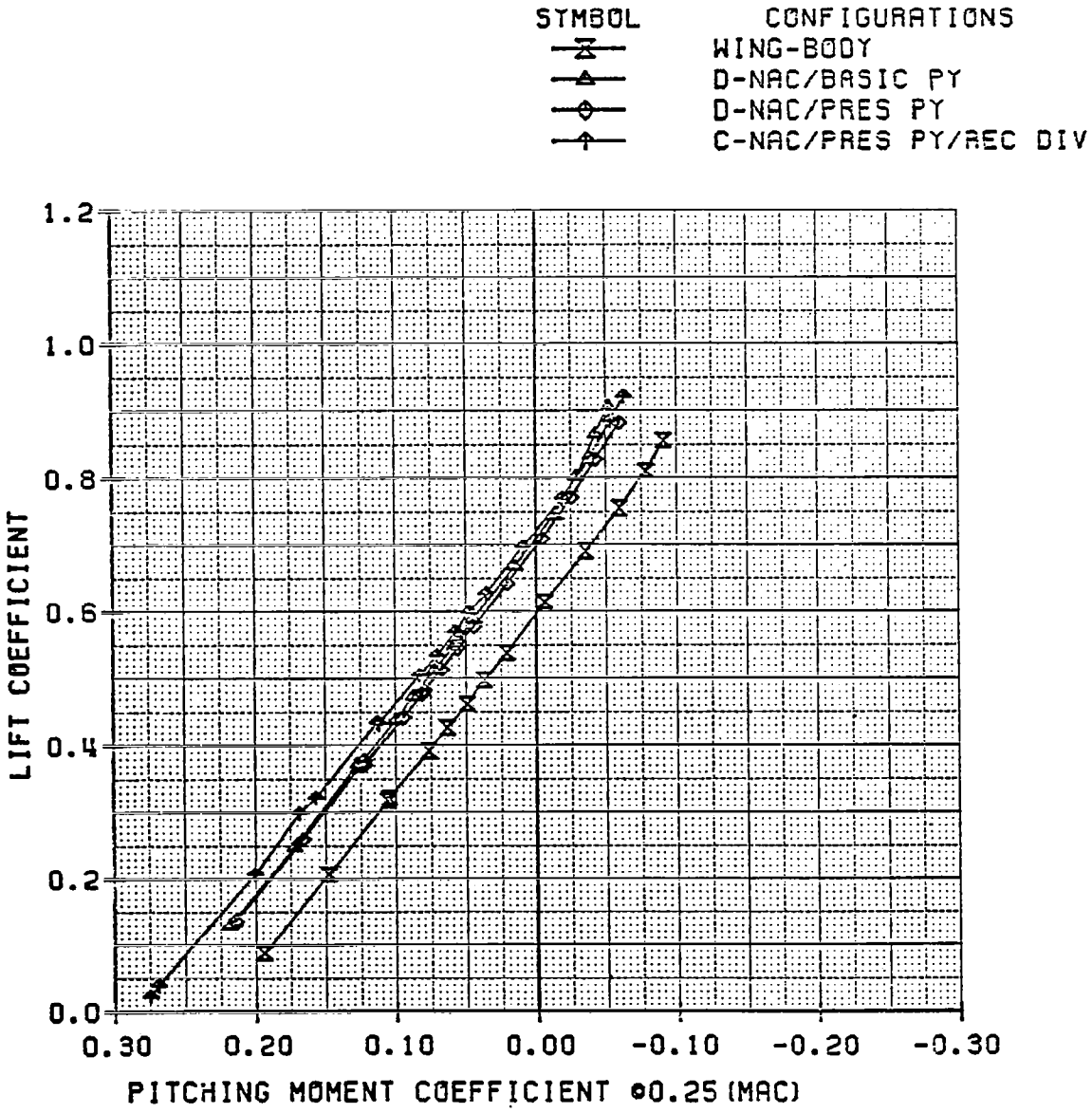

FIGURE 50. ANGLE OF ATTACK VERSUS PITCHING MOMENT COEFFICIENT AT M=0.80 FOR WB, D/BAS, D/PRES, AND C/PRES/REC CONFIG.

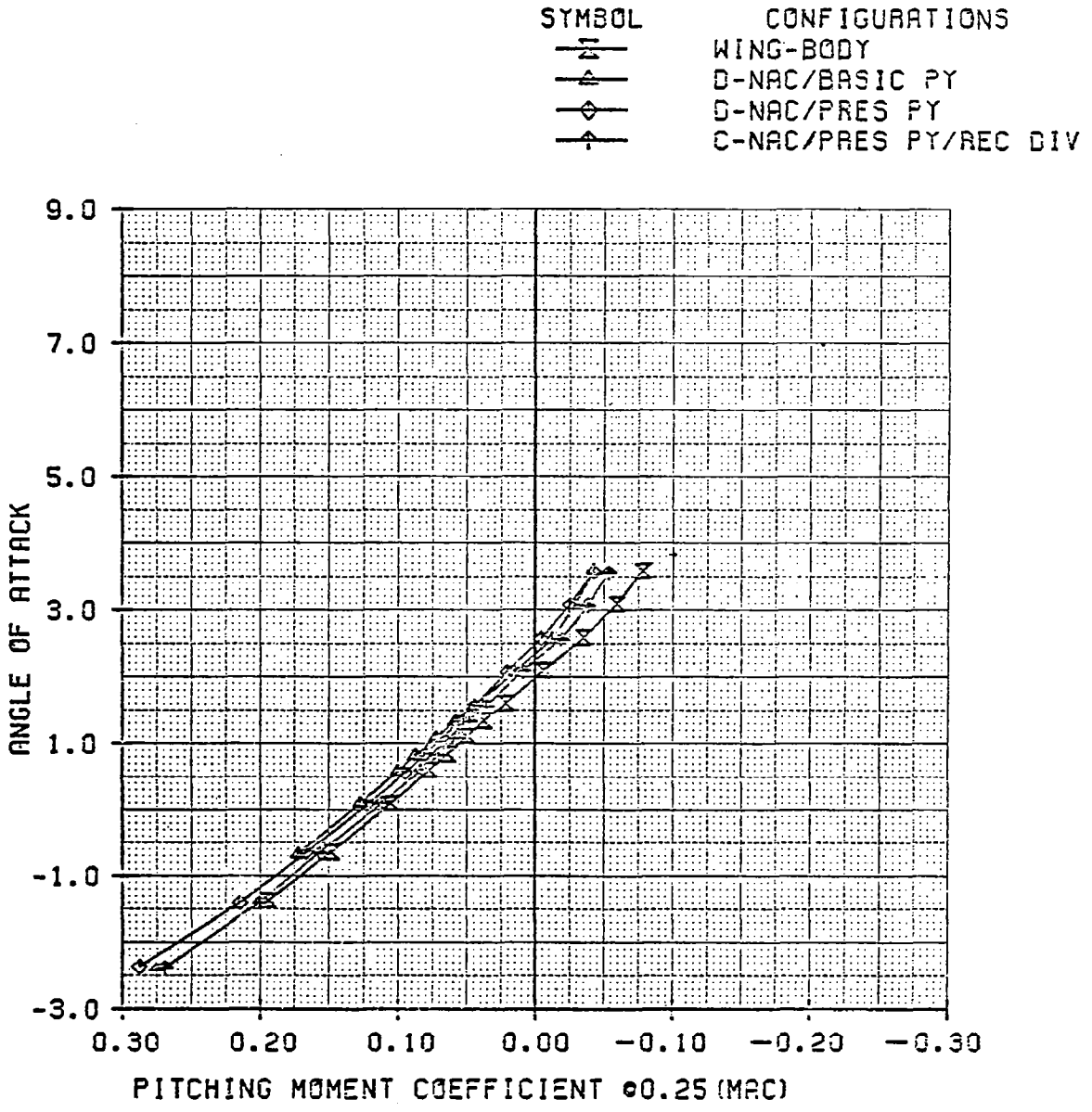

5. CONCLUSIONS

The following conclusions were drawn from the results of this study:

1. The D-nacelle (D/BAS) configuration had the smallest drag of the configurations tested. The underwing-forward, pylon-mounted (UTW) configuration had the largest drag, being 6.8 percent larger than the D/BAS at Mach number 0.80 and $C_L = 0.45$.

2. Each tested configuration still had some interference drag, over and above friction drag.

3. The interference drag of the C and D-nacelle installations can probably be reduced by eliminating the abrupt expansion and recompression at the outboard inlet lip.

4. The interference drag of the UTW installation can probably be reduced by eliminating the supersonic flow region between the nacelle and the fuselage.

5. The D/BAS and C-nacelle (C/BAS/REC) configurations and the wing-body (WB) had a drag-divergence Mach number (M_{DD}) of about 0.81; but it was about 0.78 for the UTW installation. These differences may have been caused by the more favorable cross-sectional area distribution of the aft nacelle installations.

6. The D/BAS and C/BAS/REC installations had significantly higher $(L/D)_{MAX}$ than the UTW installation. At Mach number 0.80, the value for the UTW was about 11 percent lower than for the D/BAS.

7. The C-nacelle with highlight diverter (C/BAS/HL) had only small differences in drag, lift, and pitching moment compared with the

C-nacelle with recessed diverter (C/BAS/REC). The drag of the C/BAS/HL was about 1.4 percent greater than that of the C/BAS/REC at Mach number 0.80 and $C_L = 0.45$.

8. Drag differences for the installations with pressure pylons (D/PRES and C/PRES/REC), relative to those with basic pylons, were small at Mach numbers less than M_{DD}. The D/PRES and C/PRES/REC had relatively higher wave drag and possibly lower M_{DD}, however. This may have been caused by the small increases in maximum cross-sectional area for the D/PRES and the C/PRES/REC. There were only small effects of the pressure pylons on C_L and C_M.

9. The effect of the aft nacelles on C_L was to shift the lift curve upward relative to the WB, and to shift the zero-lift angle of attack to a more negative value. The effect of the UTW nacelles on C_L was opposite to that of the aft nacelles.

10. The aft-nacelle installations had higher lift on the inboard wing sections than the WB, because of higher pressures on the wing lower surface.

11. The UTW installation had much lower lift on the inboard wing sections than the WB, because of lower pressures on the wing lower surface. (The flow became supersonic.)

6. RECOMMENDATIONS

The following recommendations for future work are made as a result of this study:

1. Modify the shape, attitude, and position of the aft nacelles, with the goal of eliminating the remaining interference drag. In particular, eliminate the abrupt expansion and recompression at the outboard inlet lip.

2. Perform future tests of the aft nacelles with both tail on and tail off. This will resolve uncertainties about the influence of tail lift and pitching moment on airplane C_L and C_M.

3. Perform an aircraft design study for an aircraft with an aft nacelle installation. This will allow a quantitative comparison of aft nacelle installation performance benefits with possible structural penalties.

7. REFERENCES

1. Henderson, W. P., and J. C. Patterson, Jr., "Propulsion Installation Characteristics for Turbofan Transports." AIAA Paper 83-0087, January 1983.

2. Butler, S. F. J., "Aircraft Drag Prediction for Project Appraisal and Performance Estimation." AGARD CP-124, April 1973.

3. Re, Richard J., "An Investigation of Several NACA 1-Series Axisymmetric Inlets at Mach Numbers From 0.4 to 1.29." NASA TM X-2917, March 1974.

4. Krivec, D. K., and L. H. Bangert, "Effects of Nacelle Configuration/Position on Performance of Subsonic Transport: Tabulated Coordinates of Model Nacelles." Lockheed Report 29906, July 1981.

APPENDIX

This Appendix shows complete force and moment data for all of the configurations at test Mach numbers 0.70, 0.75, 0.78, 0.79, 0.81, 0.83, and 0.85. Representative pressure data are also shown.

The contents of this Appendix are as follows:

Figures A1 - A21	:	Drag polars, C_L versus C_D
Figures A22 - A28	:	Wing C_p profiles
Figures A29 - A32	:	Nacelle C_p profiles
Figures A33 - A37	:	Oil Flow Photographs
Figures A38 - A51	:	Lift curves , C_L versus α
Figures A52 - A65	:	Pitching moments, C_M versus C_L

FIGURE A1. DRAG POLARS AT MACH 0.70 FOR WB, D/BAS, C/BAS/REC, AND UTW CONFIGURATIONS

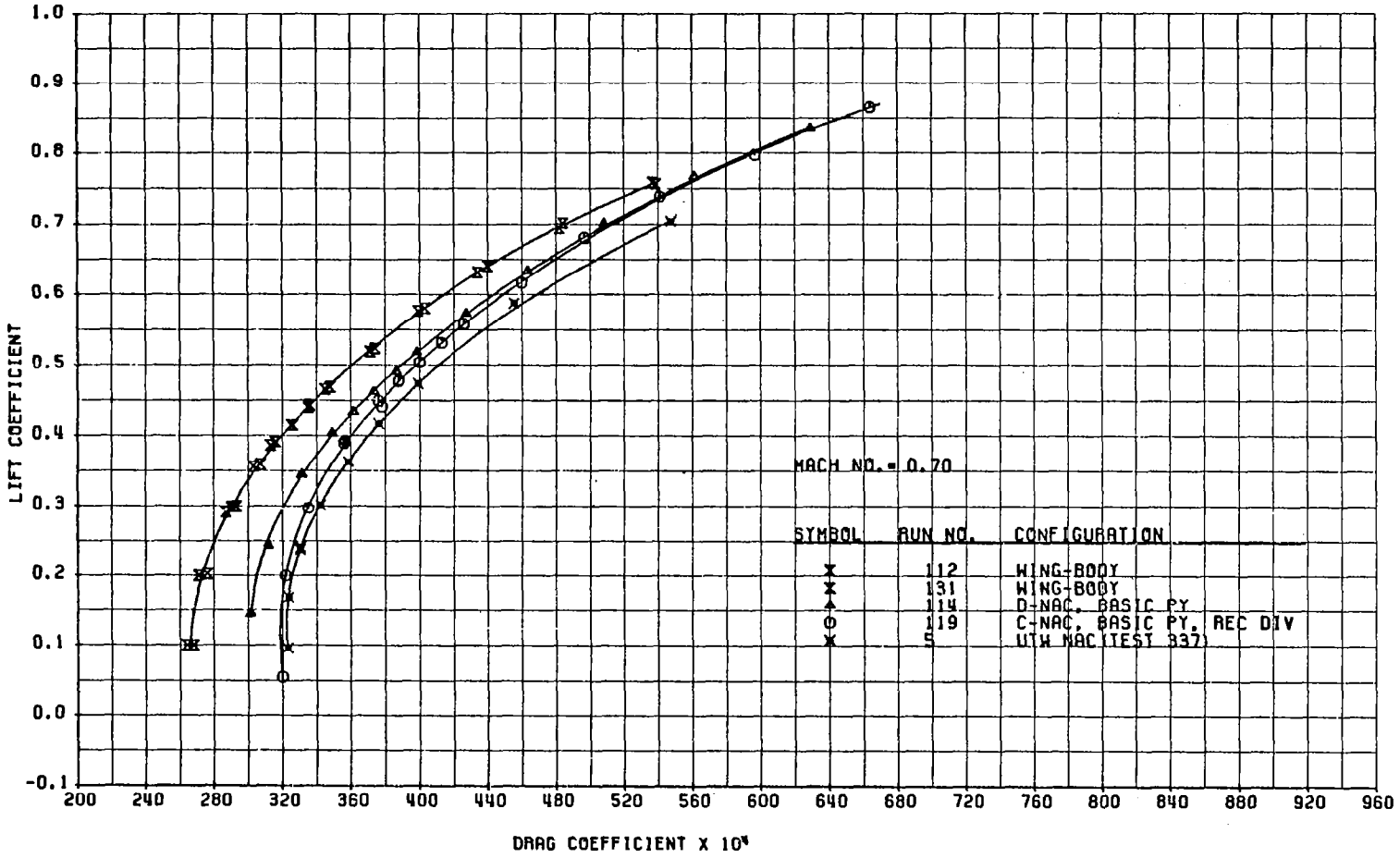

FIGURE A2. DRAG POLARS AT MACH 0.70 FOR WB, C/BAS/REC, AND C/BAS/HL CONFIGURATIONS

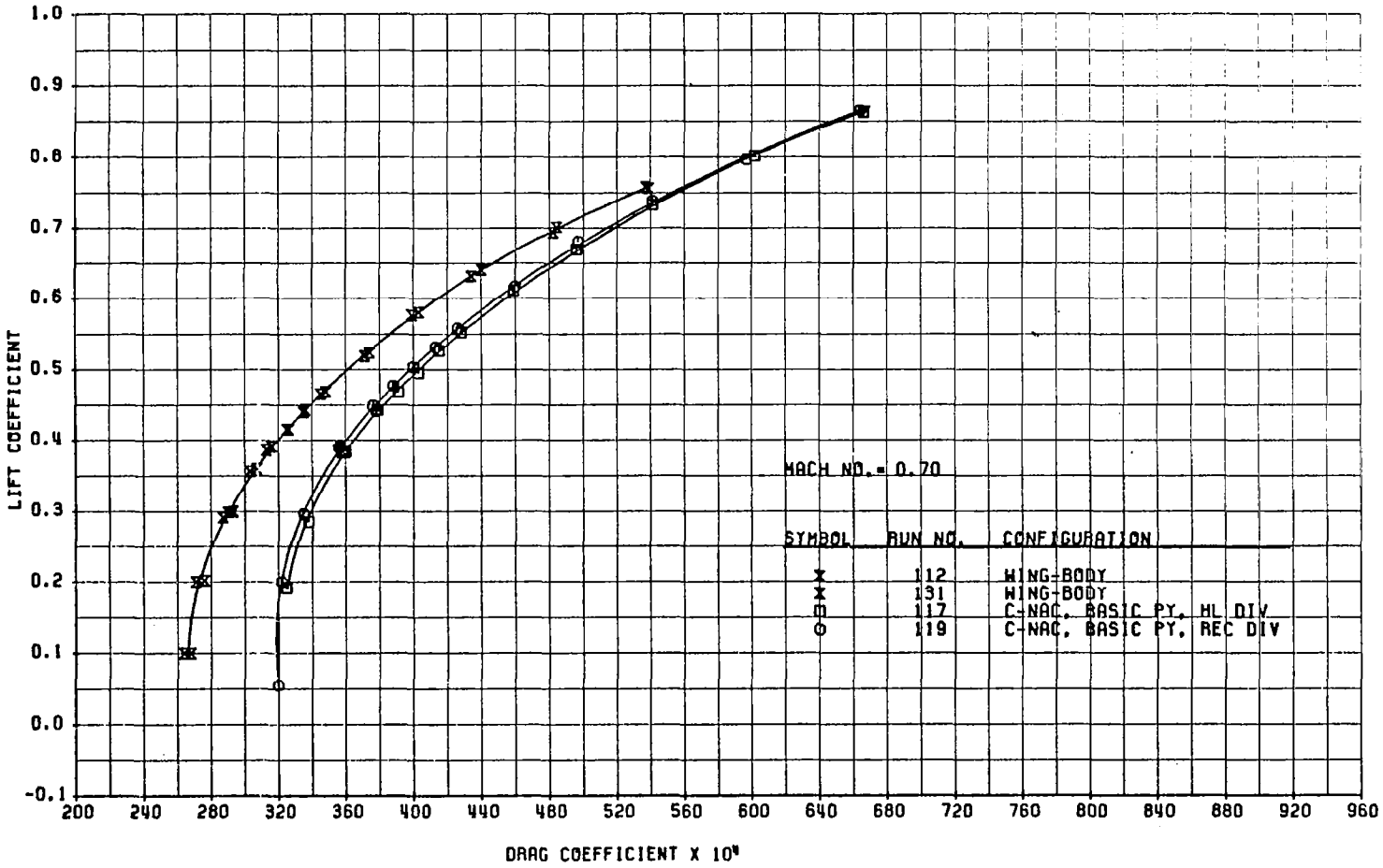

FIGURE A3. DRAG POLARS AT MACH 0.70 FOR WB, D/BAS, D/PRES, AND C/PRES/REC CONFIGURATIONS

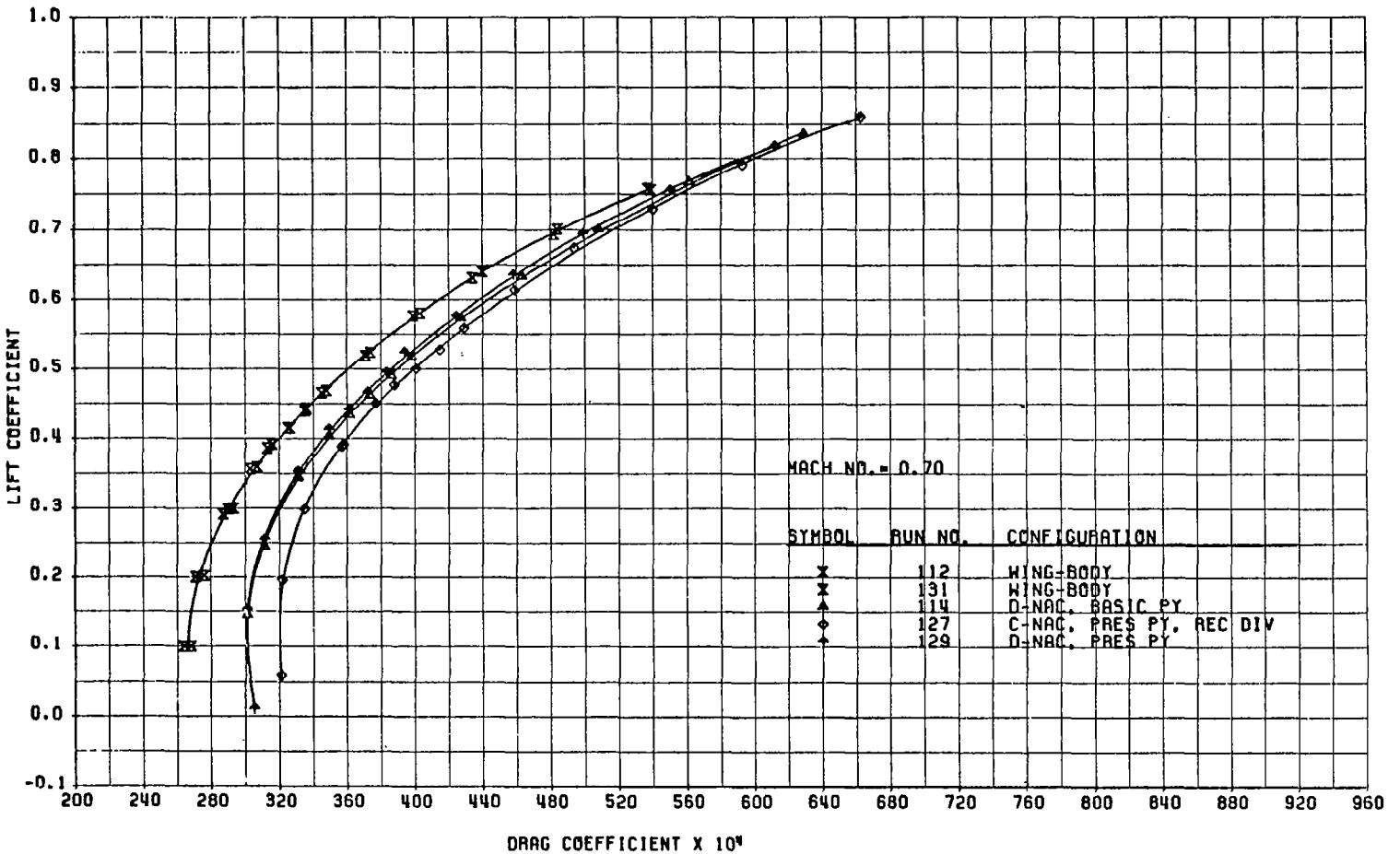

FIGURE A4. DRAG POLARS AT MACH 0.75 FOR WB, D/BAS, C/BAS/REC, AND UTW CONFIGURATIONS

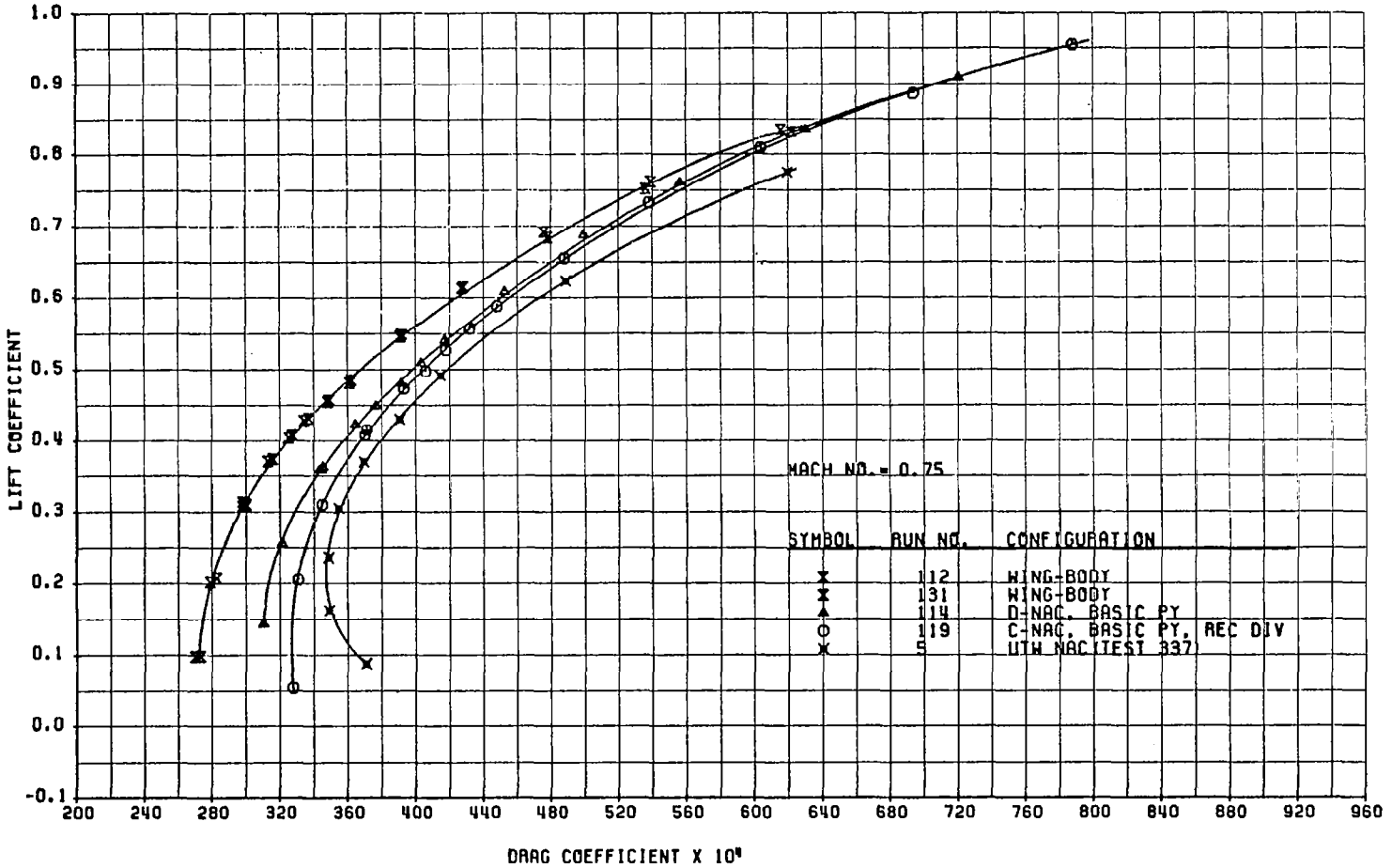

FIGURE A5. DRAG POLARS AT MACH 0.75 FOR WB, C/BAS/REC, AND C/BAS/HL CONFIGURATIONS

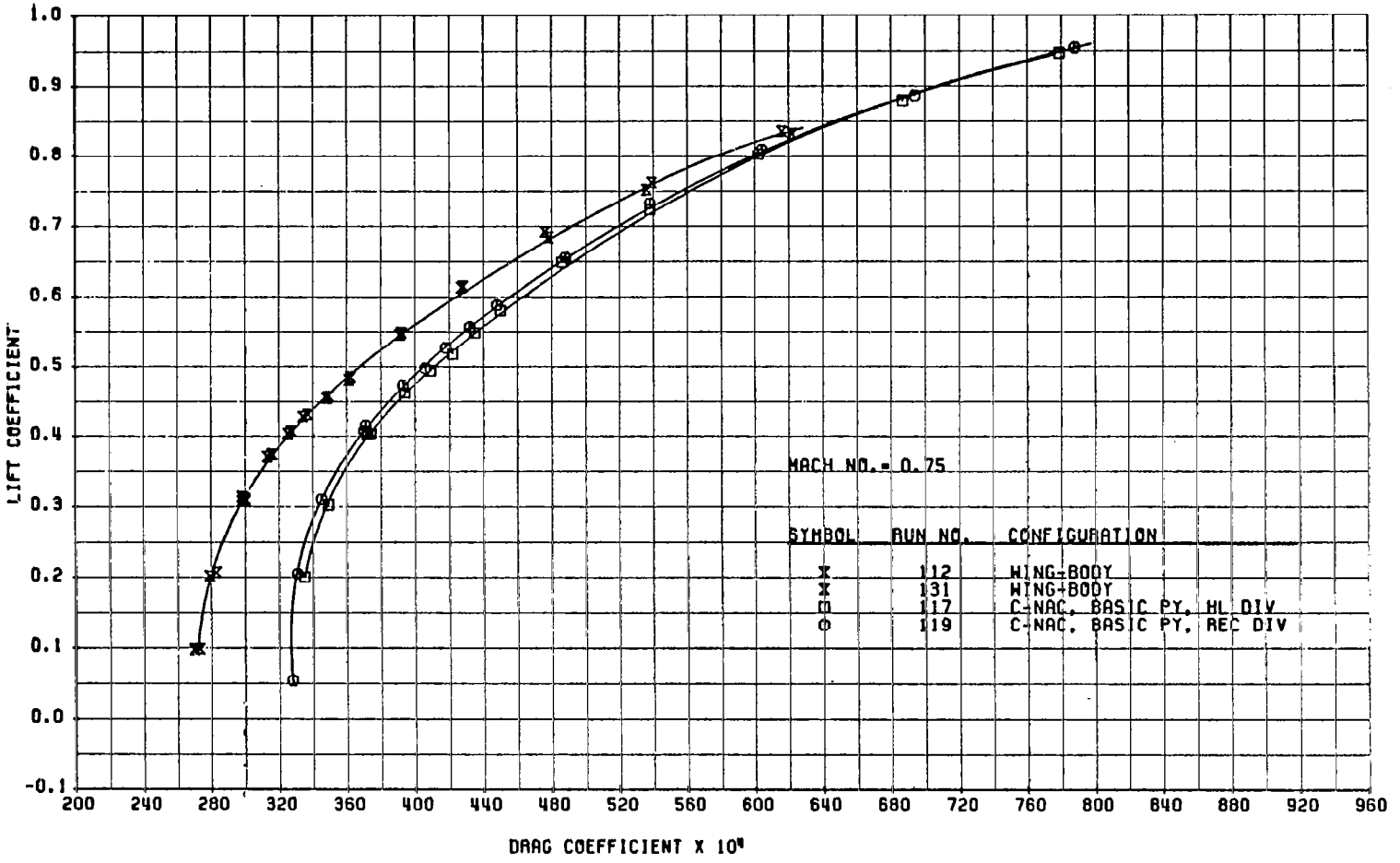

FIGURE A6. DRAG POLARS AT MACH 0.75 FOR WB, D/BAS, D/PRES, AND C/PRES/REC CONFIGURATIONS

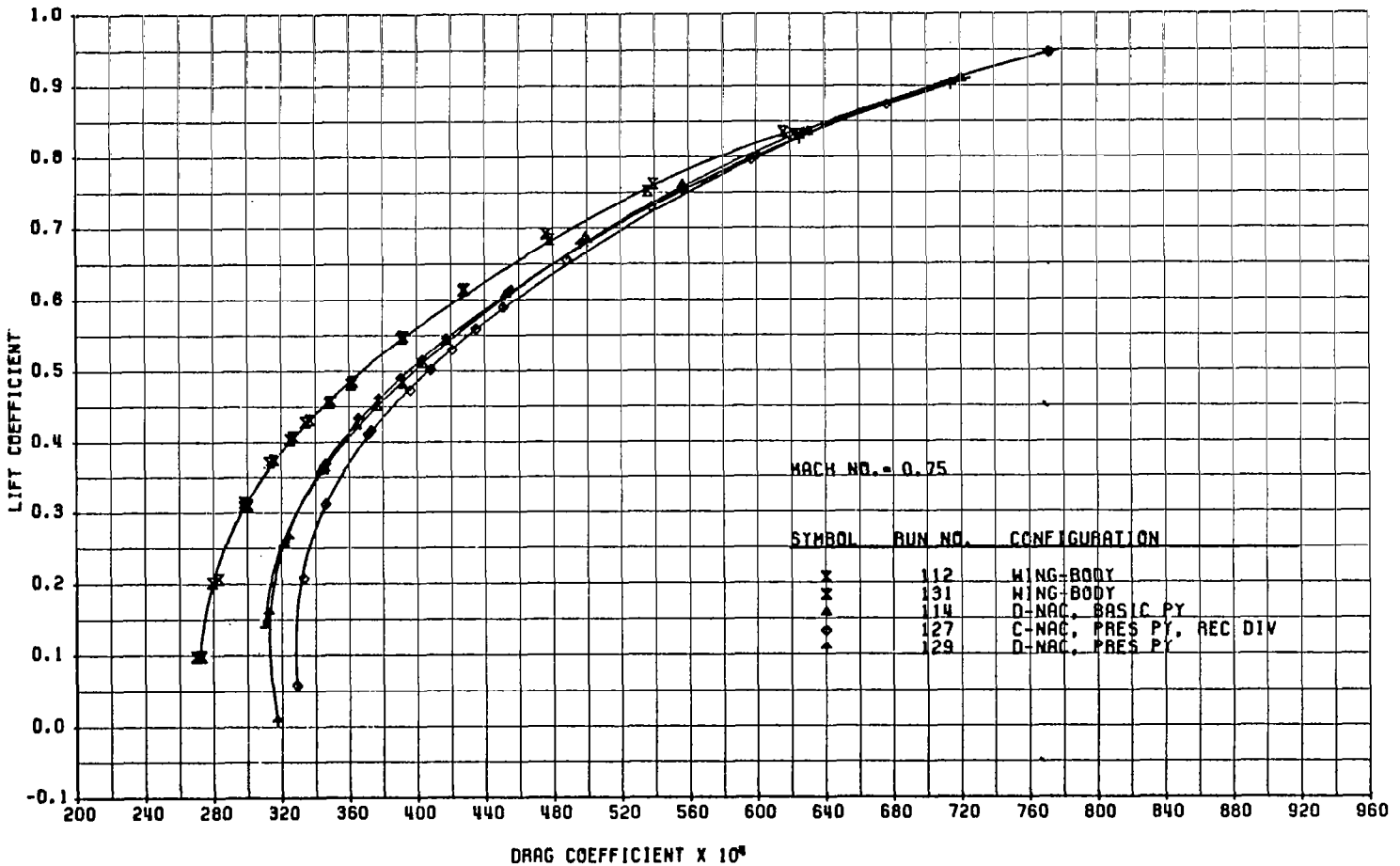

FIGURE A7. DRAG POLARS AT MACH 0.78 FOR WB, D/BAS, C/BAS/REC, AND UTW CONFIGURATIONS

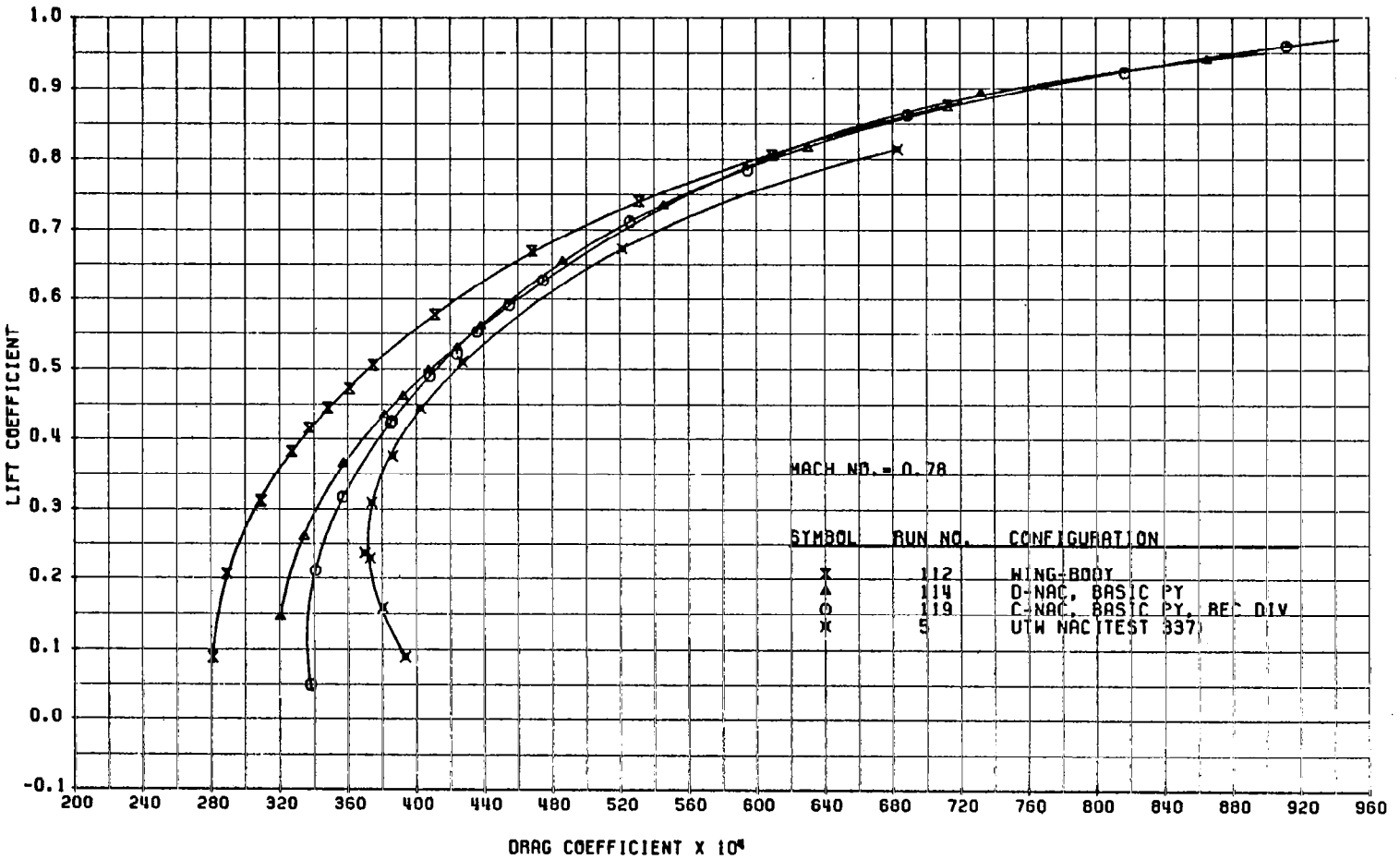

FIGURE A8. DRAG POLARS AT MACH 0.78 FOR WB, C/BAS/REC, AND C/BAS/HL CONFIGURATIONS

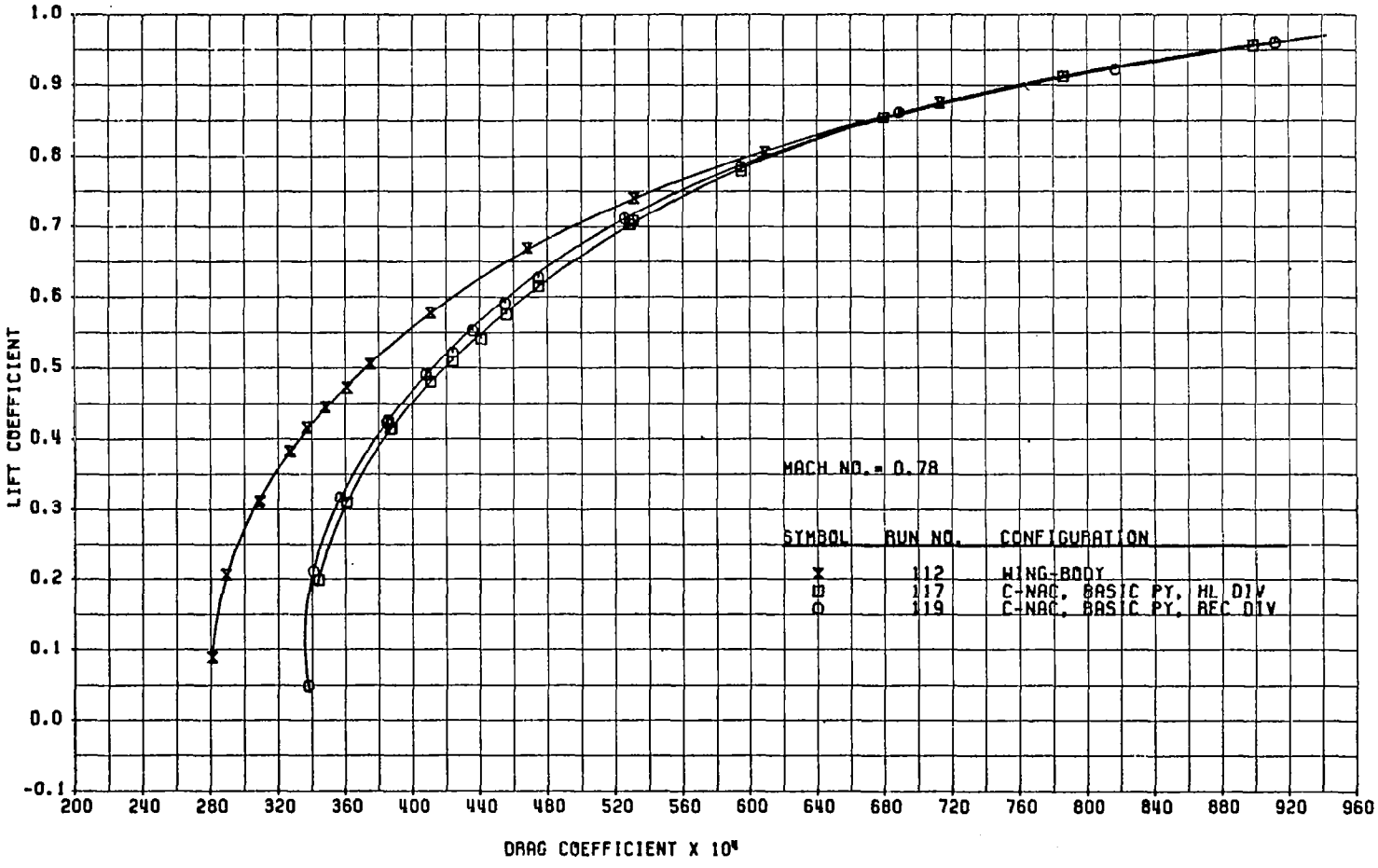

FIGURE A9. DRAG POLARS AT MACH 0.78 FOR WB, D/BAS, D/PRES, AND C/PRES/REC CONFIGURATIONS

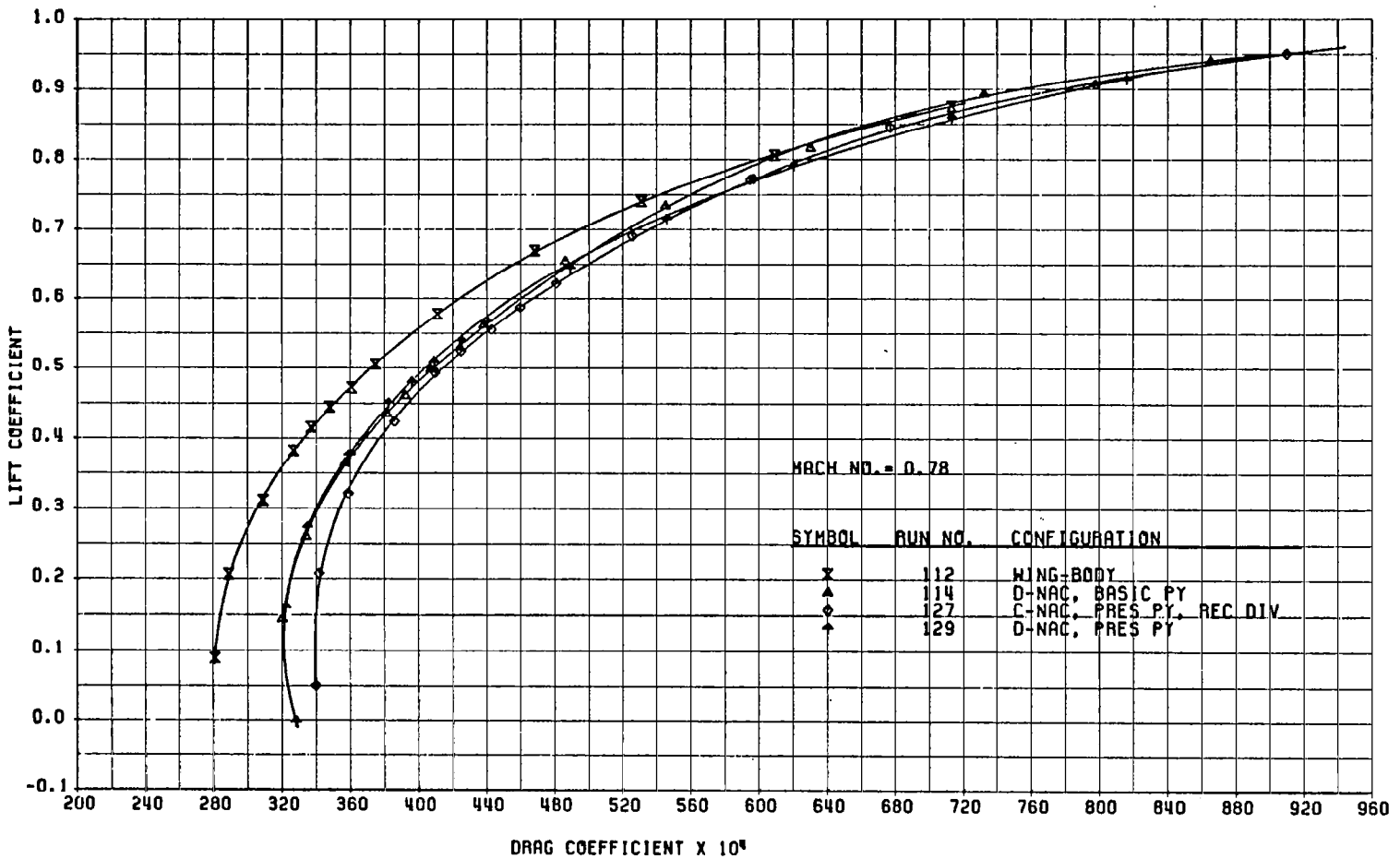

FIGURE A10. DRAG POLARS AT MACH 0.79 FOR WB, D/BAS, C/BAS/REC, AND UTW CONFIGURATIONS

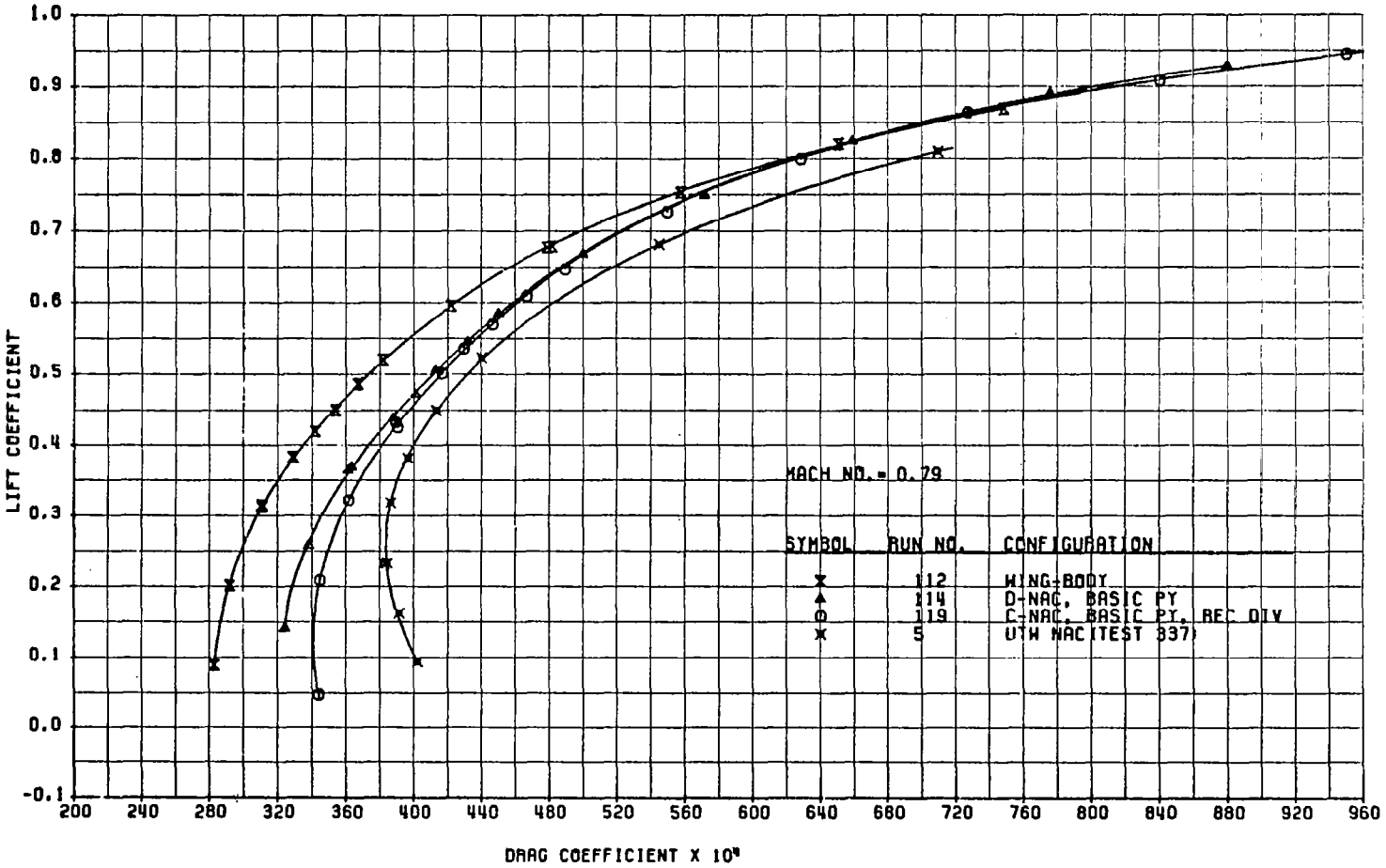

FIGURE A11. DRAG POLARS AT MACH 0.79 FOR WB, C/BAS/REC, AND C/BAS/HL CONFIGURATIONS

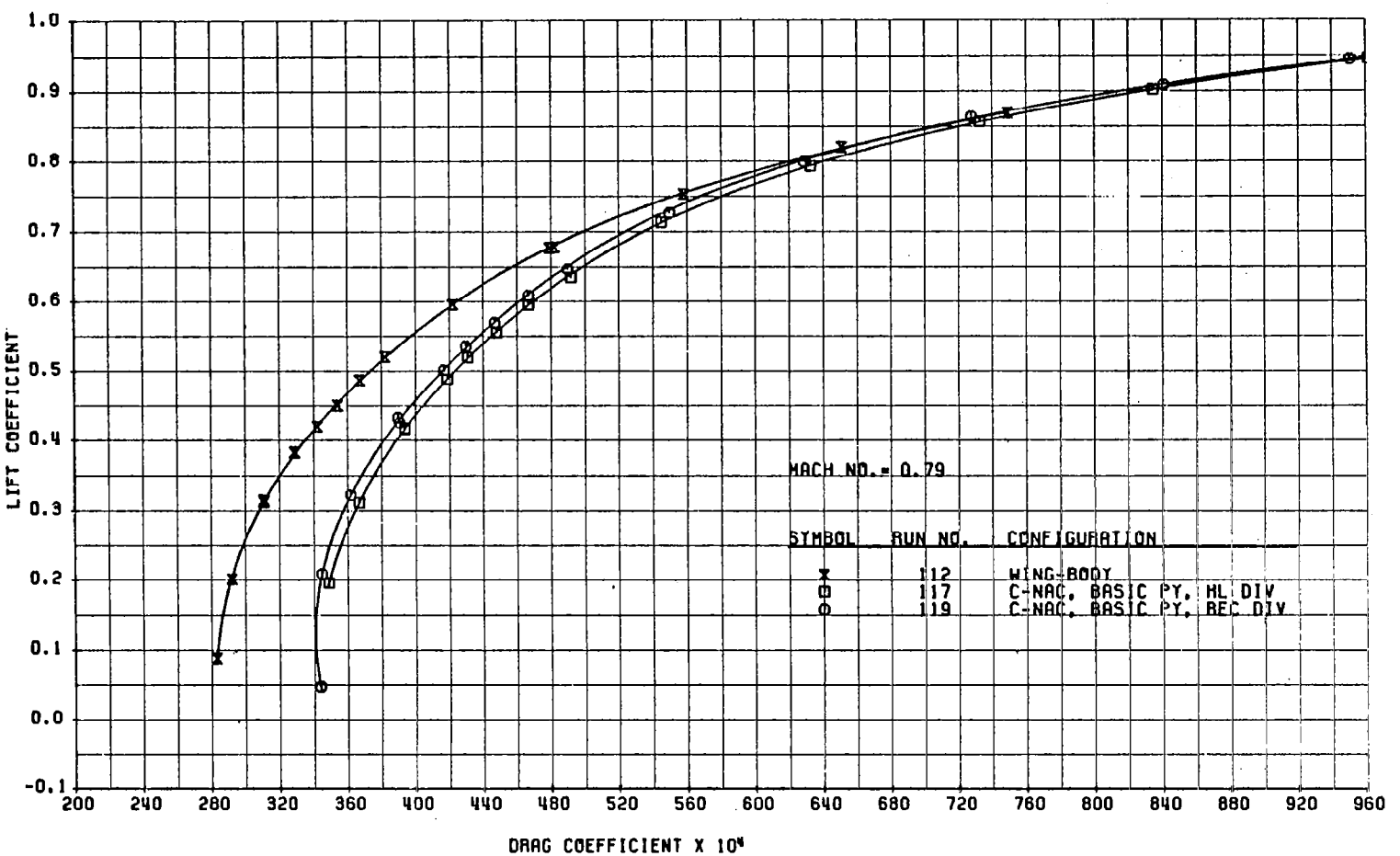

FIGURE A12. DRAG POLARS AT MACH 0.79 FOR WB, D/BAS, D/PRES, AND C/PRES/REC CONFIGURATIONS

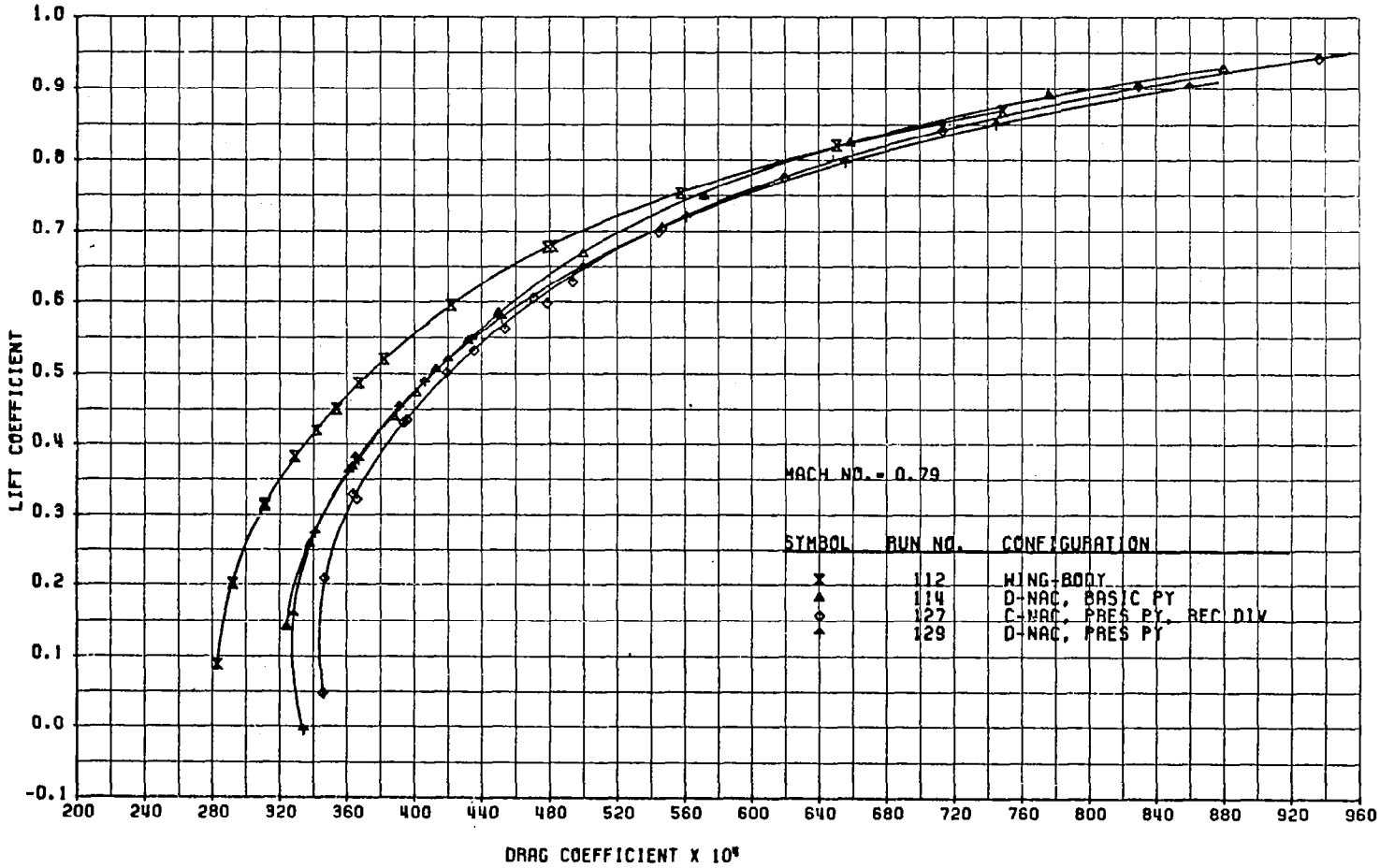

FIGURE A13. DRAG POLARS AT MACH 0.81 FOR WB, D/BAS, C/BAS/REC, AND UTW CONFIGURATIONS

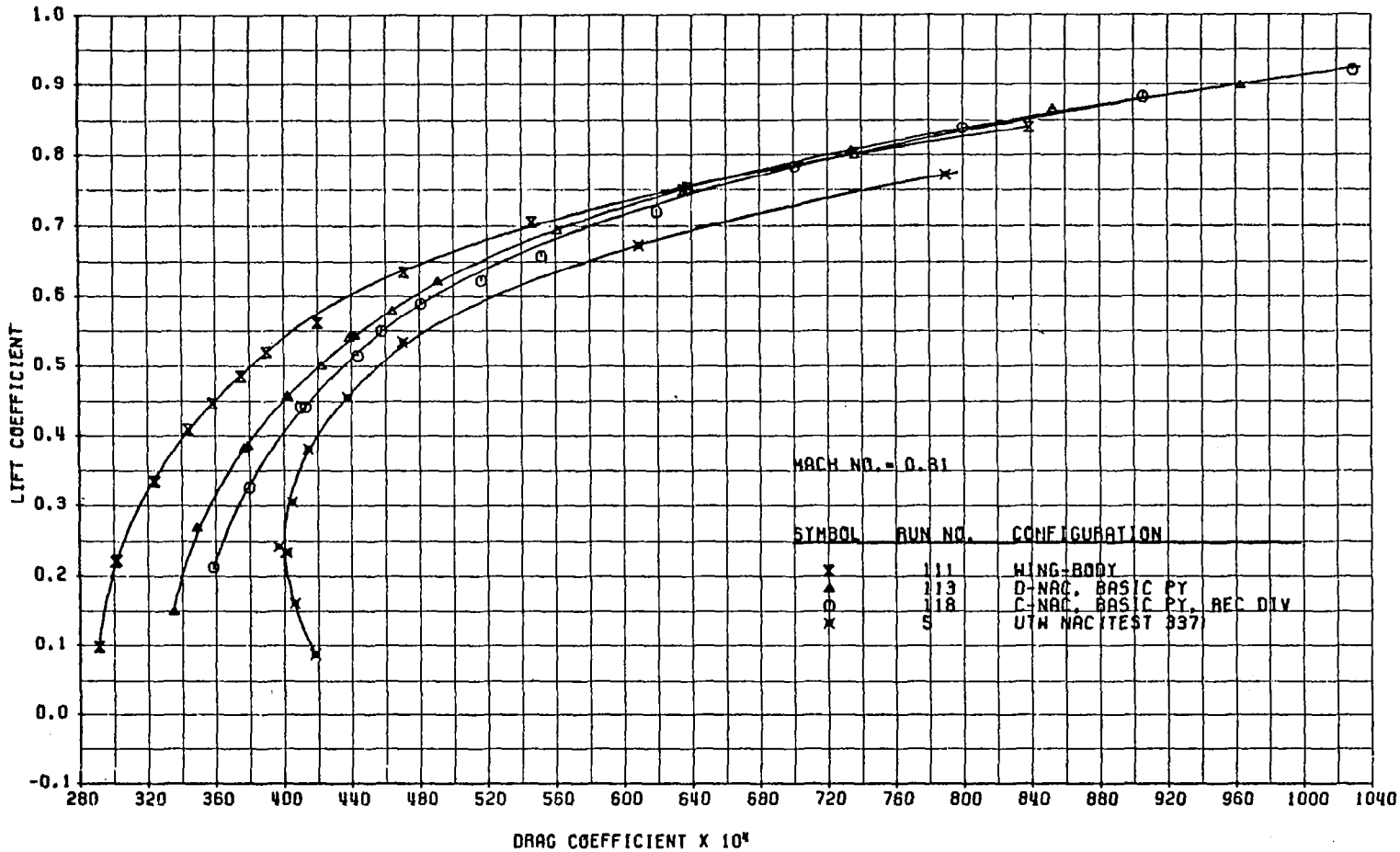

FIGURE A14. DRAG POLARS AT MACH 0.81 FOR WB, C/BAS/REC, AND C/BAS/HL CONFIGURATIONS

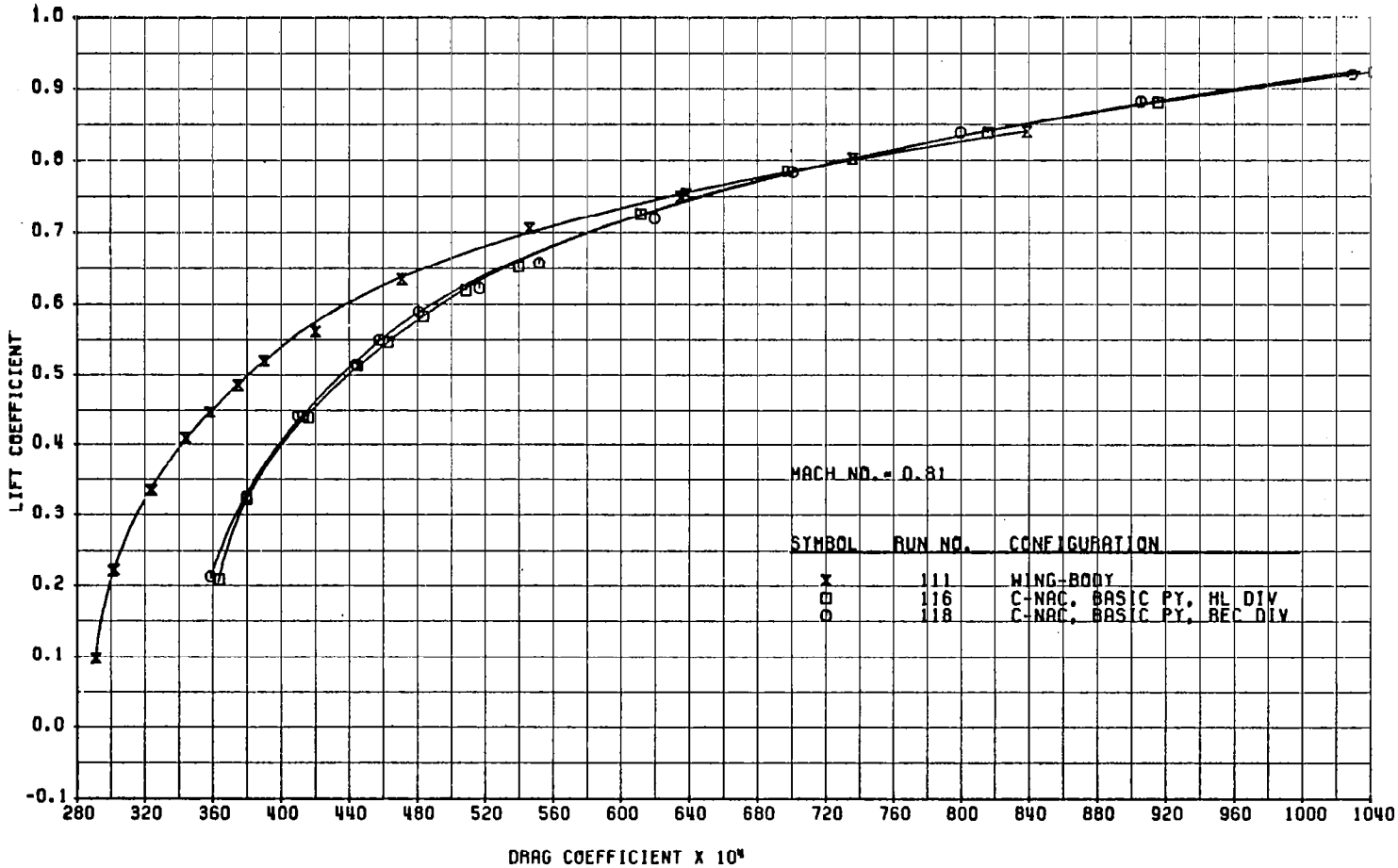

FIGURE A15. DRAG POLARS AT MACH 0.81 FOR WB, D/BAS, D/PRES, AND C/PRES/REC CONFIGURATIONS

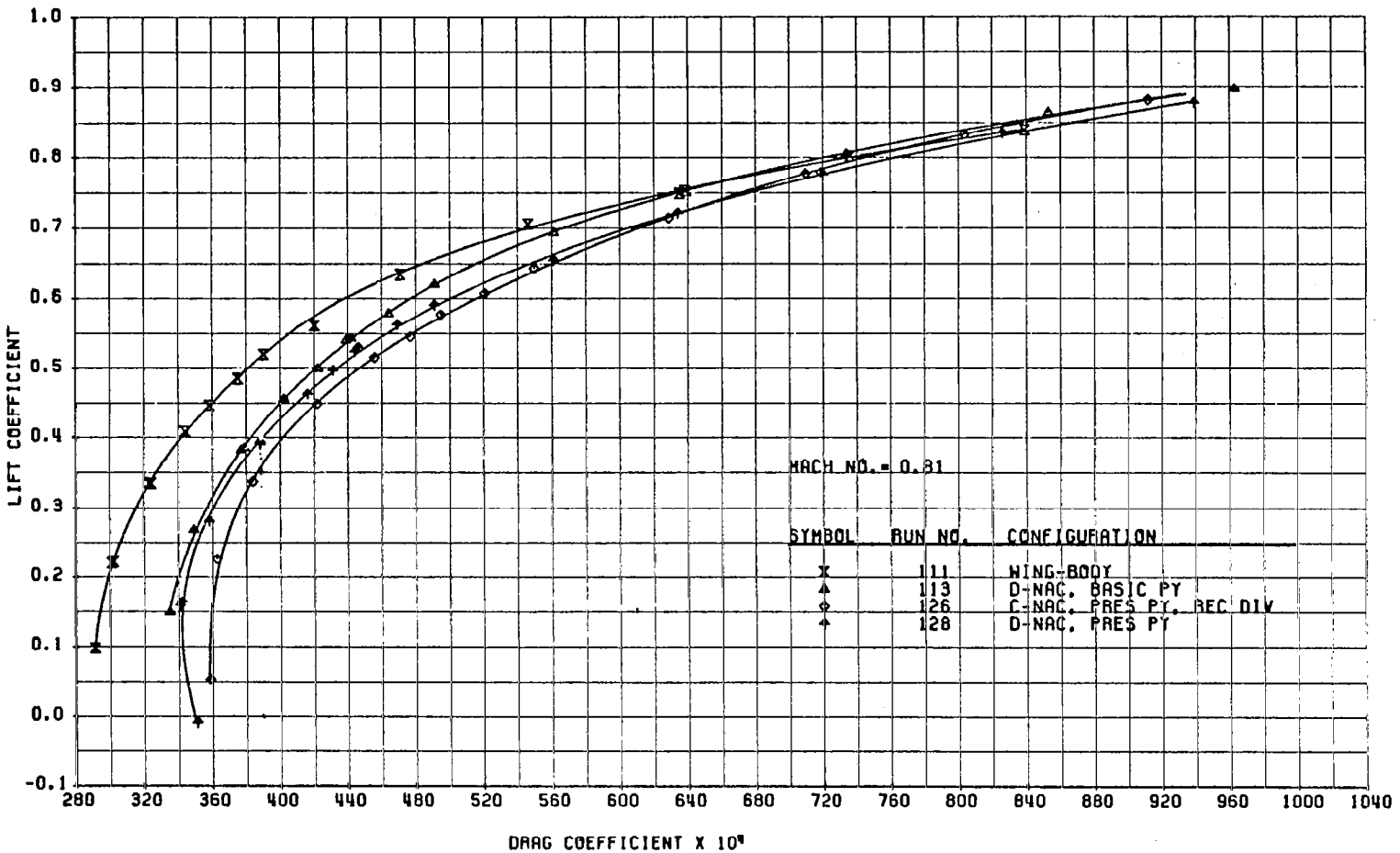

FIGURE A16. DRAG POLARS AT MACH 0.83 FOR WB, D/BAS, AND C/BAS/REC CONFIGURATIONS

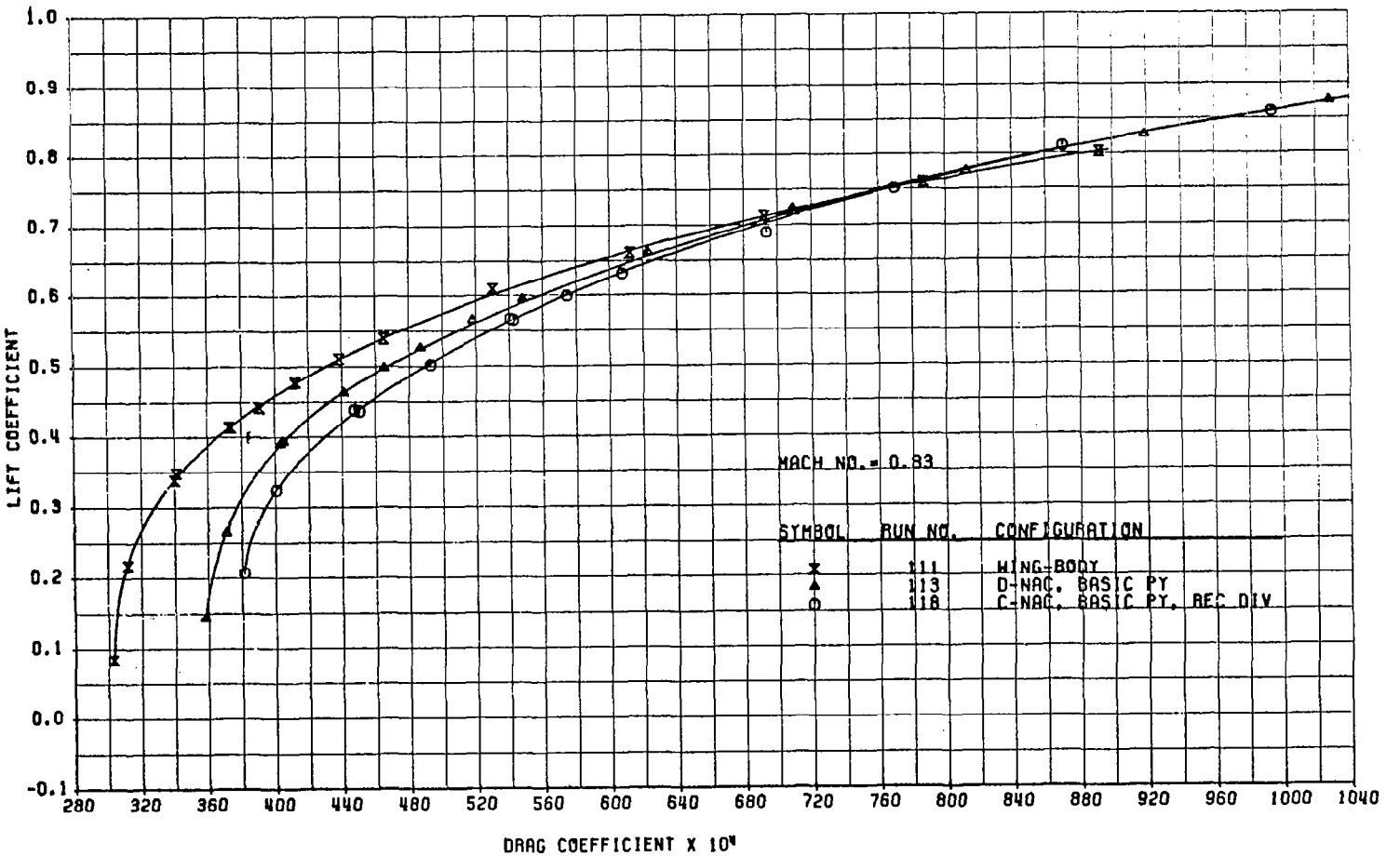

FIGURE A17. DRAG POLARS AT MACH 0.83 FOR WB, C/BAS/REC, AND C/BAS/HL CONFIGURATIONS

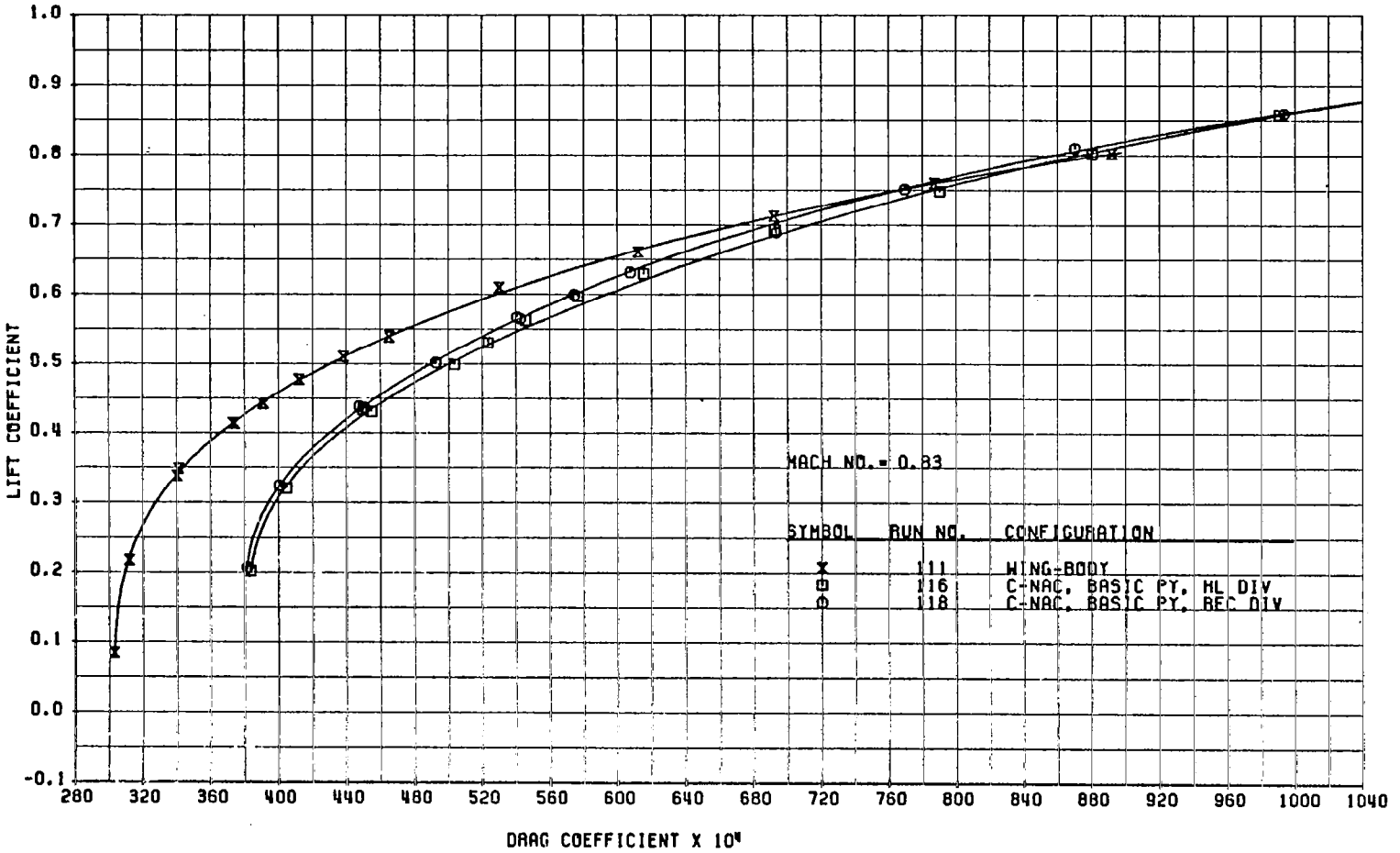

FIGURE A18. DRAG POLARS AT MACH 0.83 FOR WB, D/BAS, D/PRES, AND C/PRES/REC CONFIGURATIONS

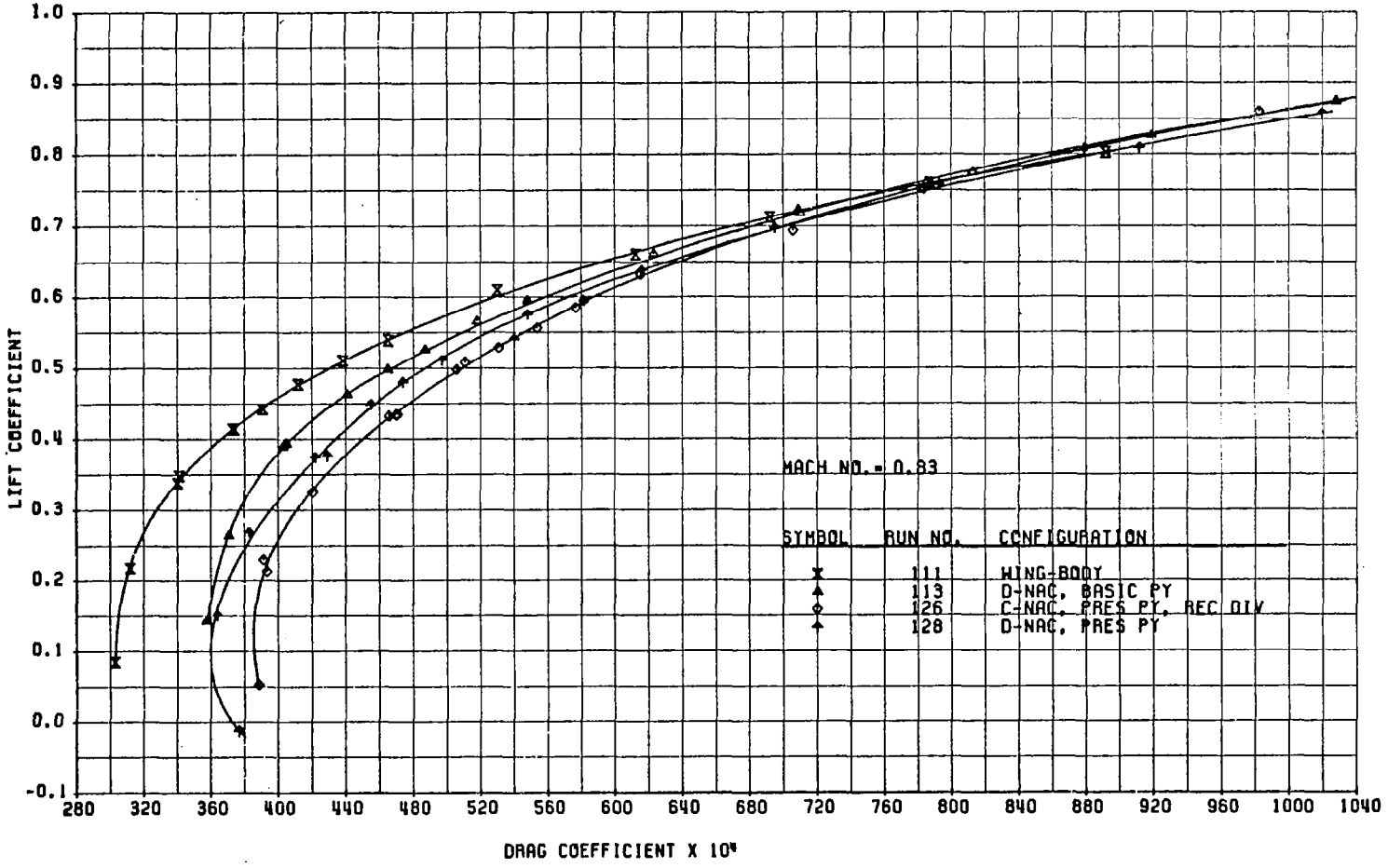

FIGURE A19. DRAG POLARS AT MACH 0.85 FOR WB, D/BAS, AND C/BAS/REC CONFIGURATIONS

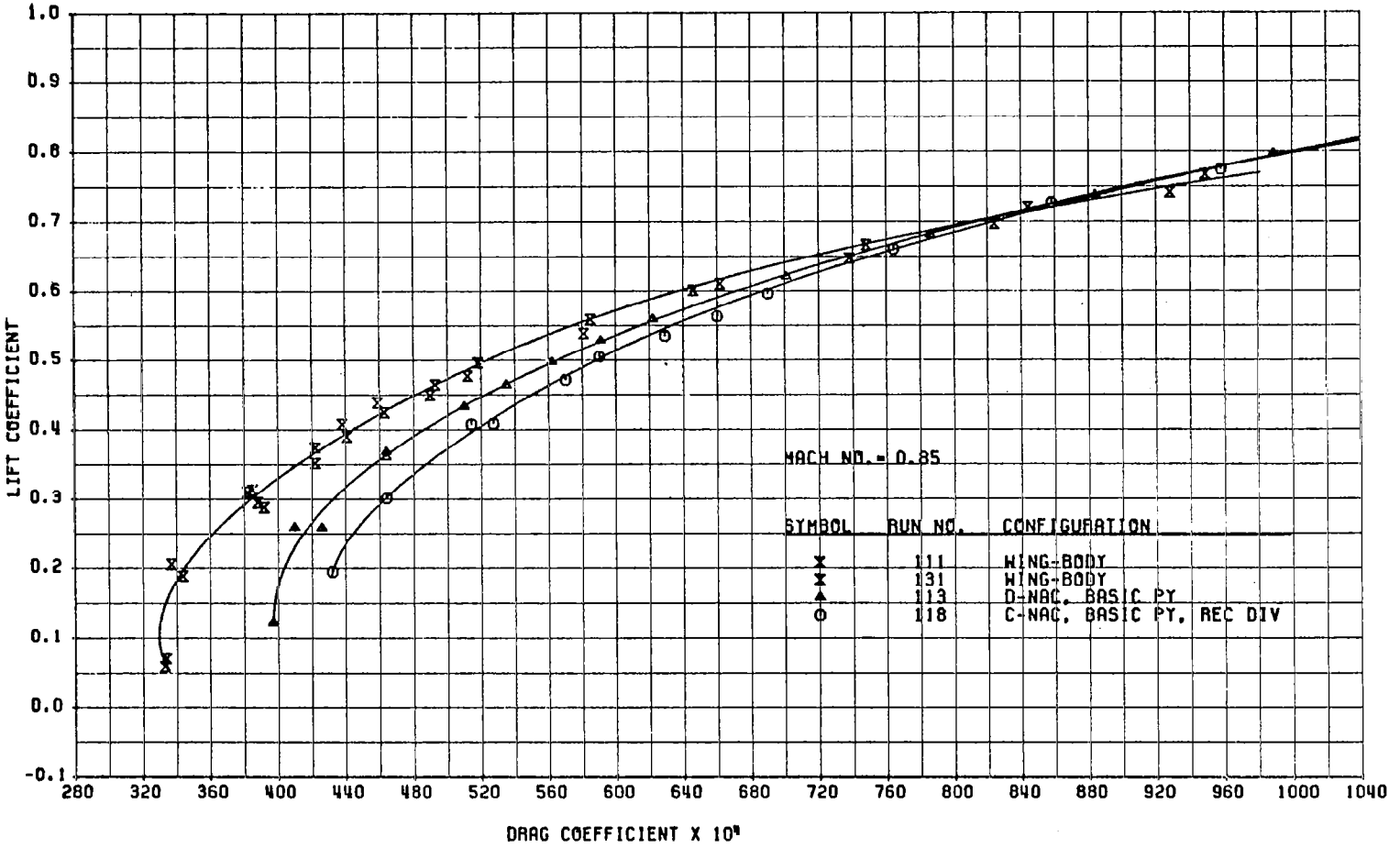

FIGURE A20. DRAG POLARS AT MACH 0.85 FOR WB, C/BAS/REC, AND C/BAS/HL CONFIGURATIONS

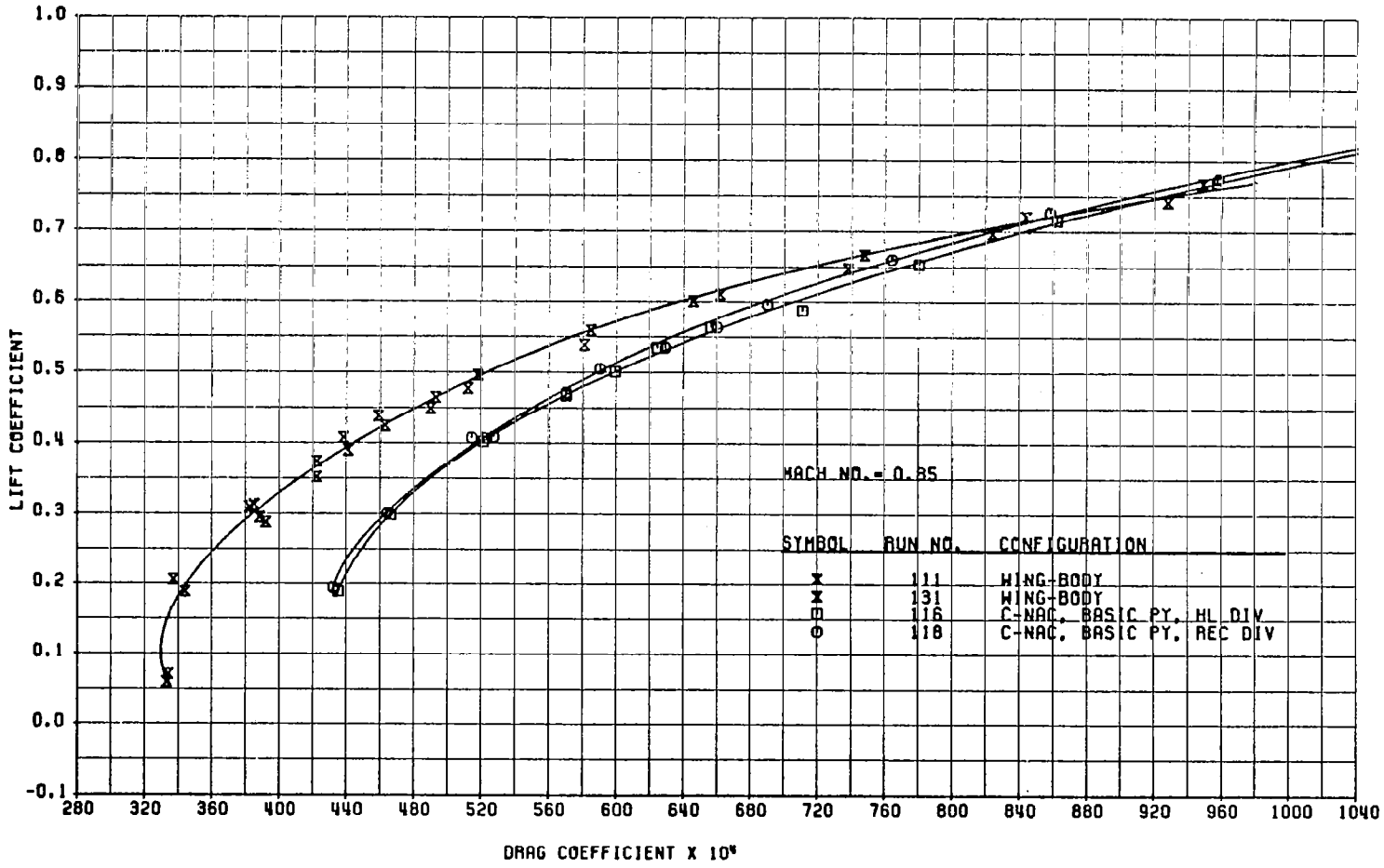

FIGURE A21. DRAG POLARS AT MACH 0.85 FOR WB, D/BAS, D/PRES, AND C/PRES/REC CONFIGURATIONS

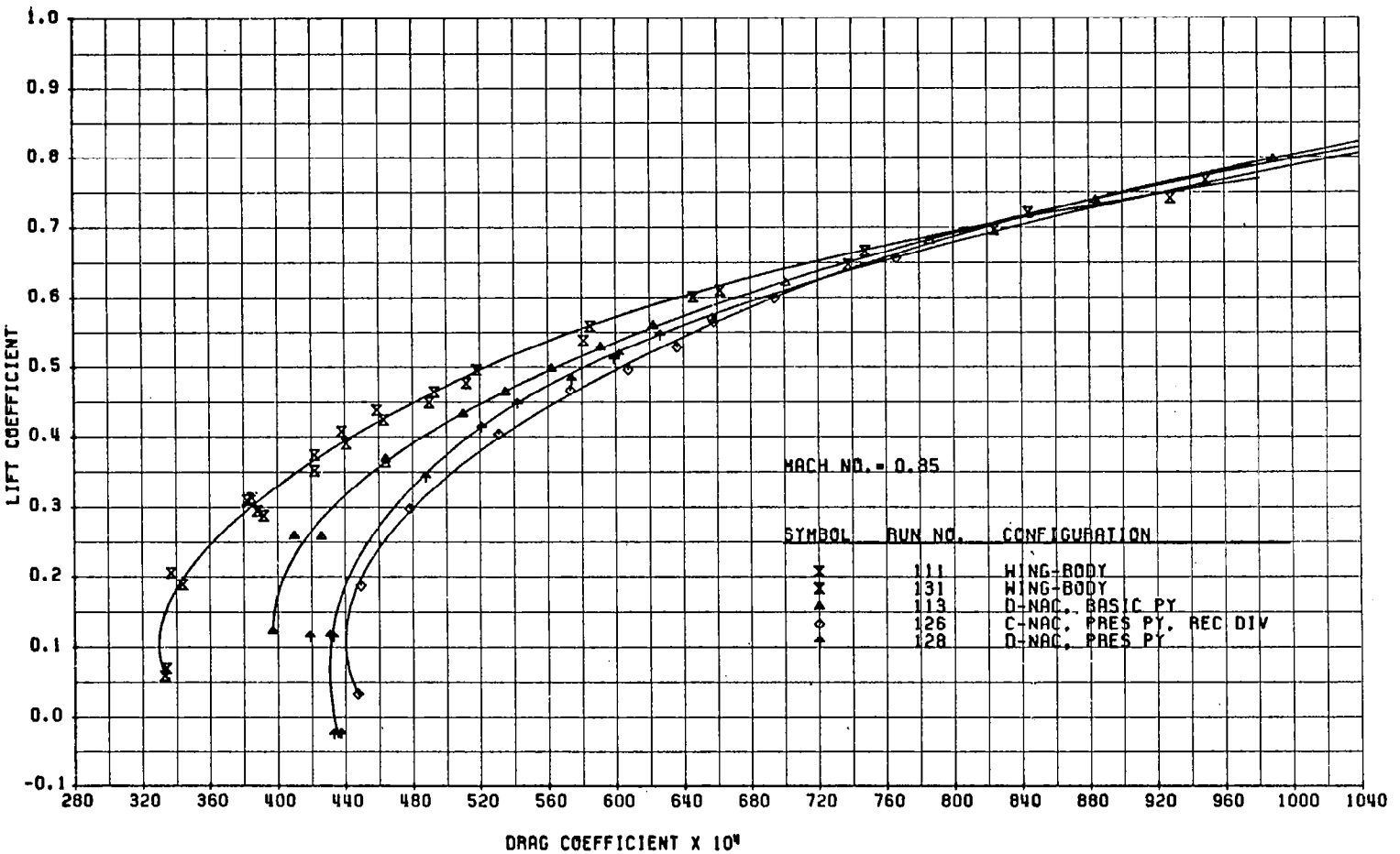

FIGURE A22a.

WING UPPER SURFACE PRESSURE DISTRIBUTION

WING BODY

MACH NUMBER = 0.700 CL = 0.4419

1.2820 DEG. ANGLE OF ATTACK

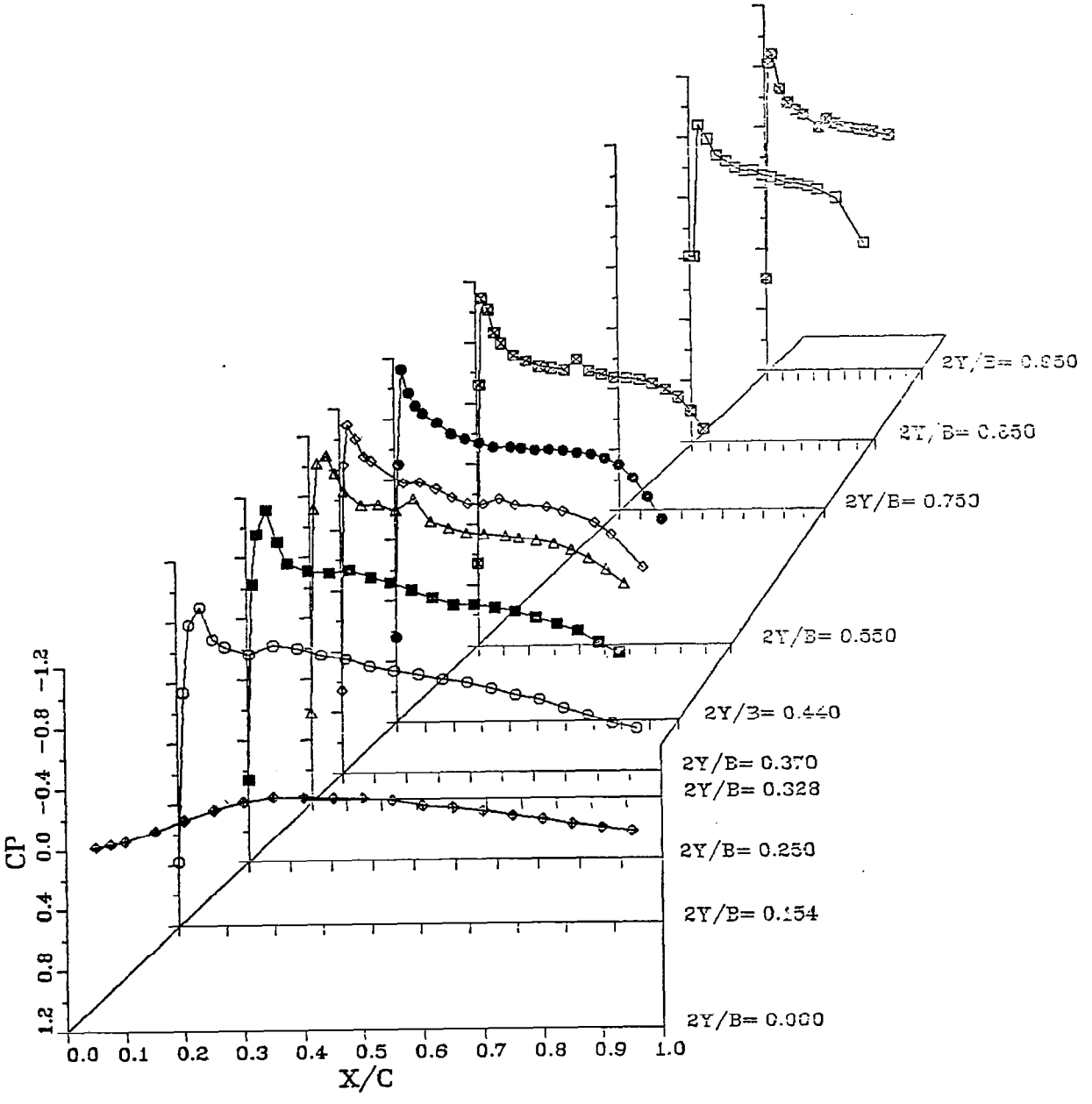

FIGURE A22b.

WING LOWER SURFACE PRESSURE DISTRIBUTION

WING BODY

MACH NUMBER = 0.700 CL = 0.4419

1.2820 DEG. ANGLE OF ATTACK

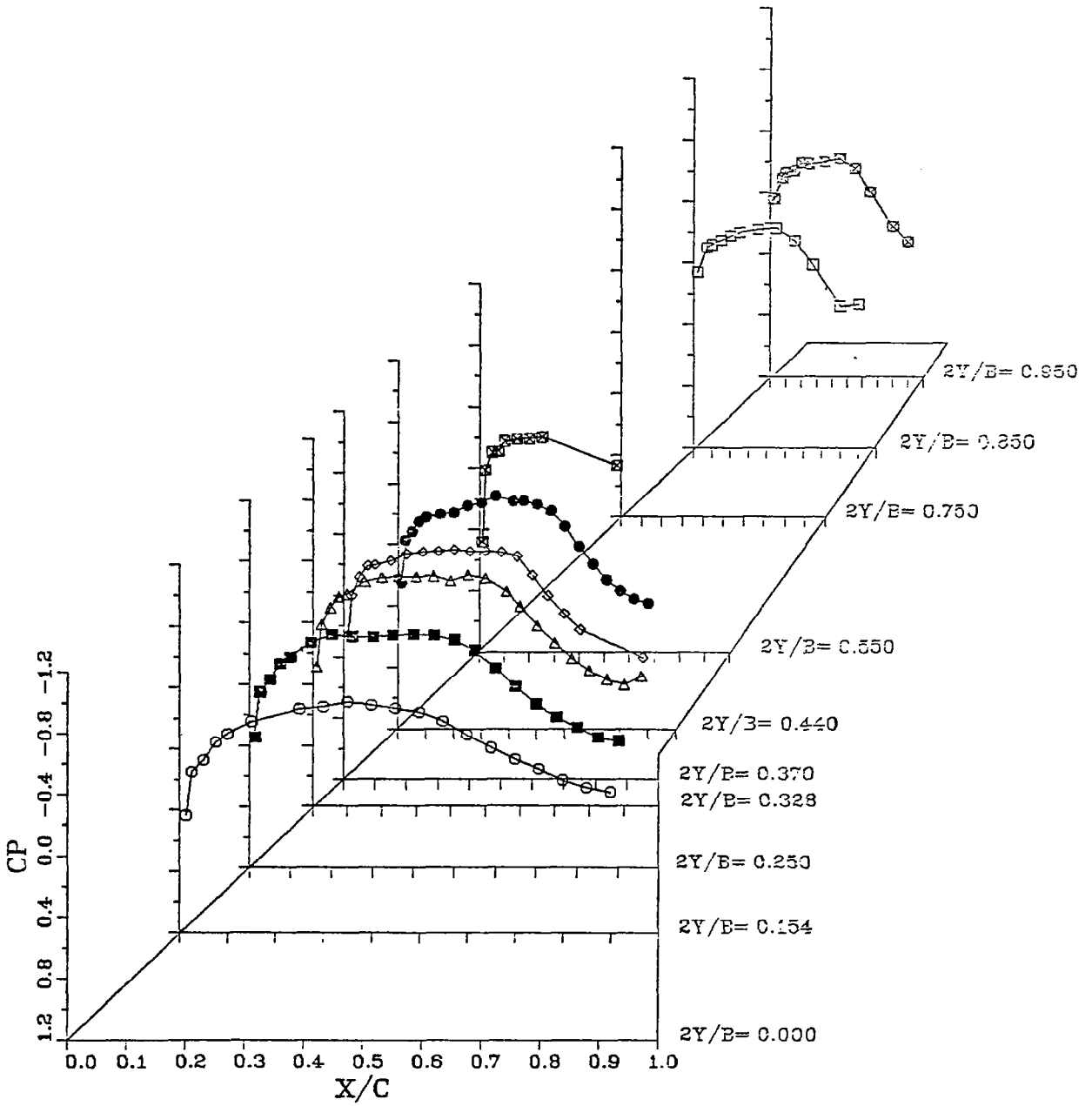

FIGURE A23a.

WING UPPER SURFACE PRESSURE DISTRIBUTION

D NACELLE / BASIC PYLON

MACH NUMBER = 0.700 CL = 0.4621

1.0637 DEG. ANGLE OF ATTACK

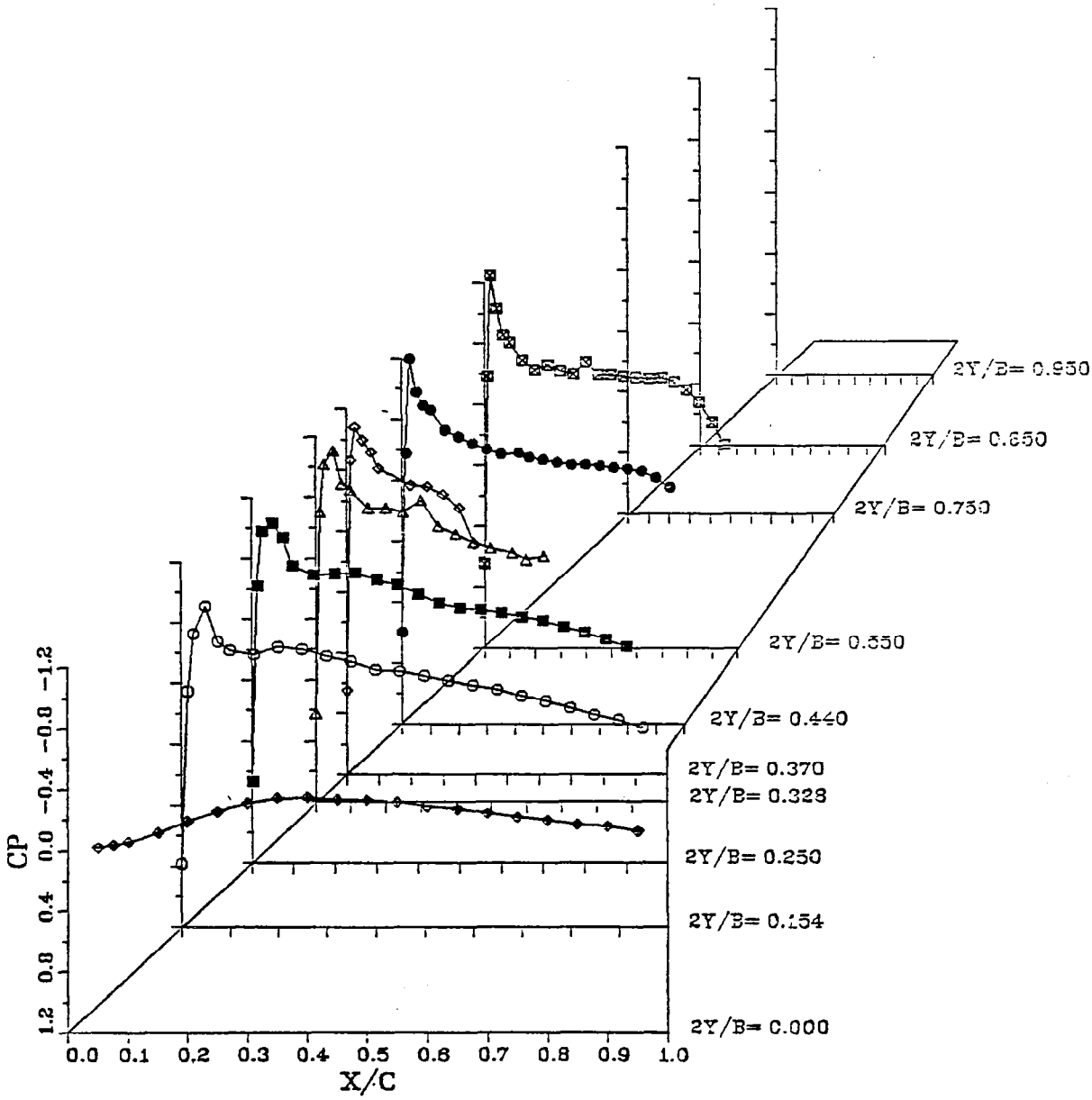

FIGURE A23b.

WING LOWER SURFACE PRESSURE DISTRIBUTION

D NACELLE / BASIC PYLON

MACH NUMBER = 0.700 CL = 0.4621

1.0637 DEG. ANGLE OF ATTACK

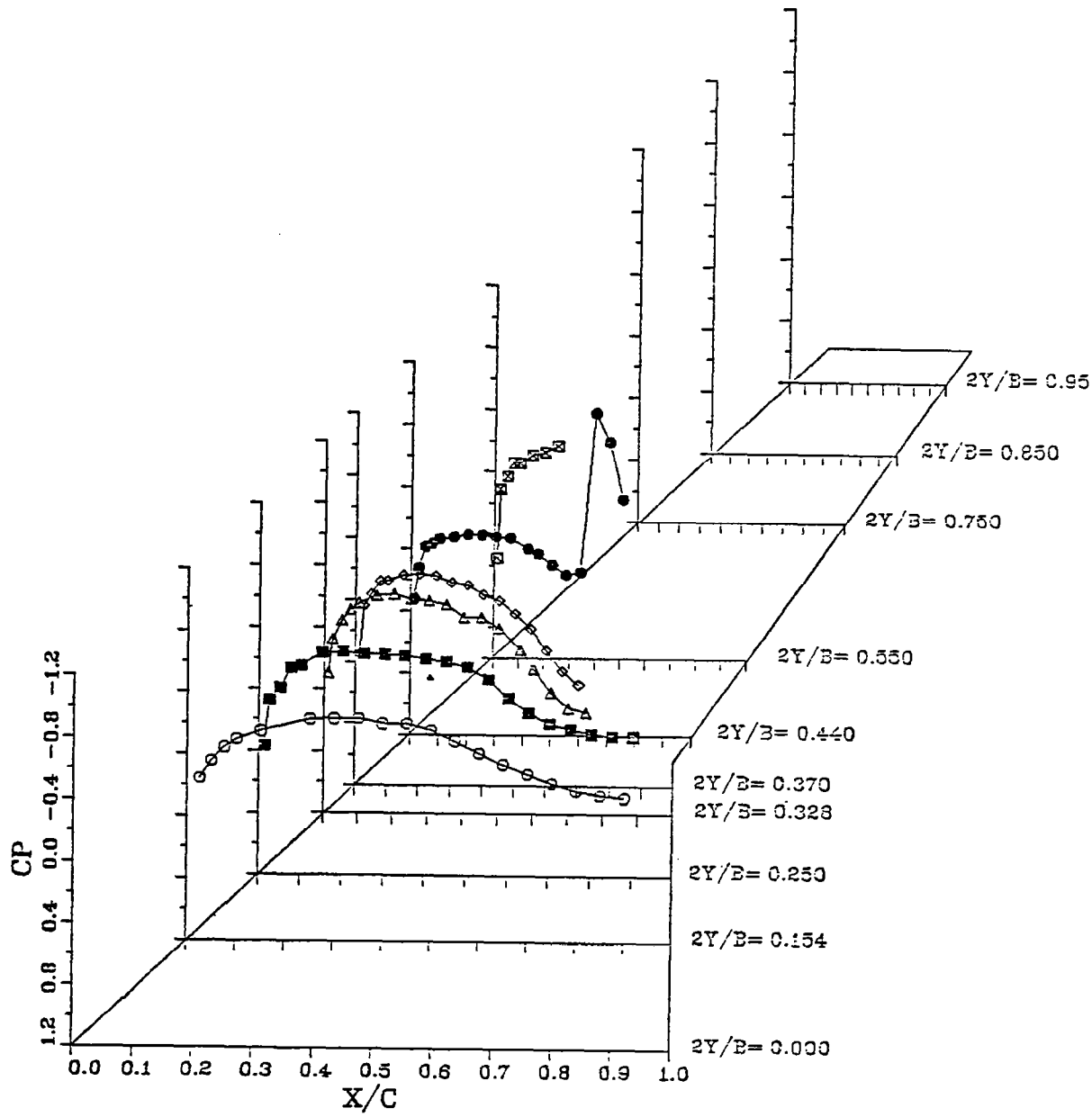

FIGURE A24a.

WING UPPER SURFACE PRESSURE DISTRIBUTION

C NACELLE / BASIC PYLON / REC DIV

MACH NUMBER = 0.700 CL = 0.4491

0.5517 DEG. ANGLE OF ATTACK

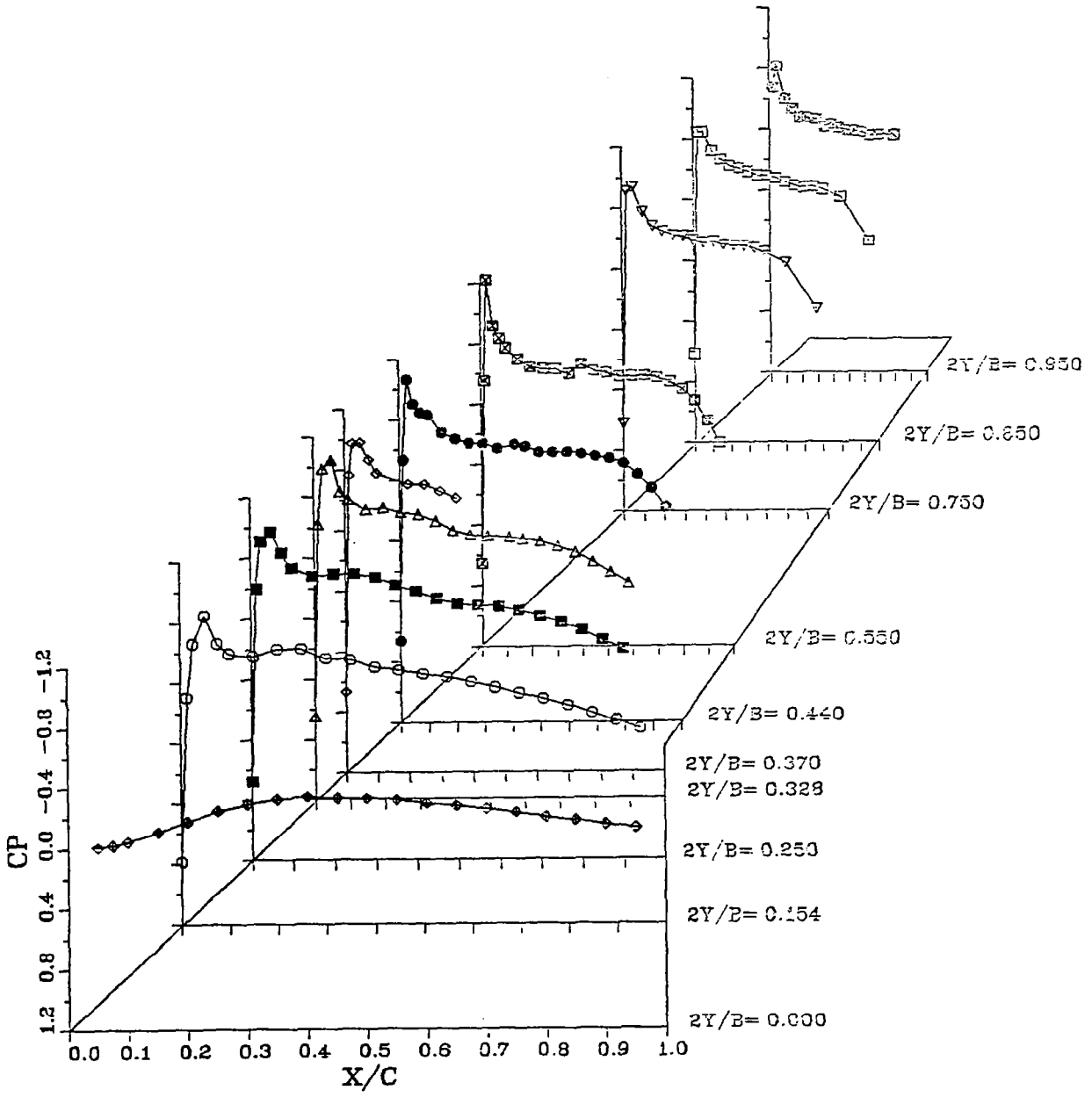

FIGURE A24b.

WING LOWER SURFACE PRESSURE DISTRIBUTION

C NACELLE / BASIC PYLON / REC DIV

MACH NUMBER = 0.700 CL = 0.4491

0.5517 DEG. ANGLE OF ATTACK

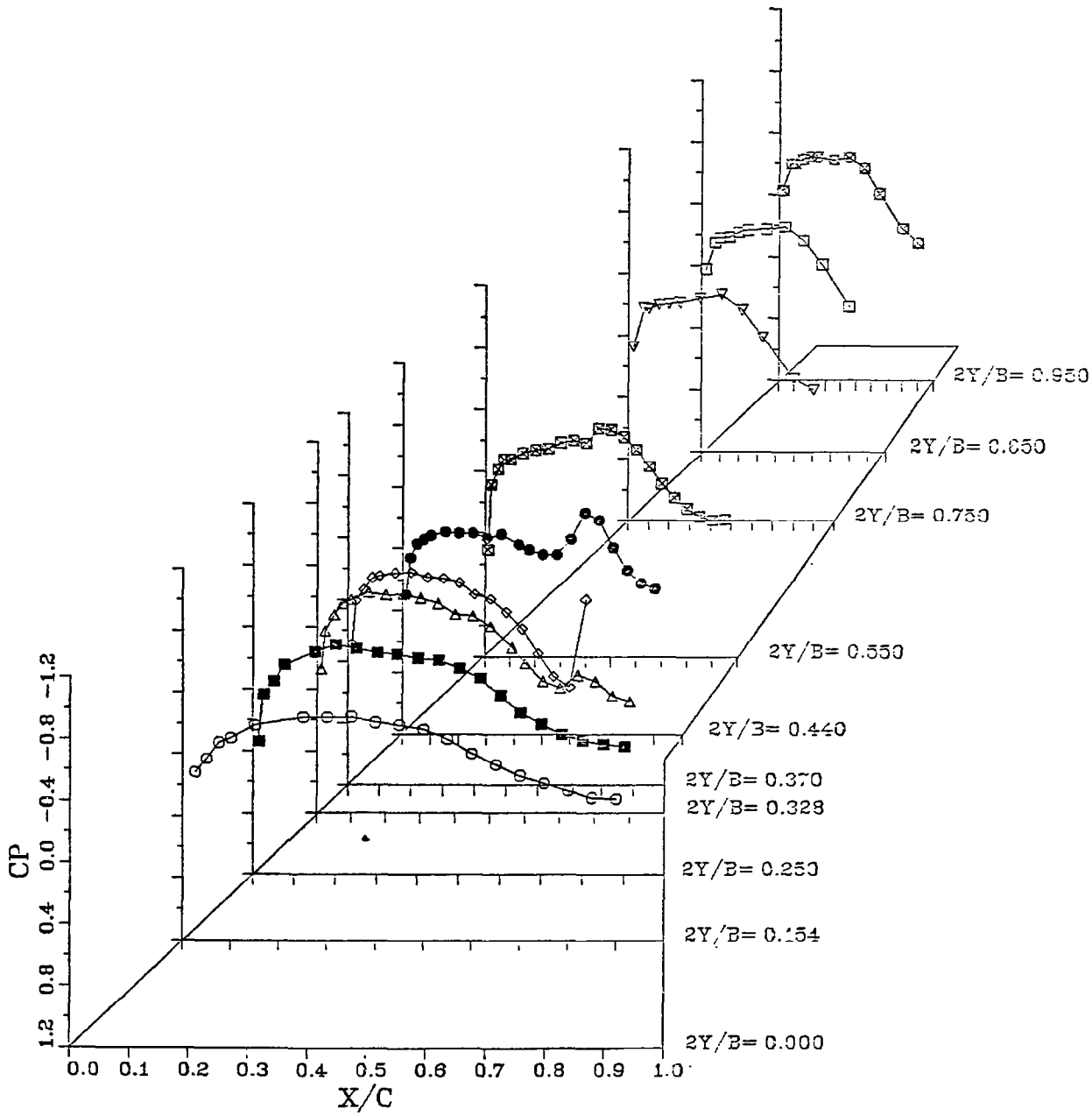

FIGURE A25a.

WING UPPER SURFACE PRESSURE DISTRIBUTION

UTW NACELLE

MACH NUMBER = 0.700 CL = 0.4734

2.1730 DEG. ANGLE OF ATTACK

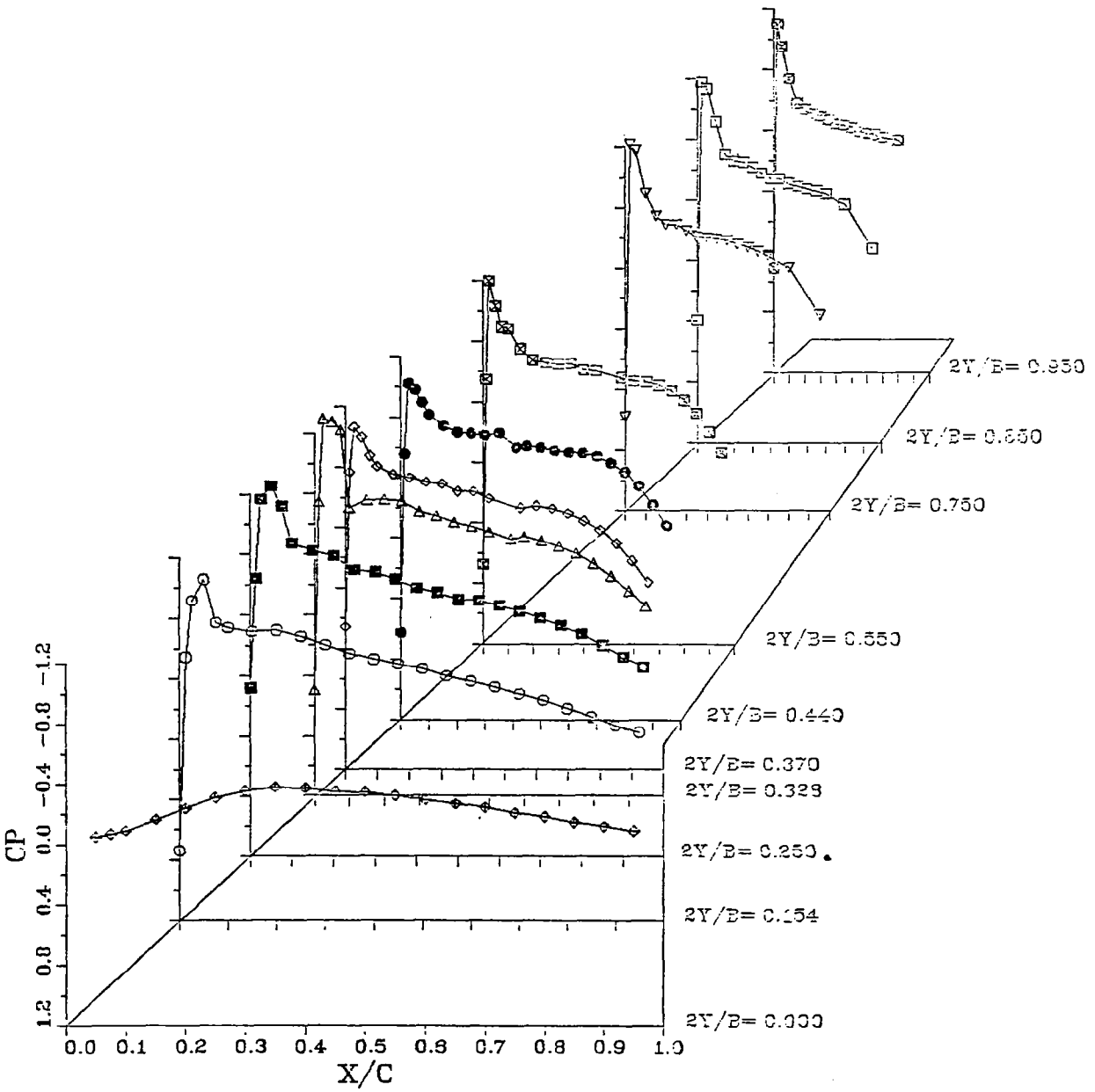

FIGURE A25b.

WING LOWER SURFACE PRESSURE DISTRIBUTION

UTW NACELLE

MACH NUMBER = 0.700 CL = 0.4734

2.1730 DEG. ANGLE OF ATTACK

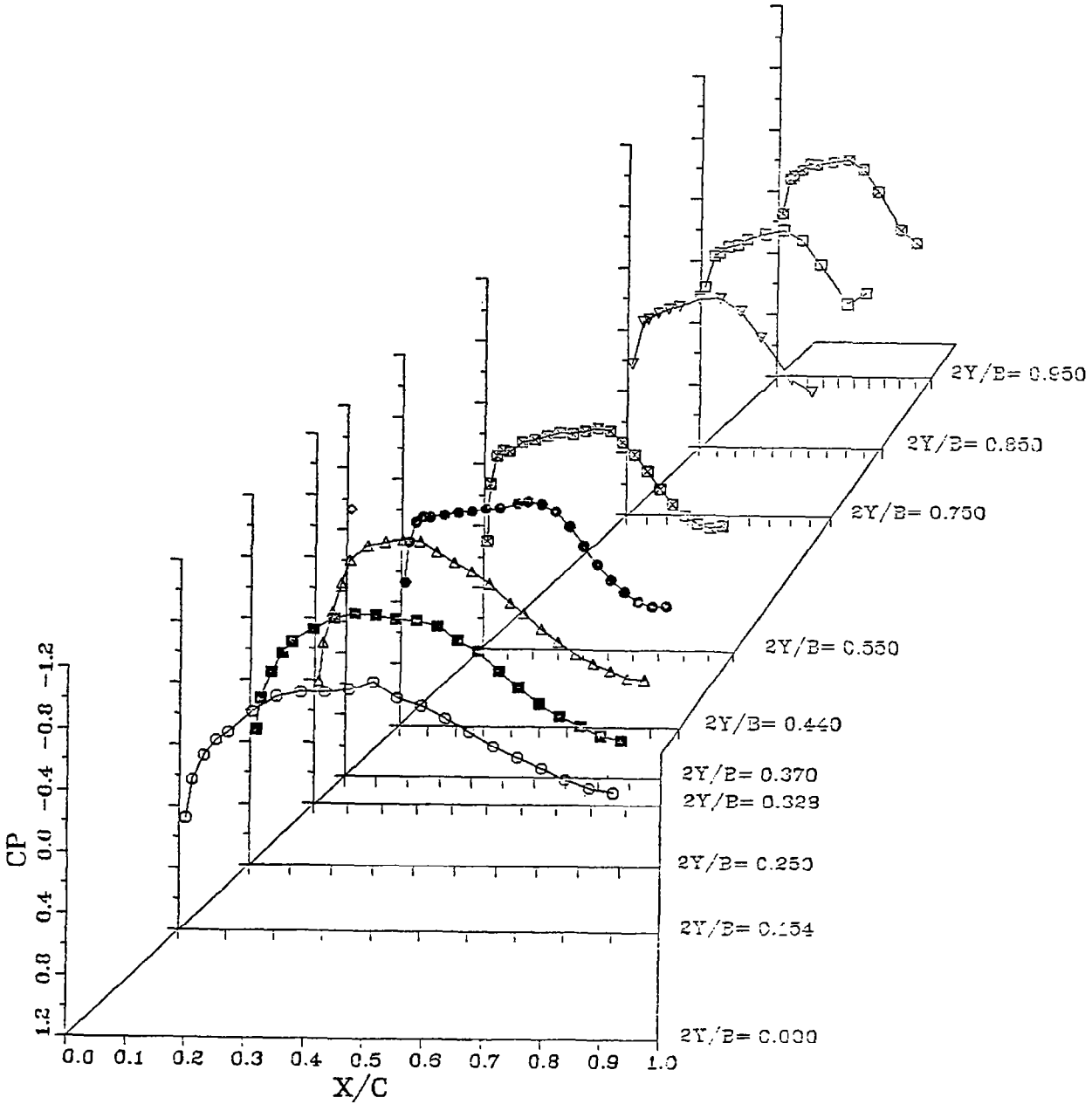

FIGURE A26a.

WING UPPER SURFACE PRESSURE DISTRIBUTION

WING BODY

MACH NUMBER = 0.850 CL = 0.4385

1.1070 DEG. ANGLE OF ATTACK

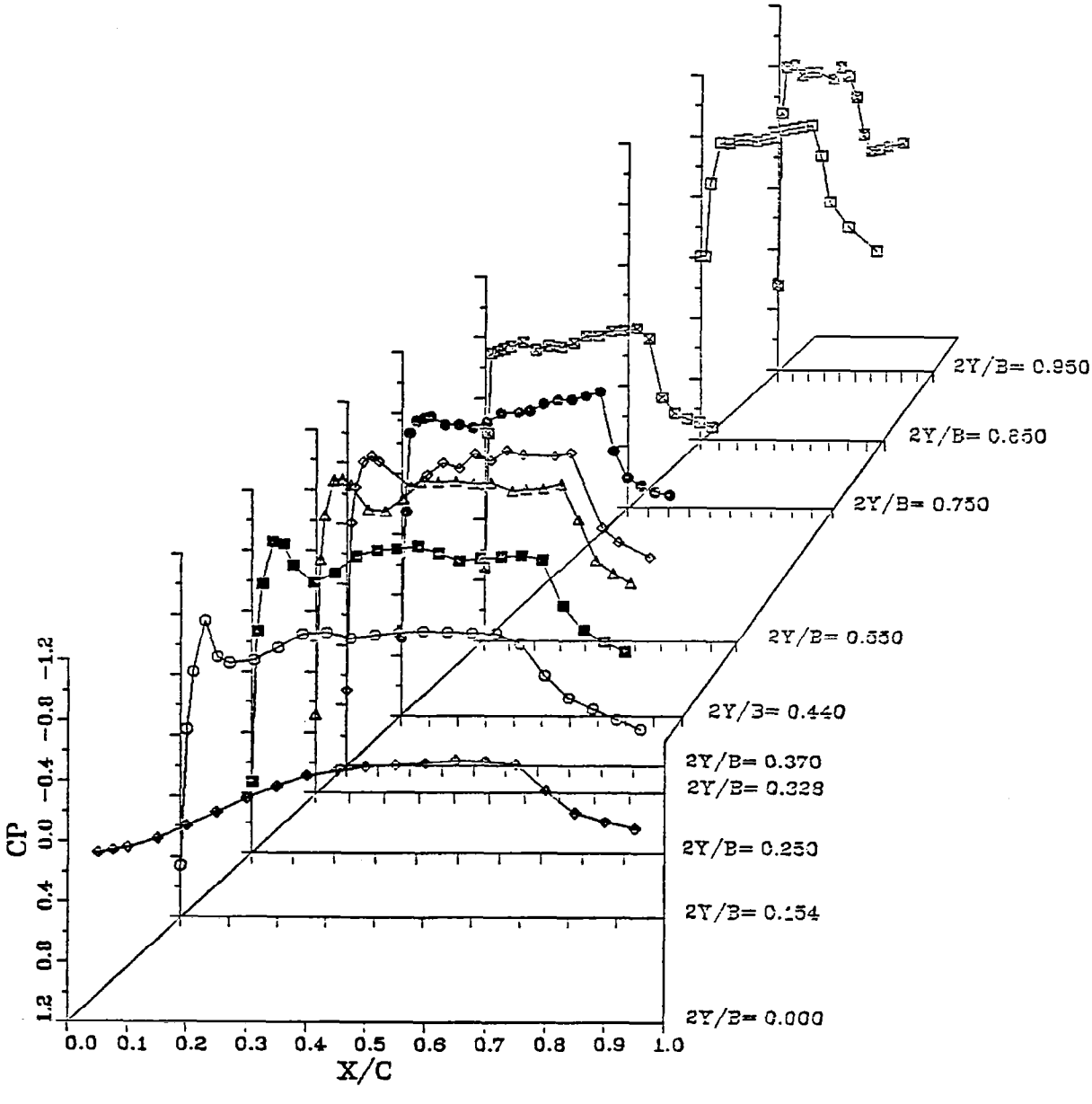

FIGURE A26b.

WING LOWER SURFACE PRESSURE DISTRIBUTION

WING BODY

MACH NUMBER = 0.850 CL = 0.4385

1.1070 DEG. ANGLE OF ATTACK

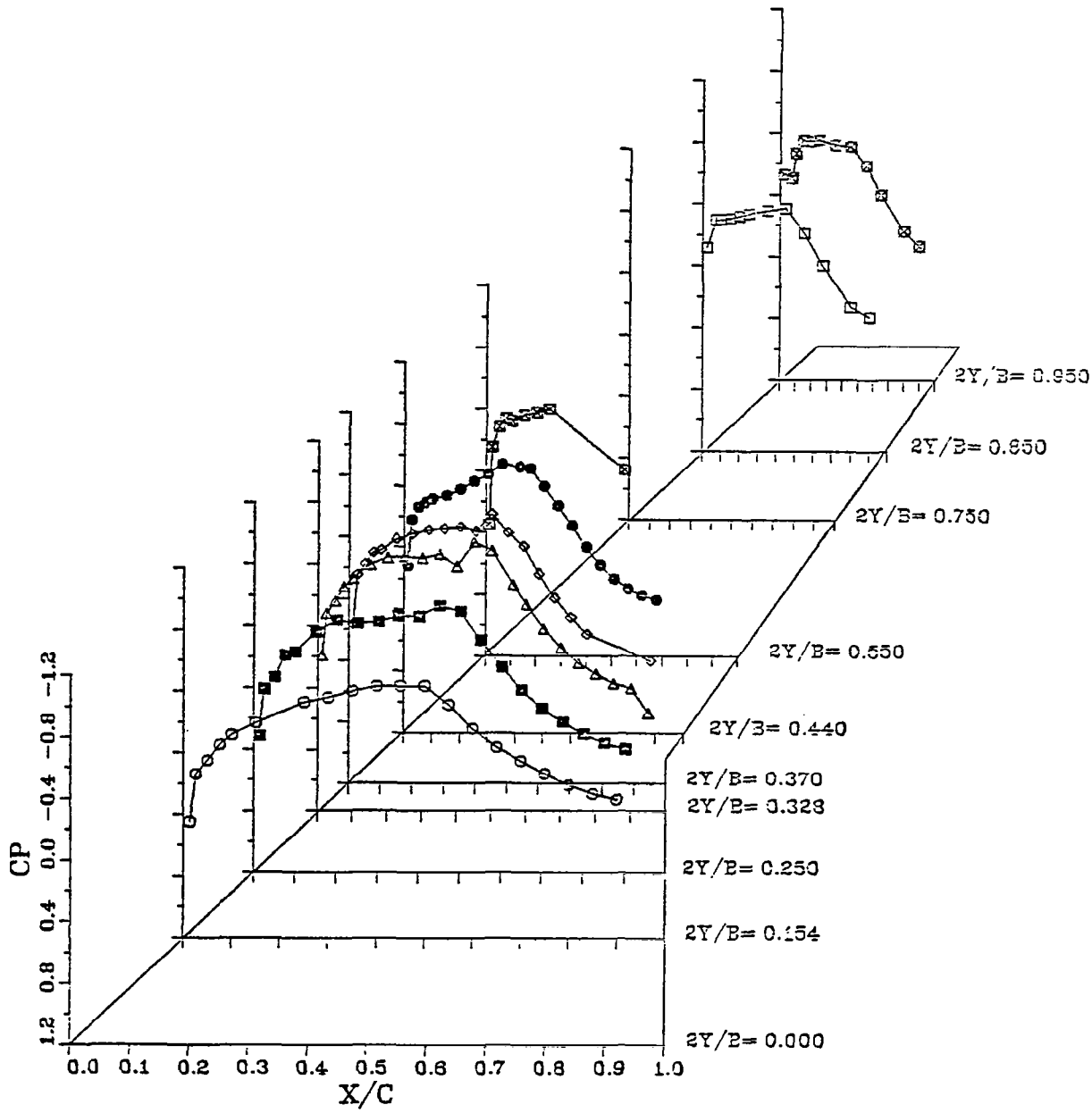

FIGURE A27a.

WING UPPER SURFACE PRESSURE DISTRIBUTION

D NACELLE / BASIC PYLON

MACH NUMBER = 0.850 CL = 0.4641

0.8533 DEG. ANGLE OF ATTACK

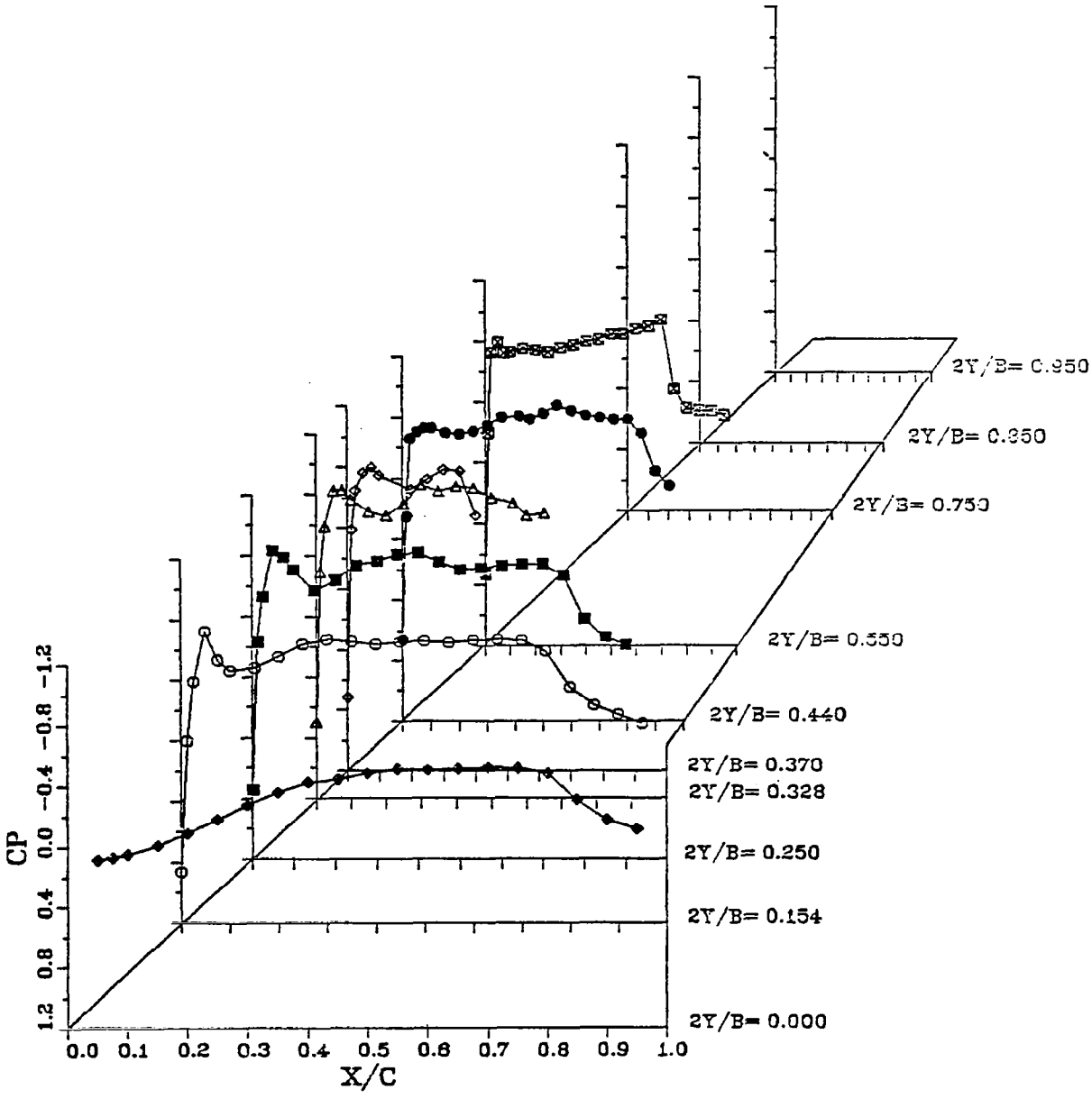

FIGURE A27b.

WING LOWER SURFACE PRESSURE DISTRIBUTION

D NACELLE / BASIC PYLON

MACH NUMBER = 0.850 CL = 0.4641

0.8533 DEG. ANGLE OF ATTACK

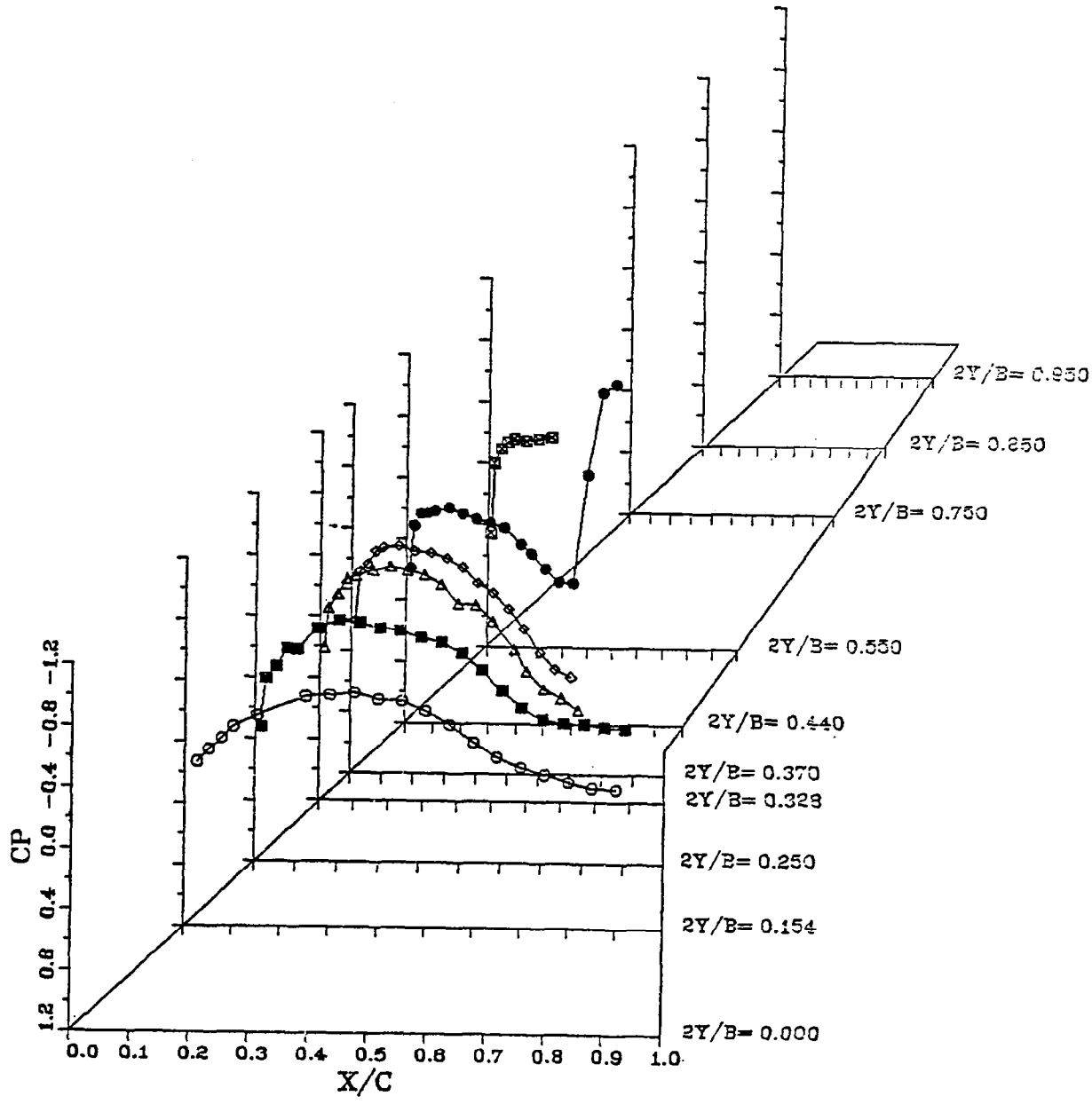

FIGURE A28a.

WING UPPER SURFACE PRESSURE DISTRIBUTION

C NACELLE / BASIC PYLON / REC DIV

MACH NUMBER = 0.850 CL = 0.4715

0.5949 DEG. ANGLE OF ATTACK

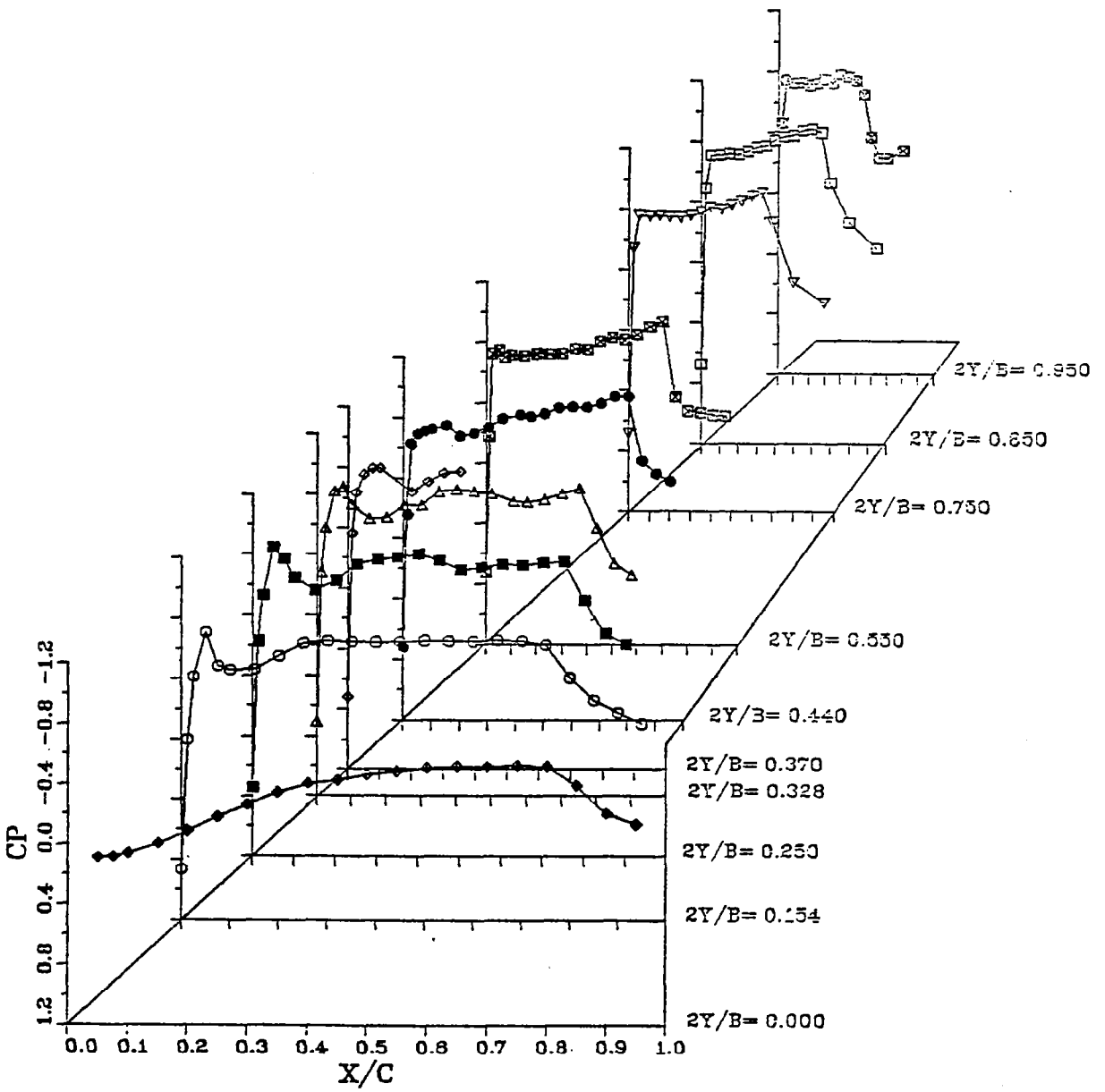

FIGURE A28b.

WING LOWER SURFACE PRESSURE DISTRIBUTION

C NACELLE / BASIC PYLON / REC DIV

MACH NUMBER = 0.850 CL = 0.4715

0.5949 DEG. ANGLE OF ATTACK

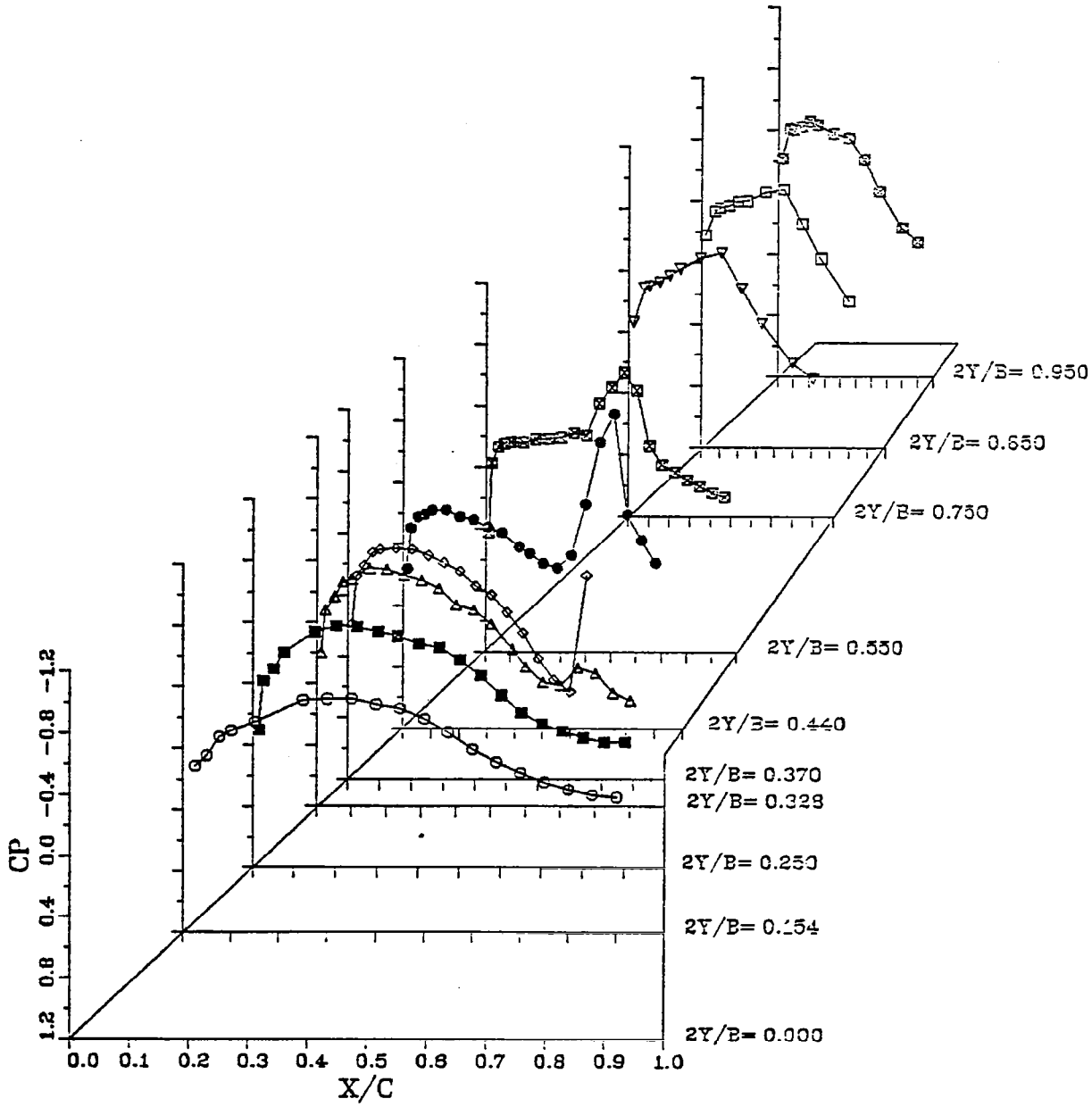

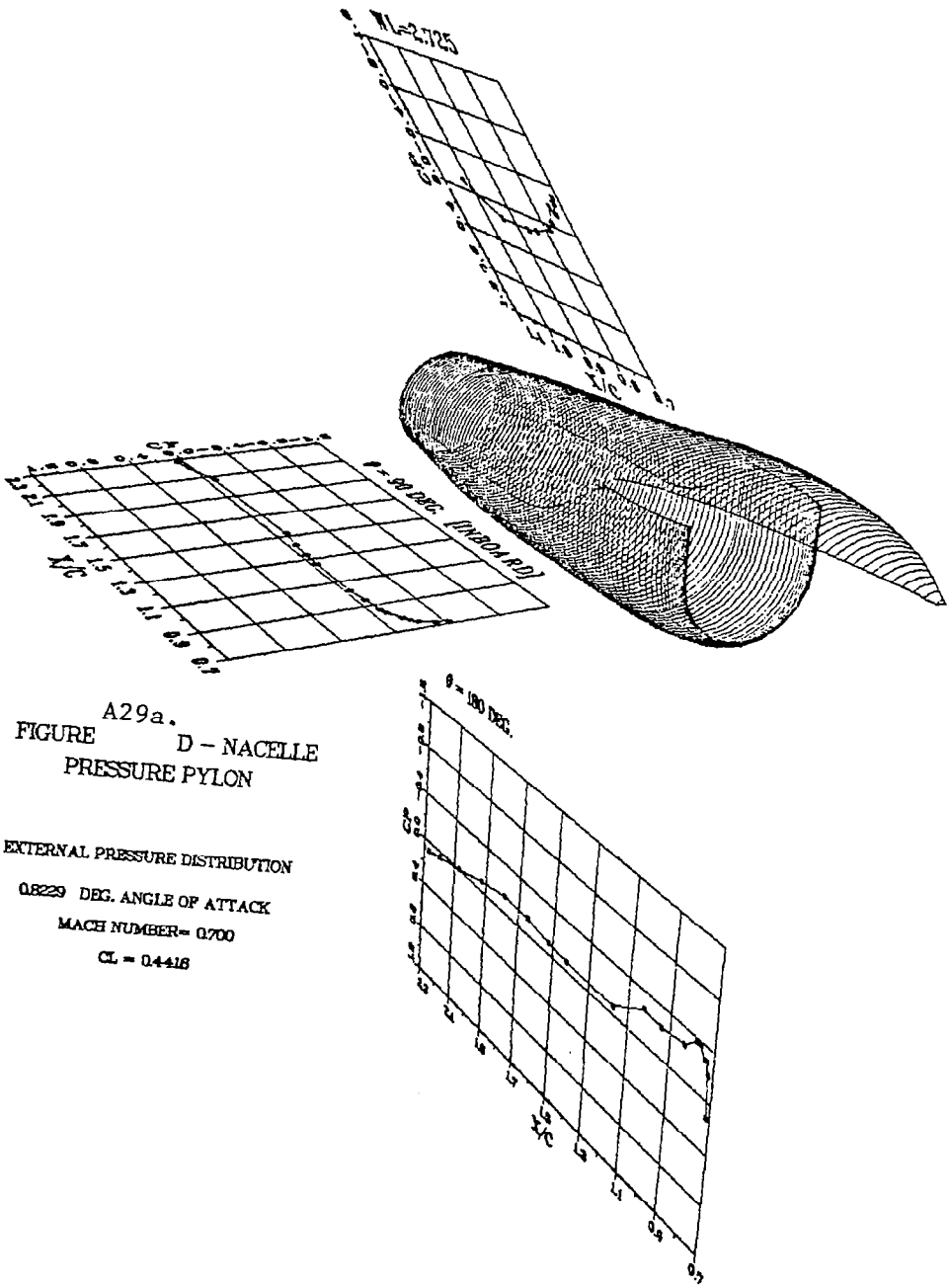

FIGURE A29a. D – NACELLE PRESSURE PYLON

EXTERNAL PRESSURE DISTRIBUTION

0.8229 DEG. ANGLE OF ATTACK

MACH NUMBER= 0.700

CL = 0.4418

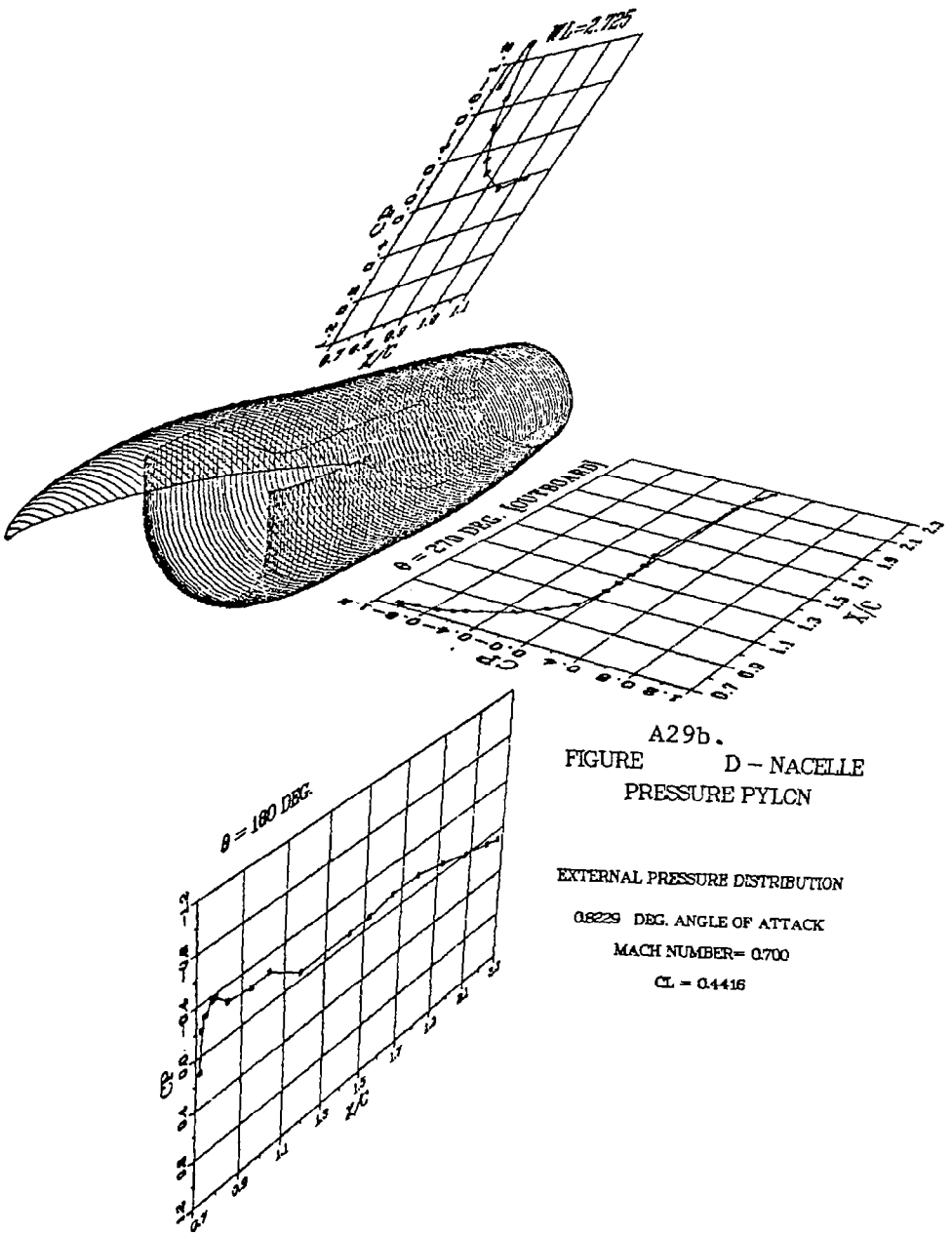

A29b.

FIGURE D – NACELLE PRESSURE PYLON

EXTERNAL PRESSURE DISTRIBUTION

0.8229 DEG. ANGLE OF ATTACK

MACH NUMBER= 0.700

CL = 0.4416

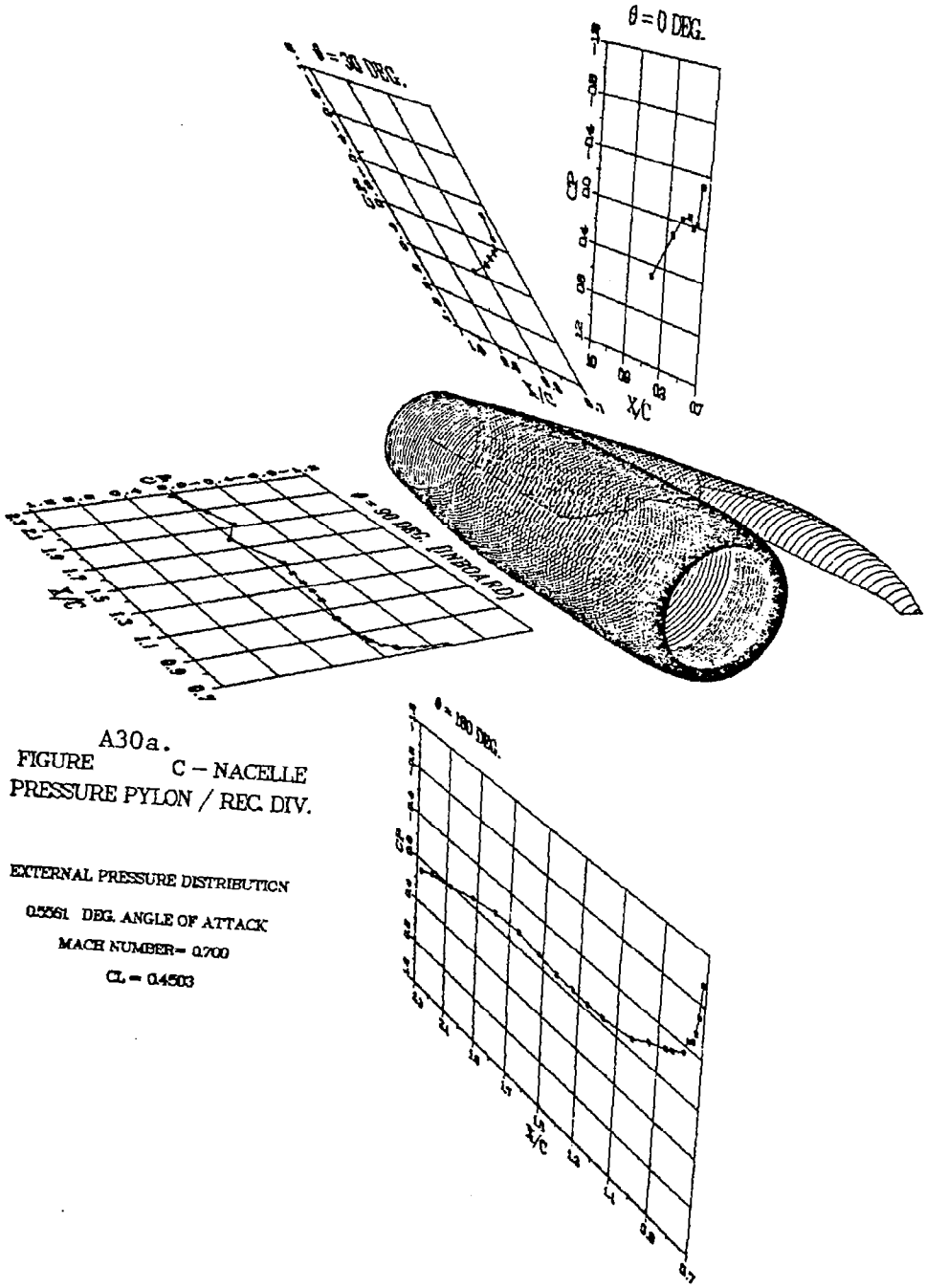

FIGURE A30a.
C – NACELLE
PRESSURE PYLON / REC. DIV.

EXTERNAL PRESSURE DISTRIBUTION

0.5561 DEG. ANGLE OF ATTACK

MACH NUMBER= 0.700

CL = 0.4503

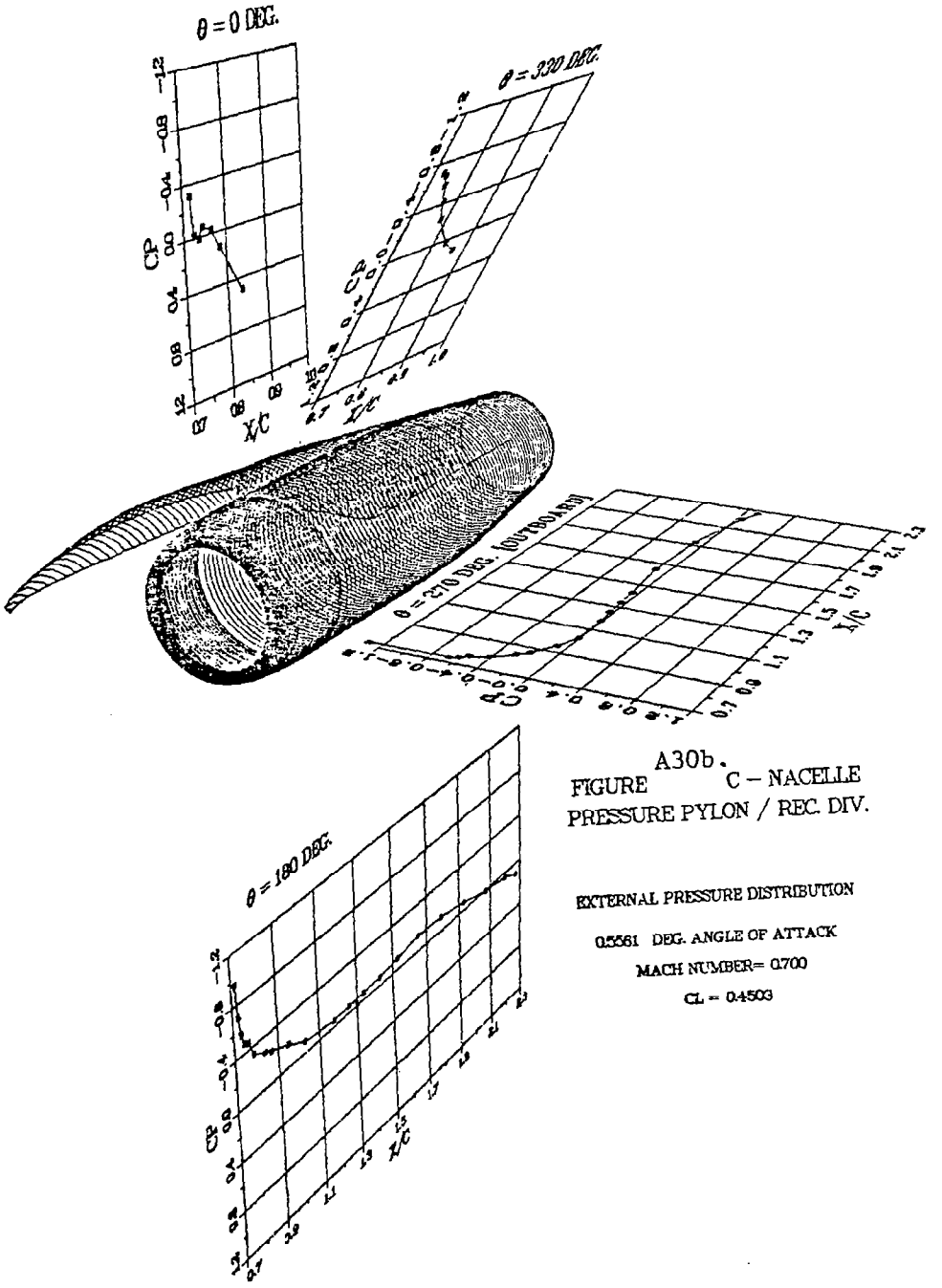

FIGURE A30b. C – NACELLE PRESSURE PYLON / REC. DIV.

EXTERNAL PRESSURE DISTRIBUTION

0.5561 DEG. ANGLE OF ATTACK

MACH NUMBER= 0.700

CL = 0.4503

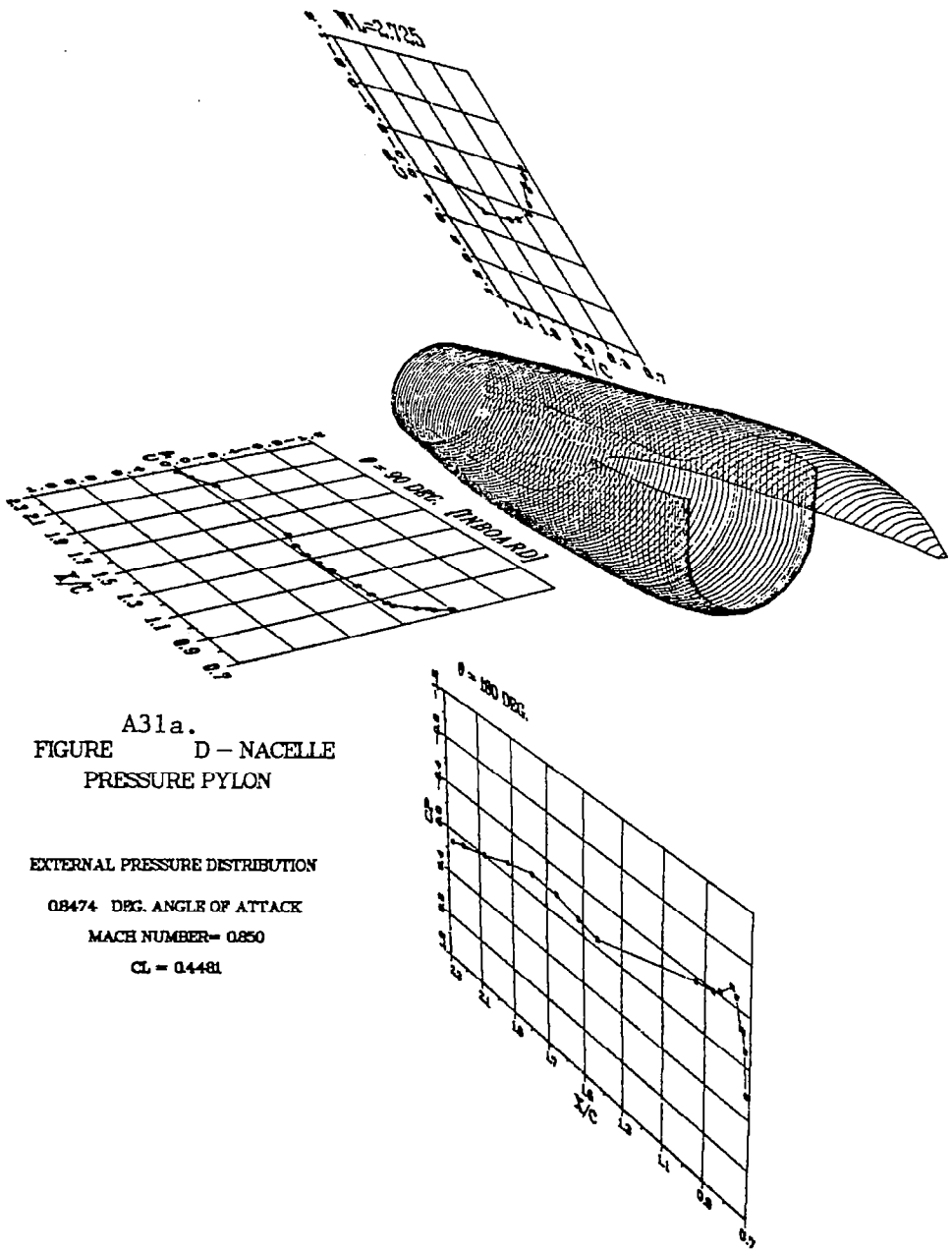

A31a.
FIGURE D – NACELLE
PRESSURE PYLON

EXTERNAL PRESSURE DISTRIBUTION

0.8474 DEG. ANGLE OF ATTACK

MACH NUMBER= 0.850

CL = 0.4481

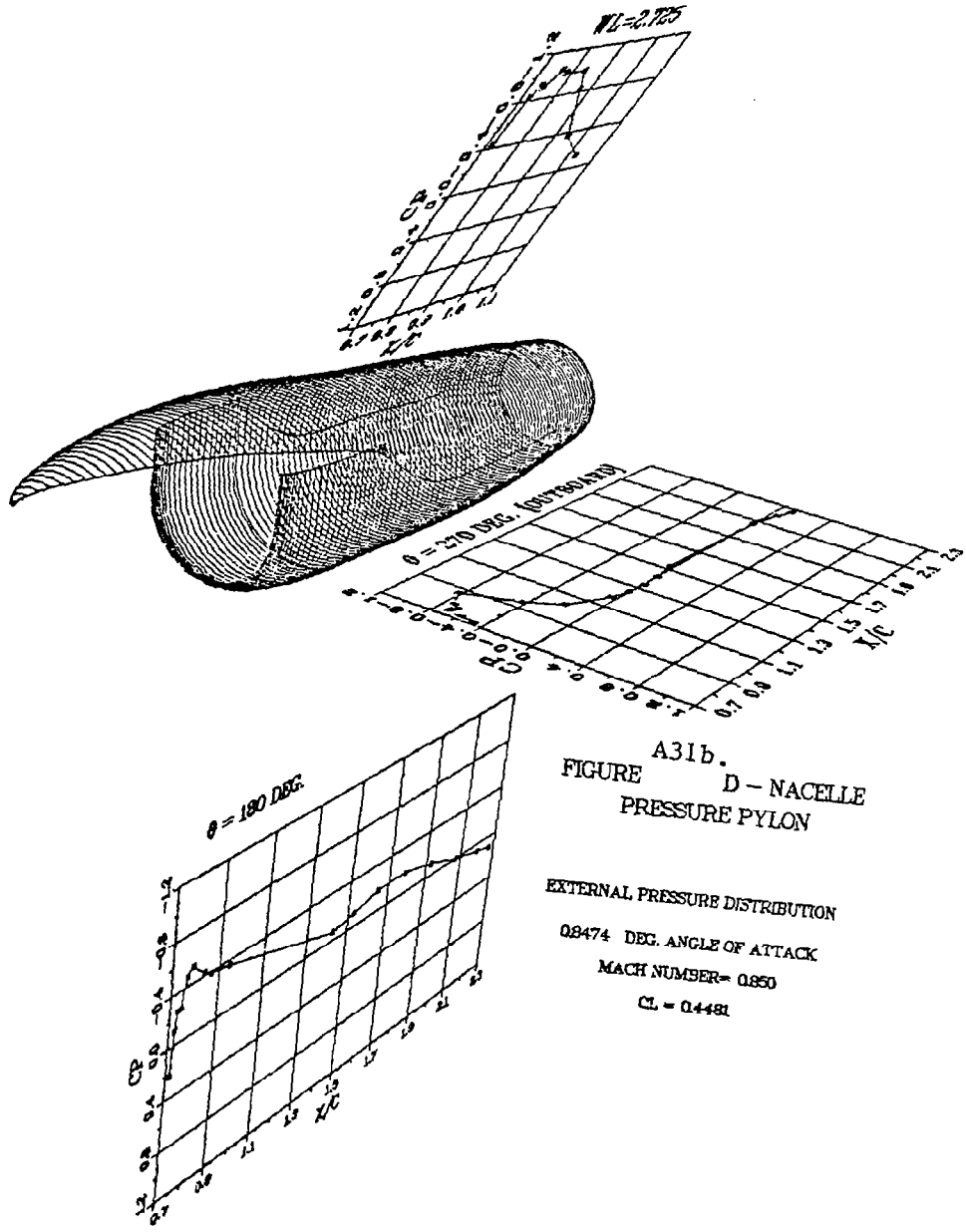

FIGURE A31b.
D – NACELLE
PRESSURE PYLON

EXTERNAL PRESSURE DISTRIBUTION

0.8474 DEG. ANGLE OF ATTACK

MACH NUMBER= 0.850

CL = 0.4481

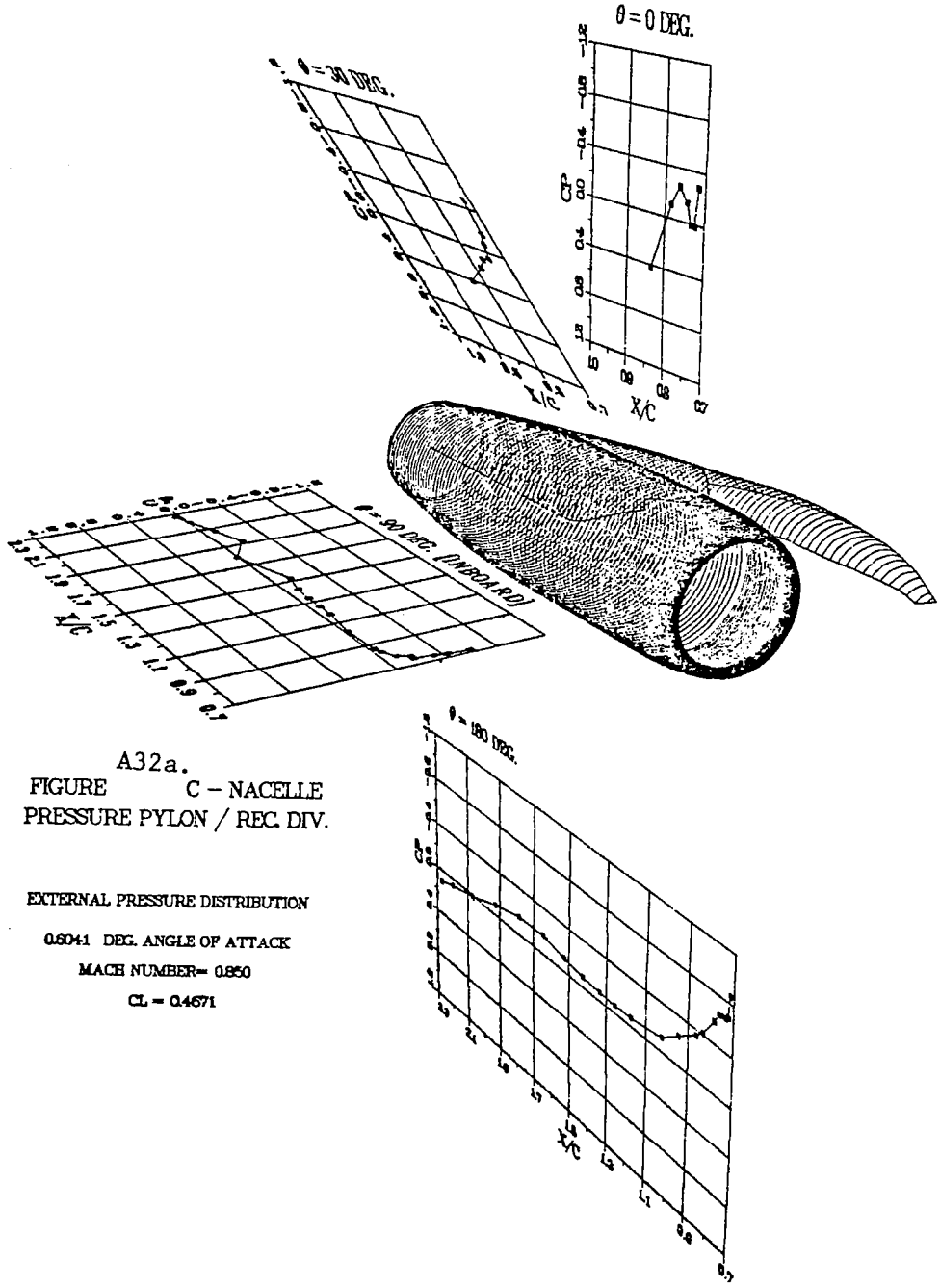

A32a.
FIGURE C – NACELLE
PRESSURE PYLON / REC. DIV.

EXTERNAL PRESSURE DISTRIBUTION

0.8041 DEG. ANGLE OF ATTACK

MACH NUMBER= 0.850

CL = 0.4671

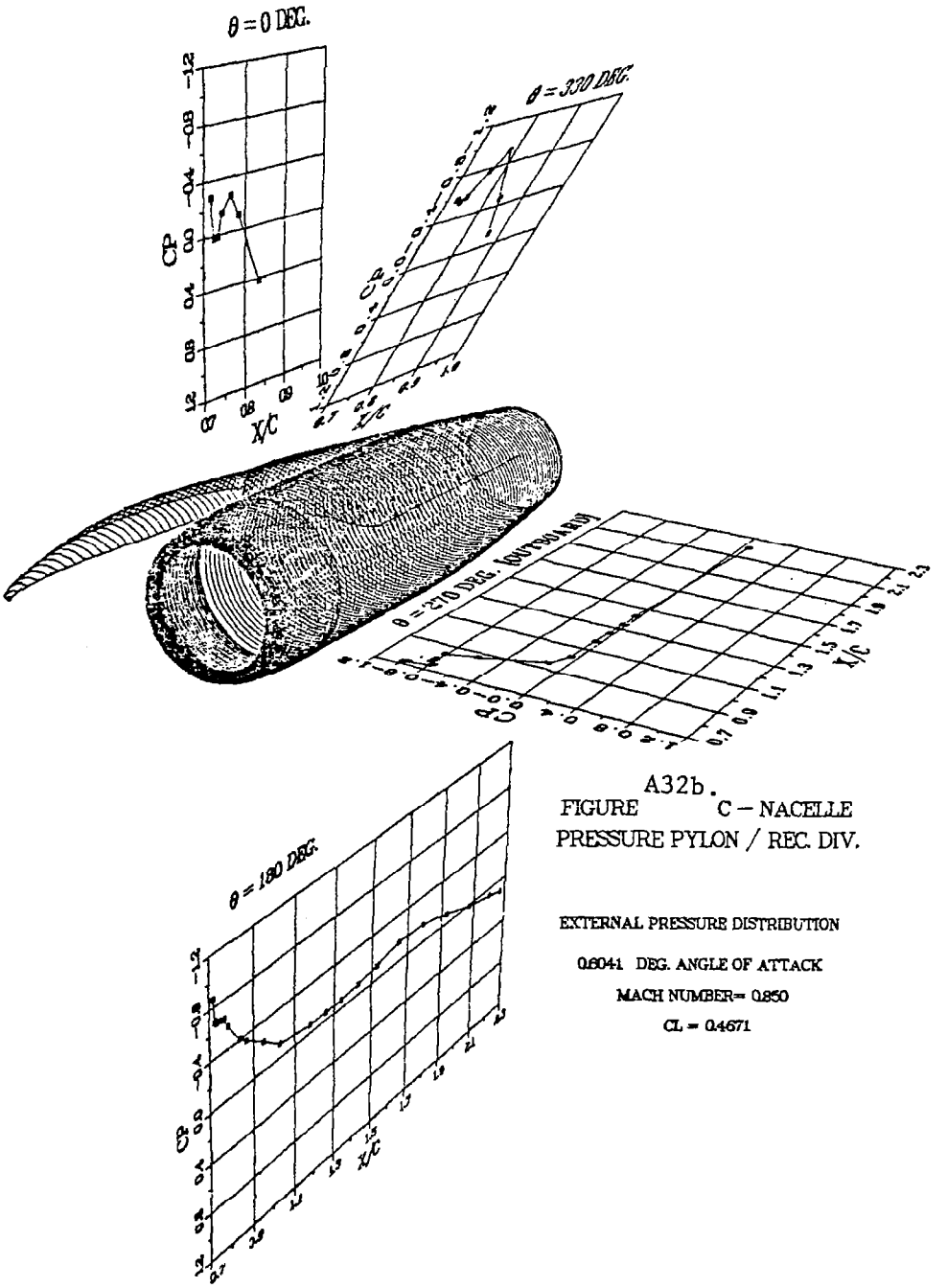

FIGURE A32b. C – NACELLE PRESSURE PYLON / REC. DIV.

EXTERNAL PRESSURE DISTRIBUTION

0.6041 DEG. ANGLE OF ATTACK

MACH NUMBER= 0.850

CL = 0.4671

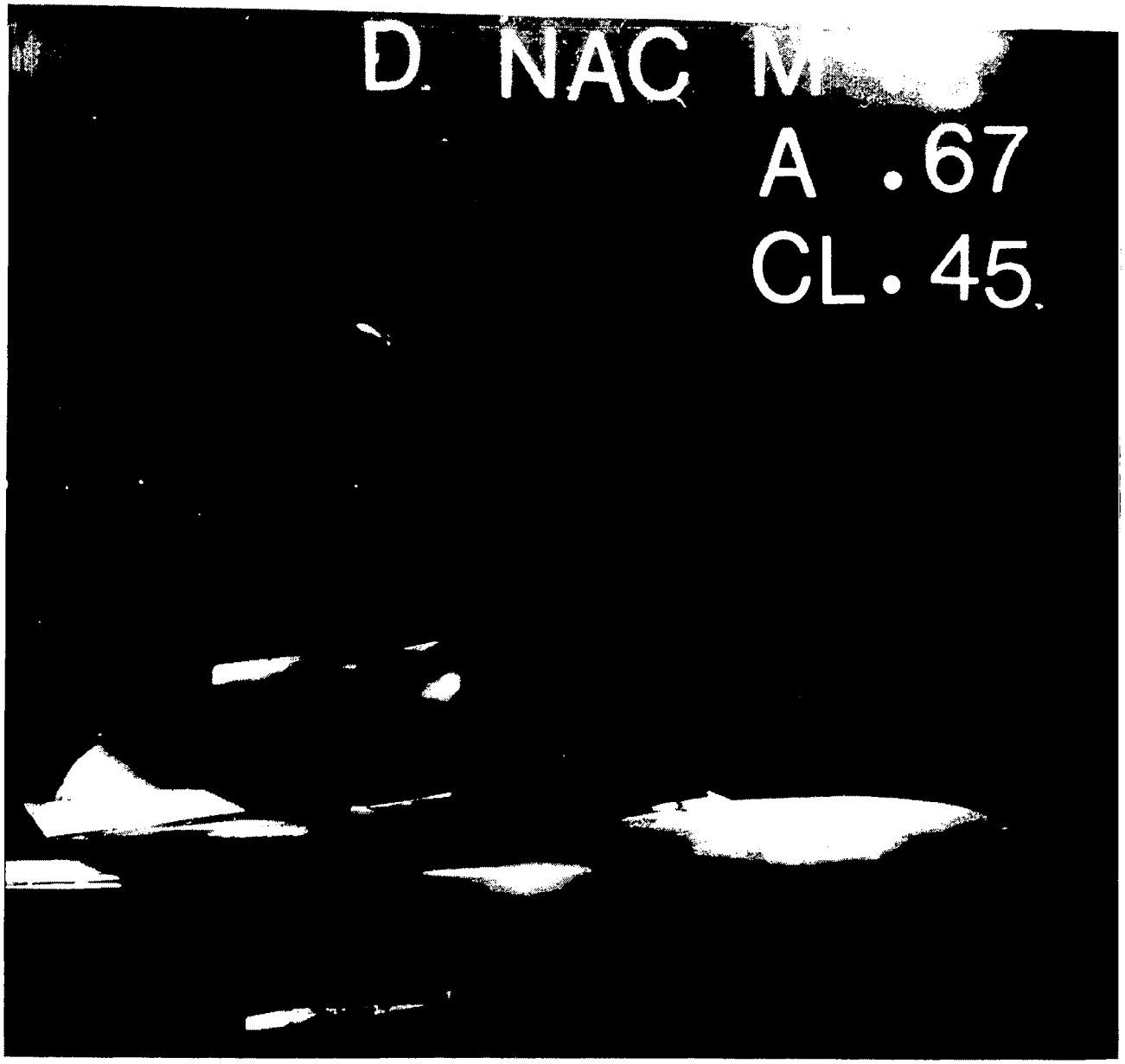

Figure A33a. - Oil flow photograph for D/BAS configuration at M=0.8, α=0.67°.

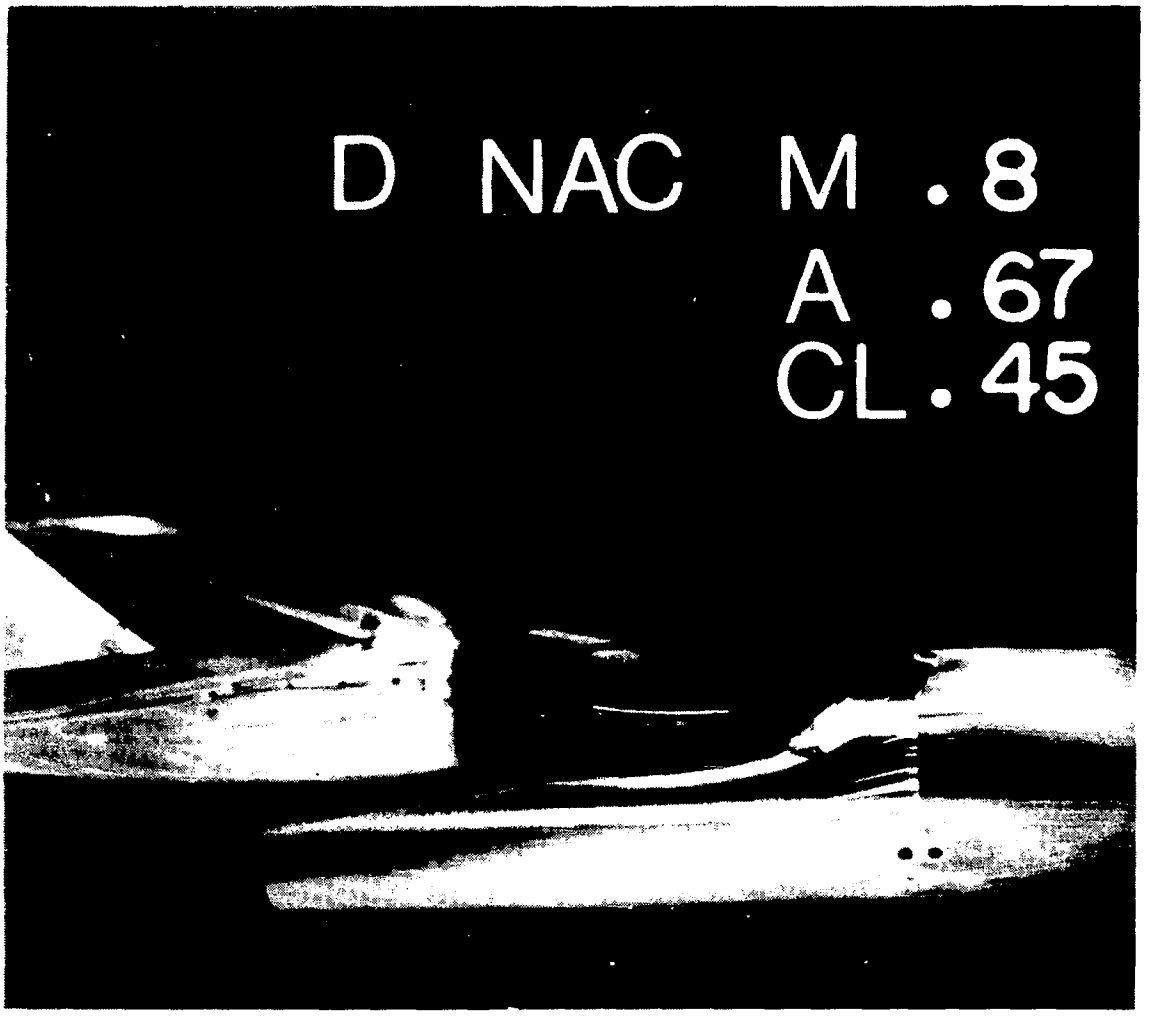

Figure A33b. - Oil flow photograph for D/BAS configuration at M=0.8, α=0.67°.

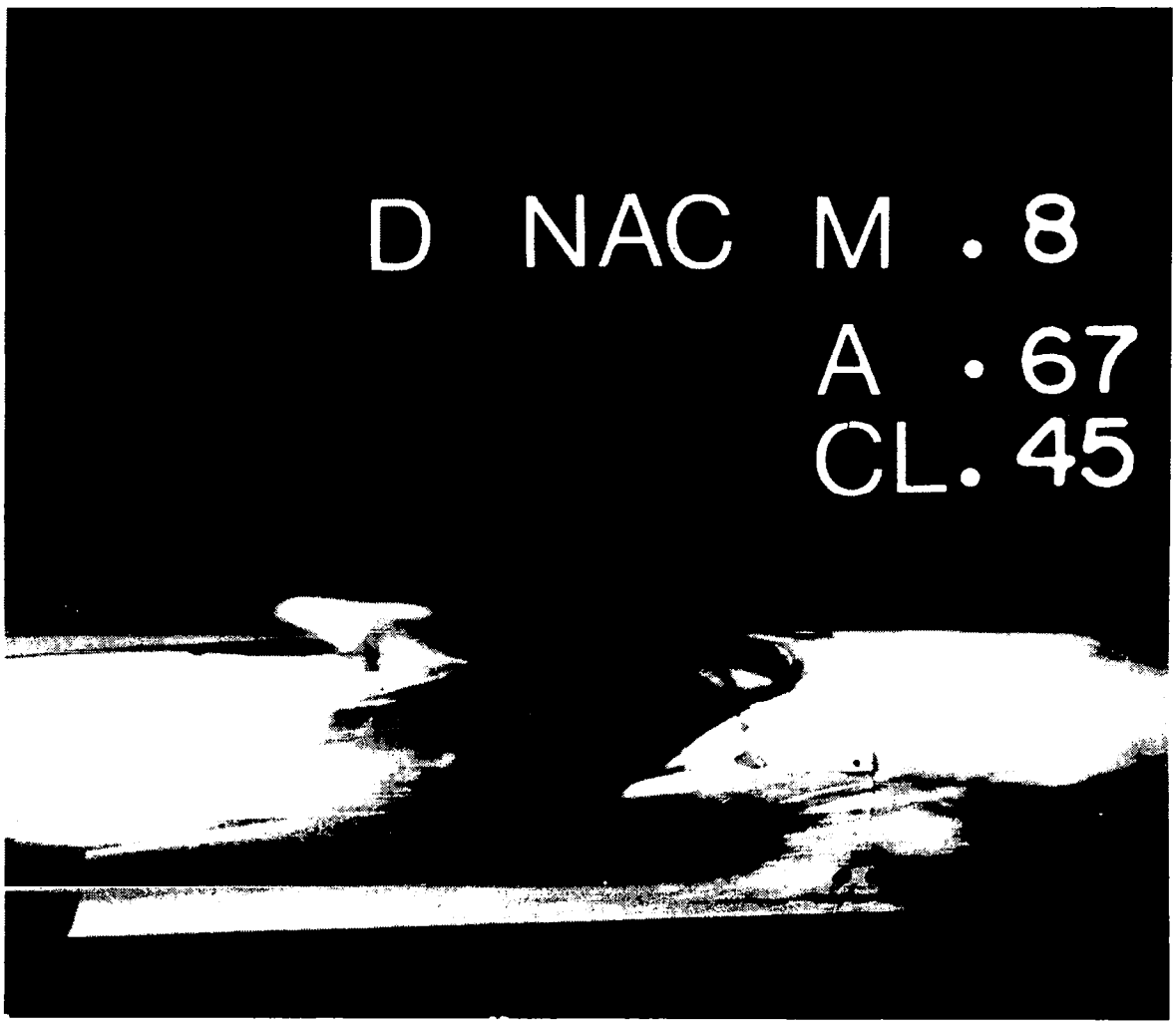

Figure A33c. - Oil flow photograph for D/BAS configuration at M=0.8, α=0.67°.

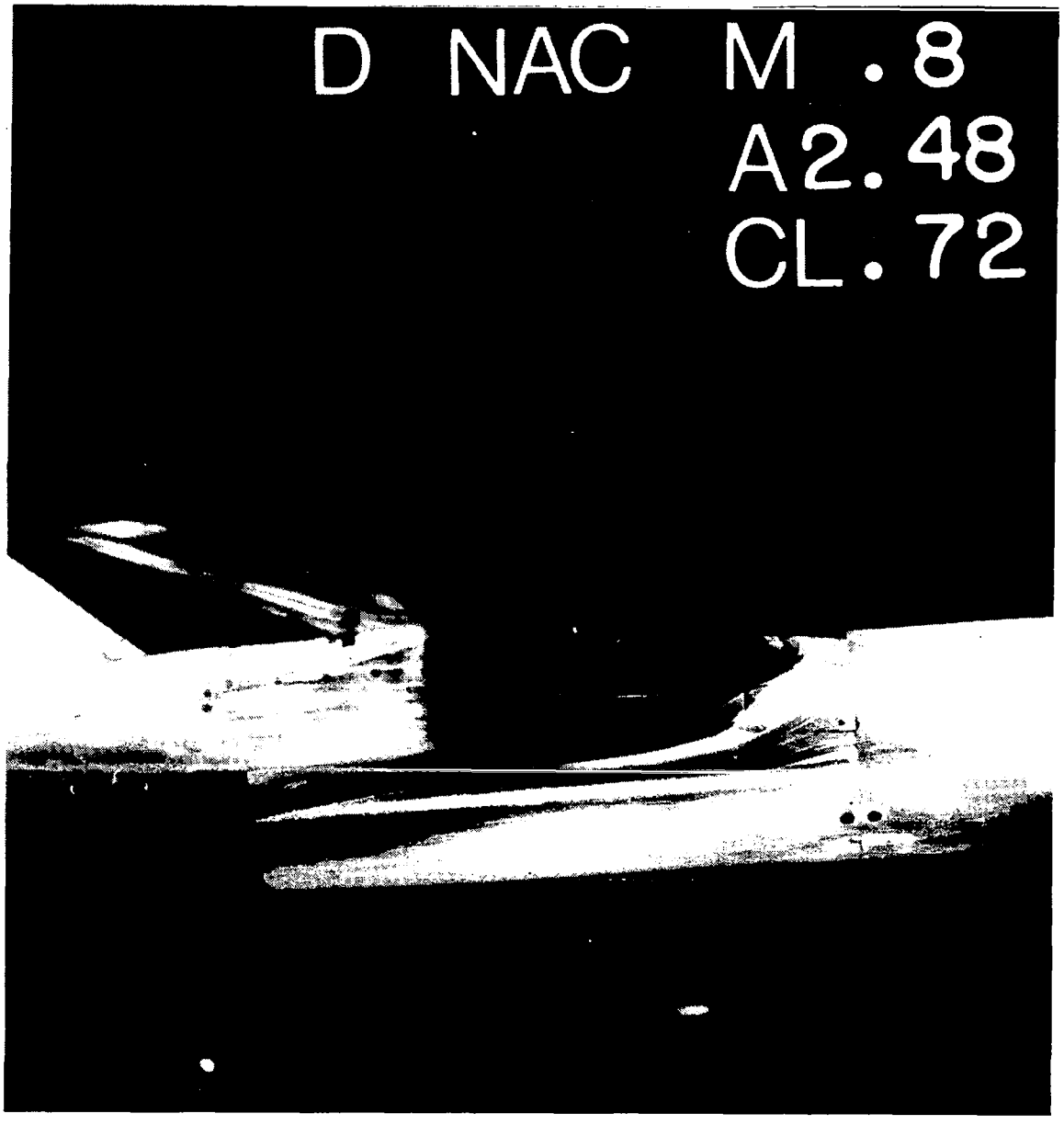

Figure A34a. - Oil flow photograph for D/BAS configuration at M=0.8, α=2.48^{o}.

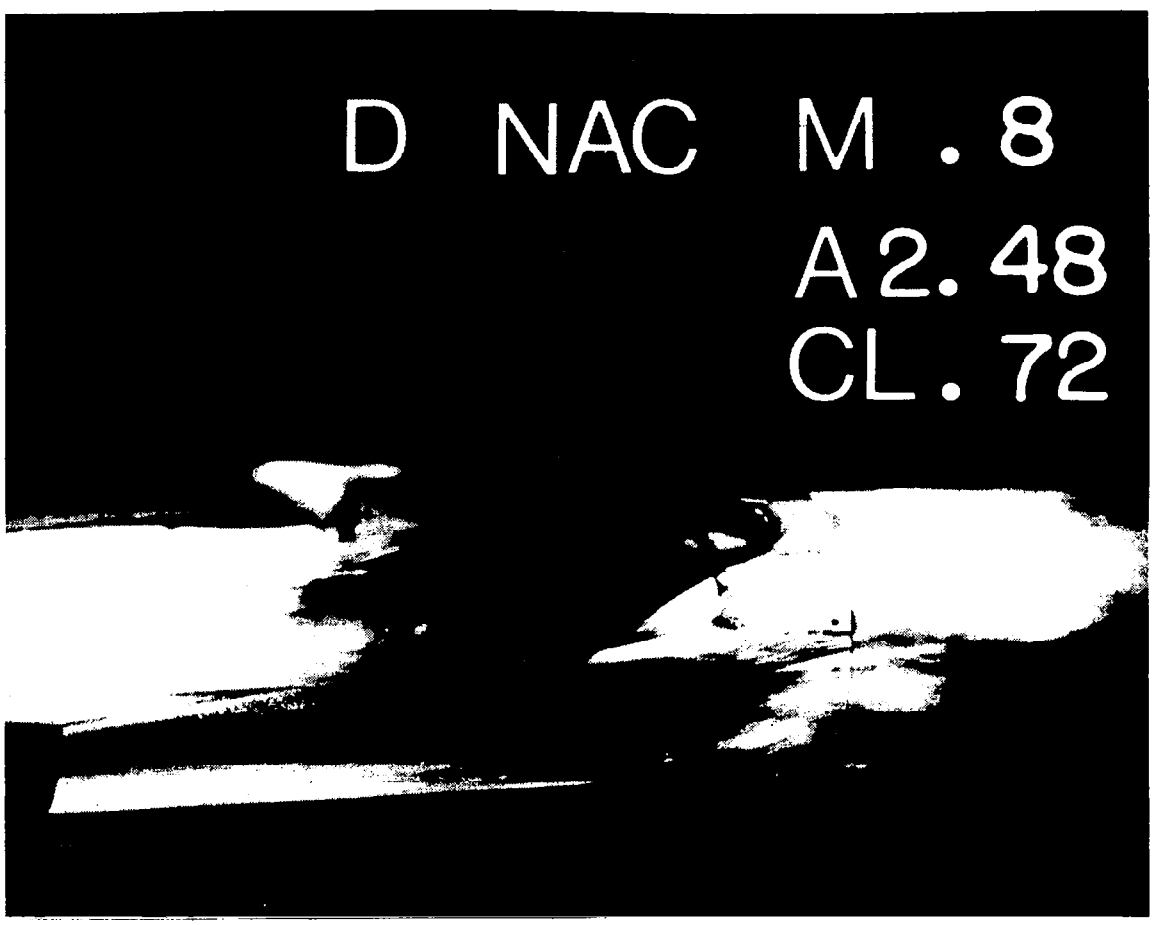

Figure A34b. - Oil flow photograph for D/BAS configuration at M=0.8, α=2.48°.

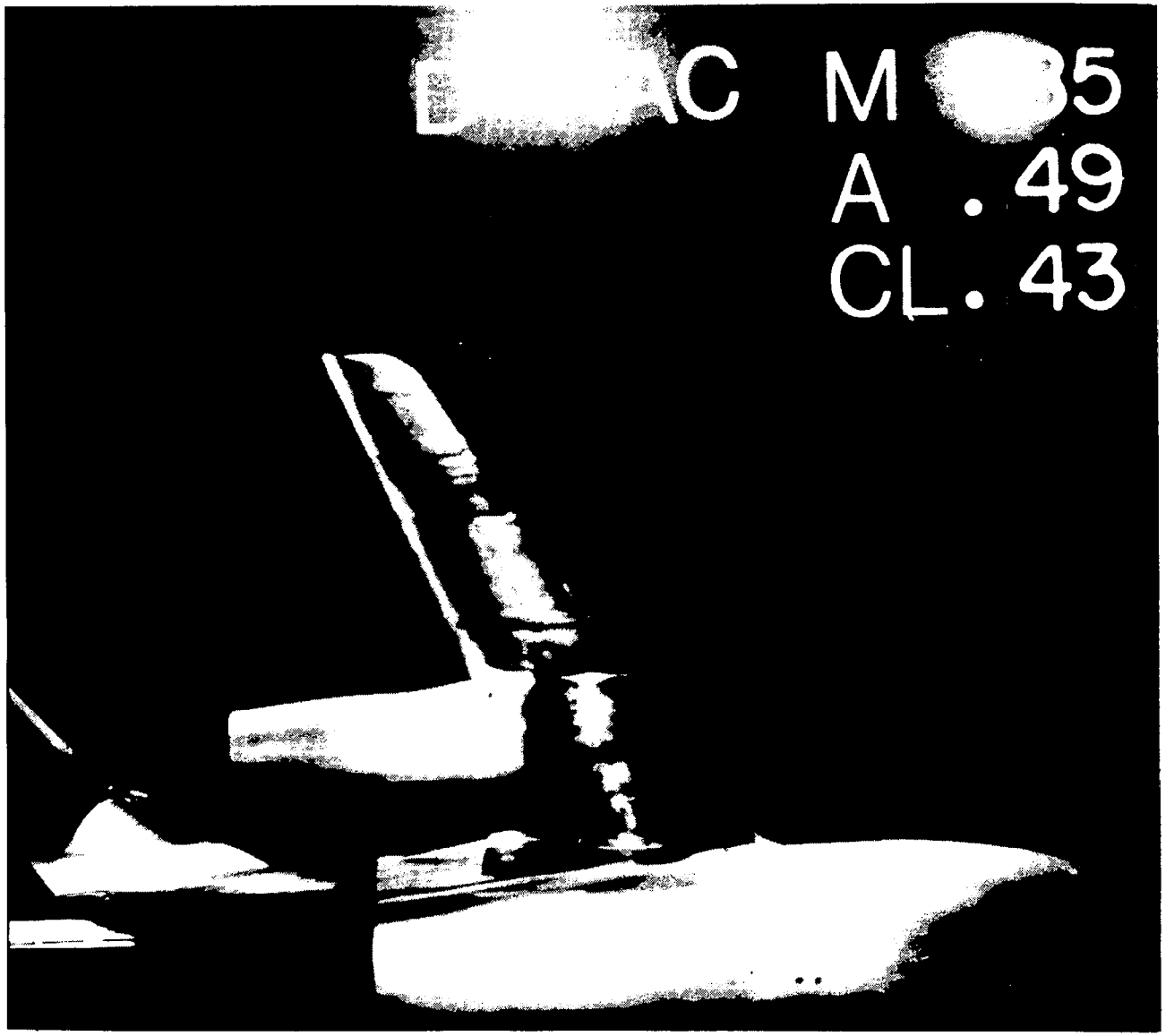

Figure A35. - Oil flow photograph for D/BAS configuration at M=0.85, α=0.49°.

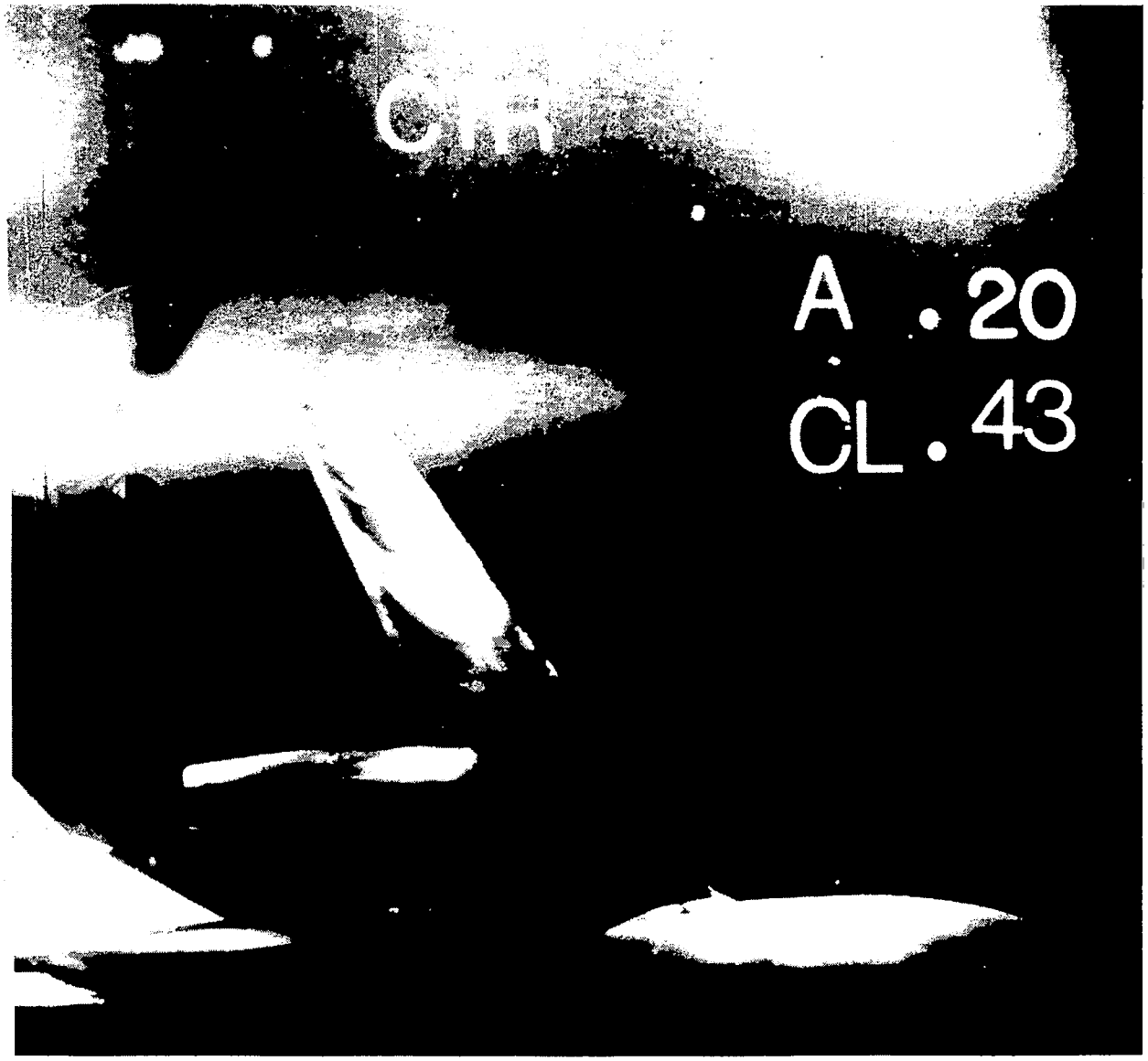

Figure A36a. - Oil flow photograph for C/BAS/REC configuration at M=0.8, α=0.20^{o}.

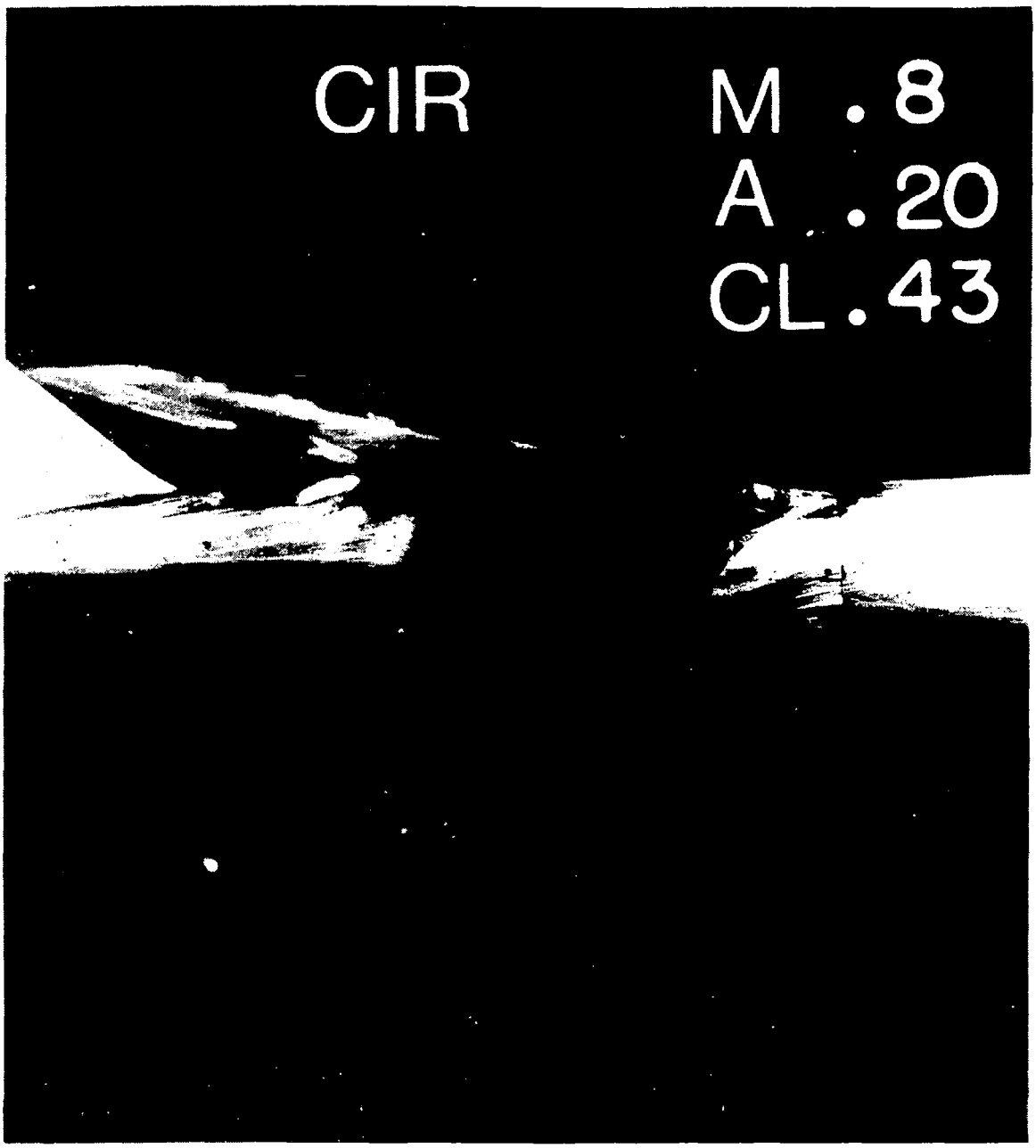

Figure A36b. - Oil flow photograph for C/BAS/REC configuration at M=0.8, α=0.20°.

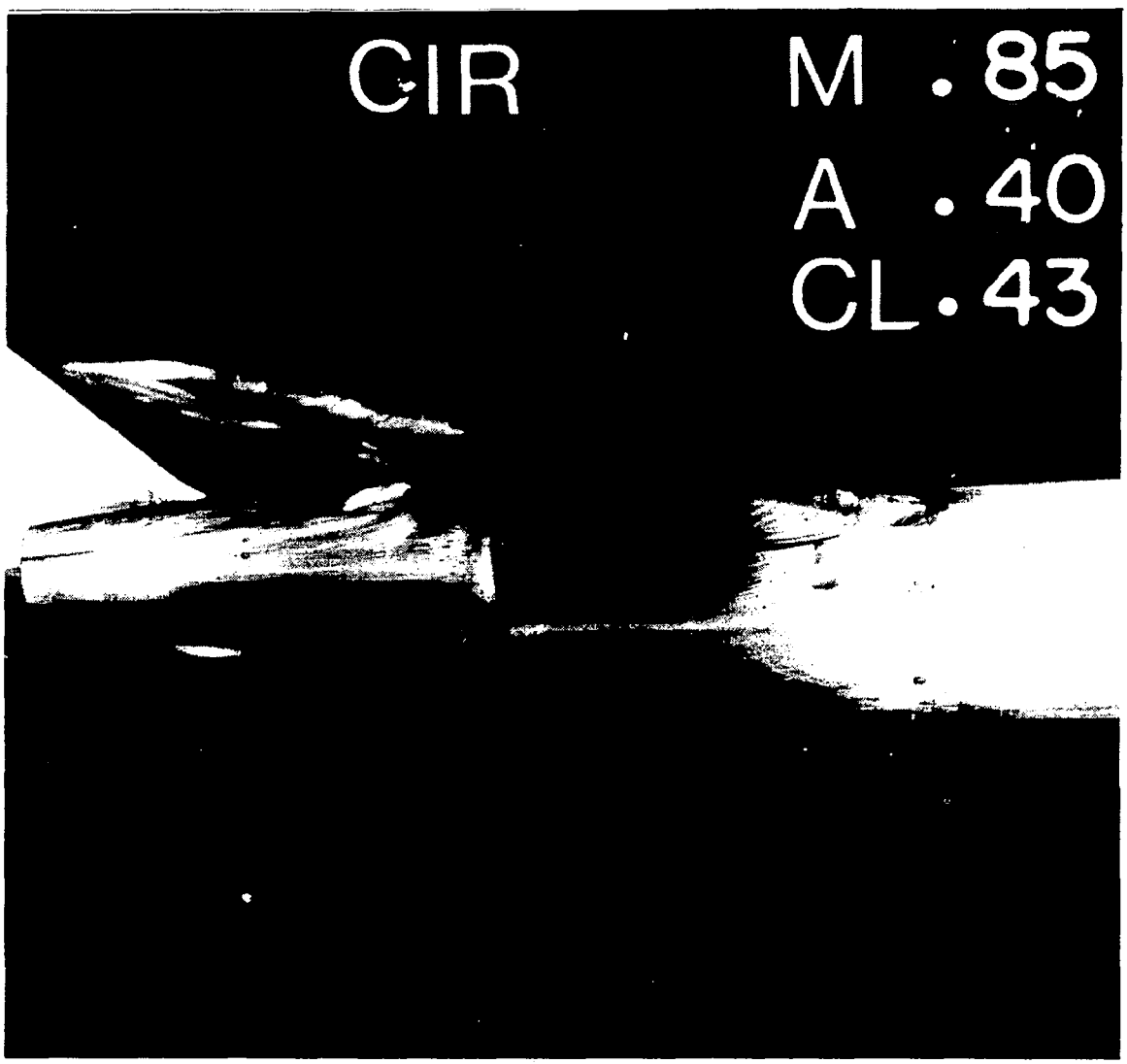

Figure A37a. - Oil flow photograph for C/BAS/REC configuration at M=0.85, α=0.40°.

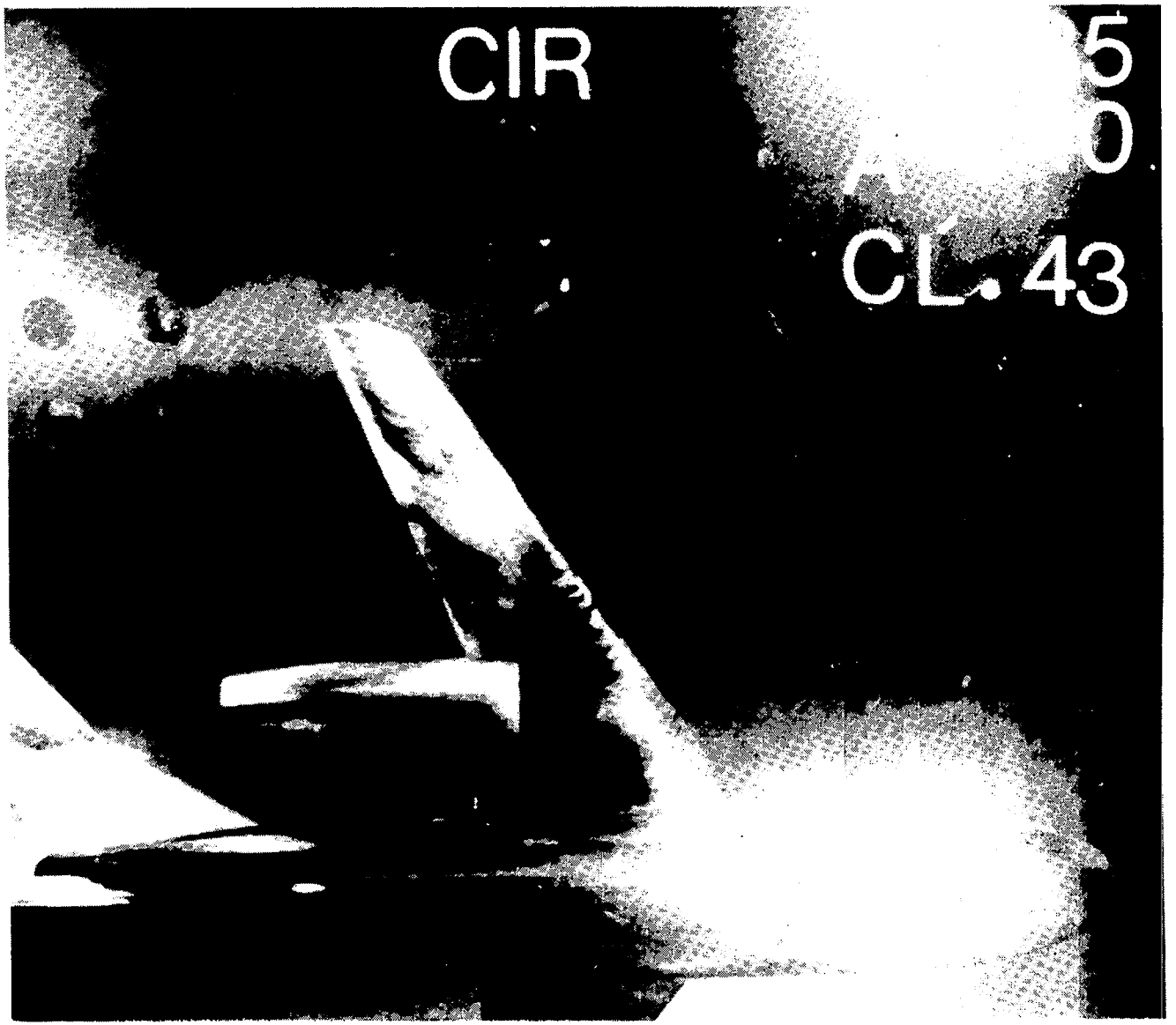

Figure A37b. - Oil flow photograph for C/BAS/REC configuration at M=0.85, α=0.40°.

FIGURE A38. LIFT COEFFICIENT VERSUS ANGLE OF ATTACK AT M=0.70 FOR WB, D/BAS, C/BAS/REC, C/BAS/HL AND UTW CONFIGURATIONS

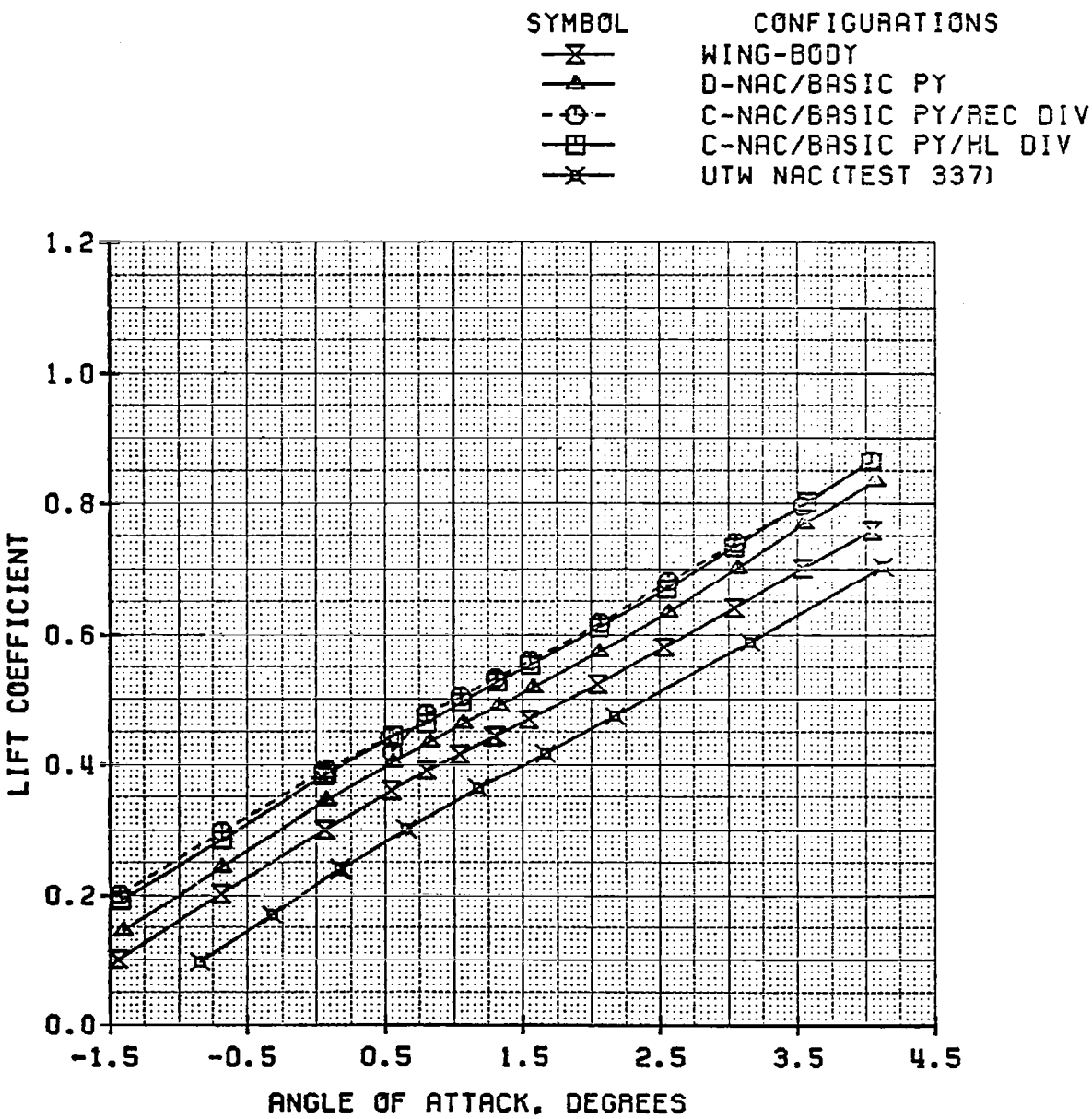

FIGURE A39. LIFT COEFFICIENT VERSUS ANGLE OF ATTACK AT MACH 0.70 FOR WB, D/BAS, D/PRES AND C/PRES/REC CONFIGURATIONS

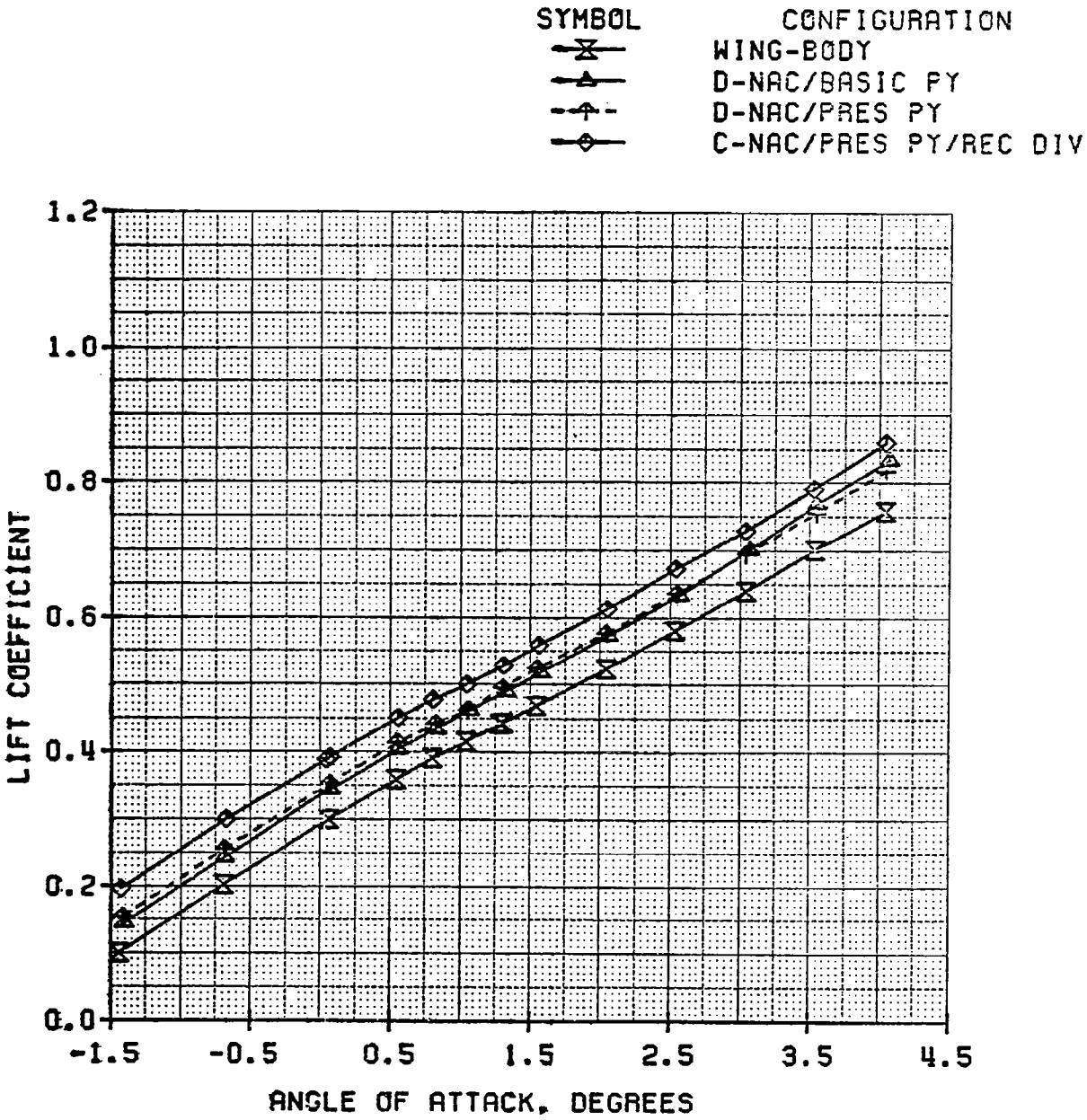

FIGURE A40. LIFT COEFFICIENT VERSUS ANGLE OF ATTACK

AT M=0.75 FOR WB, D/BAS, C/BAS/REC,

C/BAS/HL AND UTW CONFIGURATIONS

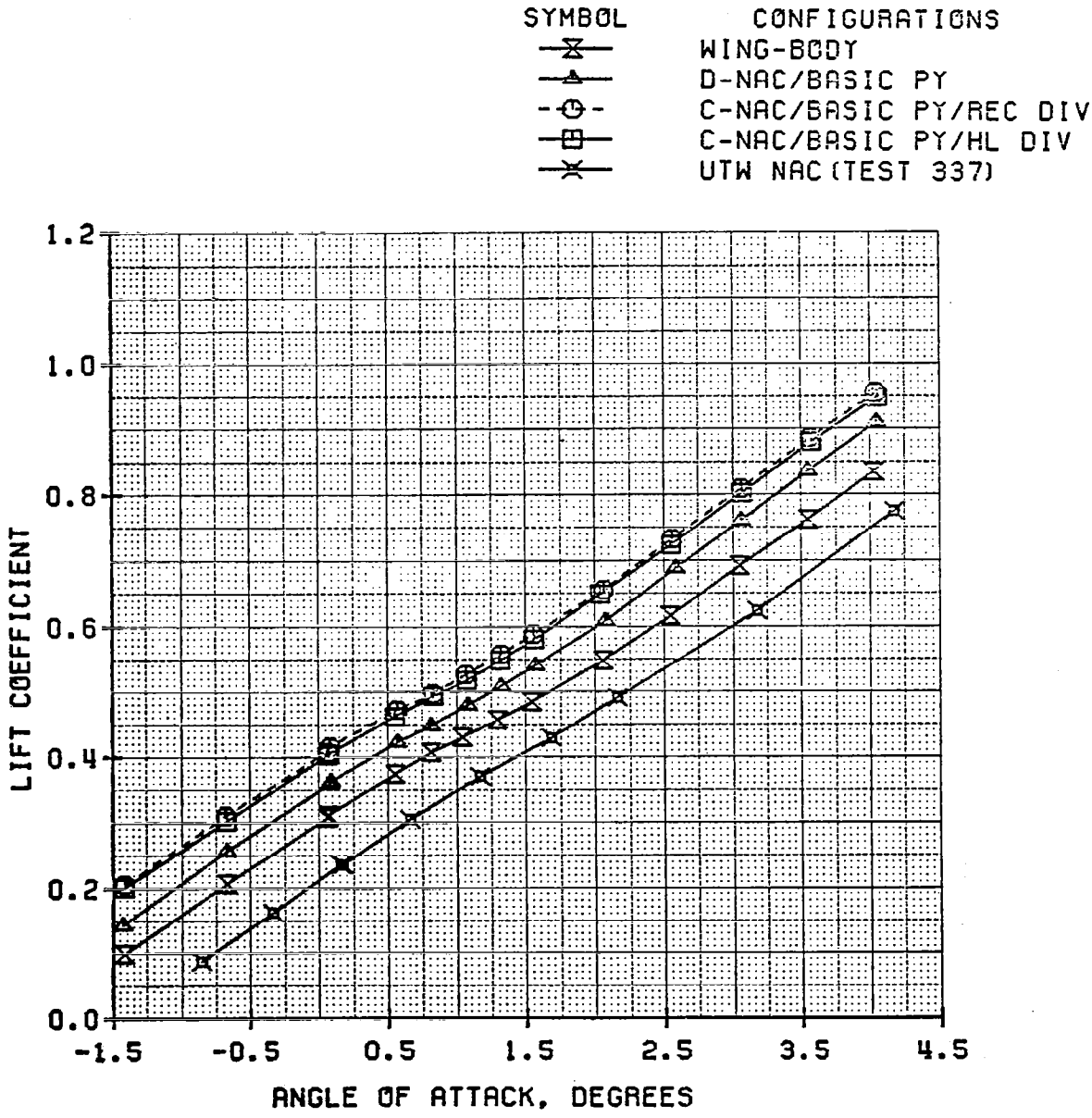

FIGURE A41. LIFT COEFFICIENT VERSUS ANGLE OF ATTACK

AT MACH 0.75 FOR WB, D/BAS, D/PRES

AND C/PRES/REC CONFIGURATIONS

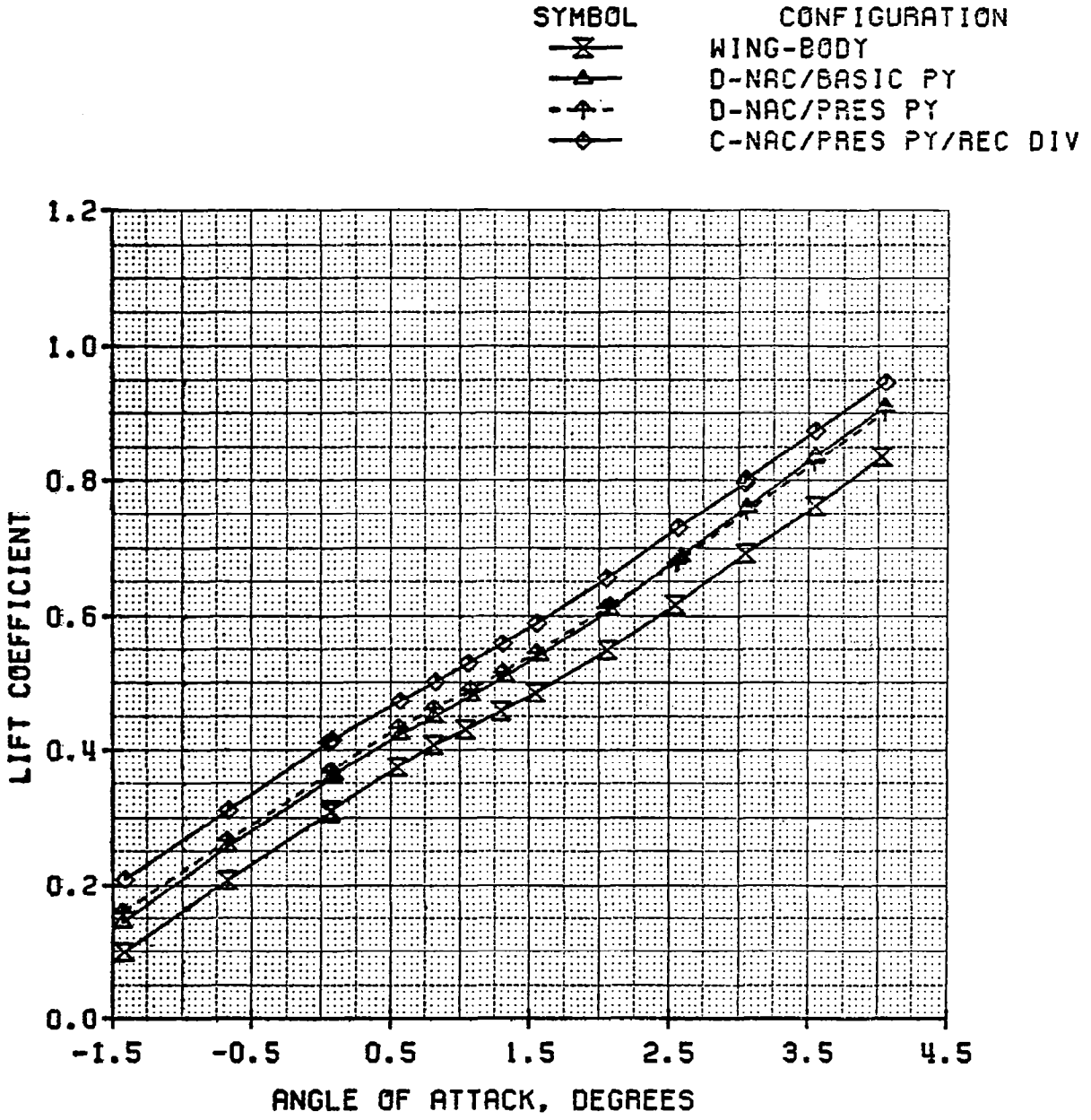

FIGURE A42. LIFT COEFFICIENT VERSUS ANGLE OF ATTACK AT M=0.78 FOR WB, D/BAS, C/BAS/REC, C/BAS/HL AND UTW CONFIGURATIONS

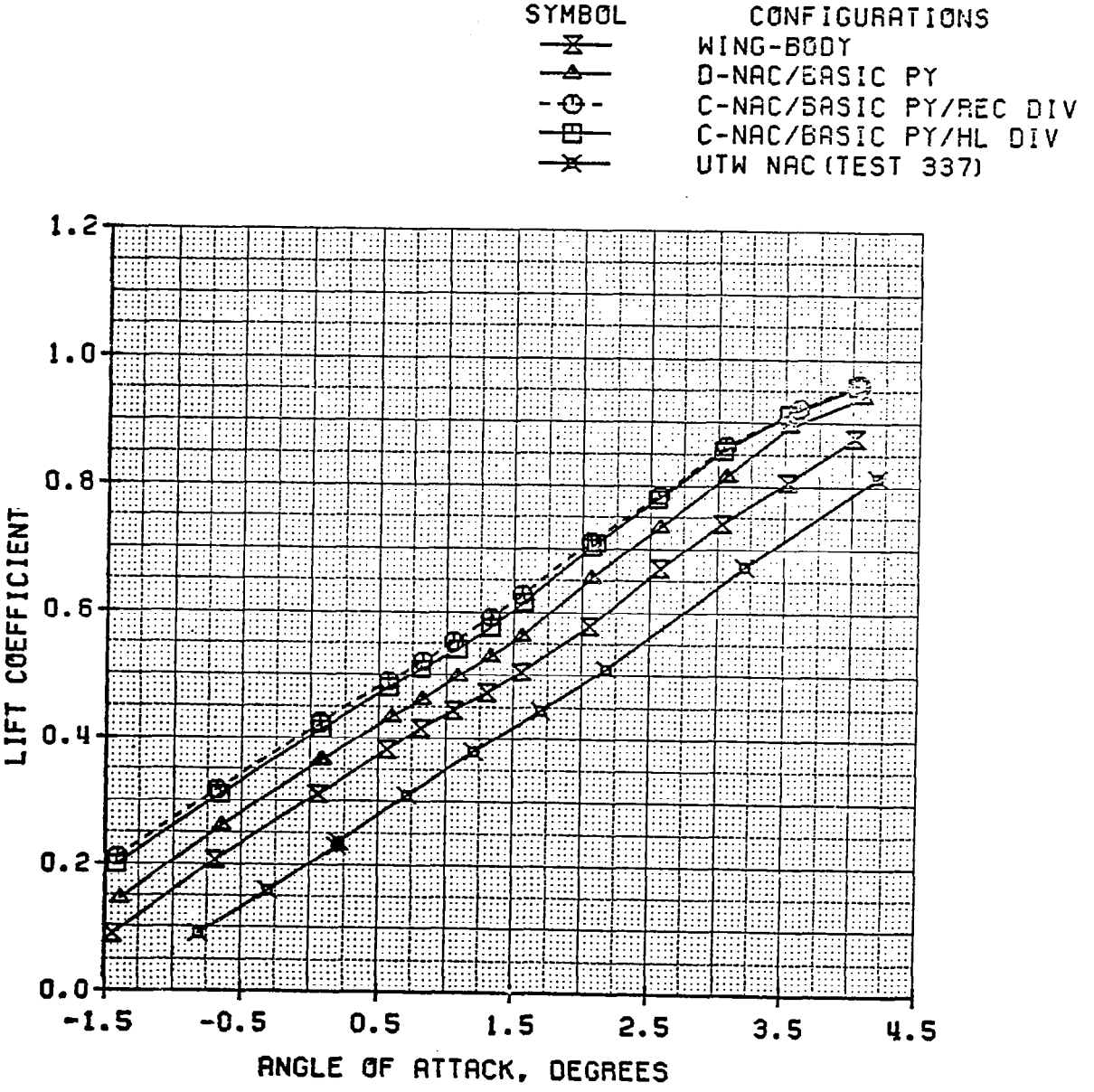

FIGURE A43. LIFT COEFFICIENT VERSUS ANGLE OF ATTACK

AT MACH 0.78 FOR WB, D/BAS, D/PRES

AND C/PRES/REC CONFIGURATIONS

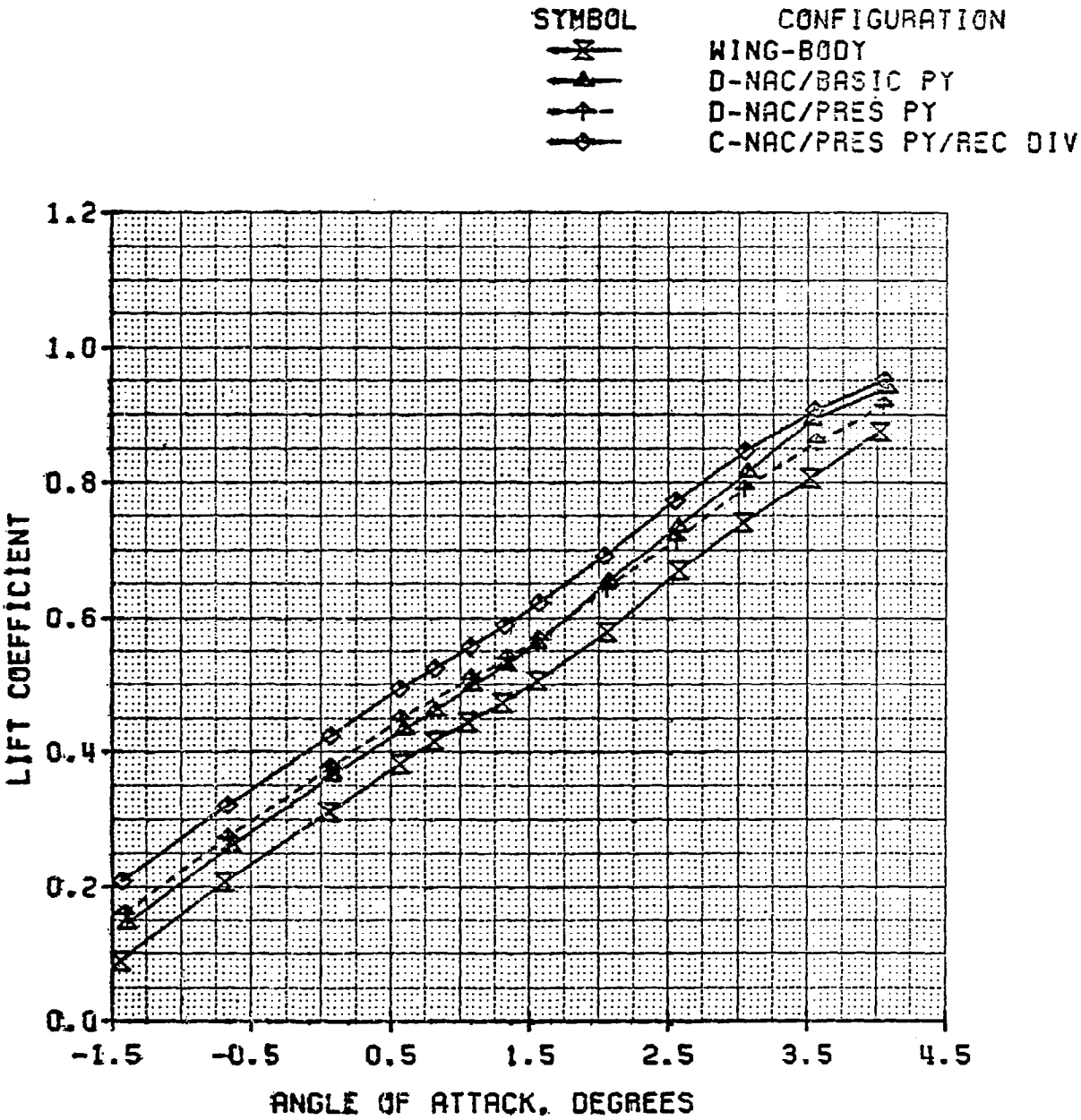

FIGURE A44. LIFT COEFFICIENT VERSUS ANGLE OF ATTACK

AT M=0.79 FOR WB, D/BAS, C/BAS/REC,

C/BAS/HL AND UTW CONFIGURATIONS

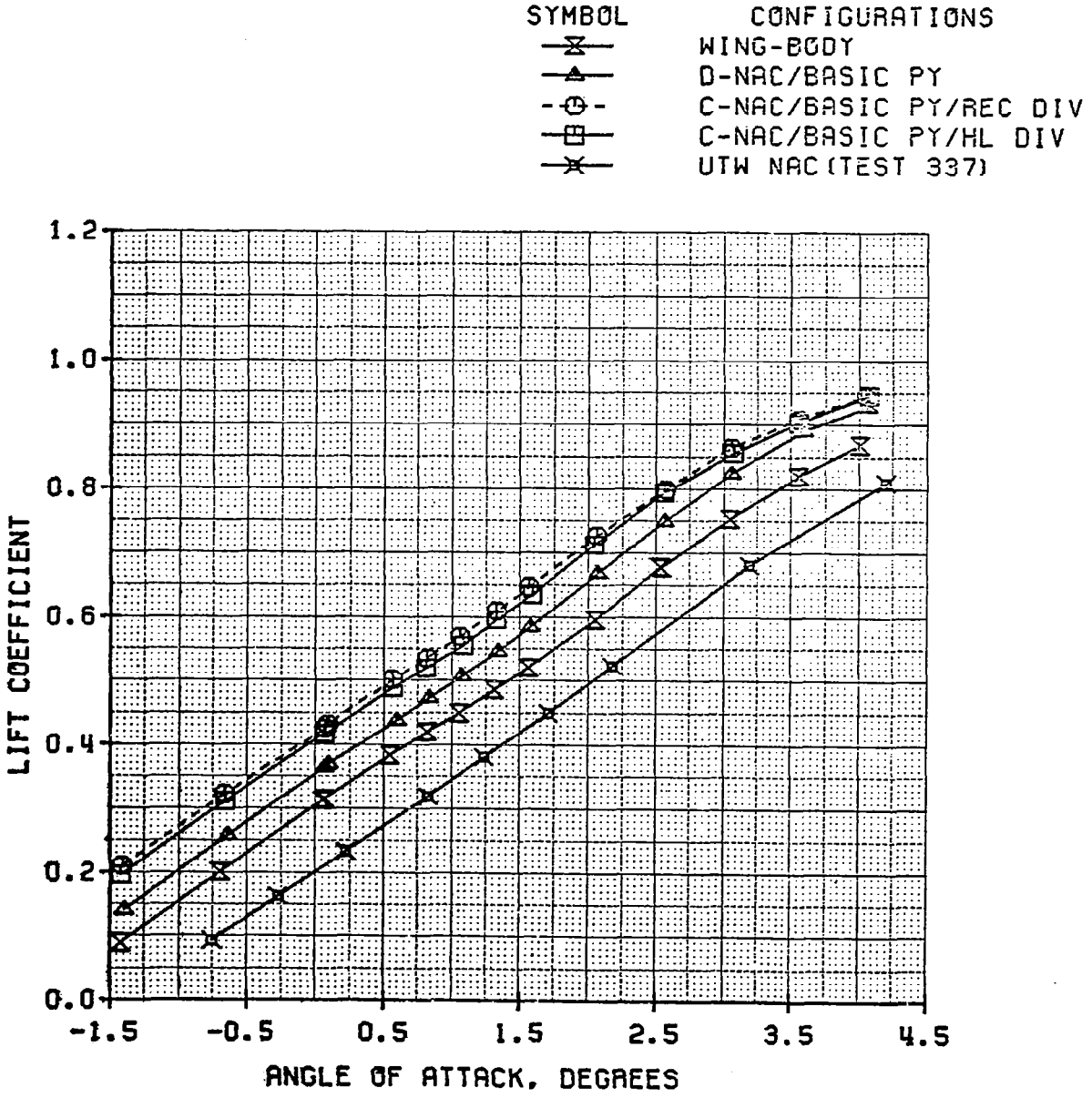

FIGURE A45. LIFT COEFFICIENT VERSUS ANGLE OF ATTACK

AT MACH 0.79 FOR WB, D/BAS, D/PRES

AND C/PRES/REC CONFIGURATIONS

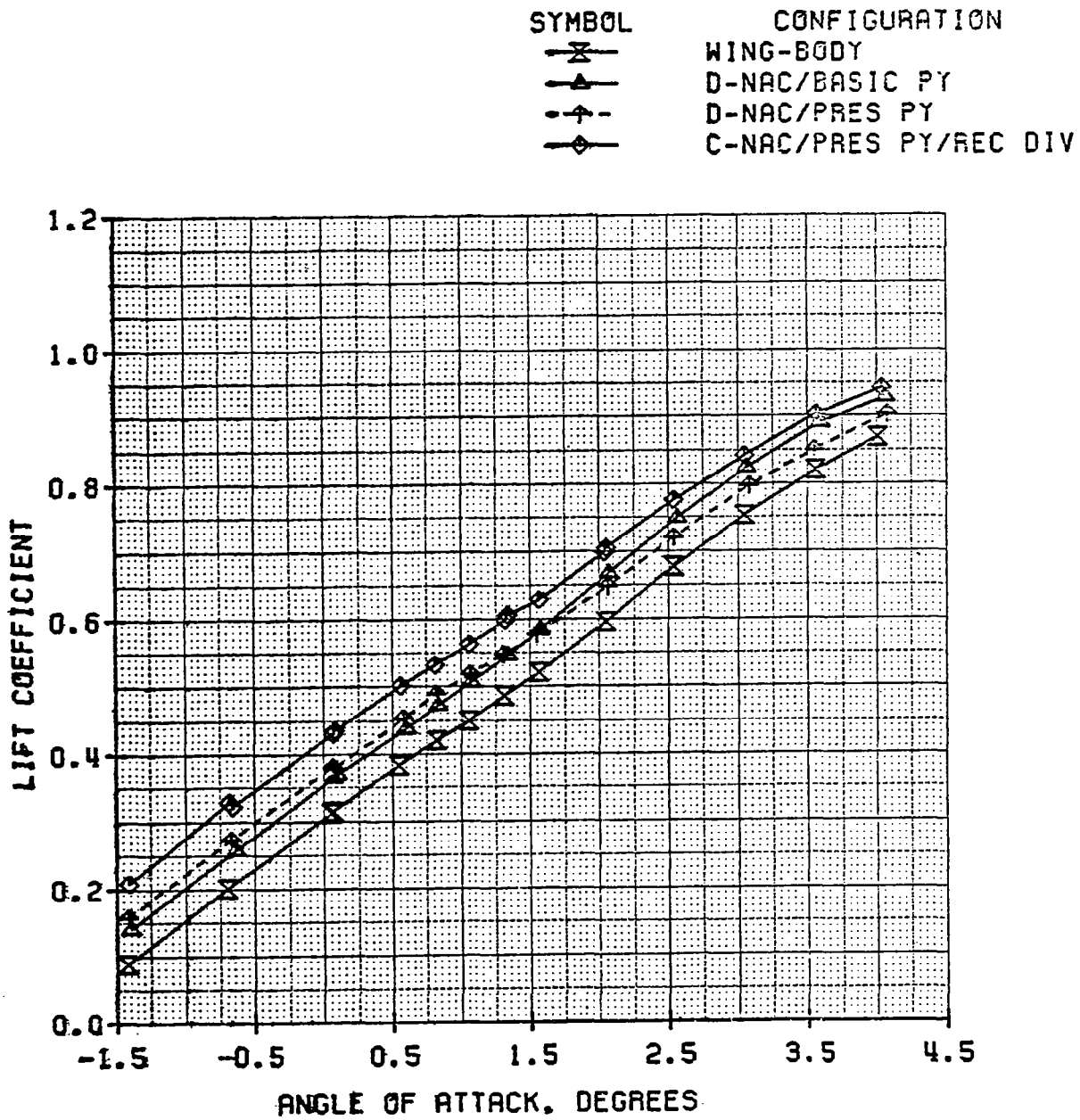

FIGURE A46. LIFT COEFFICIENT VERSUS ANGLE OF ATTACK

AT M=0.81 FOR WB, D/BAS, C/BAS/REC,

C/BAS/HL AND UTW CONFIGURATIONS

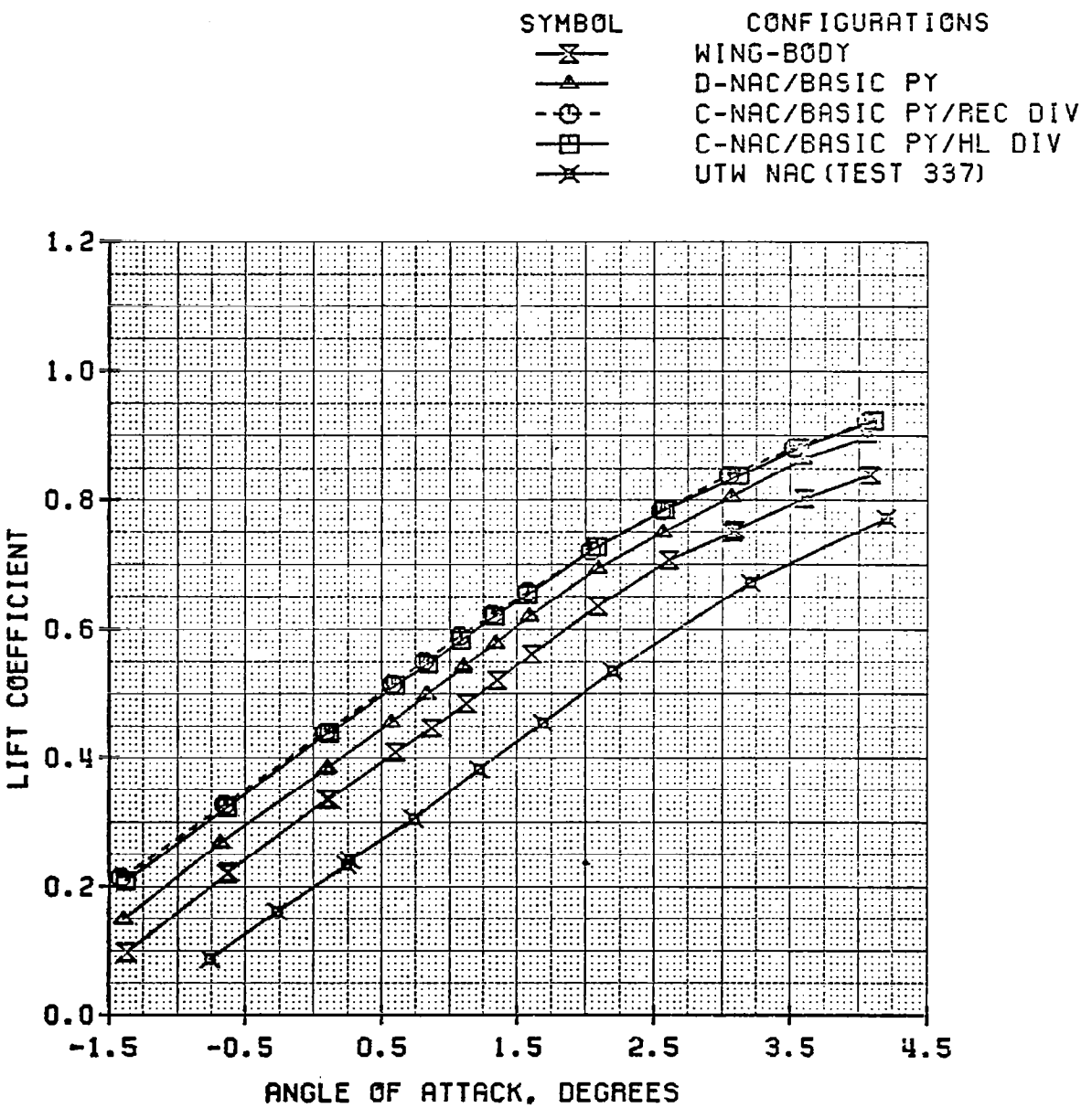

FIGURE A47. LIFT COEFFICIENT VERSUS ANGLE OF ATTACK

AT MACH 0.81 FOR WB, D/BAS, D/PRES

AND C/PRES/REC CONFIGURATIONS

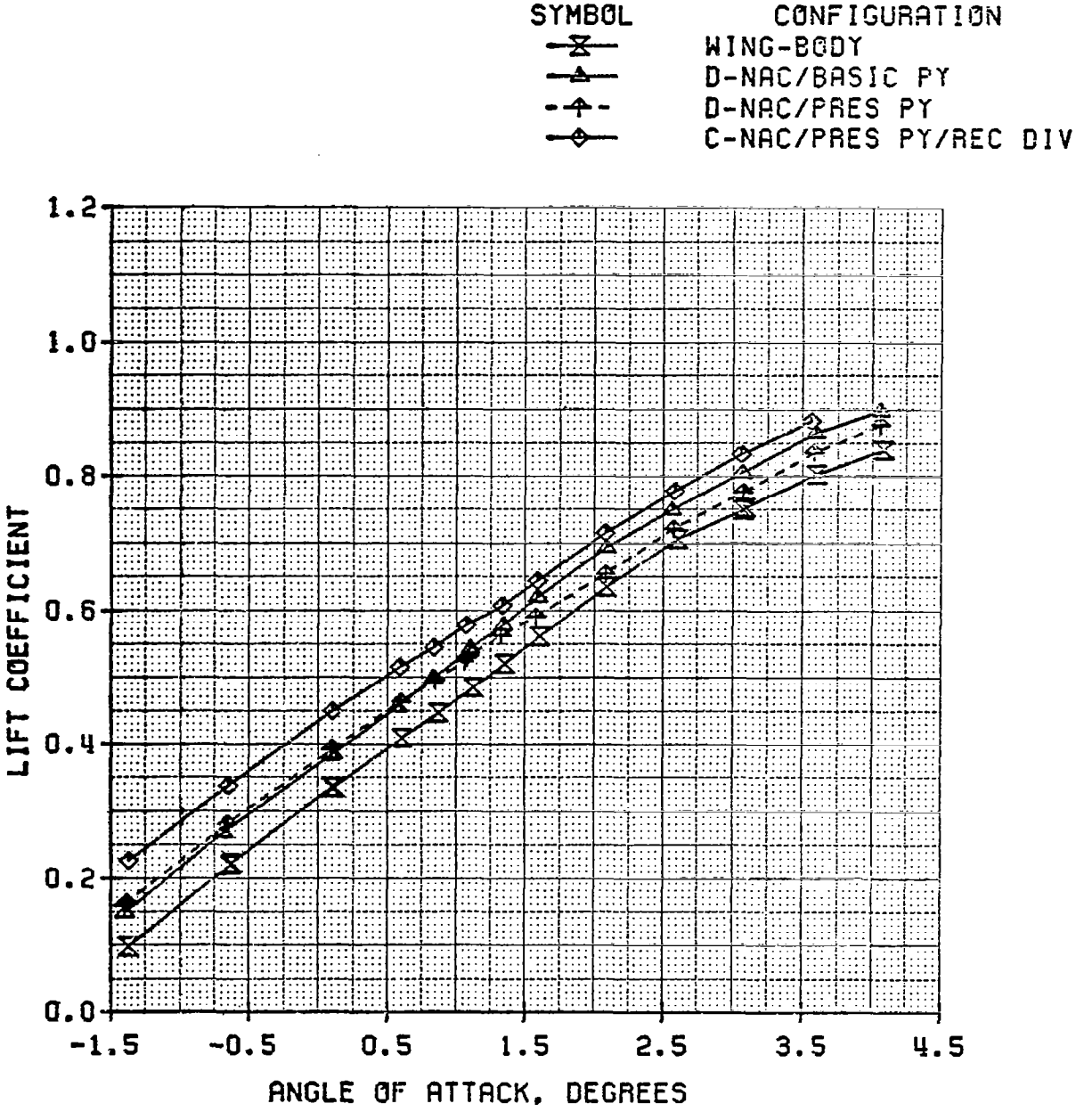

FIGURE A48. LIFT COEFFICIENT VERSUS ANGLE OF ATTACK AT M=0.83 FOR WB, D/BAS, C/BAS/REC AND C/BAS/HL CONFIGURATIONS

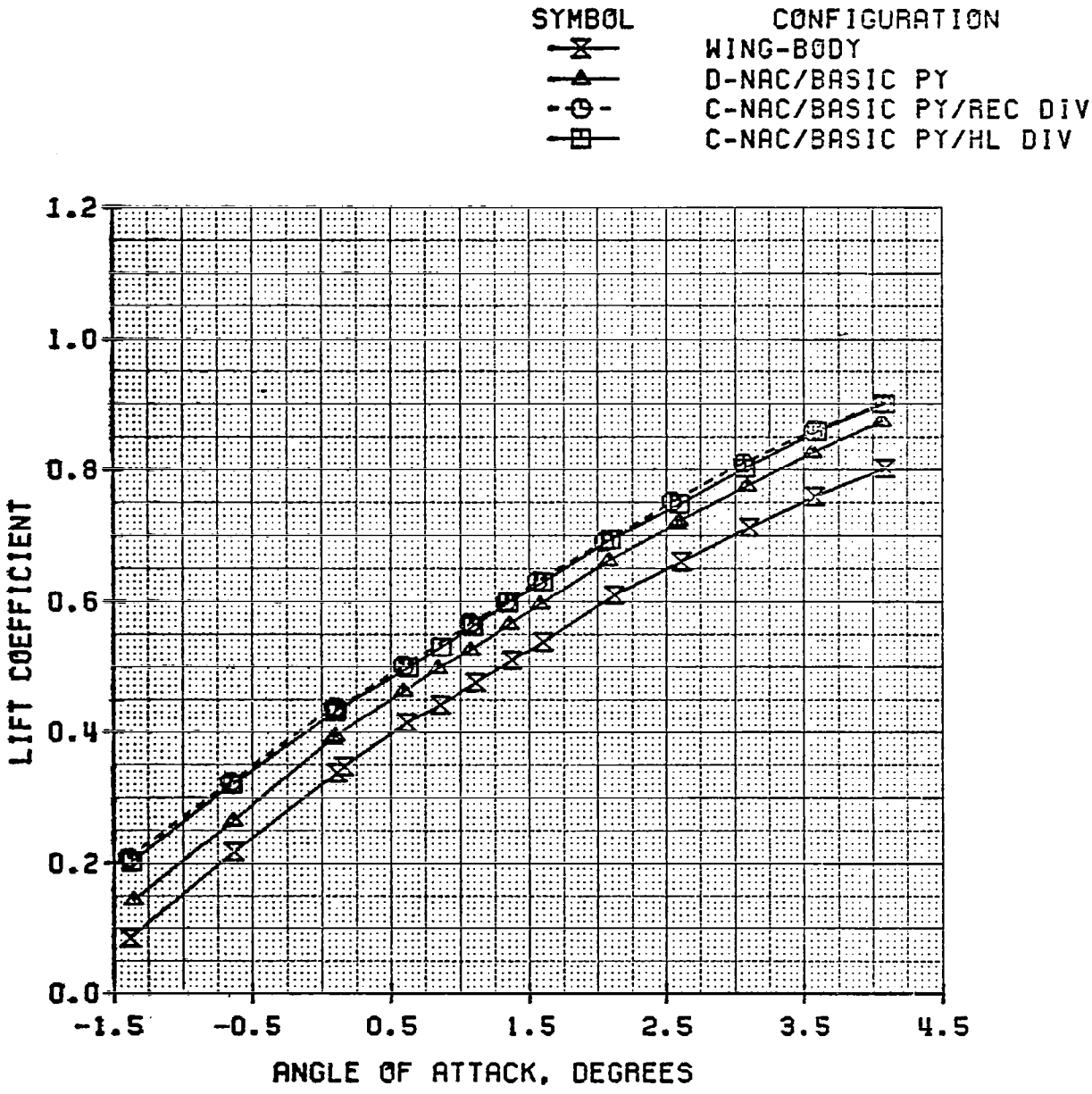

FIGURE A49. LIFT COEFFICIENT VERSUS ANGLE OF ATTACK

AT MACH 0.83 FOR WB, D/BAS, D/PRES

AND C/PRES/REC CONFIGURATIONS

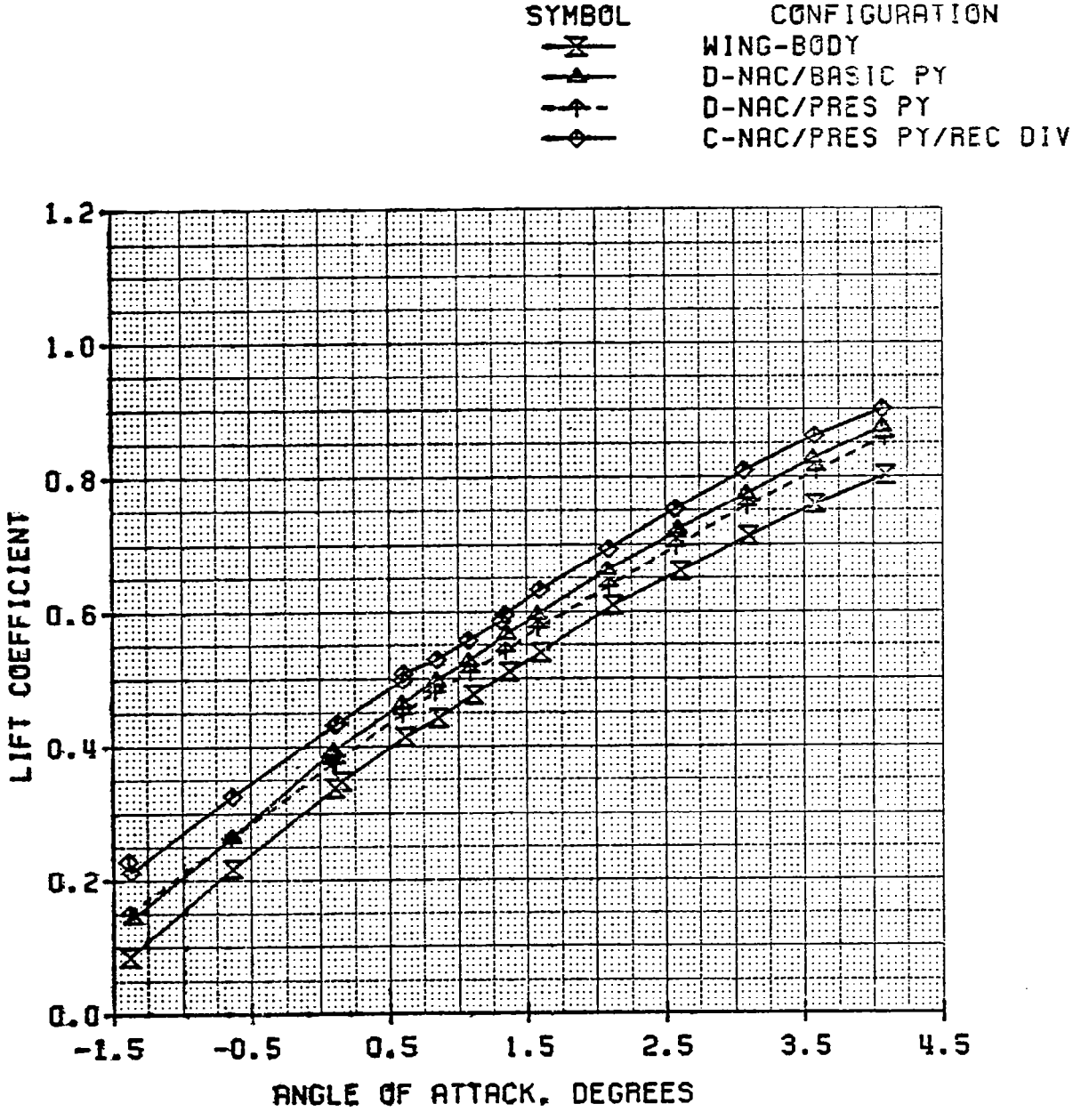

FIGURE A50. LIFT COEFFICIENT VERSUS ANGLE OF ATTACK AT M=0.85 FOR WB, D/BAS, C/BAS/REC AND C/BAS/HL CONFIGURATIONS

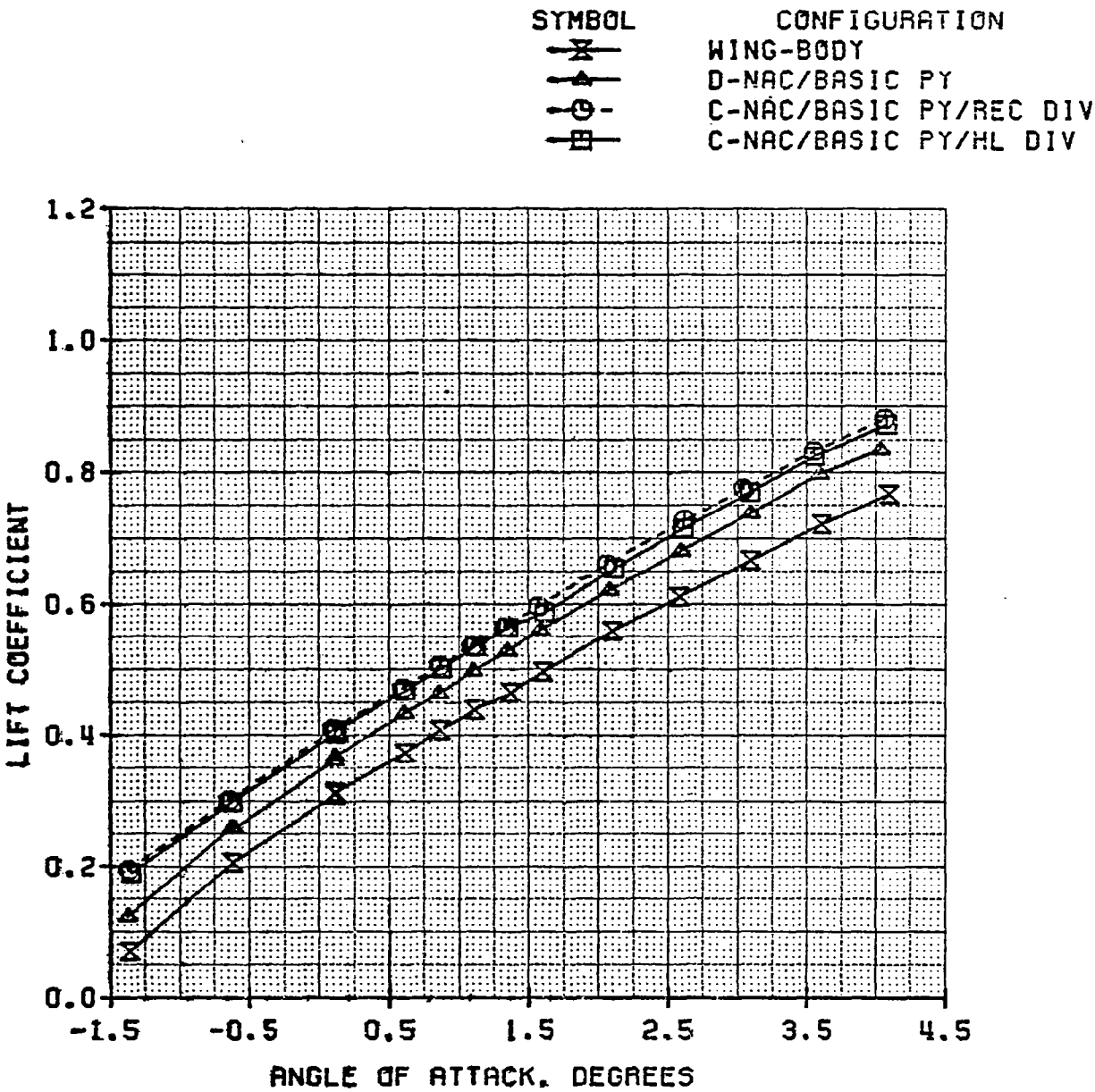

FIGURE A51. LIFT COEFFICIENT VERSUS ANGLE OF ATTACK

AT MACH 0.85 FOR WB, D/BAS, D/PRES

AND C/PRES/REC CONFIGURATIONS

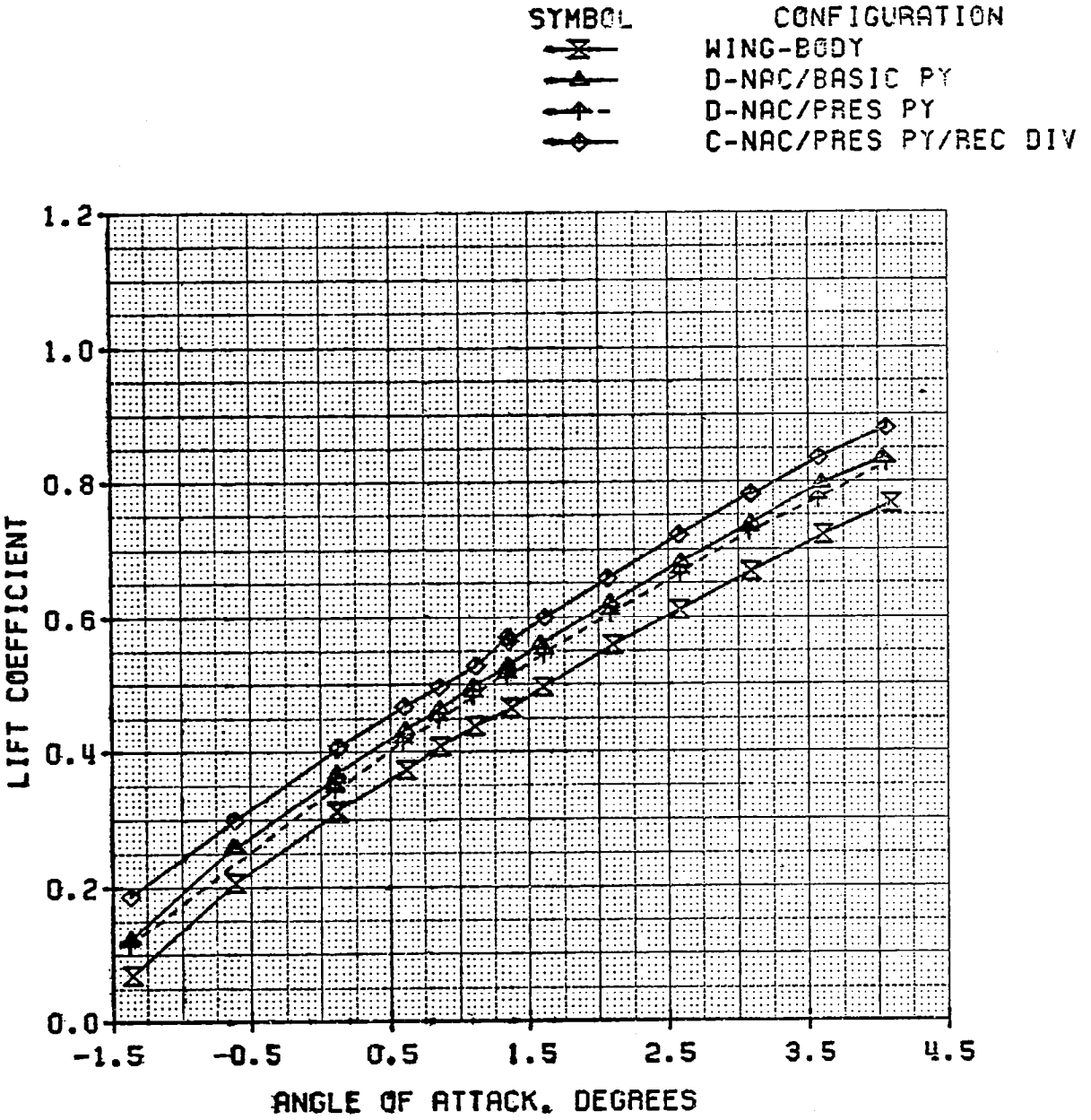

FIGURE A52. LIFT COEFFICIENT VERSUS PITCHING MOMENT COEFFICIENT AT M=0.70 FOR WB, D/BAS, C/BAS/HL, C/BAS/REC AND UTW CONFIG.

SYMBOL	CONFIGURATIONS
	WING-BODY
	D-NAC/BASIC PY
	C-NAC/BASIC PY/HL DIV
	C-NAC/BASIC PY/REC DIV
	UTW NAC (TEST 337)

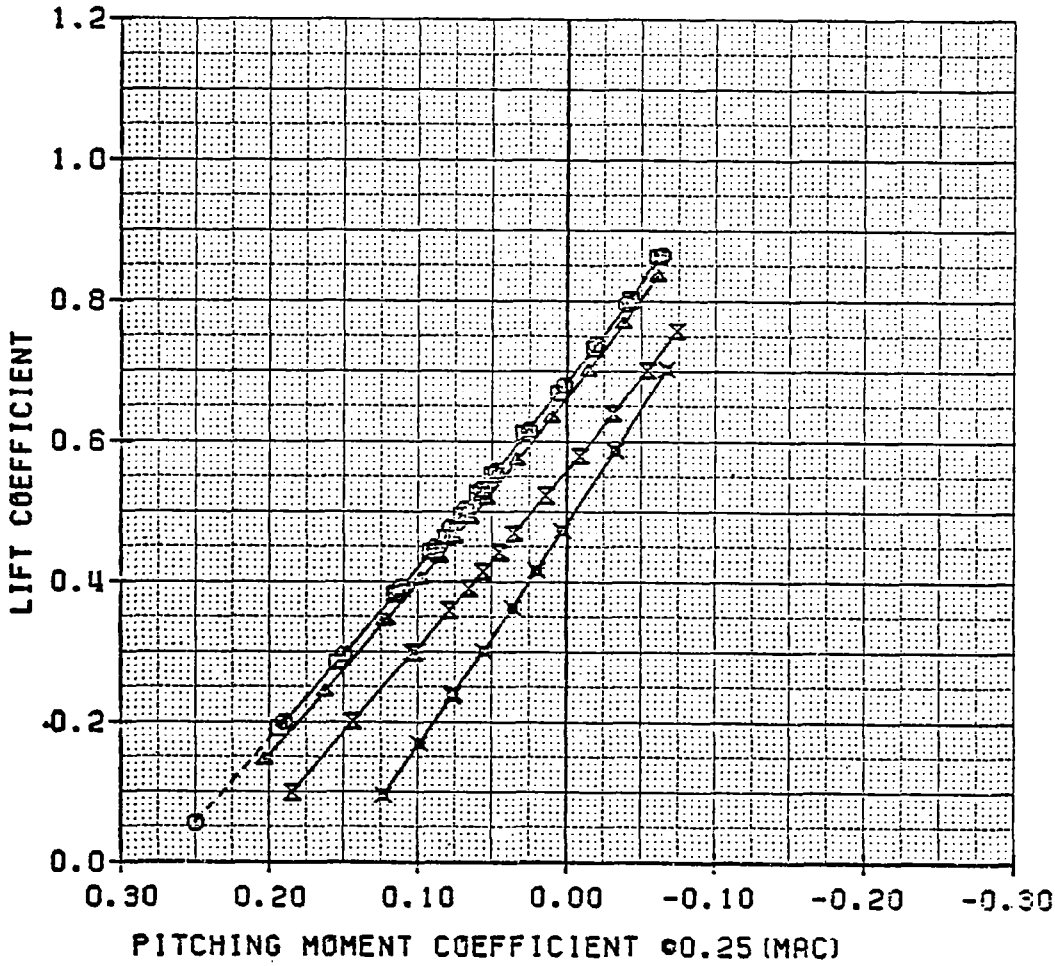

FIGURE A53. LIFT COEFFICIENT VERSUS PITCHING MOMENT COEFFICIENT AT M=0.70 FOR WB, D/BAS, D/PRES AND C/PRES/REC CONFIG.

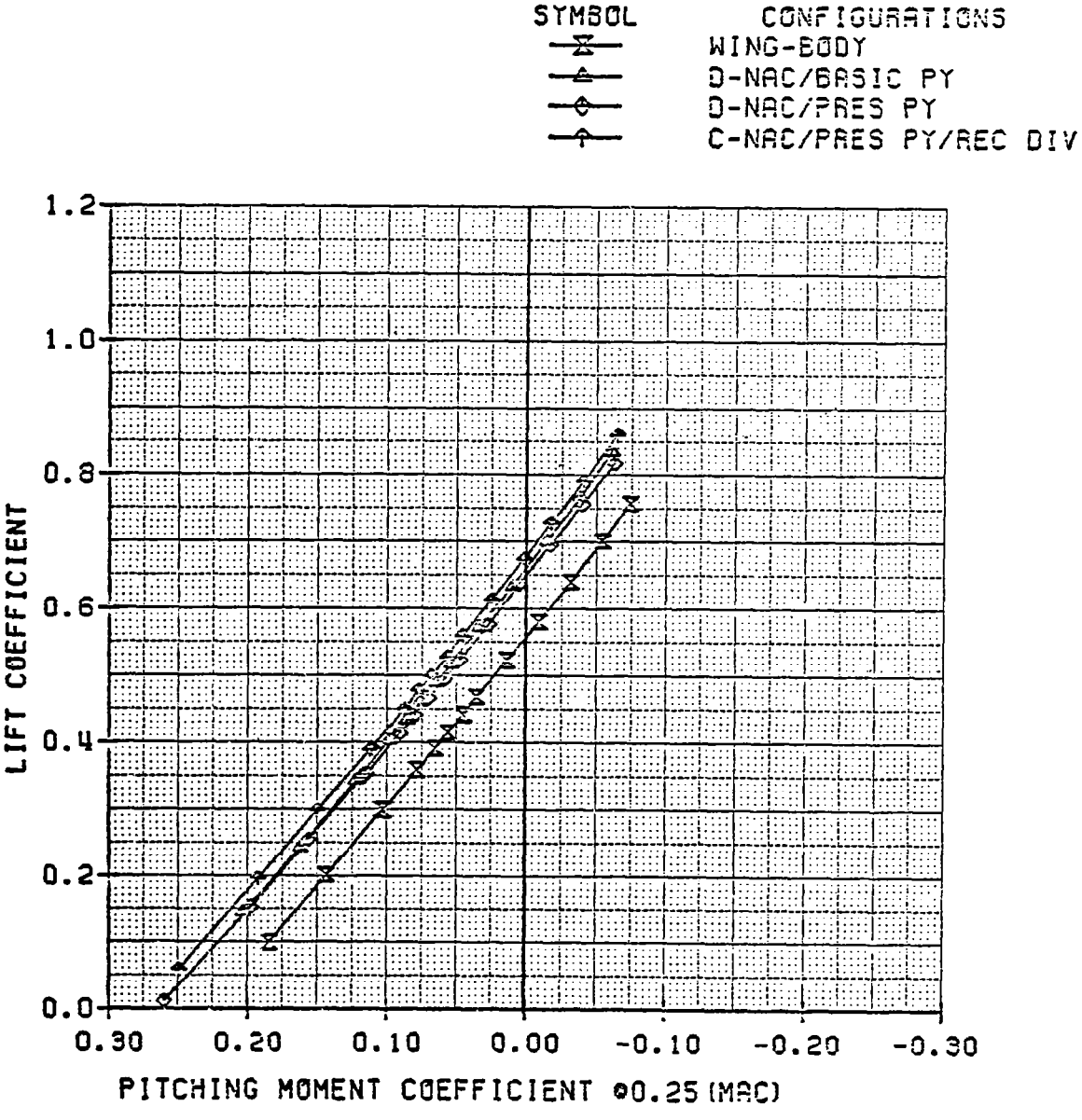

FIGURE A54. LIFT COEFFICIENT VERSUS PITCHING MOMENT COEFFICIENT AT M=0.75 FOR WB, D/BAS, C/BAS/HL, C/BAS/REC AND UTW CONFIG.

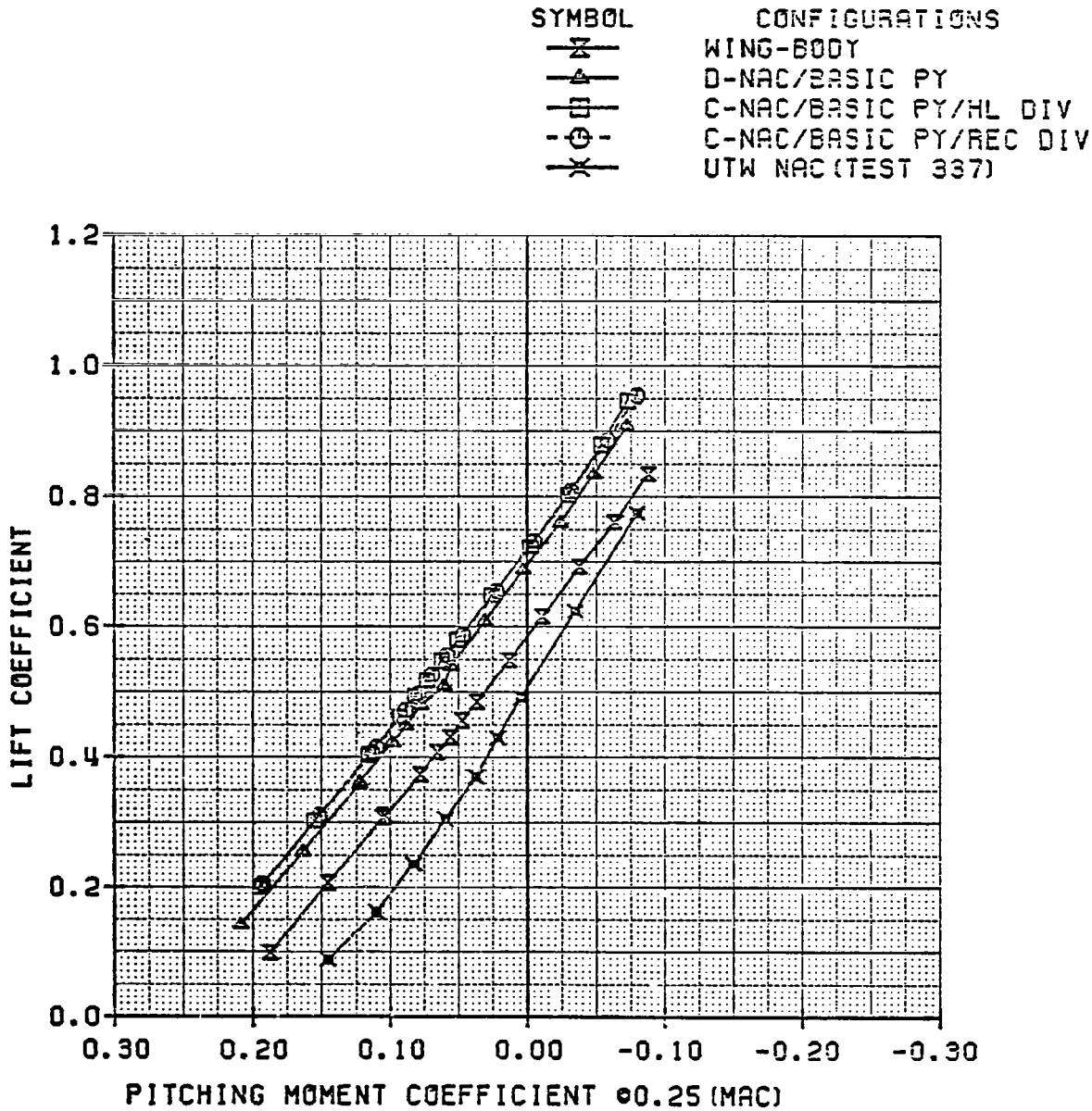

FIGURE A55. LIFT COEFFICIENT VERSUS PITCHING MOMENT COEFFICIENT AT M=0.75 FOR WB, D/BAS, D/PRES AND C/PRES/REC CONFIG.

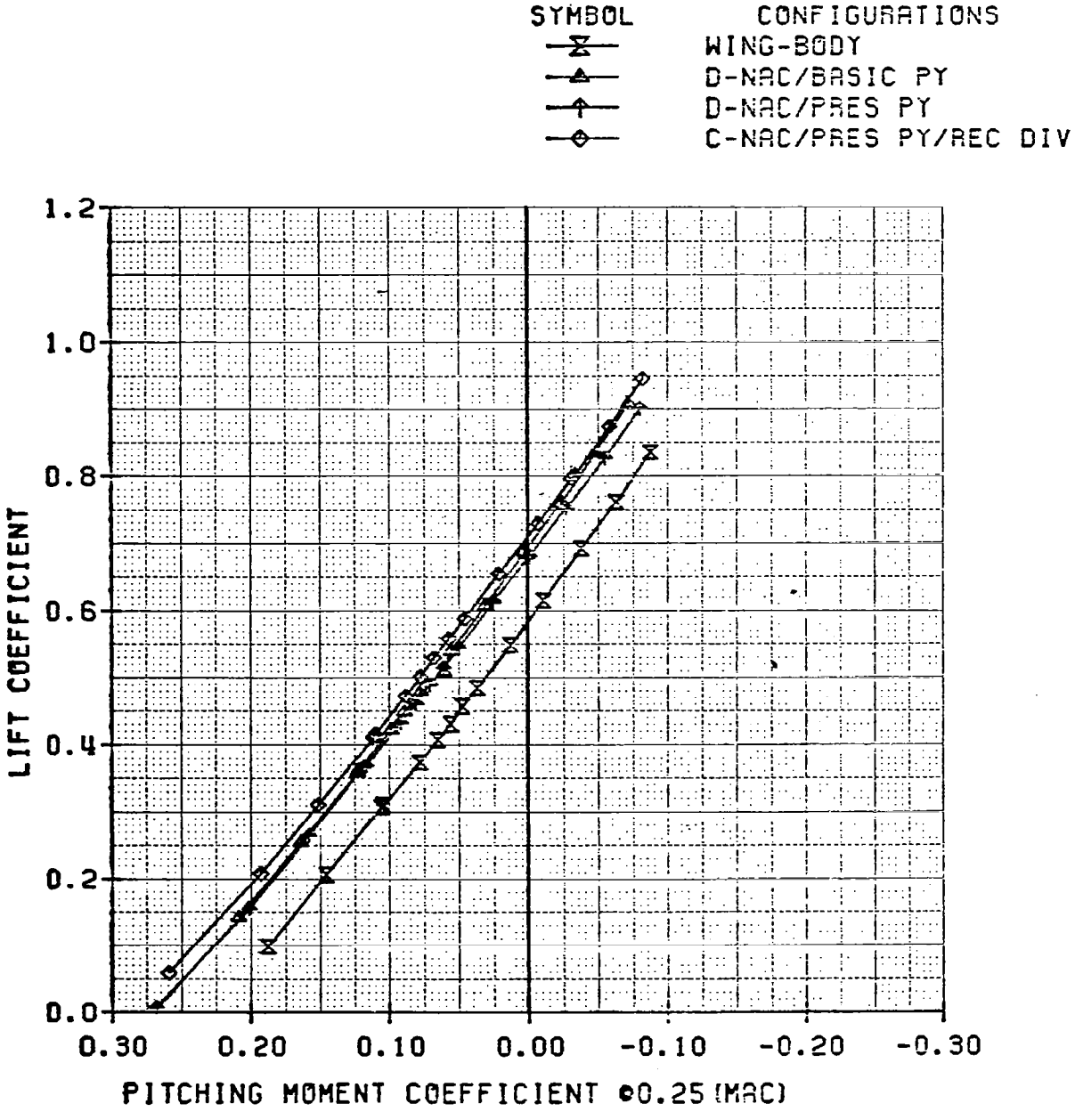

FIGURE A56. LIFT COEFFICIENT VERSUS PITCHING MOMENT COEFFICIENT AT M=0.78 FOR WB, D/BAS, C/BAS/HL, C/BAS/REC, AND UTW CONFIG.

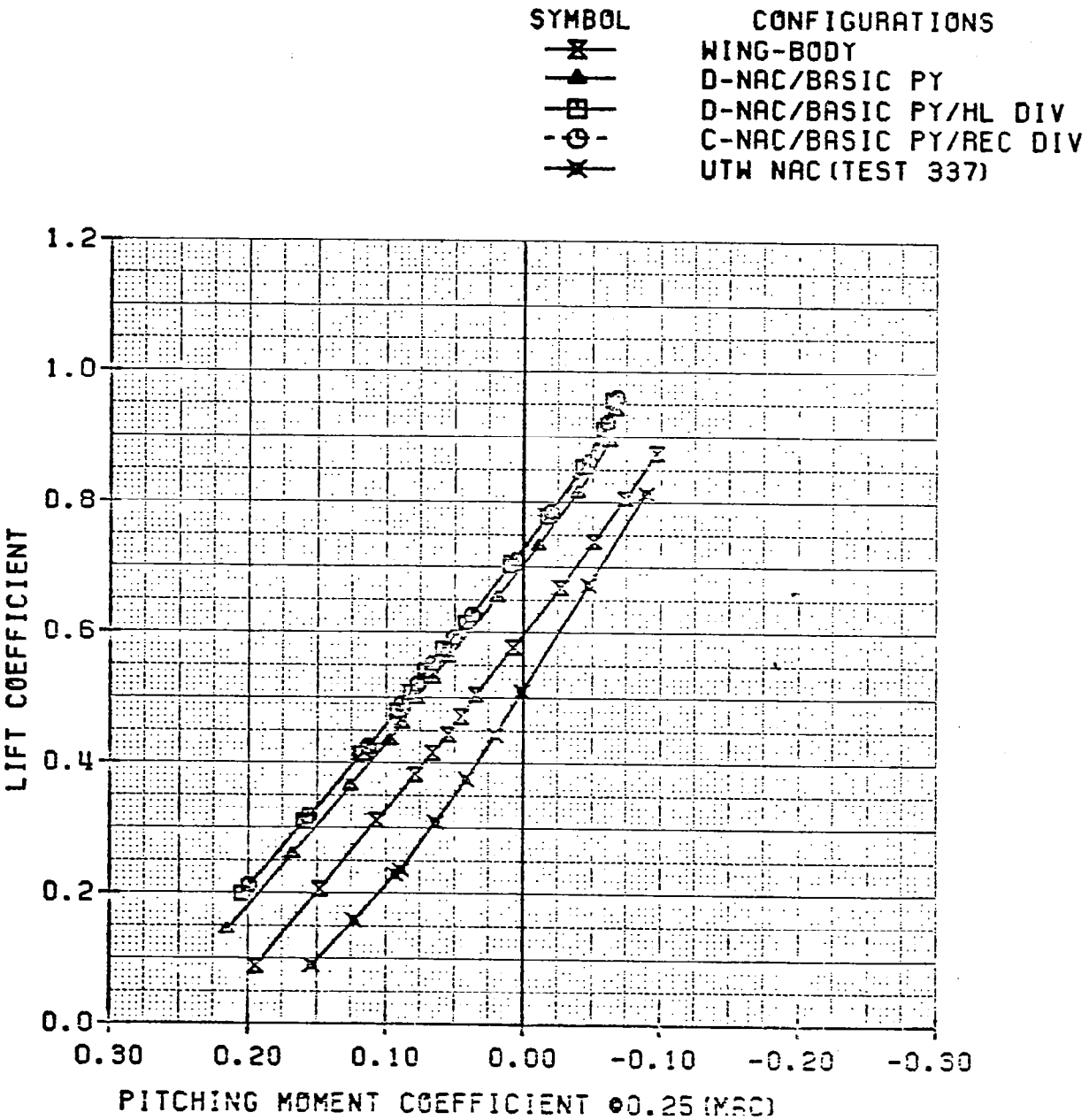

FIGURE A57. LIFT COEFFICIENT VERSUS PITCHING MOMENT COEFFICIENT AT M=0.78 FOR WB, D/BAS, D/PRES AND C/PRES/REC CONFIG.

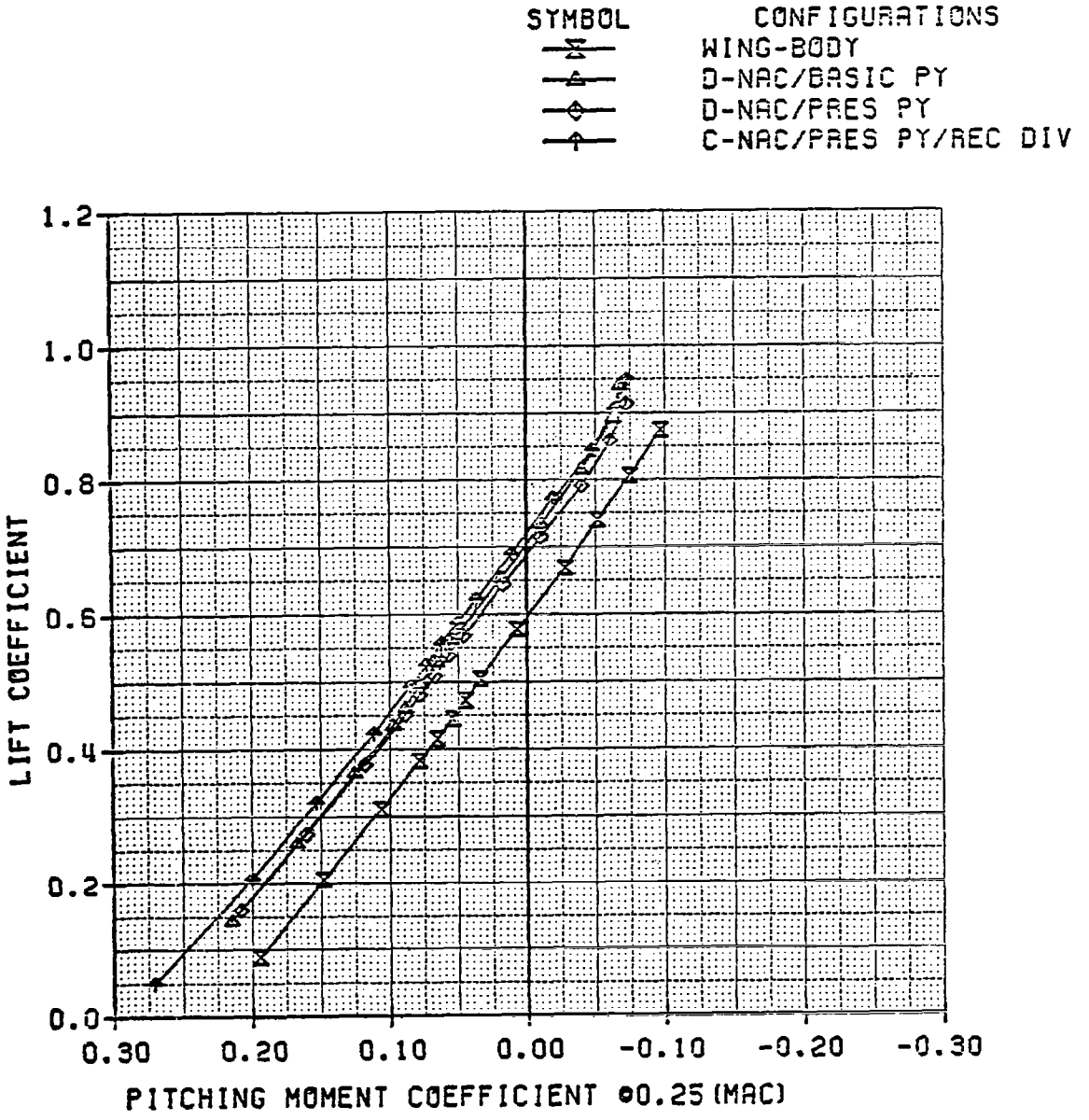

FIGURE A58. LIFT COEFFICIENT VERSUS PITCHING MOMENT COEFFICIENT AT M=0.79 FOR WB, D/BAS, C/BAS/HL, C/BAS/REC AND UTW CONFIG.

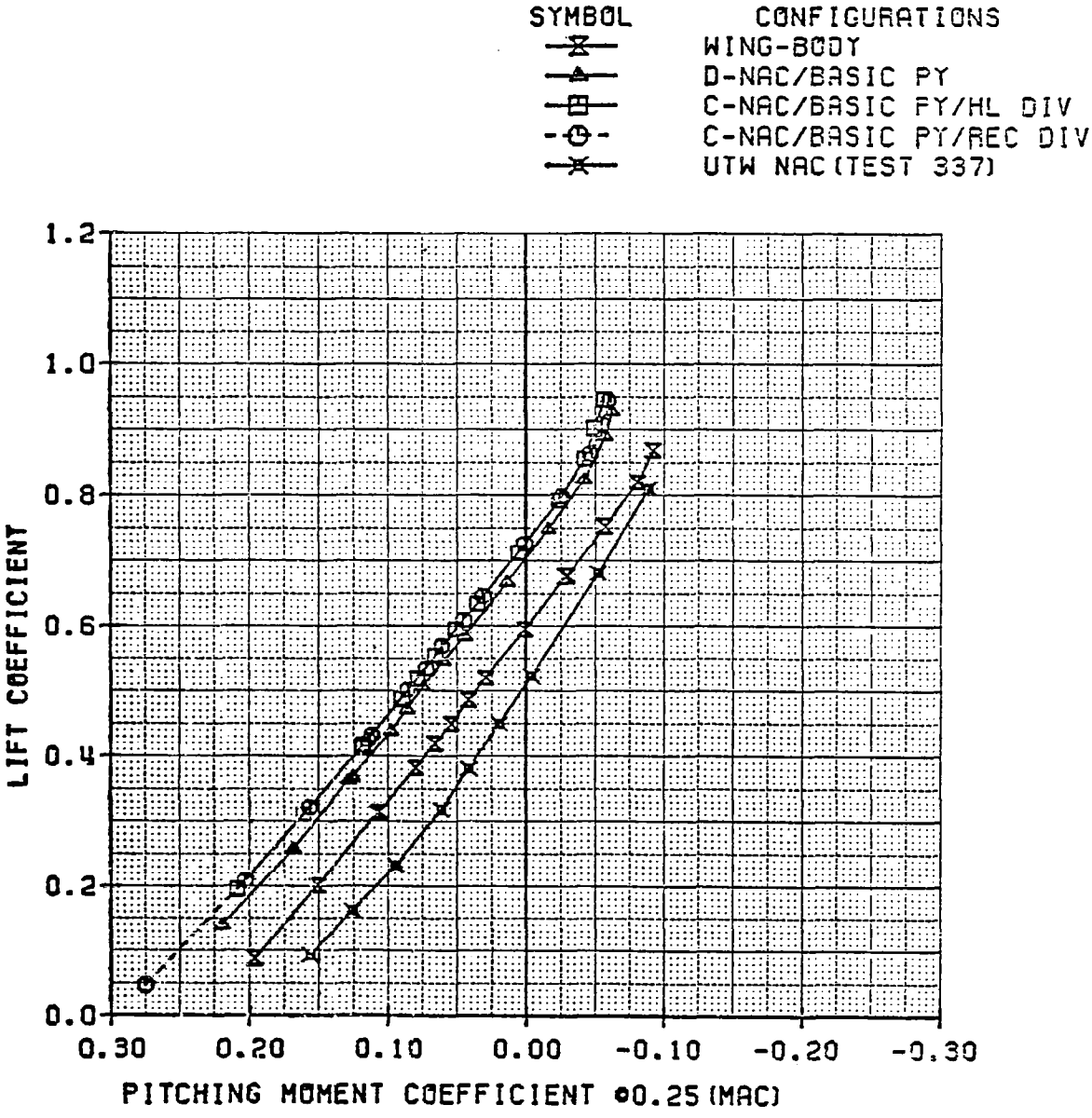

FIGURE A59. LIFT COEFFICIENT VERSUS PITCHING MOMENT COEFFICIENT AT M=0.79 FOR WB, D/BAS, D/PRES AND C/PRES/REC CONFIG.

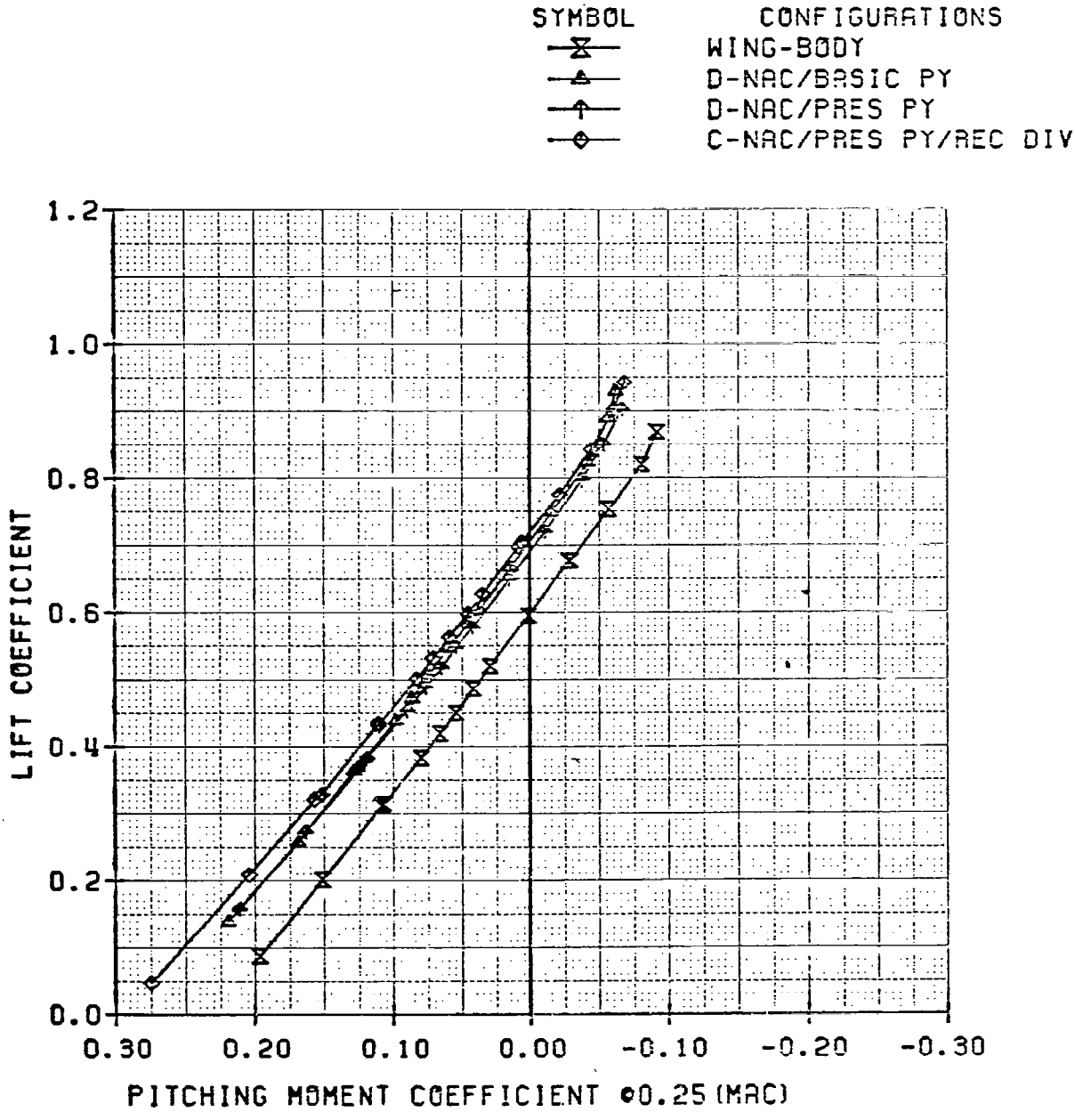

FIGURE A60. LIFT COEFFICIENT VERSUS PITCHING MOMENT COEFFICIENT AT M=0.81 FOR WB, D/BAS, C/BAS/HL, C/BAS/REC AND UTW CONFIG.

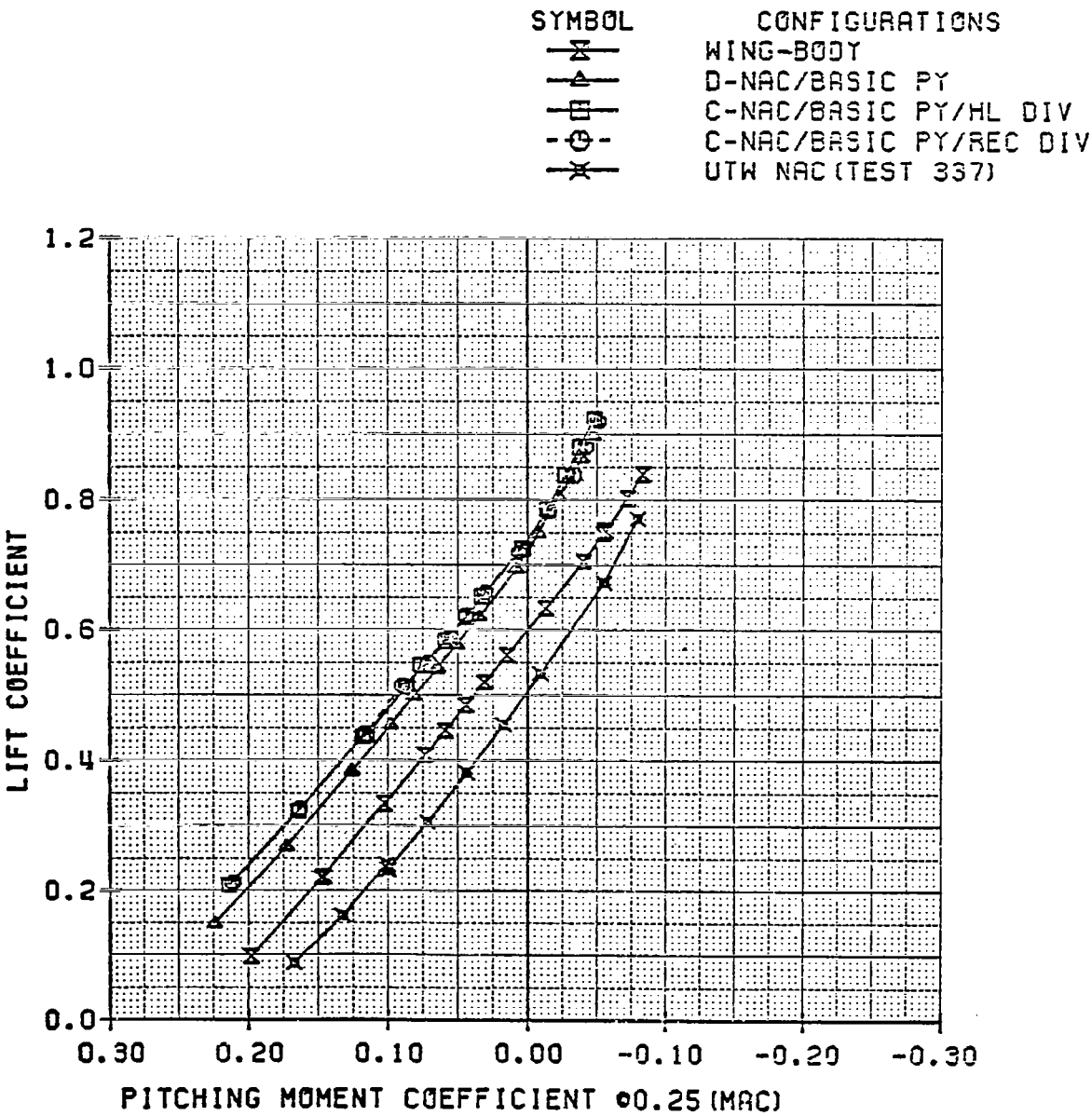

FIGURE A61. LIFT COEFFICIENT VERSUS PITCHING MOMENT COEFFICIENT AT M=0.81 FOR WB, D/BAS, D/PRES AND C/PRES/REC CONFIG.

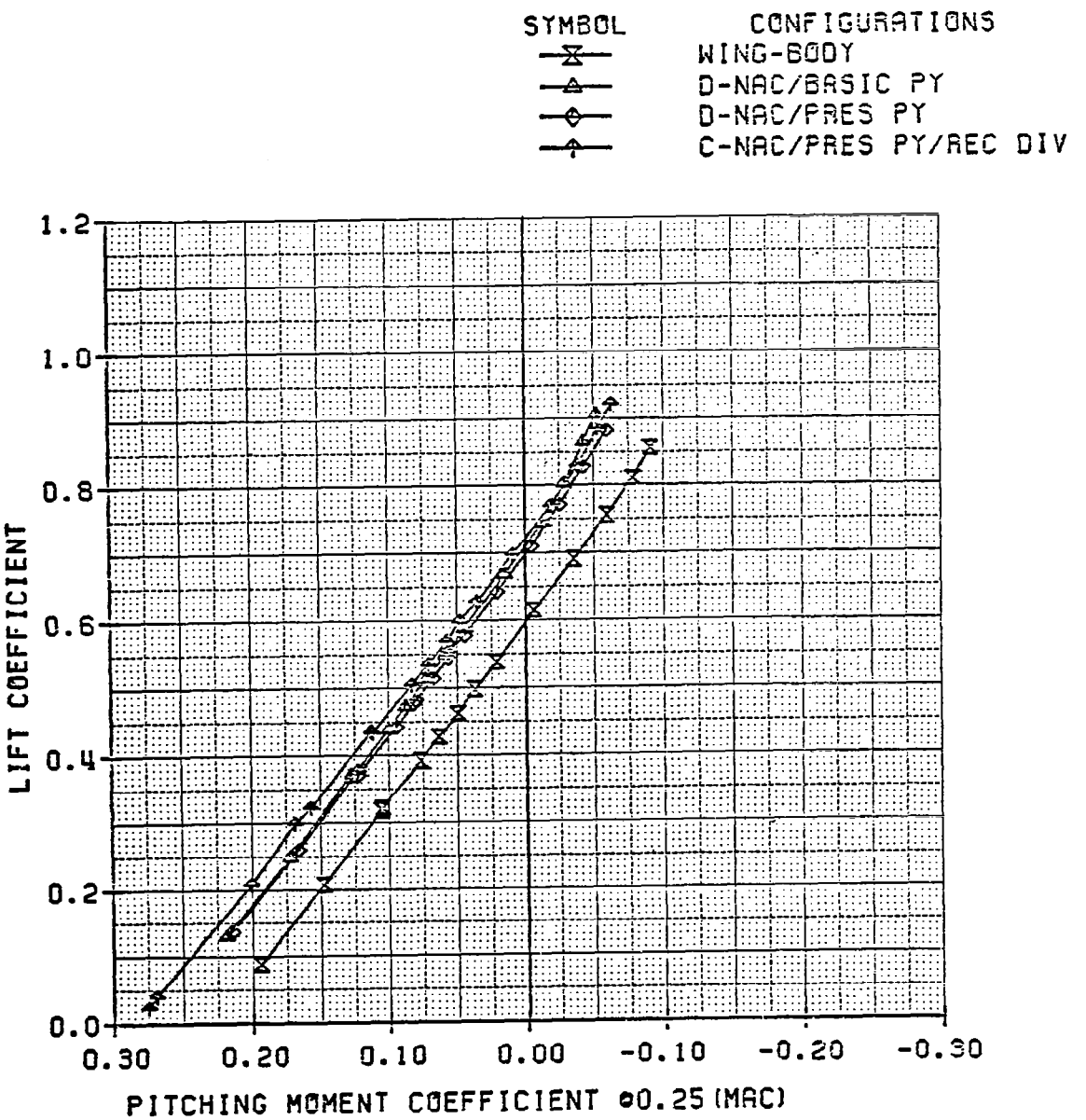

FIGURE A62. LIFT COEFFICIENT VERSUS PITCHING MOMENT COEFFICIENT AT M=0.83 FOR WB, D/BAS, C/BAS/HL AND C/BAS/REC CONFIG.

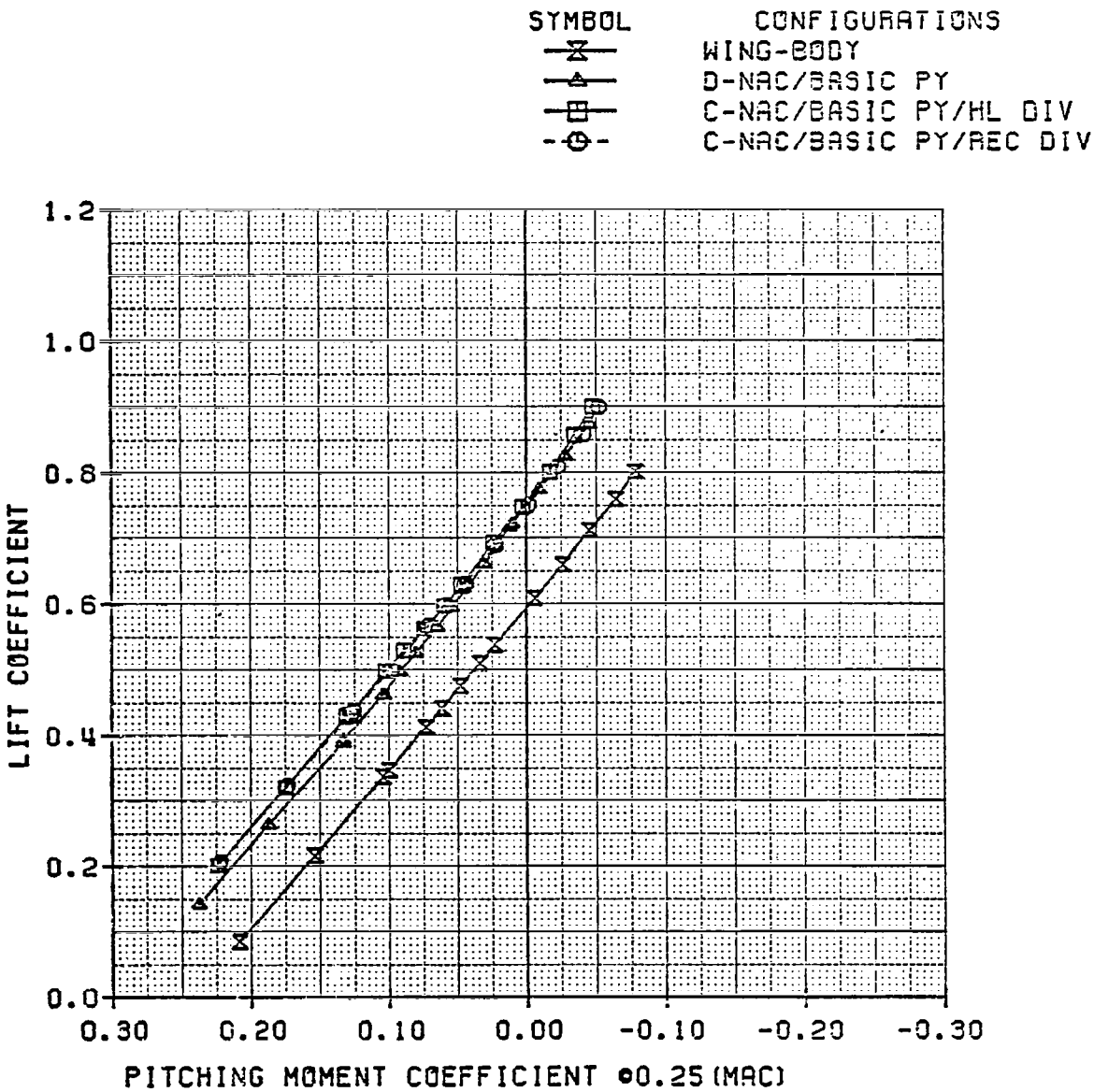

FIGURE A63. LIFT COEFFICIENT VERSUS PITCHING MOMENT COEFFICIENT AT M=0.83 FOR WB, D/BAS, D/PRES AND C/PRES/REC CONFIG.

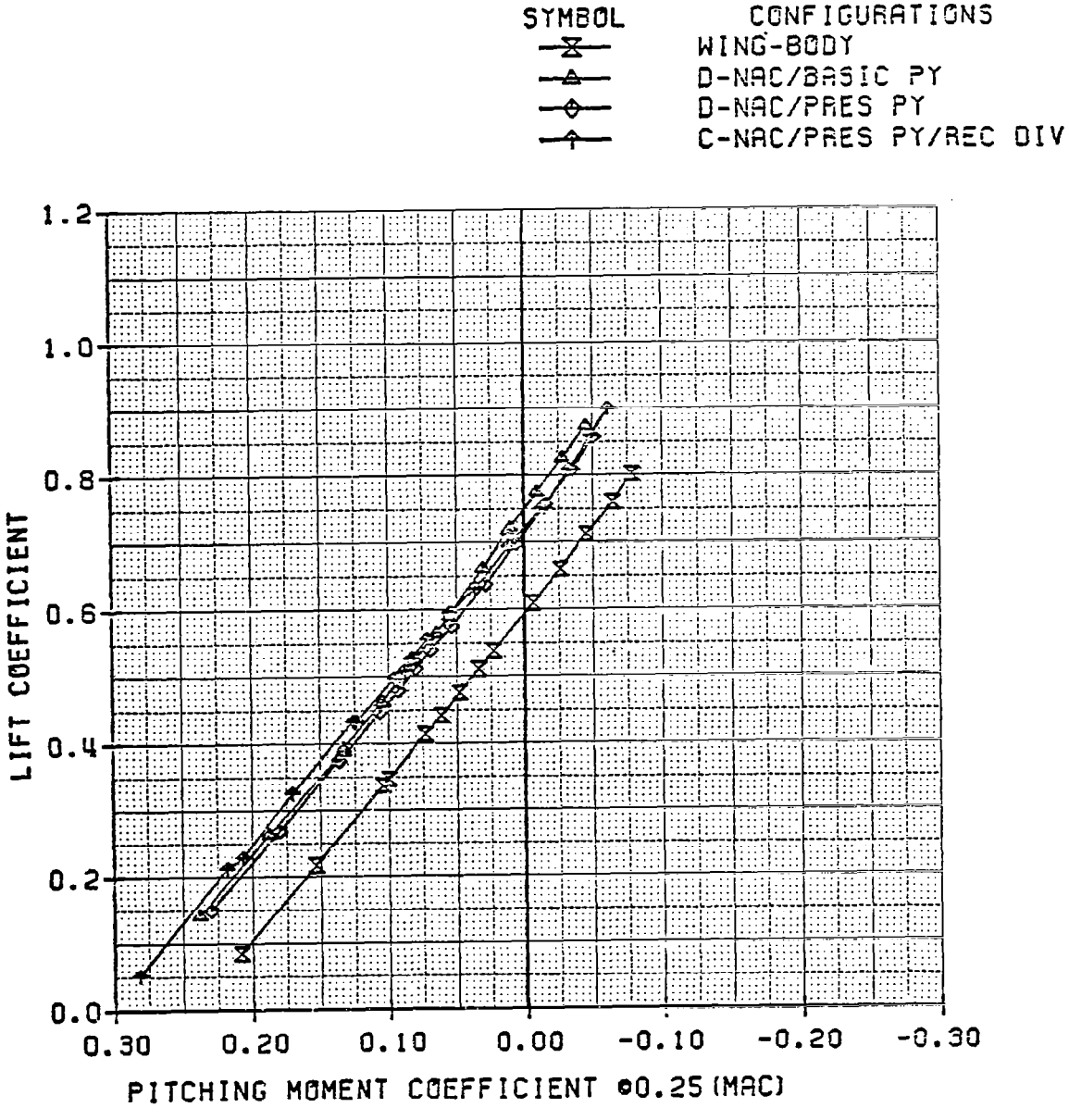

FIGURE A64. LIFT COEFFICIENT VERSUS PITCHING MOMENT COEFFICIENT AT M=0.85 FOR WB, D/BAS, C/BAS/HL AND C/BAS/REC CONFIG.

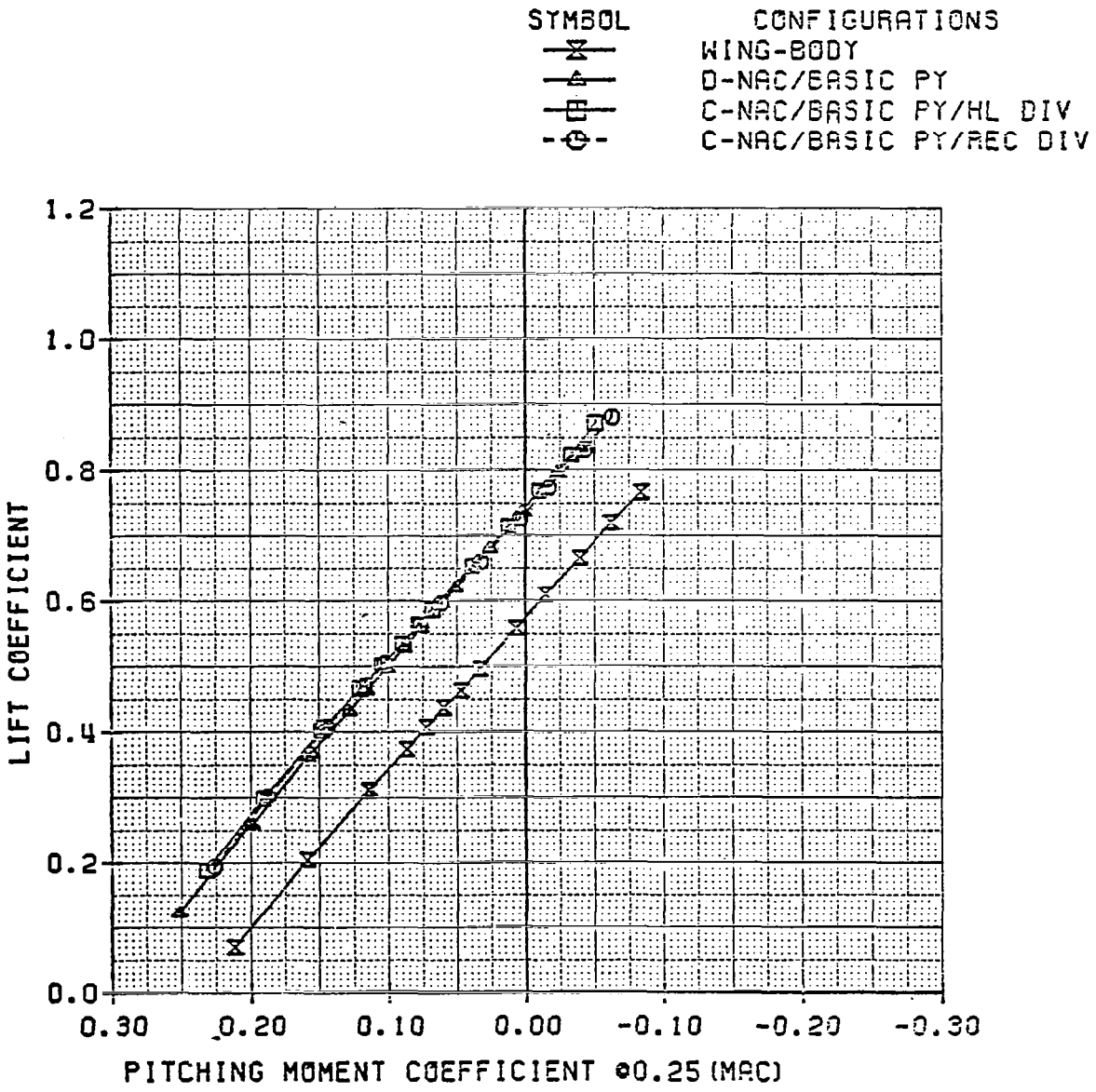

FIGURE A65. LIFT COEFFICIENT VERSUS PITCHING MOMENT COEFFICIENT AT M=0.85 FOR WB, D/BAS, D/PRES AND C/PRES/REC CONFIG.

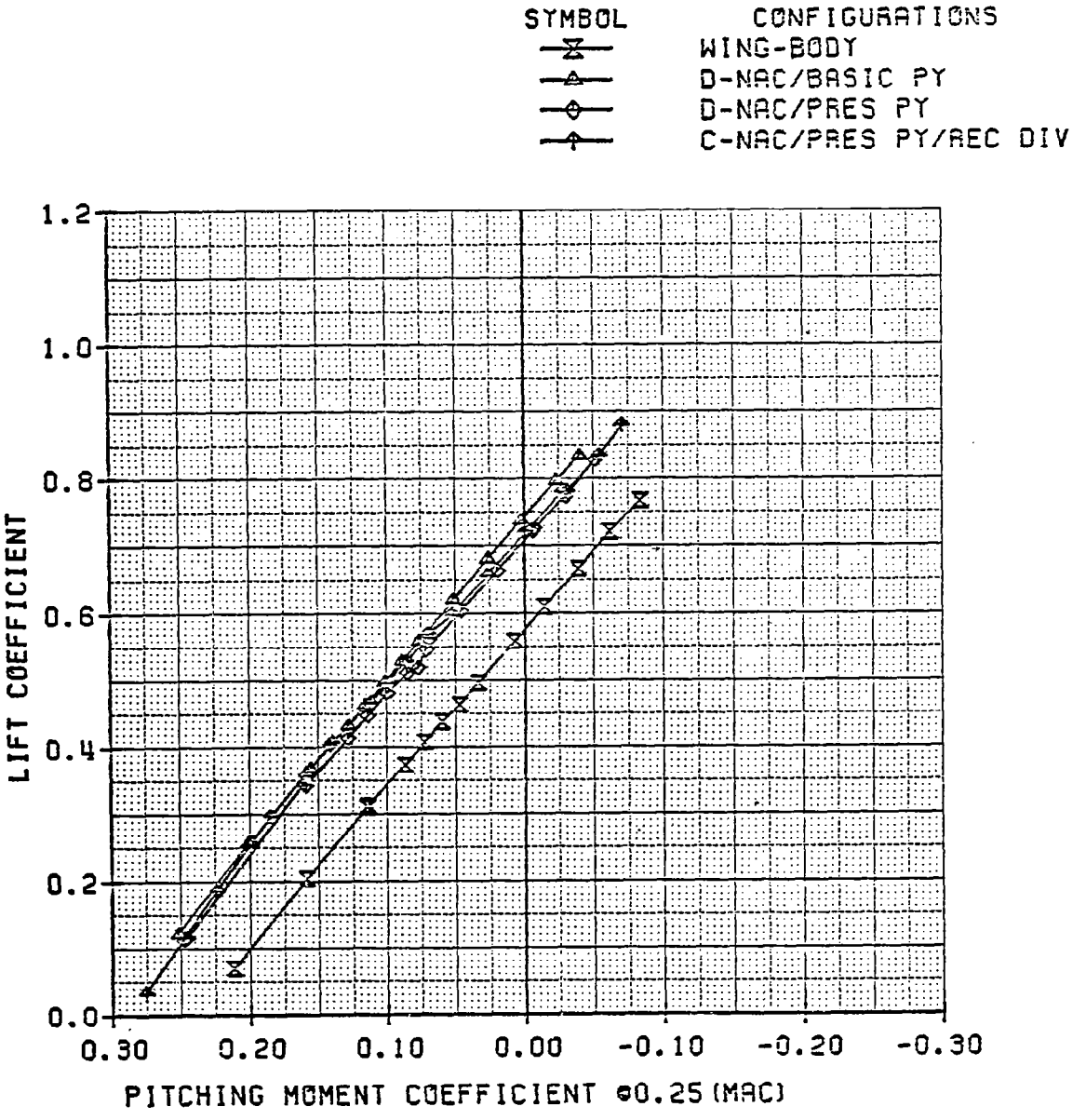

1. Report No.	2. Government Accession No.	3. Recipient's Catalog No.
NASA CR-3743		

4. Title and Subtitle	5. Report Date
EFFECTS OF NACELLE CONFIGURATION/POSITION ON PERFORMANCE OF SUBSONIC TRANSPORT	November 1983
	6. Performing Organization Code
7. Author(s)	8. Performing Organization Report No.
L. H. Bangert, D. K. Krivec, and R. N. Segall	LR 30436
	10. Work Unit No.
9. Performing Organization Name and Address Lockheed-California Company P. O. Box 551 Burbank, California 91520	11. Contract or Grant No. NAS1-16644
	13. Type of Report and Period Covered Contractor report
12. Sponsoring Agency Name and Address National Aeronautics and Space Administration Washington, DC 20546	14. Sponsoring Agency Code

15. Supplementary Notes

Langley technical monitor: William P. Henderson
Final Report

16. Abstract

An experimental study was conducted to explore possible reductions in installed propulsion system drag due to underwing-aft nacelle locations. Both circular (C) and D inlet cross section nacelles were tested. The primary objectives were: to determine the relative installed drag of the C and D-nacelle installations; and, to compare the drag of each aft nacelle installation with that of a conventional underwing-forward, pylon-mounted (UTW) nacelle installation. The tests were performed in the NASA-Langley Research Center 16-Foot Transonic Wind Tunnel at Mach numbers from 0.70 to 0.85, airplane angles of attack from -2.5 to 4.1 degrees, and Reynolds numbers per foot from 3.4 to 4.0 million. The nacelles were installed on the NASA USB full-span transonic transport model with horizontal tail on. The D-nacelle installation had the smallest drag of those tested. The UTW nacelle installation had the largest drag, at 6.8 percent larger than the D at Mach number 0.80 and lift coefficient (C_L) 0.45. Each tested configuration still had some interference drag, however. The effect of the aft nacelles on airplane lift was to increase C_L at a fixed angle of attack relative to the wing-body. There was higher lift on the inboard wing sections because of higher pressures on the wing lower surface. The effects of the UTW installation on lift were opposite to those of the aft nacelles.

17. Key Words (Suggested by Author(s))	18. Distribution Statement
Airframe-Propulsion Integration Aft Nacelle Interference Drag Propulsion System Drag	Unclassified-Unlimited Subject Category 02

19. Security Classif. (of this report)	20. Security Classif. (of this page)	21. No. of Pages	22. Price
Unclassified	Unclassified	202	A10

For sale by the National Technical Information Service, Springfield, Virginia 22161

NASA-Langley, 1983